uOttawa

L'Université canadienne
Canada's university

FACULTÉ DES ÉTUDES SUPÉRIEURES ET POSTOCTORALES

uOttawa

L'Université canadienne
Canada's university

FACULTY OF GRADUATE AND POSDOCTORAL STUDIES

W. Leonardo Cortés Puentes

AUTEUR DE LA THÈSE / AUTHOR OF THESIS

M.A.Sc. (Civil Engineering)

GRADE / DEGREE

School of Information Technology and Engineering

FACULTÉ, ÉCOLE, DÉPARTEMENT / FACULTY, SCHOOL, DEPARTMENT

Nonlinear Modelling and Analysis of Repaired and Retrofitted Shear Walls

TITRE DE LA THÈSE / TITLE OF THESIS

Dan Palermo

DIRECTEUR (DIRECTRICE) DE LA THÈSE / THESIS SUPERVISOR

CO-DIRECTEUR (CO-DIRECTRICE) DE LA THÈSE / THESIS CO-SUPERVISOR

Hassan Aoude

B. Martin-Perez

D. Lau

Gary W. Slater

Le Doyen de la Faculté des études supérieures et postdoctorales / Dean of the Faculty of Graduate and Postdoctoral Studies

Nonlinear Modelling and Analysis of Repaired and Retrofitted Shear Walls

By

W. Leonardo Cortés Puentes

Thesis submitted to the
Faculty of Graduate and Postdoctoral Studies
in partial fulfillment of the requirements
for the degree of Master of Applied Science in
Civil Engineering

Department of Civil Engineering
Faculty of Engineering
University of Ottawa

Your file Votre référence
ISBN: 978-0-494-65494-1
Our file Notre référence
ISBN: 978-0-494-65494-1

Abstract

With advancements in seismic code provisions, mainly as a response to major earthquakes, important parameters such as ductility and energy dissipation have become central in design, resulting in additional detailing for shear walls and other seismic force resisting systems. Due to the large inventory of existing buildings lacking proper detailing for seismic resistance, cost-effective repair and retrofitting techniques have emerged to mitigate seismic risk and satisfy the requirements of current seismic codes.

The finite element method (FEM) has emerged as a complementary analytical tool to investigate and assess various repair and retrofitting techniques. This research provides and validates nonlinear modelling procedures for the analysis of repaired and/or retrofitted shear walls using the FEM. Practical techniques including replacement of concrete, addition of reinforcing bars, external bonding of steel/FRP sheets and plates, addition of unbonded steel rods and plates with delay mechanisms, local replacement of concrete, and bolting of steel plates were investigated.

Table of Contents

List of Figures

List of Tables

To my Beloved son, Sebastián

Acknowledgements

I would like to express all my gratitude to my supervisor Dr. Dan Palermo for providing me with guidance, continuous support and constant discussion throughout this research. His knowledge and experience in seismic behaviour of shear walls was crucial.

Sincere gratitude is due to Dr. Husham Almansour, research associate at the National Research Council (NRC), for being interested in my work.

I gratefully acknowledge the Canadian Bureau for International Education (CBIE) for granting me the Government of Canada Award (GCA) on behalf of the Department of Foreign Affairs and International Trades (DFAIT), and the Canadian Seismic Research Network (CSRN) for financial assistance.

Thanks to my research colleagues at the University of Ottawa, specifically Alaa Abdulridha, for expending his time to discuss topics related to my research. Also thanks to my friend and colleague Alan Lloyd.

Special thanks to my family, my mother, Martha Puentes Castaño; and my sisters, Yeny Cortés Puentes and Jessica Cortés Puentes. Most importantly, I infinitely appreciate the support of my wife, Yomara Calderón, and my son, Sebastián Cortés-Calderón. Their understanding and love have encouraged me to achieve my goals. They will always dignify my life.

Chapter 1

1 Introduction

1.1 General

Repair and/or retrofitting of existing buildings have emerged as a viable solution for seismic upgrading to meet new requirements in modern seismic design provisions, such as ductility and energy dissipation. Failure of a structural element, such as a shear wall, due to an inappropriate repair/retrofit scheme can be catastrophic; therefore, detailed assessment of repair and retrofitting techniques is necessary. In this respect, analysis tools based on the finite element method (FEM) have become useful and economic for academics and practicing engineers. These tools, however, should be investigated and corroborated against experimental data in order to demonstrate their applicability and reliability.

Shear walls are highly efficient seismic force resisting elements when correctly located in a building, owing in part to their high in-plane stiffness. Because of these benefits, use of shear walls has become common in concrete construction, specifically for high-rise buildings. Meanwhile, modern seismic design provisions have incorporated new requirements for design and construction of these elements in response to lessons

learnt from major earthquakes and research conducted worldwide. New requirements have been addressed through stringent reinforcement detailing to guarantee adequate ductility and energy dissipation of the building. Even though new seismic requirements can easily be implemented in the design and construction of new buildings, for the vast majority of existing buildings physical intervention is necessary. Therefore, repair and retrofitting of structural elements such as shear walls have become critical, resulting in emerging and reliable cost-effective repair and retrofitting techniques. These new techniques have focused on seismic response parameters such as energy dissipation and ductility, in addition to traditional global stiffening approaches.

Repair techniques aim to re-establish the initial performance, while retrofitting techniques aim to improve the performance of structural elements such as shear walls. For pre-earthquake scenarios, existing non-damaged shear walls are intervened mainly to meet new seismic code requirements such as ductility and energy dissipation or to increase the stiffness if the former are not possible. On the other hand, for post-earthquake scenarios, damaged shear walls (depending on the level of damage) can be intervened by adding new materials and/or replacing old materials to meet performance requirements of the structural element.

Traditional retrofitting has focused on global stiffening, while other seismic response parameters such as energy dissipation and ductility were not necessarily addressed; this can lead to undesirable behaviour in the intervened structure. Therefore, recent research, specifically experimentally based, has been geared toward investigating and assessing diverse repair/retrofitting techniques to achieve improved seismic performance. Lagging has been complementary analytical tools, which would provide an economical alternative to assess various repair/retrofitting schemes, allowing a systematic evaluation of different design parameters. Significant advancements in the FEM have provided capabilities to perform reliable analysis of repair and retrofitting of concrete structures.

An accurate analysis of a repaired/retrofitted RC structure requires nonlinear algorithms that simulate the construction sequence of the repair and/or retrofitting

intervention. In this regard, the nonlinear finite element program VecTor2 allows changes in the structural model by adding (engaging) unstressed elements and eliminating (disengaging) previously stressed elements. This technique is described by Vecchio and Bucci (1999). Furthermore, the program permits modelling of the interface between the new and old materials. The conceptual bases of VecTor2 are the Modified Compression Field Theory (MCFT) and the Disturbed Stress Field Model (DSFM). The program has an extensive library of models for concrete, steel and fibre reinforced polymers (FRP), which can be extended to other emerging repair/retrofitting materials.

1.2 Research Significance

Due to the increased necessity of retrofitting RC shear walls to satisfy modern seismic code provisions, significant experimental studies have been performed to investigate and assess different repair/retrofitting techniques; however, limited complementary numerical analyses have been reported.

Numerical procedures based on the FEM provide an effective and economic tool to analyze and assess repair and/or retrofit techniques applied to reinforced concrete structures. These procedures allow the analysis of a large number of structures by systematically varying crucial parameters, aiding in the selection and design of effective repair/retrofit strategies.

Furthermore, numerical procedures can be used in engineering offices for specialized works in which nonlinear analyses are necessary, specifically when repair and retrofitting techniques are not well documented in current standards.

1.3 Objectives and Scope

The main objective is to demonstrate the applicability of the FEM method as a procedure capable of simulating repaired and/or retrofitted reinforced concrete shear walls, and to provide modelling procedures for various practical intervention methodologies. Furthermore, this work aims to validate the reliability of the FEM as a useful tool in predicting the behaviour of repaired and/or retrofitted RC shear walls.

The analyses presented herein include representative repair and retrofitting techniques available in the literature that have effectively improved the seismic response of RC shear walls. These techniques are classified in six categories, namely: replacement of concrete, addition of reinforcing bars, external bonding of steel plates, addition of unbonded steel rods and plates with delay mechanisms, external bonding of FRP sheets, and other techniques (local replacement of concrete and bolting of steel plates). The success of the FEM in the analysis of repaired/retrofitted structures depends on the geometric discretization (meshing), the constitutive models, and accurate simulation of the structure before damage.

1.4 Thesis Outline

This thesis focuses on the modelling and analysis of repair and retrofitting techniques and consists of six chapters. Chapter 1 presents a general introduction on nonlinear finite element modelling and analysis of repaired and/or retrofitted shear walls. Furthermore, Chapter 1 presents the research significance, objectives and scope, and thesis outline. Chapter 2 contains a review of repair and retrofitting concepts currently available in the literature. Chapter 3 describes the finite element program VecTor2 and the methodology used for modelling and analyzing repaired/retrofitted shear walls. Chapter 4 presents a parametric study to assess salient constitutive models for reinforced concrete, which are available in the FE program VecTor2. Chapter 5 describes the modelling, and discusses results of the analysis of the repaired and/or retrofitted shear walls presented in this study. Finally, Chapter 6 summarizes

and concludes the work presented in this thesis, and provides recommendations for future work.

Chapter 2

2 Literature Review

2.1 Introduction

This chapter provides a review of existing studies concerning modelling and nonlinear analysis of repaired and retrofitted reinforced concrete structures, specifically shear walls, for seismic applications.

Section 2, Repair and Retrofitting of Shear Walls, summarizes existing experimental research on typical repair/retrofitting techniques applied to reinforced concrete (RC) shear walls to improve seismic behaviour. The techniques included in this review are: replacement of concrete; replacement of steel; external bonding of steel plates; external bonding of FRP sheets; addition of shape memory alloys; and other techniques, such as bolting of steel plates and addition of steel rods/plates with delay mechanisms.

Section 3, Analysis of Repaired/Retrofitted Structures, presents analytical and numerical methods that have been used for the assessment of repair/retrofitting techniques applied to RC structures.

Finally, Section 4 discusses the shortcomings of the existing research on repair and/or retrofitting techniques applied to reinforced concrete structures and the numerical analysis procedures used to assess these techniques.

2.2 Seismic Repair and Retrofitting of Shear Walls

2.2.1 Overview

As stated by Fintel (1991), shear walls are efficient in controlling lateral displacements and severe damage. Furthermore, RC shear walls not specifically detailed for seismic effects have been reported to provide satisfactory behaviour in terms of global performance. On the other hand, modern seismic code provisions have imposed new requirements aimed to improve important seismic behavioural aspects such as ductility, energy dissipation and control of undesirable brittle modes of failure. To ensure acceptable seismic behaviour of existing RC shear walls, cost-effective repair and retrofitting techniques have emerged to improve the performance of this structural element. There are two approaches for seismic repair and retrofitting of RC structures: global modification of the structural system, and local modification of the isolated structural components.

Global modification of the structure is aimed to improve the structural and non-structural element capacity to be greater than the target global performance demand (often target displacement) (Moehle, 2000). The intervention can be performed by adding RC shear walls to reduce drift and decrease ductility demand. Design of the intervention involves the analysis of the new rehabilitated structure with special attention to the transfer of inertial forces through the new elements and the integration of these elements to the existing structure. Other global modifications are the addition of concentric and eccentric steel bracing to existing frames, and the use of seismic isolating systems.

Local modification of structures is aimed to improve deficient components so that they will not reach their limit states as the building responds at the required level (Moehle,

2000). Some of the common rehabilitation techniques are: replacement of concrete (including shotcreting), injection of cracks, addition/replacement of steel reinforcing bars, bonding of steel plates (including jacketing of steel plates), bonding of FRP sheets/plates, addition of shape memory alloys, and others techniques, such as bolting of steel plates, addition of external unbonded steel plates/bars with delay mechanisms, and addition of headed steel reinforcing bars. This study is focused on local intervention techniques; therefore, Chapter 2 contains a review of repair and retrofitting of RC shear walls by these techniques.

2.2.2 Replacement of Concrete and Injection of Cracks

Injection of cracks is a versatile and economical method for repairing RC structures. The effectiveness of the repair depends on the ability of the adhesive material to penetrate into the fine cracks of the damaged concrete. Epoxy injection can be used in cracks up to 5 to 6 mm; beyond this size, cement grout is the appropriate material for the injection (Thermou and Elnashai, 2006). When the concrete is heavily cracked, and injection of cracks is not sufficient to restore the initial capacity of the structure, removal of the old concrete and addition of new concrete is necessary. Replacement of concrete depends on material compatibility, properties of the new concrete, ease of application, and cost-effectiveness. New concrete can be regularly casted, grouted, dry-packed, or sprayed (shotcrete).

Lefas and Kotsovos (1990) conducted tests on RC shear walls repaired by replacement of concrete and injection of cracks as part of an investigation on the effects of loading history and repair methods on structural characteristics of RC walls. The experimental program consisted of testing four rectangular slender walls to damage, repairing three of these walls, and retesting. Loading of the repaired walls consisted of monotonic and reverse cyclic regimes, similar to the loading protocol applied to the original walls. In all the cases, replacement of concrete was implemented in the lower 150 mm x 100 mm compressive zone, including straightening of the slightly buckled steel bars. Figure 2-1 depicts the replaced concrete in the left lower zone of one of the

walls (Wall SW33R). Injection of the cracks involved applying epoxy resin in flexural cracks greater than 0.2 mm. The repaired walls exhibited lower stiffness and less ductility than the original walls. Lefas and Kotsovos demonstrated that repairing the damaged regions of the compressive zone was sufficient to fully restore wall strength, and that injection of cracks provided marginal improvement of the structural characteristics of the repaired walls. Crack patterns and failure modes of both the original and repaired walls implied marginal effect of the repairing methods on these structural characteristics.

Fig. 2-1 Repaired Shear Wall SW33R (Lefas and Kotsovos, 1990)

Fiorato, Oesterle, and Corley (1983) tested shear walls repaired by replacement of concrete as part of an experimental program of slender shear walls in the Portland Cement Association (PCA) laboratories. The walls had a barbell section with high-to-length ratio of 2.4. Repair consisted of removing the concrete in the lower portion of the web up to 2600 mm and replacing it with high strength concrete. The repair procedure also included hand packing of concrete in damaged zones of the boundary columns. The walls were subjected to reverse cyclic loading and axial loading. The

replacement of concrete technique proved to be capable of restoring the lateral strength capacity and ductility; however, the initial stiffness of the repaired walls was lower than that of the original walls.

Vecchio, Haro de la Peña, Bucci, and Palermo (2002) tested two repaired wide-flanged squat shear walls, Wall DP1R and Wall DP2R, subjected to lateral loading. The original walls, Wall DP1 and Wall DP2, were subjected to reverse cyclic loads and tested to failure (Palermo and Vecchio, 2002). The walls were 2020 mm high and 2885 mm long, with web thickness of 75 mm. End flange walls measured 3045 mm in width, and were 95 mm and 100 mm thick for DP1/DP1R and DP2/DP2R, respectively. The walls were provided with a stiff foundation slab for anchorage to the strong floor, and a stiff top slab for transferring the applied load to the walls. Repair of Wall DP1R consisted of replacing concrete in the web portion of the wall, while keeping the reinforcement intact. The new concrete was approximately double the strength of the concrete in the original wall. The top 180 mm of the wall was filled with a non-shrink epoxy grout. Repair of Wall DP2R followed the same procedure described for Wall DP1R, and in addition, included full height concrete replacement of the flanges over a width of 750 mm at the intersection with the web wall. Wall DP1R and Wall DP2R were subjected to a constant axial load during the test. Furthermore, Wall DP1R was subjected to reverse cyclic lateral loading, while Wall DP2R was subjected to monotonic lateral loading. Test results indicated that shear walls repaired by concrete replacement can recover seismic characteristics such as strength, stiffness, and energy dissipation. However, the repair procedure, strength of repair materials, and residual damage in the unrepaired zones may have a significant influence on the wall behavior and can alter the failure mode. Repair of DP1R and DP2R walls is depicted in Fig. 2-2.

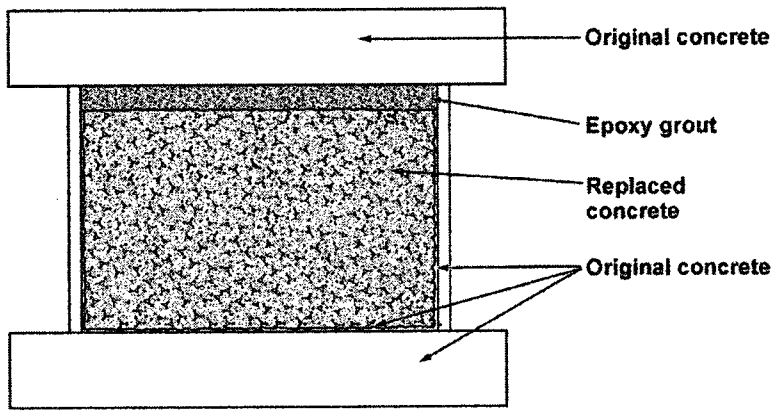

Fig. 2-2 Repair Scheme of Walls DP1R and DP2R (Vecchio et al., 2002)

2.2.3 Addition/Replacement of Reinforcing Bars

Addition/replacement of reinforcing bars, accompanied with replacement of concrete, is a common technique for seismic applications that aims to restore or improve specific aspects of seismic behaviour, such as strength, ductility, and shear sliding.

Diagonal reinforcement has proven to be efficient in controlling shear sliding in RC shear walls. Furthermore, it can contribute to flexural strength, and consequently increase the shear load (Paulay, Priestley, and Synge, 1982). However, when appropriately designed, the shear associated with the increase in flexural capacity does not exceed the total shear capacity of the shear wall. Fiorato et al. (1983) incorporated diagonal reinforcing bars (Fig. 2-3) in the repair and retrofitting of a slender shear wall tested to damage under reverse cyclic loading. Repair and retrofitting of the shear wall comprised replacement of concrete from the foundation slab up to 2600 mm in height, and addition of four diagonals reinforcing bars (two in each direction) as shown in Fig. 2-3. Both the original, Wall B11, and repaired, Wall B11R, walls were subjected to reverse cyclic loading history. Damage of the original wall was characterized by inclined cracks in both directions, as well as crushing of the concrete in the web, specifically near the boundary elements. By replacing the

damaged concrete and adding diagonal reinforcing bars, the peak strength and displacement capacity were increased relative to the original wall. However, the repair and retrofitting procedure did not result in recovering of the initial stiffness. The improvements in strength and ductility were mainly due to the bi-diagonal bars, which increased the shear capacity of the section and, therefore, delayed failure.

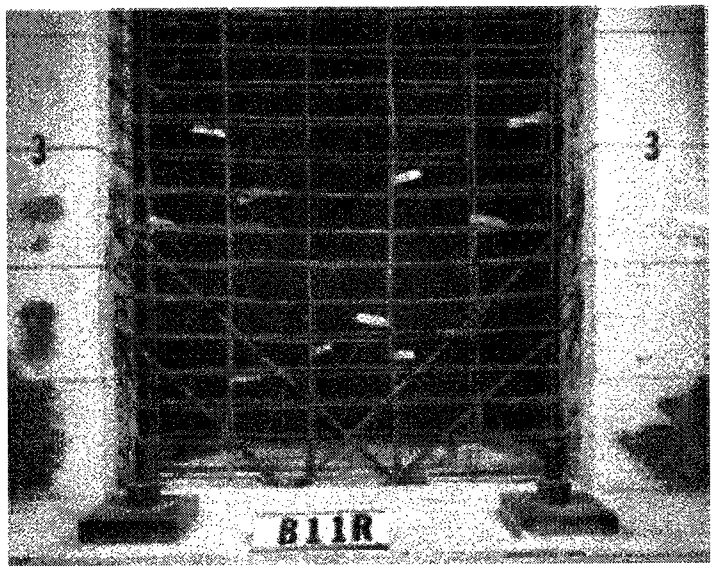

Fig. 2-3 Diagonal Reinforcement of Repaired and Retrofitted Shear Wall B11R (Fiorato et al., 1983)

Haroun (2000) investigated repair of six damaged ½-scale bridge pier walls subjected to reverse cyclic loading in the weak, out-of-plane, direction. The pier walls were tested with vertical loading of about 5% of its compressive strength capacity. The main objectives of the study were: assessment of the repair procedure, and comparison of aspects of seismic behaviour of the repaired pier wall with the original pier wall. The study investigated two vertical reinforcement and three cross-tie configurations. The cross-tie hooked around both the longitudinal and the transverse reinforcement. The original walls failed due to buckling of the vertical reinforcement. Furthermore, most of the cross-tie legs opened in the lower portion of the pier walls at latter stages of the tests. Damage in the walls without cross-ties was relatively more severe. Repair of the walls along the plastic hinge consisted of replacing damaged concrete with an increased section of new concrete, addition of horizontal reinforcement around the

existing vertical reinforcement, and addition of cross-ties. Five wall specimens were provided with double alternating 90 and 135 degree cross-ties, while one wall specimen was provided with T-headed cross-ties (Fig. 2-4). Testing of the repaired walls followed the same loading protocol as the original specimens. Responses of the repaired walls were in good agreement with the responses of the original walls. Both the double 90/135 degree and T-headed cross-ties were effective in preventing buckling of vertical reinforcement and providing adequate confinement. The T-headed cross-tie reinforcement performed as well, or better than the regular cross-tie reinforcement.

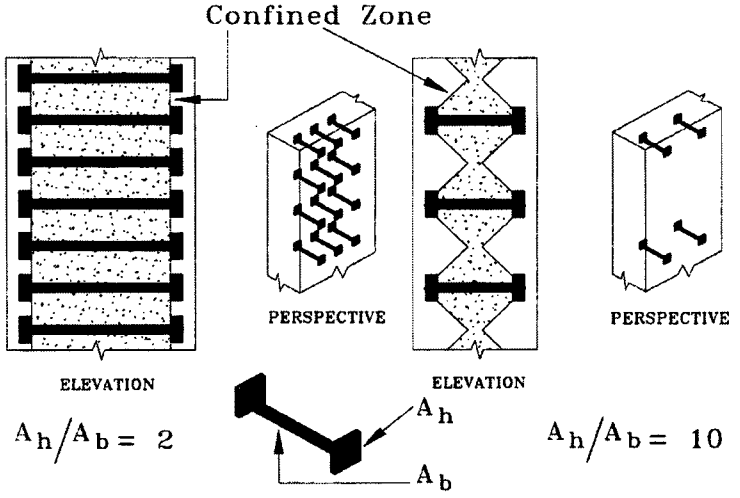

Fig. 2-4 Different T-headed Confinement Reinforcement Configurations (Haroun, 2000)

2.2.4 Bonding of Steel Plates

Bonding of steel plates is applicable to seismic repair/retrofitting of shear walls for enhancement of strength (flexural and shear), ductility, and stiffness. During the repair/retrofitting intervention, the execution of the bonding work is of great importance to achieve a composite action between the adherents (concrete and steel plate) (Thermou and Elnashai, 2006). Elnashai and Salama (1992), and Elnashai and Pinho (1998) assessed some of these techniques in a study aimed to develop selective (stiffness-only and ductility-only), and complete (shear strength) intervention

techniques for seismic repair/retrofitting of RC shear walls. Selective intervention techniques address possible counterproductive effects of local strengthening of elements when designed to satisfy capacity requirements of seismic codes. Furthermore, restoring of selective parameters can help to meet target safety requirements of displacement-based design methods.

To investigate the stiffness-only intervention, Elnashai and Salama (1992), and Elnashai and Pinho (1998) tested a wall to a lateral displacement corresponding to a displacement ductility of 2.0 to simulate partial damage induced by a moderate earthquake. At that point, the wall was unloaded and repaired. Repair consisted of bonding four steel plates (1100 mm x 190 mm x 3.6 mm) with epoxy near the edges of the wall preceded by preparation of the surface, but without epoxy injection of the cracks. Wide cracks were treated with emulsion paint as a protection from corrosion. The steel plates were placed 50 mm above and below the foundation and top beam, respectively, to avoid contribution to the overall strength of the wall. The retrofitting method implemented to assess the ductility-only intervention consisted of bonding of U-shaped external confinement steel plates in the boundary elements, which were fastened in the lower portion of the wall. The plates were bonded with high strength epoxy and fastened with pre-stressed bolts. The dimensions of the U-shaped plates were 480 mm x 120 mm x 3.6 mm. A gap of 20 mm between the plates and foundation was necessary to avoid any enhancement in the strength of the wall. The complete shear-strength repair and retrofitting technique consisted of a combination of injection of cracks and bonding of steel plates. After testing to failure (concrete crushing), the damaged wall was repaired by epoxy injection of cracks, and then retrofitted with horizontal steel strips to prevent shear failure. The steel strips were attached to the RC shear wall in a staggered pattern using high strength epoxy resin. Figure 2-5 illustrates the techniques involving bonding of steel for the stiffness-only, ductility-only, and shear-strength interventions. The techniques were successful in restoring strength, ductility, and shear-strength characteristics of RC shear walls subjected to seismic loading.

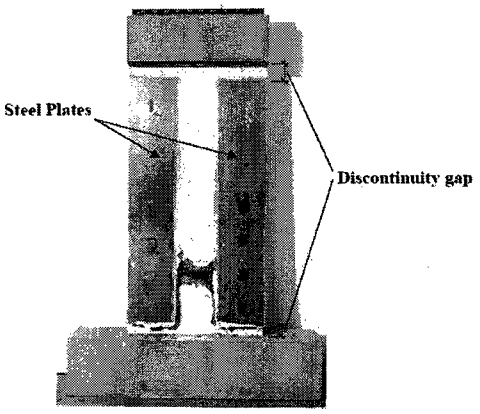

a) Stiffness-Only Intervention

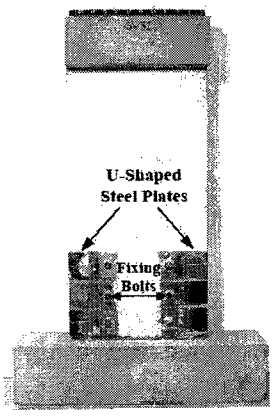

b) Ductility-Only Intervention

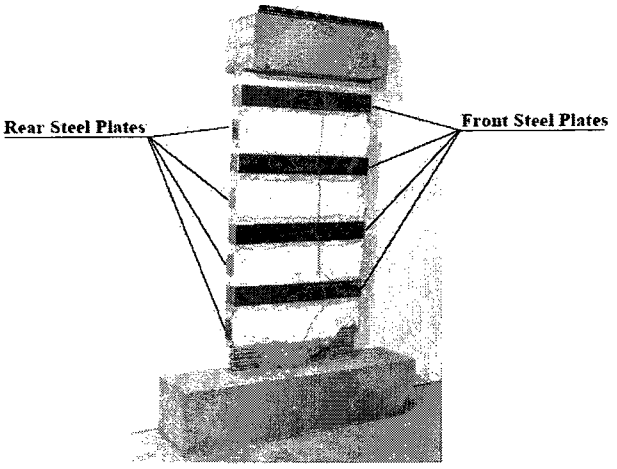

c) Shear-Strength Intervention

Fig. 2-5 Selective Intervention Techniques: a) Stiffness-Only Intervention, b) Ductility-Only Intervention, and c) Shear-Strength Intervention (Elnashai and Pinho, 1998)

2.2.5 Bonding of FRP Sheets/Plates

The ease of application of FRP composites (FRP sheets/plates) renders them attractive for use in structural applications; specifically in cases where weight, space or time restrictions exist (Thermou and Elnashai, 2006). In general, FRP composites behave linear elastically to failure without any significant yielding or plastic deformation, and carry only tensile forces (Thermou and Elnashai, 2006). Failure of FRP composites can

occur by either debonding at the concrete-FRP interface or fracture of the fibres. The quality of bonding of the FRP composite is crucial for an adequate load transfer through the concrete-FRP interface.

Lombard, Lau, Humar, Foo, and Cheung (2000) studied the effectiveness of using externally bonded carbon fibre tow sheets for the seismic strengthening and repair of reinforced concrete shear walls. Four 2000 mm high x 1500 mm long x 100 mm thick reinforced concrete shear wall specimens loaded to failure in the in-plane direction according to a predetermined quasi-static cyclic loading sequence were tested. The test program included a control wall, a repaired wall and two strengthened walls. An anchorage system consisting of L-plates (150 mm x 150 mm x 10 mm) bonded to the FRP sheets and clamped to the foundation by means of bolts was utilized. Lombard et al. also performed analytical predictions of the behaviour of the retrofitted walls with a semi-empirical model developed in the study, which showed good agreement with the experimental results. The proposed analytical model is intended for reinforced concrete shear walls, which have aspect ratios greater than 1.0, and are designed to fail in a ductile flexural manner.

Antoniades, Salonikios, and Kappos (2003, 2005) conducted a series of tests on repaired and strengthened 1:2.5 scaled reinforced concrete shear walls with aspect ratio of 1.0 (1200 mm x 1200 mm x 100 mm) and 1.5 (1800 mm x 1800 mm x 100 mm) with different steel reinforcement configurations, including four walls with inclined ties at the base. The original specimens were cyclically loaded to failure, repaired with conventional techniques: replacement of concrete and lap-welding of reinforcement, and then retrofitted with FRP jackets and FRP strips at the edges of the walls to enhance flexural and shear capacities, respectively. The FRP repair system was anchored to the foundation in several ways to study the influence on strength, initial stiffness, and ductility of the repaired wall. Typical repair and strengthening procedures of the specimens are illustrated in Fig. 2-6.

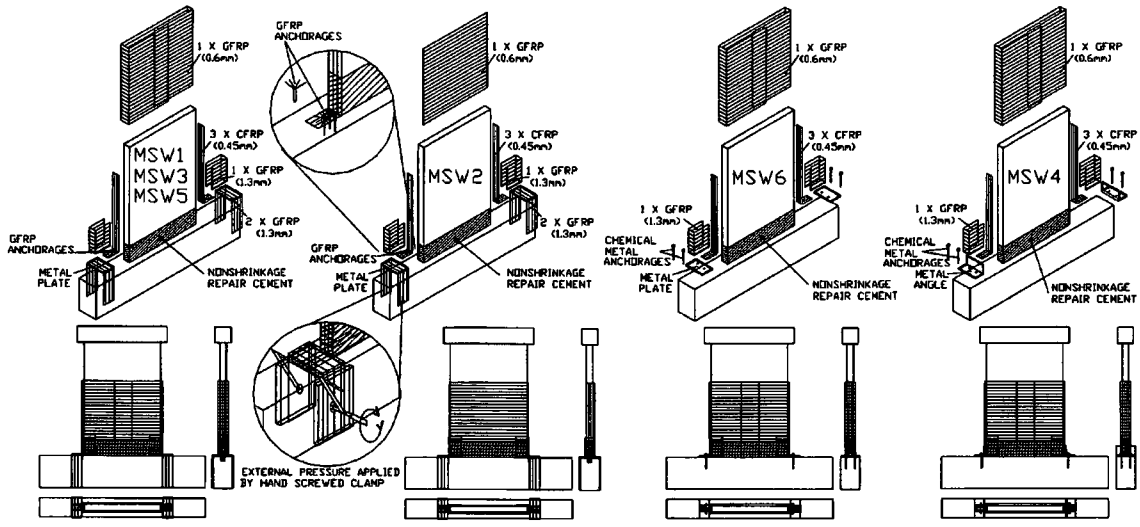

Fig. 2-6 Repair and Strengthening Procedures Applied to Shear Walls with Aspect Ratio of 1.5 (Antoniades et al., 2005)

Khalil and Ghobarah (2005) undertook a series of experiments to investigate potential rehabilitation schemes for shear walls damaged by earthquake loads. Three walls were tested: one control wall, CW; and two rehabilitated walls, RW1 and RW2 (Fig. 2-7). Two types of CFRP sheets were used for the rehabilitation of the wall: a bi-directional CFRP with the primary fibres oriented in the ±45° direction, and a unidirectional carbon fabric with the primary fibres oriented in the 0° direction (parallel to the length of the wall). The loads were chosen so that shear ratio M/VL would be held constant to 2.25, therefore the specimens represented shear walls with predominant flexural behaviour. The control wall was purposely designed to be deficient in shear and ductility, therefore the rehabilitation schemes were chosen to improve these deficiencies. The test results demonstrated an increase in lateral load capacity and ductility, which were attributed to two reasons: elimination of the premature shear failure mode, and the increased confinement of the boundary elements.

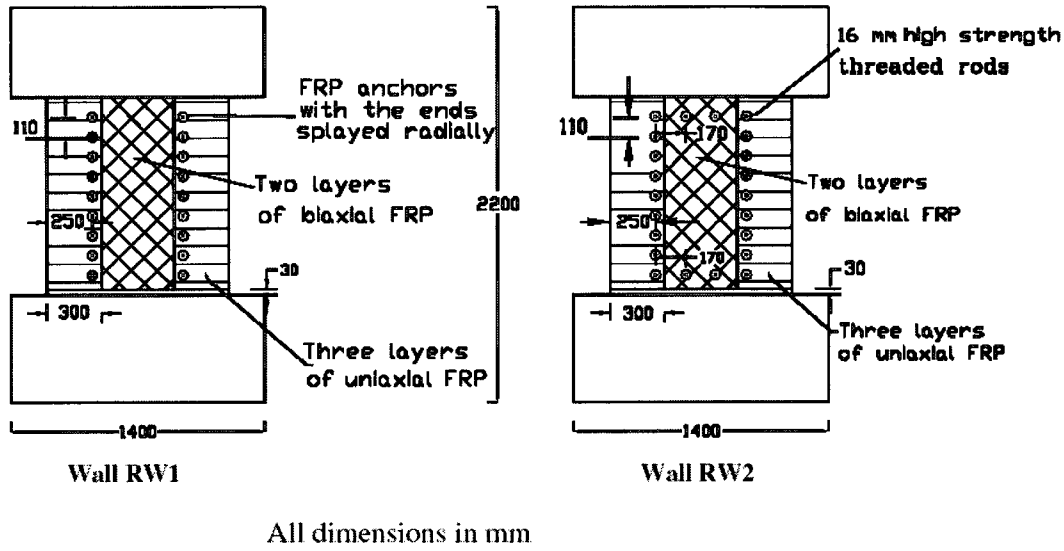

Fig. 2-7 Rehabilitation Schemes for Walls RW1 and RW2 (Khalil and Ghobarah, 2005)

2.2.6 Addition of Shape Memory Alloys

Shape memory alloys (SMA) are a class of materials that can recover from large strains through heating (Shape-memory or Martensite SMA) or unloading (Superelastic SMA) (Desroches and Smith, 2004). Superelastic SMA possesses stable hysteretic behaviour over a certain range of temperature, where its shape is recoverable upon removal of load. On the other hand, Shape-memory (Martensite) SMA also possesses the ability to recover its shape after undergoing large deformations through heating (Liao et al., 2006). SMA capabilities such as energy dissipation, large inelastic deformations, and re-centering provide great potential for seismic repair/retrofitting applications.

Liao et al. (2006) evaluated the effect of SMA applications to three low-rise barbell-shaped shear walls tested under reverse cyclic loading. Two wall specimens had SMA bars as external bracing: one with Superelastic SMA, and one with Martensite SMA, while the third specimen was the control wall. The height-to-width ratio of the walls was 0.5, and the dimensions were 1000 mm in height, 2000 mm in length, and 120 mm in thickness. External bracing consisted of two SMA bars (Superelastic, or Martensite)

inclined 27 degrees to the horizontal as illustrated in Fig. 2-8. The ratio of both SMA and steel reinforcing bars was 0.24%. Test results showed the effect of SMA bars on the maximum shear strength, and response of low-height shear walls. However, buckling of one SMA bar limited the energy dissipation capacity of the shear wall retrofitted with Superelastic bars. Liao et al. found that the shear wall with Superelastic SMA bars had less residual displacement than the shear wall with Martensite SMA bars.

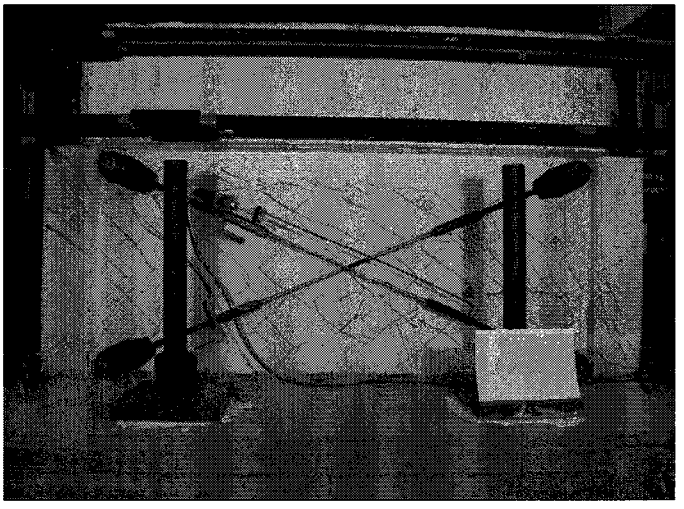

Fig. 2-8 Shear Wall Retrofitted with SMA Bars (Liao et al., 2006)

2.2.7 Other Techniques

Altering the sequence of plastic hinge formation to achieve a predetermined failure mode becomes an essential objective for seismic safety. This requires increase in strength of strategically located members. To address this, Elnashai and Pinho (1998) re-assessed previous tests conducted by Elnashai and Salama (1992) on retrofitted RC shear walls using strength-only techniques. Elnashai and Pinho reported results of tested scaled 1:2.5 (approximately) shear walls retrofitted by the addition of either external unbonded reinforcing bars (EURB) or external unbonded steel plates (EUSP), which were designed only to contribute to the strength of the walls. This was achieved by means of a delay mechanism, which engaged the bars or plates after achieving the yield displacement of the walls (Fig. 2-9). The delay mechanism prevented buckling at

the compression side of the walls. Furthermore, Elnashai and Pinho modelled the selective technique using the finite element (FE) Program ADAPTIC, and performed a parametric study in which design guidelines for practical application were proposed.

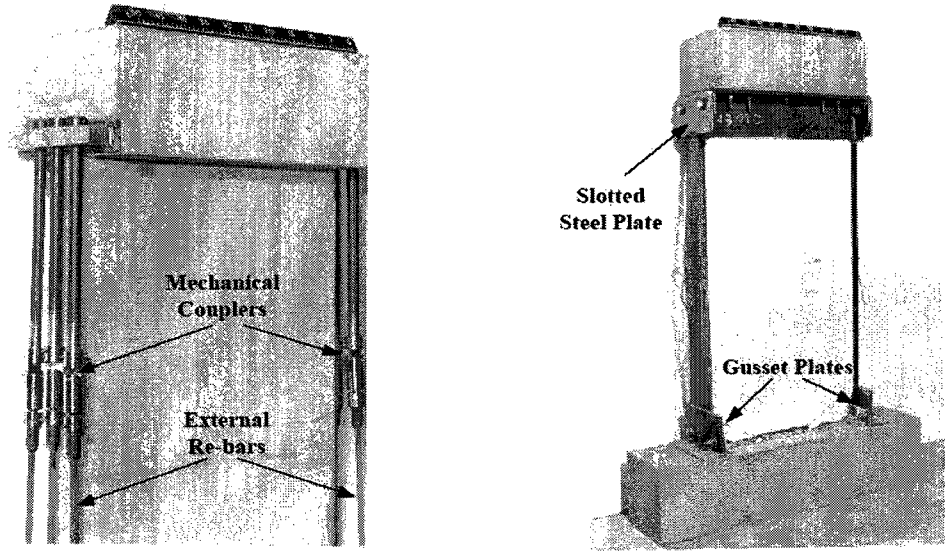

Fig. 2-9 Strength-Only Intervention Test Specimens: a) EURB; b) EUSP (Elnashai and Pinho, 1998)

Taghdi, Bruneau, and Saatciouglu (2000b) investigated the in-plane cyclic behaviour of low-rise masonry and lightly reinforced concrete shear walls retrofitted using steel strips. The testing program consisted of six large-scale walls: four concrete block masonry walls and two reinforced concrete walls, with height of 1800 mm, length of 1800 mm and aspect ratio of 1.0; the thickness was 190 mm for the masonry walls and 100 mm for the reinforced concrete walls. The walls were designed according to old code provisions. The retrofitting system consisted of diagonal and vertical strips attached to the walls with through-thickness bolts, and connected to the foundation by means of stiff steel angles. The tests showed that the retrofitting scheme is effective for strength and ductility enhancement of low-rise masonry and lightly reinforced concrete shear walls. Taghdi et al. also developed a simply truss model to perform a step-by-step calculation to determine the strength and deformation capacity. The

results obtained with this model were in good agreement with the experimental results, therefore a displacement-based design procedure was proposed based on this model. Figure 2-10 depicts the retrofitting scheme of one concrete block masonry wall using steel strips.

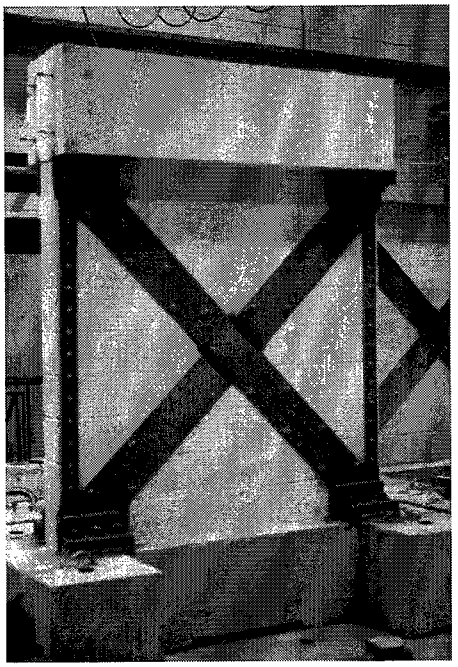

Fig. 2-10 Wall Retrofitted Using Steel Strips (Taghdi et al., 2000b)

Paterson and Mitchell (2003) tested four shear wall specimens to evaluate a proposed procedure for the seismic retrofitting of a core wall of an existing building. The building, designed and constructed in the 1960's, was provided with poor seismic detailing. The retrofitting techniques included the use of headed reinforcement and carbon FRP. Wall W1R was retrofitted by casting a concrete collar reinforced with headed reinforcement and FRP jackets in the lower zone (flexural hinge region) of the wall to address the presence of lap splice in this zone in the non-retrofitted Wall W1. Additional jackets along the wall were also provided to improve shear capacity. Wall W2R was retrofitted with FRP jackets clamped to the concrete by headed through-wall confinement reinforcement. No concrete collar was used in W2R since the lap splice region was 600 mm from the base of the wall in the non-retrofitted Wall W2. Both W1R and W2R showed that the retrofitting techniques used in the study were efficient

in terms of ductility enhancement. The retrofitting schemes of Walls W1R and W2R are illustrated in Fig. 2-11.

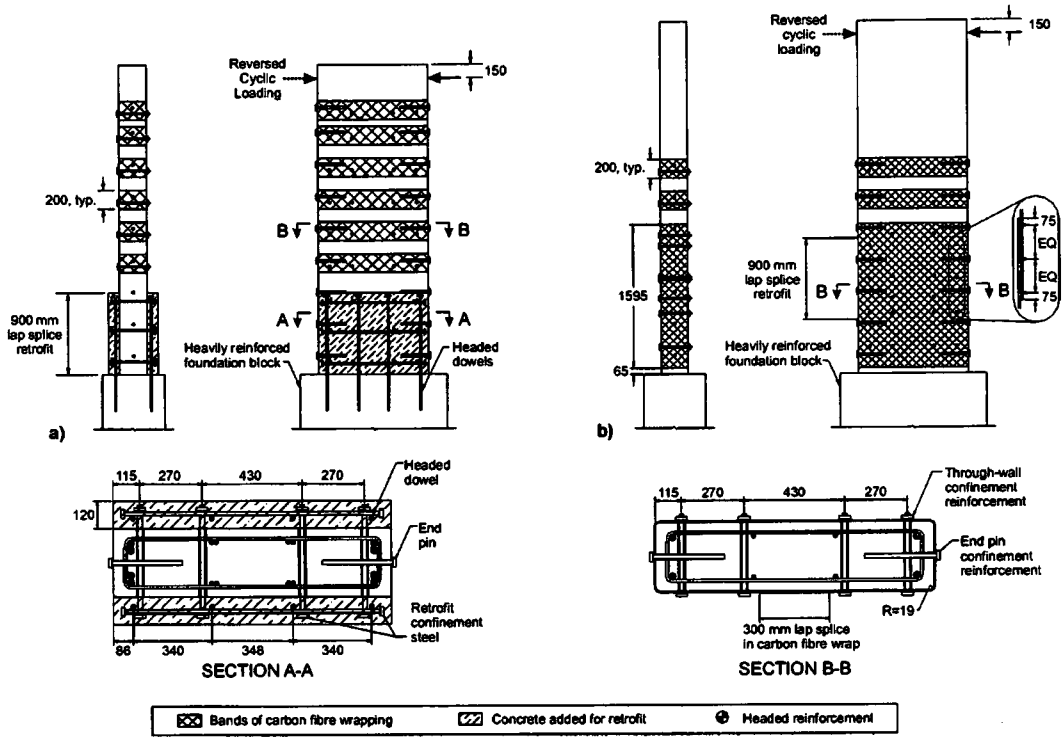

Fig. 2-11 Retrofit Details: a) Specimen W1R, and b) Specimen W2R (Paterson and Mitchell, 2003)

2.3 Analysis of Repaired/Retrofitted RC Structures

2.3.1 Overview

The behaviour of RC structures under incremental loading is predominantly nonlinear, and therefore, they must be analyzed with algorithms that include these nonlinearities. In addition, the algorithms must take into account the construction process of the repair/retrofitting intervention.

Classical analytical methods, including strength of materials and elastic methods are limited to simple structural elements in the elastic range. Therefore, nonlinear numerical analysis methods have emerged as useful tools for design of repaired and/or

retrofitted RC structures. Nonlinear numerical analyses are performed by dividing the load into steps so that iterative calculations are performed based on equilibrium, constitutive, and compatibility relations until convergence of important parameters, such as stiffness or displacements, is achieved. At the end of each load step, the algorithm updates the stiffness matrix to reflect nonlinearity of materials, which is used as the initial values of the subsequent step.

A very popular numerical method for nonlinear analysis of RC structures is the finite element method (FEM). The FEM formulates the problem in variational form with a system of partial differential equations of the RC solid continuum, which is discretized with finite elements interconnected by joints. Then, the problem is solved with numerical techniques. The term finite element method was first introduced by Clough (1960) in the paper: "Finite element method in plane stress analysis"; however, more than a decade before, a similar method, based on the Ritz method (Ritz, 1909), was proposed by Courant (1943). Ngo and Scordelis (1967), and Nilson (1968) presented incipient works on nonlinear numerical analysis of RC structures using the FEM.

Other popular methods are those based on the truss analogy in which the RC structural element is discretized by means of tensile and compressive members representing the internal forces, which are interconnected by joints. The method was first proposed by Ritter (1899), and has been refined and extended through the years to include important features such as nonlinearity. One such method is the strut-and-tie method proposed by Schlaich, Schäfer, and Jennewein (1987). The strut-and-tie method incorporates the lower bound theorem of the theory of plasticity to account for nonlinearities.

Few analytical studies have simulated the response of repaired and retrofitted RC shear walls. However, a large number of studies have focused on repair and retrofitting of simply supported RC beams.

2.3.2 Repaired and/or Retrofitted RC Shear Walls

Extensive experimental studies aimed to assess and understand repair and retrofitting techniques applied to RC shear walls have been reported to date; however, only few of them have included analytical or numerical simulations. Elnashai and Pinho (1998) carried out numerical analysis of selective intervention (repair/retrofitting) techniques on shear walls with the FE Program ADAPTIC to assess individual design response parameters such as stiffness, strength, and ductility. Selective interventions (stiffness-only, strength-only, and ductility-only) involved external bonding of steel plates, and addition of external unbonded steel bars/plates. The validated numerical models were used to perform parametric studies aimed to develop practical expressions for designing of selective repair/retrofitting interventions. The repaired/retrofitted shear walls were modelled with two-dimensional (2-D) plane frame elements consisting of two Gaussian sections subdivided into 150 fibres, where strains and stresses were calculated. The concrete compression model accounted for confinement and enabled the prediction of continuing cyclic stiffness and strength degradation. The steel was modelled using a multi-surface plasticity model, which included a yield plateau, nonlinear strain hardening, and cyclic degradation. The external plates and reinforcing bars were modelled with a simple bilinear elastic-plastic steel model with strain hardening, which did not include a yield plateau. An eccentric steel section was used for modelling of the stiffness-only intervention. Gap elements were used for modelling of the strength-only intervention. No physical representation of the ductility-only intervention was modelled; instead, the effect of the intervention was included in the stress-strain relation by using a confinement factor. The finite element program failed to simulate the stiffness-only intervention since it was not capable of reproducing the construction process of the repair intervention. However, monotonic analysis of a previously non-damaged wall retrofitted with the stiffness-only technique was compared with monotonic analysis of the original wall to verify the modelling concept. For the case of strength-only intervention, good agreement was reported between the analytical response and the experimental response. The predicted response of the ductility-only intervention was

less satisfactory compared to the other predictions, perhaps due to deficiencies in modelling the intervention in the finite element program.

Taghdi, Bruneau, and Saatciouglu (2000a) developed truss models to investigate the cyclic response of walls repaired and retrofitted by bolted vertical and diagonal steel strips. The models incorporated the lower theory of plasticity for the calculation of the ultimate strength. The analysis did not include cyclic loading since the proposed models considered only increasing static lateral loads; therefore, stiffness and strength degradation were ignored. Concrete degradation due to crushing was taken into account by reducing the stiffness and strength in the push-over, step-by-step analysis. Two truss models were reported: a simplified model with five truss members (Fig. 2-12); and an improved model with seven truss members (Fig. 2-13). The improved model better captured the progress of inelastic behaviour and final failure mechanism; however, the ductility of the walls was not accurately predicted. The lower bound theory of plasticity, which assumes yielding of the steel in tension, provided conservative estimates of the ultimate strength, but did not provide any information about the corresponding deformation capacity. Furthermore, the lower boundary calculations did not account for the contribution of the concrete.

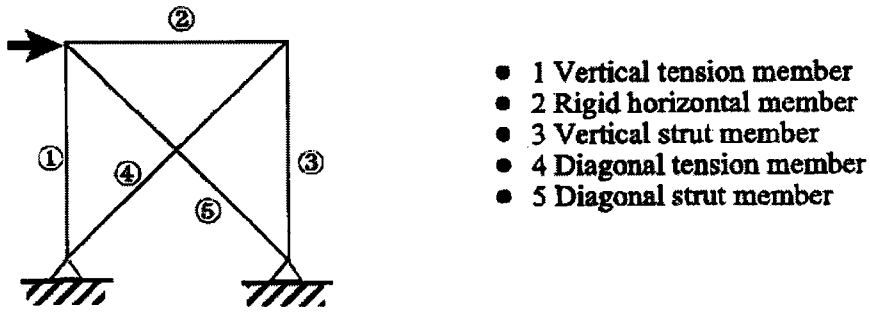

Fig. 2-12 Simplified Truss Model (Taghdi et al., 2000a)

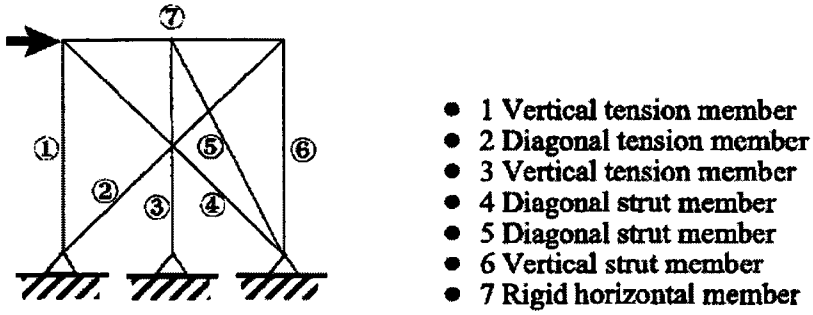

Fig. 2-13 Improved Truss Model (Taghdi et al., 2000a)

Vecchio et al. (2002) modelled squat flanged walls (DP1R and DP2R), repaired by replacing damaged concrete in the web wall, following the engaging/disengaging process introduced by Vecchio and Bucci (1999). The analyses were performed with the 2-D Program VecTor2, and incorporated material models describing the nonlinear and load-history behaviour of concrete and reinforcement. The 2-D modelling assumed the flange walls of both DP1R and DP2R were fully effective in the plane with the web, thus overestimating somewhat both the shear and flexural stiffness of the walls. The predicted behavioural response of Wall DP1R was reasonably well simulated. The analysis captured the final failure in the form of shear sliding at the base of the wall; however, the strength and stiffness were slightly overestimated. The calculated response of Wall DP2R overestimated the stiffness and strength, and underestimated the ductility. Some of these discrepancies were attributed to the 2-D representation of a structure with three-dimensional (3-D) behavioural aspects. Vecchio et al. concluded that proper consideration of previous loading and residual damage is essential if analytical procedures are to accurately represent the response of repaired walls. Observed and calculated responses of Walls DP1R and DP2R are illustrated in Fig. 2-14 and Fig. 2-15, respectively.

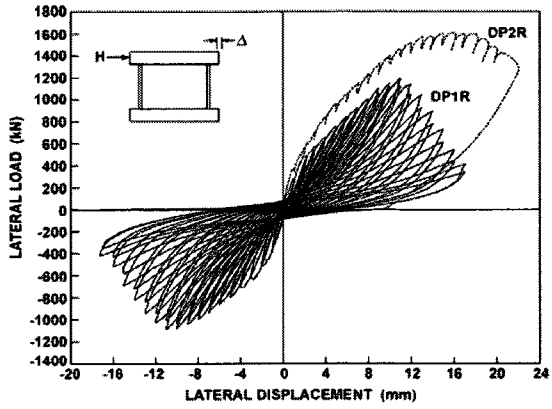

Fig. 2-14 Observed Load-Displacement Responses of Repaired Walls DP1R and DP2R (Vecchio et al., 2002)

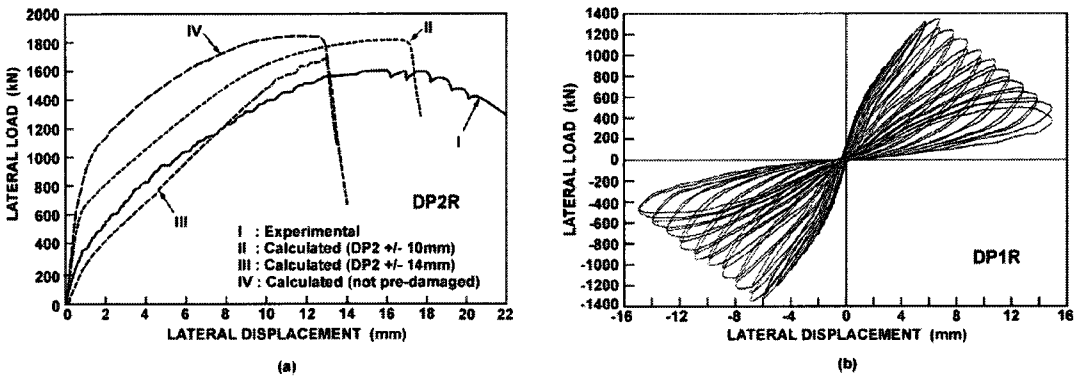

Fig. 2-15 Calculated Load-Displacement Responses of Repaired Walls: a) Wall DP2R, and b) Wall DP1R (Vecchio et al., 2002)

Li, Balendra, and Kong (2005) developed a 3-D nonlinear finite element model using Program ABAQUS to predict the response of an I-shaped (flanged) RC shear wall strengthened with glass FRP, and subjected to cyclic loading. Reinforced concrete was modelled with 220 eight-noded solid elements, following a damaged plasticity-based model. The concrete model accounted for the strength and ductility improvement due to FRP confinement, and did account for strength degradation in the post-peak range. Reinforcement was modelled with one-directional strain elements, following an elastic-perfectly plastic model. Secondary effects such as bond-slip and dowel action were modelled by introducing some tension stiffening into the concrete model. Glass FRP

was modelled with 525 SPRING finite elements to constrain deformation due to FRP wrapping.

2.3.3 Repaired and/or Retrofitted RC Beams

One of the first analytical and numerical studies on repair and/or retrofitting of RC beams were conducted by Arduini, Di Tommaso, and Nanni (1997), who attempted to incorporate externally bonded FRP into current available iterative analytical models and FEM's. The analytical and numerical investigations were based on monotonically loaded beams strengthened by Carbon FRP.

The analytical model of Arduini et al., (1997) included investigation of crack propagation and failure mechanism by considering compression confinement effect and tension softening effect of concrete. The analyses involved step-by-step loading simulation of the beams, which were discretized into a finite number of segments (Fig. 2-16). Shear stresses generated in the bonding material (adhesive) were included in the stress analysis; therefore, local bond failure of the adhesive was possible to predict in addition to FRP rupture, concrete shear and tension fracture of concrete. Interfaces between adhesive and concrete, and between adhesive and FRP were considered perfectly bonded. The program developed for the analytical model was able to disconnect the FRP plates/sheets when failure of the FRP or concrete occurred in the vicinity of the bonding interface. Numerical analyses conducted by Arduini et al. were based on the FEM following the smeared crack approach. Conversely to the analytical model, the numerical analyses did not include modelling of the adhesive, and assumed perfect bonding between FRP and concrete. Analytical and numerical predictions were in good agreement with the experimental observations in terms of load-deflection response, load-FRP strain response, and evolution of cracks.

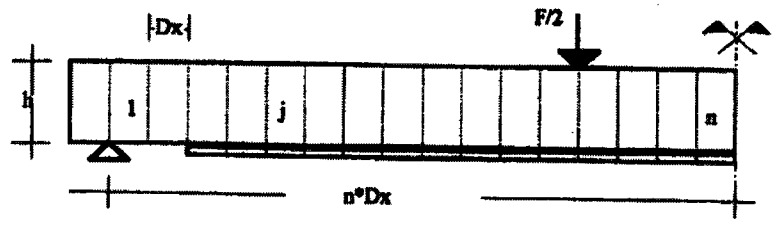

Fig. 2-16 Analytical Discrete Model (Arduini, et al., 1997)

Different approaches have been used in numerical analysis of repaired and/or retrofitted RC beams; fibre section models being one such method, which accounts for the coupling between axial and bending effects and can be combined with any beam element model. Aprile, Spacone, and Limkatanyu (2001) used an improved fibre section model in which bond-slip effects were added to account for the presence of externally bonded FRP and steel plates on RC beams and slabs. The proposed model was able to describe the shear stress distributions on the interface between the FRP/steel plates and the concrete. The model introduced an elastic-brittle bond model for the plate-concrete interface behaviour and took into account the nonlinear behaviour of the materials including the tension stiffening of concrete. The fibre model, including constitutive material models, was implemented in the FE Program FEAP. The RC beam element used for the numerical analysis had two components: a two-node concrete beam element and a two-node strengthening plate element. The nodal degrees of freedom of the concrete beam and of the strengthening plate were different to permit slip. Aprile et al. reported good agreement between the numerical predictions and the experimental observations in terms of stiffness and strength of all the tested beams and slabs.

Other researchers have approached the numerical analysis of repaired/retrofitted RC beams using two-dimensional (2-D) FEM models. Rahimi and Hutchinson (2001) carried out 2-D FEM analyses using Program LUSAS, which implements the smeared crack approach with isotropic damage models, to identify some of the variables that have a significant effect on the performance of strengthened beams and to understand the failure mechanism associated with these structures. The 2-D nonlinear model was inadequate for predicting necking across the steel plates and the debonding failure

associated with this deformation. Similar to Rahimi and Hutchinson (2001), Buyle-Bodin et al. (2002) conducted numerical analyses of repaired and retrofitted RC beams by carbon FRP plates with nonlinear FEM based on the smeared crack approach.

A series of analytical studies on repair and retrofitting of RC beams by bonding of FRP was performed at the University of Toronto using Program VecTor2, which is based on the MCFT and DSFM (Vecchio and Bucci, 1999; Wong and Vecchio, 2003; Sato and Vecchio, 2003). The analyses incorporated the rotating smeared crack approach, which freely reorients the smeared cracks.

Vecchio and Bucci (1999) introduced a finite element simulation procedure for repairing and retrofitting of concrete structures that considers engaging/disengaging elements in the structure, which models the sequence of construction of the repair/retrofit scheme. This procedure was used for 2-D analysis of RC beams and slabs retrofitted by bonding of FRP composites. In the analyses, laminates bonded on concrete side surfaces were smeared into rectangular elements, and then superimposed directly onto the concrete elements. Figure 2-17 illustrates the finite element mesh, as well as the loading history showing the engaging/disengaging process. Good predictions were obtained with this approach; strength capacity improvement of RC members strengthened by FRP was demonstrated. However, some discrepancies in terms of strength capacity, initial stiffness, and failure mode were reported.

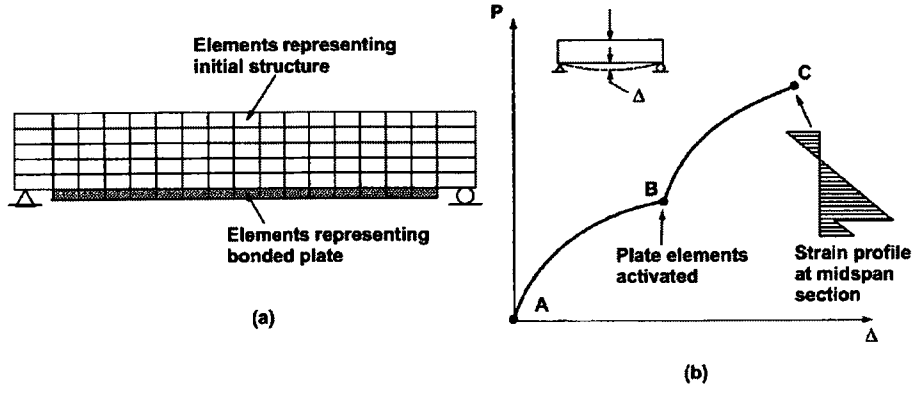

Fig. 2-17 Analysis of FRP-Repaired Beam: a) Finite-Element Mesh, and b) Loading History (Vecchio and Bucci, 1999)

Wong and Vecchio (2003) performed an experimental and 2-D numerical investigation on strengthening by bonding FRP sheets to RC slabs and beams. The investigation focused on the debonding phenomenon in the concrete-FRP interface. A non-dimensional link-bond element and one-dimensional contact-bond element (Fig. 2-18) were investigated to simulate debonding failure modes. Wong and Vecchio found that analyses with link-bond and contact-bond elements yielded similar results, and that the accuracy of the predictions depended on the stress-slip relationship used for the bonding interface. Linear elastic bond relation was found appropriate when failure was dominated by delamination of the FRP plate, while elastic-plastic bond relation was found appropriate when failure was dominated by peeling of the concrete.

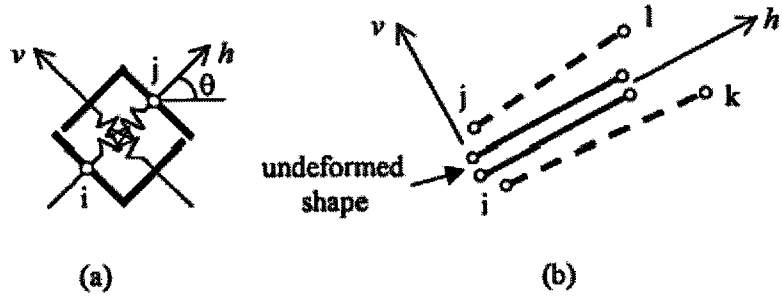

Fig. 2-18 Representation of: a) Non-Dimensional Link-Bond Element; and b) One-Dimensional Contact-Bond Element (Wong and Vecchio, 2003)

Sato and Vecchio (2003) developed models to estimate crack spacing and tension stiffening effects in RC members with externally bonded FRP sheets/plates. The proposed models were incorporated into the DSFM, and implemented into the nonlinear finite element Program VecTor2. Simplified bilinear bond stress-slip relations with adjusted maximum bond stress, as illustrated in Fig. 2-19, were used as constitutive models for the FRP-concrete bonding interface. Two series of calculations, one with the proposed models, and one with VecTor2 default models were performed for each beam. The responses obtained with both series of calculations indicated slight difference between them; however, crack width and tension stiffening effect were better predicted with the proposed model.

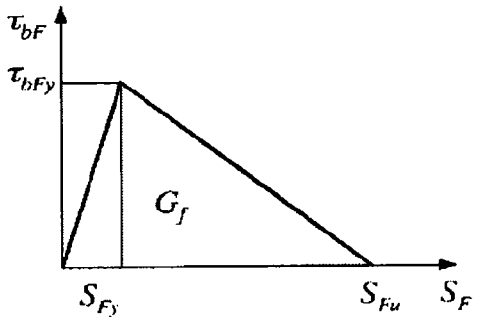

Fig. 2-19 Bilinear Bond Stress-Slip Relation for FRP (Sato and Vecchio, 2003)

Pham and Al-Mahaidi (2005) conducted 2-D numerical analyses with Program DIANA on RC beams retrofitted by carbon FRP. The objective was to address deficiencies of existing finite element procedures to predict local failure and cracking pattern near the FRP-concrete debonding interface. Reinforced concrete was modelled with a combination of rotating smeared crack and fixed smeared crack models. Constitutive models for concrete included nonlinear tension softening based on the cracking fracture energy and the crack bandwidth of elements. Carbon FRP was modelled with a linear elastic relation, and FRP-concrete interface was modelled with a pre-peak linear and post-peak linear decay bond stress-slip relation. Pham and Al-Mahaidi concluded that the FE model was able to capture behavioural features, such as ultimate capacity, crack patterns, and strain distributions of the carbon FRP.

Three-dimensional (3-D) numerical analyses are necessary when 2-D plane stress analyses are not capable of representing the geometry and loading of repaired and retrofitted structures. Hii and Al-Mahaidi (2006) performed 3-D analyses on solid and box-section RC beams strengthened in torsion with wrapped carbon FRP laminates. The strengthened RC beams were simulated with Program DIANA, which is based on the MCFT and the smeared crack approach. The bonding interface between FRP and concrete was modelled as perfectly bonded, providing unlikely debonding of the wrapped carbon FRP. Predicted responses were reported to be in good agreement with those observed; however, an adequate selection of a shear retention factor to avoid stress-locking was required. Figure 2-20 depicts the typical finite element mesh of the box-section RC beams.

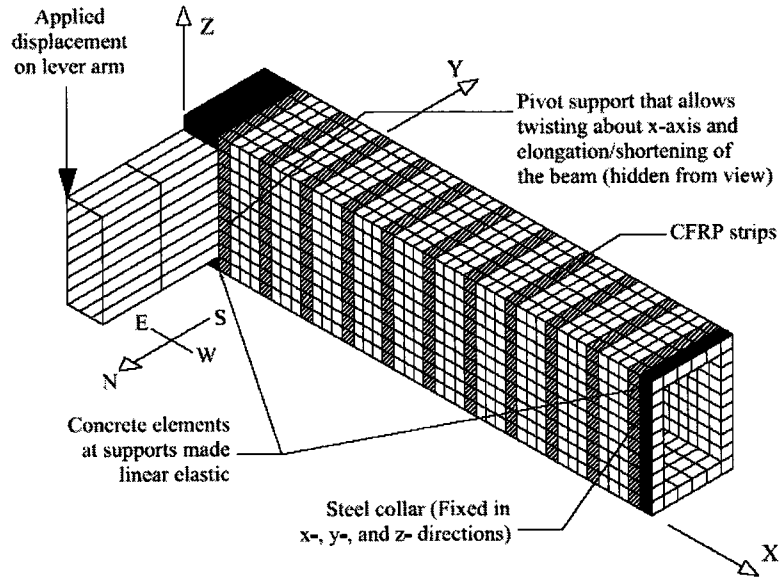

Fig. 2-20 Typical FE Mesh of Box-Section RC Beams (Hii and Al-Mahaidi, 2006)

Kachlakev, Miller, and Yim (2001) conducted 3-D analyses with Program ANSYS to assess strengthening techniques to be applied in the rehabilitation of the Horsetail Creek Bridge as part of a research project for the Oregon Department of Transportation in the USA. The numerical investigation consisted of analyses of previously tested RC beams strengthened by FRP. Cracking and nonlinear behaviour was modelled with the smeared cracking approach with a constant shear retention factor. A simplified compressive uniaxial stress-strain relation without strength degradation in the post-peak phase was assumed for the concrete. Internal reinforcing steel and externally bonded FRP were assumed perfectly bonded. Internal reinforcement was assumed to be elastic-perfectly plastic without strain hardening, while FRP was assumed to be linear elastic to failure. Kachlakev et al. concluded that the predicted responses were in good agreement with the observed responses; however, slightly stiffer responses were predicted. Furthermore, the predicted crack pattern at ultimate load corresponded to that observed during testing of the beams.

2.4 Concluding Remarks

Shear walls are very efficient in controlling lateral drift of buildings, and since the late 1950s significant studies have focused on the performance of shear walls, specifically under seismic loading. Furthermore, Fintel (1991) concluded that buildings containing shear walls performed very well during major earthquakes from the 1960s to the 1990s, and recommended the use of shear walls for residential buildings to avoid loss of life during severe earthquakes. Therefore, repair and retrofitting of shear walls to meet seismic requirements of modern code provisions is an effective means for improving the seismic performance of existing buildings.

Repair and retrofitting techniques applied to shear walls range from simple concrete replacement to addition of emerging materials, such as fibre reinforced polymers (FRP) and shape memory alloys (SMA). The performance of repaired/retrofitted shear walls depends on the repair/retrofitting technique employed. Replacement of concrete and addition of steel reinforcing bars results in restoring of strength and ductility capacity; however, the initial stiffness is not completely restored. In addition, the behaviour is influenced by the residual damage of the non-repaired/non-retrofitted portions of the structure. External bonding of steel plates was effective in restoring specific parameters (strength-only, stiffness-only, and ductility-only) depending on the implemented strategy, as well as providing a complete repair/retrofitting solution. However, this technique has been gradually replaced in recent years by external bonding of FRP materials. The advantage of using FRP is the high tensile strength of very thin layers of material, which allows repair and retrofitting of shear walls without significant increase of the nominal dimensions or weight of the structure. FRP can be applied in the form of sheets or plates, although the former is preferable for repair/retrofitting of shear walls due to ease of handling and application. Depending on the application, FRP sheets are capable of improving strength, ductility and energy dissipation capacity; however, it may not result in restoring of the initial stiffness. Shape memory alloys (SMA) have attracted the attention of the scientific community owing to their ability to recover their initial shape when subjected to deformation. For

retrofitting of shear walls, SMA's have been used as external steel bracing to improve energy dissipation and limit the plastic deformation at the end of seismic loading.

Significant experimental research has been conducted on repair and retrofitting of RC shear walls; however, analytical and numerical research on repair and retrofitting of RC shear walls is lacking. Most of the analytical and numerical studies have focused on retrofitting of beams, and only few studies have included numerical analysis of repaired/retrofitted shear walls. Two approaches have been widely used for numerical analysis of RC structures: the FEM and the truss analogy. Although methods based on the truss analogy, such as the strut-and-tie method, have increased in popularity, they are oriented toward design of members and are limited to the assessment of maximum capacity. Therefore, they do not capture salient seismic features, such as ductility, energy dissipation and failure mode. Some attempts have been made to improve these methods by including nonlinear constitutive models into nonlinear algorithms (Arduini et al., 1997; Taghdi et al., 2000a).

The FEM based on the smeared crack approach (fixed smeared crack approach) has been preferred to the discrete crack approach for numerical analysis of repaired/retrofitted structures due to the relatively simpler nonlinear algorithms needed to describe cracking in the continuum. Predictions using the smeared crack approach have demonstrated satisfactory agreement with experimental observations (Arduini et al., 1997; Buyle-Bodin et al., 2002; Hii and Al-Mahaidi, 2006; Katchlakev et al., 2001; Li et al., 2005; Rahimi and Hutchinson, 2001). The discrete approach requires nonlinear algorithms capable of predicting crack paths, and to refine the meshing to accommodate the propagations of the cracks. In the smeared crack approach, cracks are simulated as local discontinuities that are distributed within the entire finite element model. Success of the finite element simulation depends on the smeared crack formulation and the material models. The constitutive models should describe the reduction of stiffness, specifically in the direction perpendicular to cracks. A modified rotating smeared crack approach implemented in programs such as VecTor2 and DIANA has also been used in numerical analyses of repair and retrofitted structures with satisfactory results (Pham and Al-Mahaidi, 2005; Sato and

Vecchio, 2003; Vecchio and Bucci, 1999; Wong and Vecchio, 2003). The rotating smeared crack approach, conversely to the fixed smeared crack approach, freely reorients the smeared cracks, remaining coaxial with the changing direction of the principal concrete compressive stress field. In general, the smeared crack and the rotating smeared crack approaches necessitate adequate selection of the mesh size to achieve convergence and avoid inaccurate predictions.

Most of the reviewed studies included two-dimensional (2-D) modelling of RC structures. However, some studies included three-dimensional (3-D) modelling, specifically where 2-D plane stress models were unable to represent 3-D characteristics of the structure (Hii and Al-Mahaidi, 2006; Kachlakev et al., 2001; Li et al., 2005). The analyses followed the smeared crack approach and included constant shear retention factors to avoid stress-locking. In this group, the only model representing a retrofitted shear wall subjected to cyclic loading was that by Li et al. (2005).

The fibre section model is another approach for numerical analysis of repaired and retrofitted RC elements. Aprile et al. (2001), and Elnashai and Pinho (1998) presented fibre section models capable of predicting the strength-displacement response, but not cracking and damage of the structural elements. The model presented by Aprile et al. included simulation of the bond-slip interface between the externally bonded FRP and the concrete.

The finite element models presented in the review included simple to refined constitutive models for concrete and reinforcing steel, and, in some cases, the bonding interface between concrete and external steel/FRP. However, limited finite element models included the simulation of the repair/retrofitting construction process (Sato and Vecchio, 2003; Vecchio and Bucci, 1999; Vecchio et al., 2002; Wong and Vecchio, 2003) for the numerical analysis of previously cracked and damaged structures. The repair/retrofitting construction process can be simulated with Program VecTor2 by engaging/disengaging elements representing the new and replaced materials (Vecchio and Bucci, 1999).

Only Vecchio et al., (2002) presented simulation of repaired shear walls subjected to cyclic loading following the repair construction sequence. The simulation included replacement of concrete of the web wall and portions of the flange walls. The analysis was conducted after analysis of the original wall.

Therefore, additional numerical analyses following the repair/retrofitting construction process are needed to asses other repair and retrofitting techniques such as addition/replacement of reinforcement, bonding of steel plates, bonding of FRP sheets/plates, bolting of steel plates, and addition of SMAs. Modelling tools should be able to simulate repair and retrofitting techniques and allow nonlinear numerical analysis of shear walls according to the repair/retrofitting construction process without sacrificing accuracy of results. Furthermore, the numerical tool should be able to capture seismic nonlinear behavioural aspects, such as strength capacity, ductility, failure mode, and energy dissipation.

Chapter 3

3 Analysis Methodology

3.1 Introduction

This chapter presents the methodology followed in this study for the analysis of repaired and/or retrofitted shear walls using the nonlinear finite element method (FEM). An accurate analysis of a repaired/retrofitted RC structure requires nonlinear algorithms that simulate the construction sequence of the repair/retrofitting intervention. In this respect, Program VecTor2, as described by Vecchio and Bucci (1999), allows changes in the structural model by adding (engaging) unstressed elements and eliminating (disengaging) previously stressed elements. Additionally, the program permits modelling of the interface between the new and old material. The program has an extensive library of models for concrete, steel and fibre reinforced polymers (FRP), which can be extended to other emerging repair/retrofitting materials.

The analysis methodology consists of modelling the geometry of the original (undamaged) wall, simulation of the loading protocol, nonlinear analysis of the original wall to failure, modelling of the repaired/retrofitted wall, and finally,

nonlinear analysis of the repaired/retrofitted wall. Furthermore, the methodology includes an additional step for post-processing of the results of the analysis of repaired/retrofitted structures. In the post-processing, salient features such as maximum strength, maximum lateral displacement, failure mechanism, and energy dissipation are assessed and compared with the experimental results.

3.2 Finite Element Program VecTor2

VecTor2 (Vecchio, 1989; Wong and Vecchio, 2002) is a two-dimensional nonlinear finite element (FE) program applicable to membrane structures. The development of VecTor2 is based on implementing low-powered elements, while concentrating on developing improved compatibility, equilibrium and constitutive relationships for structural materials, such as concrete, reinforcing steel, FRP, and other emerging materials. The theoretical bases of VecTor2 are the Modified Compression Field Theory (MCFT) and the Disturbed Stress Field Model (DSFM). VecTor2 models cracked concrete as an orthotropic material with smeared, rotating cracks, which more accurately models the response of cracked reinforced concrete under general loading conditions compared to the fixed crack approach. The program utilizes an incremental total load, iterative secant stiffness algorithm to obtain an efficient and robust nonlinear solution. The flow chart in Fig. 3-1 illustrates the nonlinear iterative process, which starts with the definition of the composite stiffness matrix based on the input data.

Analysis Methodology

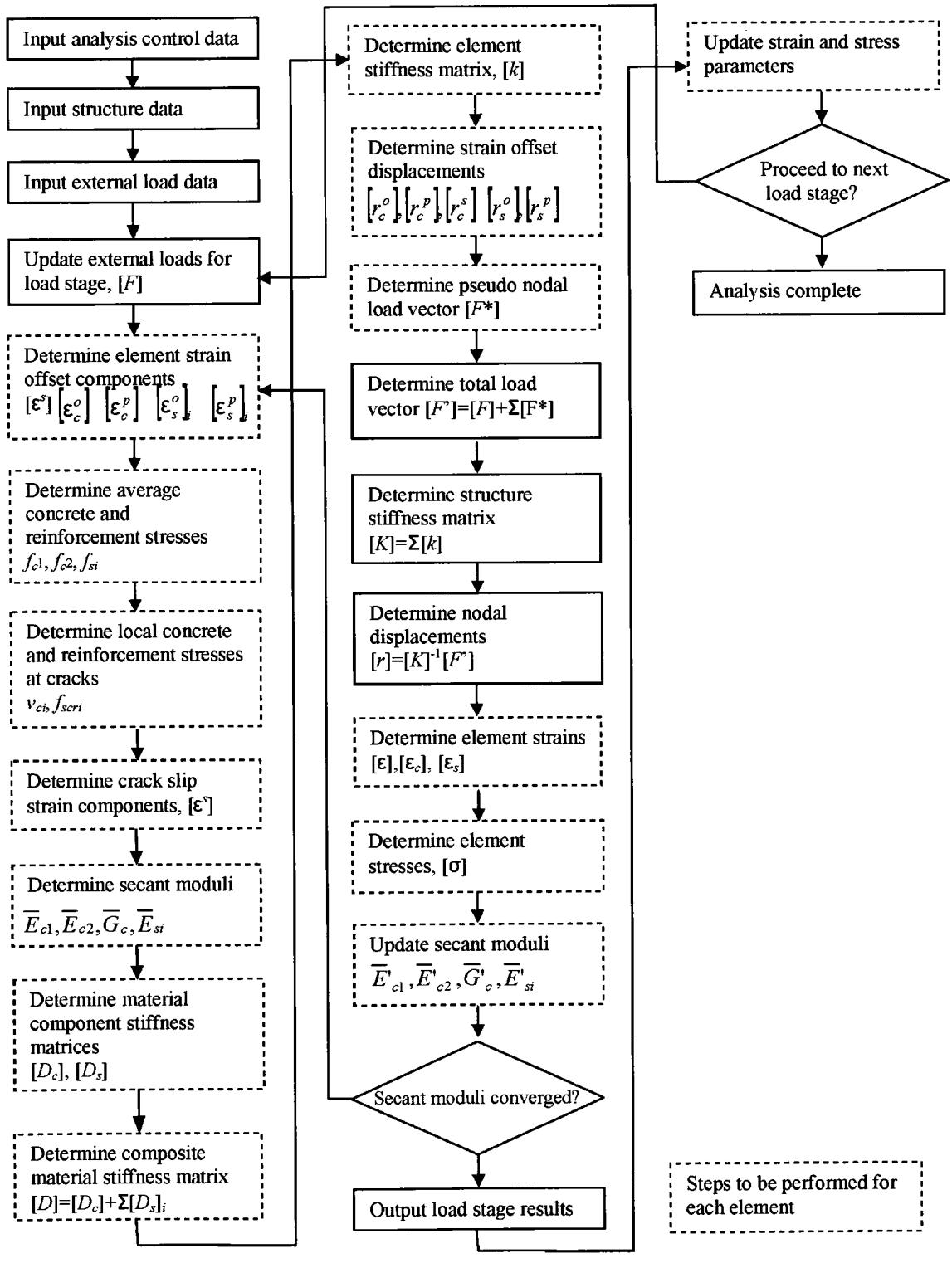

Fig. 3-1 VecTor2 Nonlinear Finite Element Algorithm (Wong and Vecchio, 2002)

Analysis Methodology

3.2.1 Modified Compression Field Theory

The Modified Compression Field Theory (MCFT), developed by Vecchio and Collins (1986), is a theory for predicting the load-deformation response of membrane elements subjected to shear and normal stresses. The MCFT determines the average strains and average stresses of the concrete and reinforcement, and the widths and orientation of cracks by modelling cracked concrete using a smeared rotating crack approach. The theory is comprised of three sets of relationships: compatibility relationships for concrete and reinforcement average strains; equilibrium relationships involving average stresses in the concrete and reinforcement; and constitutive relationships for cracked concrete and reinforcement. The formulation of the MCFT incorporates realistic constitutive models for reinforced concrete based on experimentally observed phenomena. The MCFT considers the compression softening phenomenon due to tensile strains in the transverse direction, and the tension stiffening phenomenon resulting from the tensile stresses carried by the concrete between cracks. The theory also considers local strains and stresses at cracks, as well as failure mechanisms such as yielding of reinforcement at cracks locations.

The original development of the MCFT related in-plane stresses f_x, f_y, and v_{xy} with the corresponding in-plane strains ε_x, ε_y, and γ_{xy} in a concrete membrane (Fig. 3-2) by assuming:

- Uniform distribution of longitudinal and transverse reinforcement,
- Uniform distribution of rotated cracks,
- Uniform distribution of stresses,
- Average stresses and strains over an area with several cracks,
- Unique stress state for each strain state, without consideration of strain history,
- Coinciding strain and stress orientation,

Analysis Methodology

- No bond slip between reinforcement and concrete,
- Independent constitutive relationships for concrete and reinforcement,
- Negligible shear stresses in reinforcement.

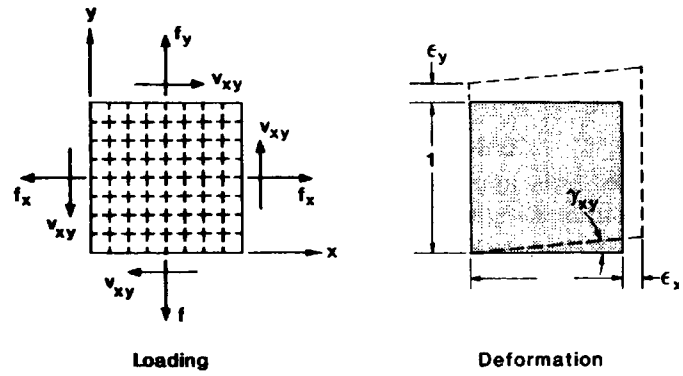

Fig. 3-2 Membrane Element (Vecchio and Collins, 1986)

3.2.1.1 Compatibility Relationships

Compatibility requires that average strains in the concrete (ε_{cx} and ε_{cy}) must be matched by identical average strains in the reinforcement (ε_{sx} and ε_{sy}).

Compatibility in the X and Y directions is expressed by the following equations, providing no bond slip between the concrete and reinforcement and no pre-stressing of the concrete element:

$$\varepsilon_x = \varepsilon_{cx} = \varepsilon_{sx} \tag{3-1}$$

$$\varepsilon_y = \varepsilon_{cy} = \varepsilon_{sy} \tag{3-2}$$

If the three strain components ε_x, ε_y, and γ_{xy} are known, then the strains in the principal directions, ε_1 and ε_2, and the principal strain inclination θ can be found using Mohr's circle of strains (Fig. 3-3).

Analysis Methodology

$$\varepsilon_1 = \tfrac{1}{2}\left(\varepsilon_x + \varepsilon_y\right) + \tfrac{1}{2}\left[\left(\varepsilon_x - \varepsilon_y\right)^2 + \gamma_{xy}{}^2\right]^{\frac{1}{2}} \quad (3\text{-}3)$$

$$\varepsilon_2 = \tfrac{1}{2}\left(\varepsilon_x + \varepsilon_y\right) - \tfrac{1}{2}\left[\left(\varepsilon_x - \varepsilon_y\right)^2 + \gamma_{xy}{}^2\right]^{\frac{1}{2}} \quad (3\text{-}4)$$

$$\theta = \tfrac{1}{2}\tan^{-1}\left(\frac{\gamma_{xy}}{\varepsilon_x - \varepsilon_y}\right) \quad (3\text{-}5)$$

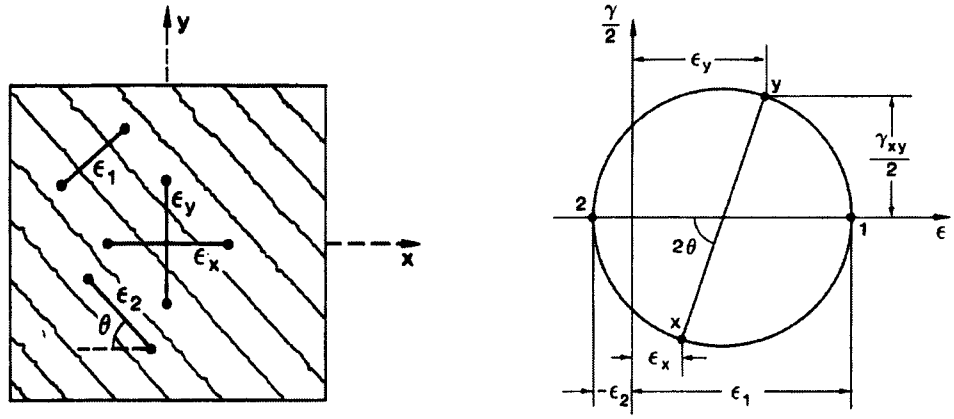

a) b)

Fig. 3-3 Compatibility Relations for Cracked Element: a) Average Strains in Cracked Element; and b) Mohr's Circle for Average Strains (Vecchio and Collins, 1986)

3.2.1.2 Equilibrium Relationships

To satisfy equilibrium relationships, the internal average stresses resisted by the concrete and reinforcement must balance the applied external forces in the X and Y directions of the coordinate system. According to the free-body diagram shown in Fig. 3-4, the following equilibrium relationships can be derived.

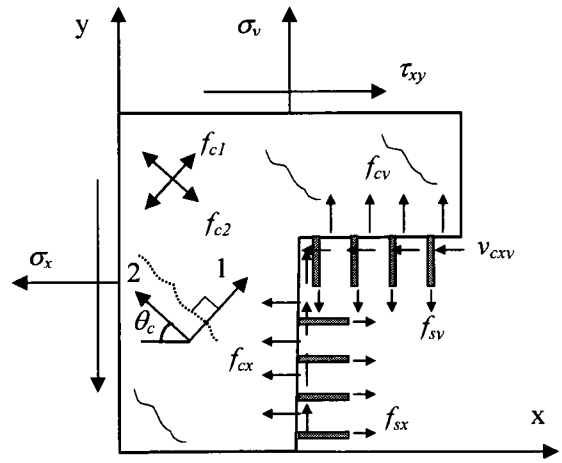

Fig. 3-4 Free Body Diagram of Reinforced Concrete Element Showing Average Stresses (Wong and Vecchio, 2002)

$$\sigma_x = f_{cx} + \rho_{sx} f_{sx} \tag{3-6}$$

$$\sigma_y = f_{cy} + \rho_{sy} f_{sy} \tag{3-7}$$

$$\tau_{xy} = v_{cxy} \tag{3-8}$$

Where σ_x and σ_y are the applied normal stress, τ_{xy} is the applied shear stress, f_{cx} and f_{cy} are the average concrete stresses, f_{sx} and f_{sy} are the reinforcement stresses, v_{cxy} is the average shear stress in the concrete, and ρ_{sx} and ρ_{sy} are the reinforcement ratios in the X and Y directions, respectively.

Using Mohr's circle of stresses shown in Fig. 3-5, the average concrete stresses f_{cx} and f_{cy} can be related to the average principal concrete stress f_1. Note that θ_c is the principal stress inclination.

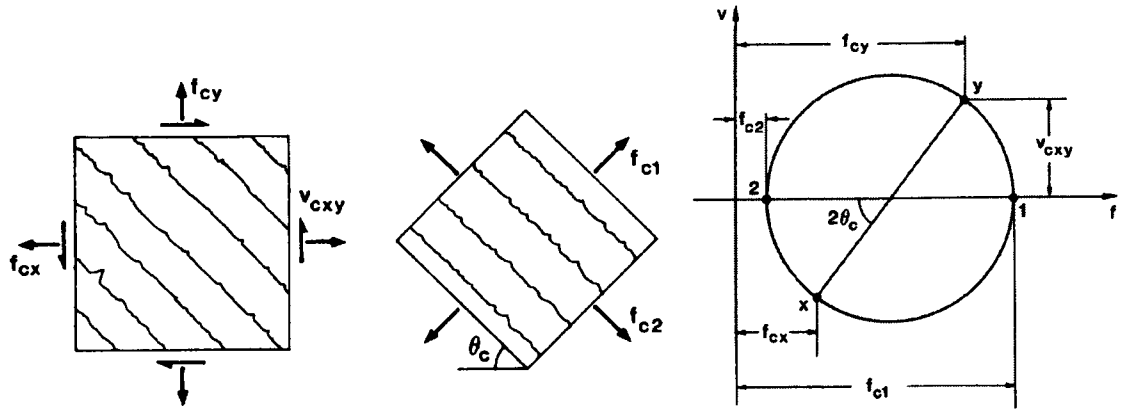

Fig. 3-5 Stresses in Cracked Concrete: a) Average Concrete Stresses; b) Principal Stresses in Concrete; and c) Mohr's Circle for Average Concrete Stresses (Vecchio and Collins, 1986)

$$f_{cx} = f_{c1} - v_{cxy} \cdot \cot\theta_c \qquad \textbf{(3-9)}$$

$$f_{cy} = f_{c1} - v_{cxy} \cdot \tan\theta_c \qquad \textbf{(3-10)}$$

3.2.1.3 Constitutive Relationships

Constitutive models relate average strains from the compatibility relationships with average stresses from the equilibrium relationships. Although the concrete and reinforcement stress-strain relationships are not completely independent, they are treated separately for simplicity of the method.

For concrete in compression, the constitutive relationship associates the principal compressive stress, f_{c2}, with the principal compressive strain, ε_{c2} (Fig. 3-6). The relationship incorporates the compression softening phenomenon due to the co-existing tensile strain, ε_{c1}, in the cracked concrete.

$$f_{c2} = \frac{f'_c \left[2(\varepsilon_{c2}/\varepsilon_o) - (\varepsilon_{c2}/\varepsilon_o)^2\right]}{0.8 - 0.34(\varepsilon_{c1}/\varepsilon_o)} \qquad \textbf{(3-11)}$$

Where f'_c is the compressive cylinder strength and ε_o is the strain corresponding to the peak cylinder strength.

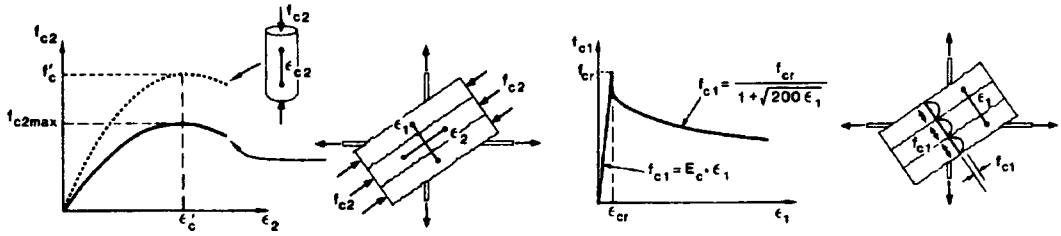

a) b)

Fig. 3-6 Constitutive Relationships: a) Cracked Concrete in Compression; and b) Cracked Concrete in Tension (Vecchio and Collins, 1986)

Before cracking, the concrete behaves linear-elastically in tension as follows:

$$f_{c1} = E_c \cdot \varepsilon_{c1} \quad for \quad 0 < \varepsilon_{c1} < \varepsilon_{cr} \tag{3-12}$$

$$\varepsilon_{cr} = \frac{f'_t}{E_c} \tag{3-13}$$

$$E_c = 2\frac{f'_c}{\varepsilon_o} \tag{3-14}$$

Where E_c is the modulus of elasticity for concrete, ε_{cr} is the cracking strain, and f'_t is the cracking stress.

After cracking, tensile stresses may continue to exist in the concrete between cracks in reinforced concrete due to bond interactions between the concrete and reinforcement. To model this phenomenon, known as tension stiffening, the following relationship is suggested.

$$f_{c1} = \frac{f'_t}{1 + \sqrt{200\varepsilon_{c1}}} \tag{3-15}$$

For the reinforcement, a tri-linear stress-strain response is assumed. Figure 3-7 illustrates the reinforcement relationship with an initial ascending linear-elastic

branch, followed by a yield plateau, and finally a linear ascending branch corresponding to the strain hardening phase.

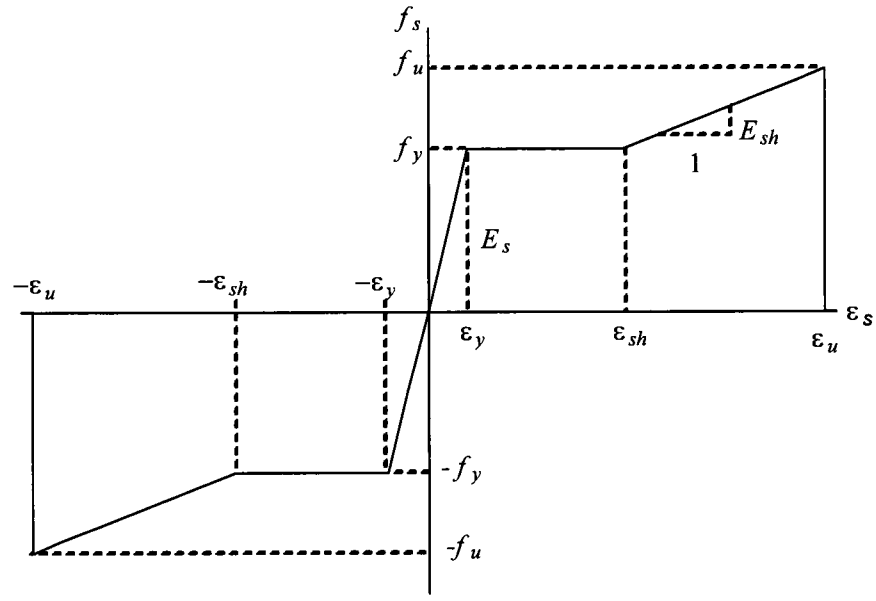

Fig. 3-7 Reinforcement Stress-Strain Response (Wong and Vecchio, 2002)

$$f_s = E_s \varepsilon_s \qquad \varepsilon_s \le \varepsilon_y \qquad \textbf{(3-16)}$$

$$f_s = f_y \qquad \varepsilon_y < \varepsilon_s \le \varepsilon_{sh} \qquad \textbf{(3-17)}$$

$$f_s = f_y + E_{sh}(\varepsilon_s - \varepsilon_{sh}) \le f_u \qquad \varepsilon_s > \varepsilon_{sh} \qquad \textbf{(3-18)}$$

Where ε_s is the strain experienced by the steel, ε_y is the yield strain, E_s is the modulus of elasticity, E_{sh} is the strain hardening modulus, ε_{sh} is the strain at the onset of the strain hardening, f_y is the yield stress, and f_u is the ultimate stress.

Local stress conditions at a crack must be checked to ensure that the reinforcement is able to transmit average tensile stresses across the crack plane. This is satisfied with the following relationship.

$$f_{c1} \le \sum_i \rho_i (f_{yi} - f_{si})(Cos\theta_{ic})^2 \qquad \textbf{(3-19)}$$

Where i refers to the direction in question, θ_{ic} is the angle between the centerline of the reinforcement and the crack normal, f_{yi} is the yield stress of the reinforcement in the i_{th} direction, and f_{si} is the average stress in the i_{th} direction reinforcement.

Furthermore, a skew angle between the reinforcement and the crack results in local shear stresses. These shear stresses, if significant, can cause shear sliding. The shear stresses are limited by aggregate interlock based on the work of Walraven (1981), which relates the shear across the crack v_{ci}, the crack width w, and the required compressive stress on the crack f_{ci}:

$$v_{ci} = 0.18 v_{ci\max} + 1.64 f_{ci} - 0.82 \frac{f_{ci}^{\ 2}}{v_{ci\max}} \tag{3-20}$$

$$v_{ci\max} = \frac{\sqrt{-f'_c}}{0.31 + 24w/(a+16)} \tag{3-21}$$

Where a is the maximum aggregate size in millimeters. If the maximum allowable average concrete tensile stress in Equation 3-19 or the local shear stress at a crack in Equation 3-20 is exceeded, the strain state of the element must be modified. This results in a lower average concrete tensile stress.

Additional details of the formulations for the MCFT can be found in Wong and Vecchio (2002).

3.2.2 Disturbed Stress Field Model

The Disturbed Stress Field Model (DSFM) (Vecchio, 2000) represents an extension of the MCFT in several important aspects. Most importantly, the DSFM augments the compatibility relationships of the MCFT to include crack shear-slip deformations as illustrated in Fig. 3-8. The strains due to these deformations are explicitly evaluated and separated from the strains of the concrete continuum due to stress. As such, the DSFM decouples the orientation of the principal stress field from that of the principal

strain field. Moreover, the DSFM eliminates the crack shear check as required by the MCFT by explicitly calculating crack-slip deformations.

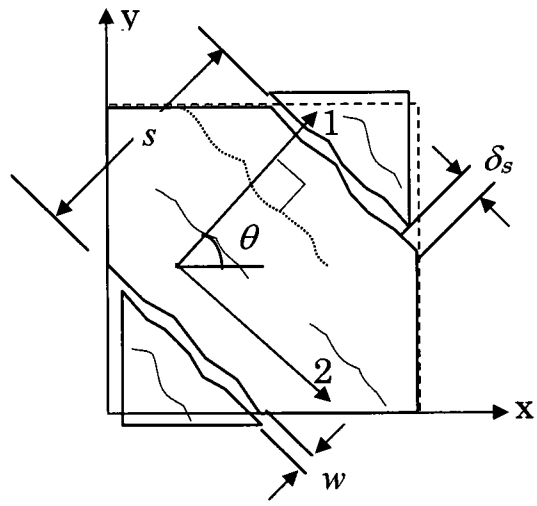

Fig. 3-8 Deformation Due to Crack Shear Slip (Wong and Vecchio, 2002)

3.2.2.1 Compatibility Relationships

The DSFM expresses the total strains, ε_x, ε_y, and γ_{xy} as the sum of net concrete strains, ε_{cx}, ε_{cy}, and γ_{cxy}, and strains due to shear slip ε^s_x, ε^s_y, and γ^s_{xy}:

$$\varepsilon_x = \varepsilon_{cx} + \varepsilon_x^s \tag{3-22}$$

$$\varepsilon_y = \varepsilon_{cy} + \varepsilon_y^s \tag{3-23}$$

$$\gamma_{xy} = \gamma_{cxy} + \gamma_{xy}^s \tag{3-24}$$

If the three strain components ε_{cx}, ε_{cy}, and γ_{cxy} are known, then the net concrete strains in the principal directions, ε_{c1} and ε_{c2}, and the principal net concrete strain inclination θ can be found using Mohr's circle of strains. Furthermore, the orientation of the concrete stresses θ_c is equal to the orientation of the principal net concrete strains θ.

Analysis Methodology

$$\varepsilon_{c1} = \tfrac{1}{2}\left(\varepsilon_{cx} + \varepsilon_{cy}\right) + \tfrac{1}{2}\left[\left(\varepsilon_{cx} - \varepsilon_{cy}\right)^2 + \gamma_{cxy}{}^2\right]^{\frac{1}{2}} \quad \textbf{(3-25)}$$

$$\varepsilon_{c2} = \tfrac{1}{2}\left(\varepsilon_{cx} + \varepsilon_{cy}\right) - \tfrac{1}{2}\left[\left(\varepsilon_{cx} - \varepsilon_{cy}\right)^2 + \gamma_{cxy}{}^2\right]^{\frac{1}{2}} \quad \textbf{(3-26)}$$

$$\theta = \theta_c = \tfrac{1}{2}\tan^{-1}\left(\frac{\gamma_{cxy}}{\varepsilon_{cx} - \varepsilon_{cy}}\right) \quad \textbf{(3-27)}$$

The crack slip shear strain components, ε^s_x, ε^s_y, and γ^s_{xy}, are calculated using Mohr's circle of strains from the average crack slip shear strain γ_s, which is defined as the crack slip, δ_s, divided by the average crack spacing, s, as follows:

$$\gamma_s = \frac{\delta_s}{s} \quad \textbf{(3-28)}$$

$$\varepsilon^s_x = -\tfrac{1}{2}\gamma_s \sin(2\theta) \quad \textbf{(3-29)}$$

$$\varepsilon^s_y = \tfrac{1}{2}\gamma_s \sin(2\theta) \quad \textbf{(3-30)}$$

$$\gamma^s_{xy} = \gamma_s \cos(2\theta) \quad \textbf{(3-31)}$$

The orientation of the principal total strain field, θ_ε, is determined from the total strain components.

$$\theta_\varepsilon = \tfrac{1}{2}\tan^{-1}\left(\frac{\gamma_{xy}}{\varepsilon_x - \varepsilon_y}\right) \quad \textbf{(3-32)}$$

The difference between the orientation of total strains θ_ε and the orientation of the principal net concrete stresses θ_c defines the rotation lag, $\Delta\theta$:

$$\Delta\theta = \theta_\varepsilon - \theta_c \quad \textbf{(3-33)}$$

Assuming perfect bond, the average strains of the reinforcement components in the X and Y directions are equal to the total strains:

$$\varepsilon_{sx} = \varepsilon_x \quad \textbf{(3-34)}$$

$$\varepsilon_{sy} = \varepsilon_y^{\ s} \tag{3-35}$$

3.2.2.2 Equilibrium Relationships

The following average stress equilibrium relationships of the DSFM are identical to those of the MCFT.

$$\sigma_x = f_{cx} + \rho_{sx} f_{sx} \tag{3-36}$$

$$\sigma_y = f_{cy} + \rho_{sy} f_{sy} \tag{3-37}$$

$$\tau_{xy} = v_{cxy} \tag{3-38}$$

The DSFM incorporates equilibrium relationships for local stresses at a crack.

$$f_{c1} = \rho_x (f_{scrx} - f_{sx}) \cos^2 \theta_{nx} + \rho_y (f_{scry} - f_{sy}) \cos^2 \theta_{ny} \tag{3-39}$$

$$v_{ci} = \rho_x (f_{scrx} - f_{sx}) \cos\theta_{nx} \cdot \sin\theta_{nx} + \rho_y (f_{scry} - f_{sy}) \cos\theta_{ny} \cdot \sin\theta_{ny} \tag{3-40}$$

Where f_{scrx} and f_{scry} are the local reinforcement stresses at a crack, and θ_{nx} and θ_{ny} are the angles between the normal to the crack and the reinforcement. Average and local stresses at a crack are depicted in Fig. 3-9.

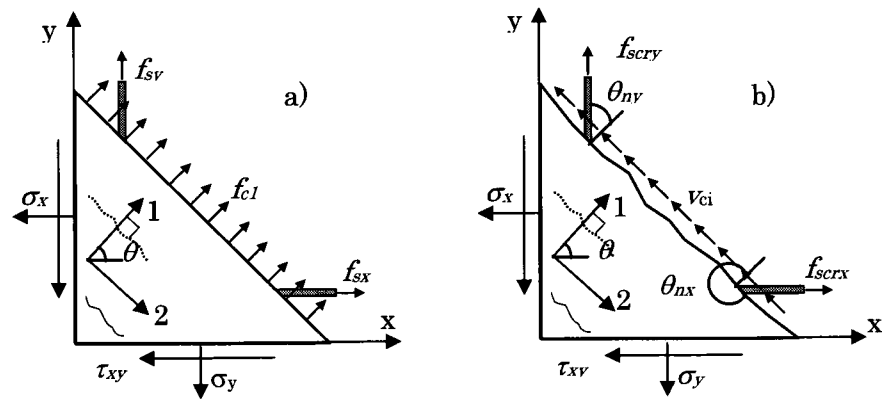

Fig. 3-9 Comparison of Average and Local Stresses at a Crack: a) Average Stresses Between Crack; and b) Local Stresses at Crack Free Surface (Wong and Vecchio, 2002)

Analysis Methodology

The average concrete tensile stress is subject to the limits of the yield strength of the reinforcement traversing the crack:

$$f_{c1} \le \rho_x \left(f_{sxyield} - f_{sx}\right)\cos^2\theta_{nx} + \rho_y \left(f_{syyield} - f_{sy}\right)\cos^2\theta_{ny} \qquad \textbf{(3-41)}$$

Furthermore, shear stresses at a crack are not limited since the DSFM explicitly incorporates deformations due to shear slip.

3.2.2.3 Constitutive Relationships

The development of the DSFM resulted in revised and refined constitutive models for cracked concrete previously developed in the MCFT. The following is a brief description of the modifications associated with the DSFM.

The reduction factor, β_d, reflects the softening effect due to the coexisting principal tensile strains; therefore, the concrete cylinder strength, f'_c, and corresponding peak strain, ε_o, are both reduced.

$$\beta_d = \frac{1}{1+C_s C_d} \le 1.0 \qquad \textbf{(3-42)}$$

$$f_p = -\beta_d f'_c \qquad \textbf{(3-43)}$$

$$\varepsilon_p = -\beta_d \varepsilon_o \qquad \textbf{(3-44)}$$

The factor C_d accounts for the softening effect of transverse tensile strains:

$$C_d = 0.35\left(-\varepsilon_{c1}/\varepsilon_{c2} - 0.28\right)^{0.8} \qquad \textbf{(3-45)}$$

The factor C_s recognizes whether the analysis accounts for element slip deformations. C_s is equal to 1.0, if the analysis is based on the MCFT, thus the softening effect of shear slippage is coupled with the softening effect due to tensile strains. In this case, slip deformations are not explicitly calculated. If the analysis if based on the DSFM, element slip deformations are explicitly considered, resulting in C_s equal to 0.55.

Analysis Methodology

Using the softened parameters, the following determines the relationship between the principal concrete compressive stress, f_{c2}, and the principal net compressive strain, ε_{c2}:

$$f_{c2} = f_p \frac{n(\varepsilon_{c2}/\varepsilon_p)}{(n-1)+(\varepsilon_{c2}/\varepsilon_p)^{nk}} \quad \textbf{(3-46)}$$

Where:

$$n = 0.80 - f_p/17 \quad (in\ MPa) \quad \textbf{(3-47)}$$

$$k = \begin{cases} 1.0 & for\ \varepsilon_p < \varepsilon_{c2} < 0 \\ 0.67 - f_p/62 & for\ \varepsilon_{c2} < \varepsilon_p < 0 \end{cases} \quad \textbf{(3-48)}$$

Before cracking, the concrete behaves linear-elastically in tension as follows:

$$f_{c1} = E_c \cdot \varepsilon_{c1} \quad for\ 0 < \varepsilon_{c1} < \varepsilon_{cr} \quad \textbf{(3-49)}$$

$$\varepsilon_{cr} = \frac{f'_t}{E_c} \quad \textbf{(3-50)}$$

$$E_c = 2\frac{f'_c}{\varepsilon_o} \quad \textbf{(3-51)}$$

Where E_c is the modulus of elasticity for concrete, ε_{cr} is the cracking strain, and f'_t is the cracking stress.

The following relationship is suggested to model the tension stiffening phenomenon after cracking.

$$f_{c1}^a = \frac{f'_t}{1+\sqrt{c_t \varepsilon_{c1}}} \quad for\ \varepsilon_{cr} < \varepsilon_{c1} \quad \textbf{(3-52)}$$

The coefficient c_t, proposed by Bentz (2000), incorporates the influence of reinforcement bond characteristics and is computed as follows:

Analysis Methodology

$$c_t = \frac{2.2}{\sum_{i=1}^{n} \frac{4\rho_i}{d_{b_i}} |\cos\theta_{n_{ii}}|} \tag{3-53}$$

Where d_{bi} is the bar diameter and ρ_i is the reinforcement ratio of each of the n reinforcement components.

In addition, post-cracking tensile stresses, $f_{c1}{}^b$, due to the tension softening phenomenon is considered in the DSFM by introducing the following linear relationship:

$$f_{c1}{}^b = f'_t \left[1 - \frac{(\varepsilon_{c1} - \varepsilon_{cr})}{(\varepsilon_{ts} - \varepsilon_{cr})} \right] \qquad for\ \varepsilon_{cr} < \varepsilon_{c1} < \varepsilon_{ts} \tag{3-54}$$

The terminal strain, ε_{ts}, which corresponds to the strain where the tensile stresses reduce to zero, is determined from the fracture energy parameter G_f and the characteristic Length, L_r.

$$\varepsilon_{ts} = 2.0 \frac{G_f}{f'_t \cdot L_r} \tag{3-55}$$

The post-cracking principal tensile stress in concrete is taken as the larger of the values predicted by tension stiffening and tension softening:

$$f_{c1} = \max\left(f_{c1}{}^a, f_{c1}{}^b\right) \tag{3-56}$$

Similar to the MCFT, a tri-linear stress-strain response (Fig. 3-7) is assumed for the reinforcement as follows:

$$f_s = E_s \varepsilon_s \qquad \varepsilon_s \le \varepsilon_y \tag{3-57}$$

$$f_s = f_y \qquad \varepsilon_y < \varepsilon_s \le \varepsilon_{sh} \tag{3-58}$$

$$f_s = f_y + E_{sh}(\varepsilon_s - \varepsilon_{sh}) \le f_u \qquad \varepsilon_s > \varepsilon_{sh} \tag{3-59}$$

3.2.2.4 Shear Slip Relationships

Two approaches can be used to determine the crack-slip and shear slip strain. The first is the aggregate interlock approach, based on the work of Walraven (1981), and the second is the constant rotation lag approach. The shear slip strain is computed by both approaches and the larger of values is used.

The crack-slip δ_s^a and shear slip strain γ_s^a according to the aggregate interlock approach are calculated with the following expressions:

$$\delta_s{}^a = \frac{v_{ci}}{1.8w^{-0.8} + \left(0.234w^{-0.707} - 0.20\right)\cdot f_{cc}} \tag{3-60}$$

$$\gamma_s{}^a = \frac{\delta_s{}^a}{s} \tag{3-61}$$

Where f_{cc} is the concrete cube strength, w is the average crack width, and s is the average crack spacing.

The second approach for modelling shear slip consists of specifying a constant rotation lag, θ^l, between the inclination of the principal total strain axis, θ_ε, and the inclination of the principal stress axis, θ_σ. To implement this approach, it is necessary to define the post-cracking rotation, $\Delta\theta_\varepsilon$, of the principal total strain axis, relative to the orientation of the principal strains and stresses at initial cracking, θ_{ic}:

$$\Delta\theta_\varepsilon = \theta_\varepsilon - \theta_{ic} \tag{3-62}$$

The post-cracking rotation, $\Delta\theta_\sigma$, of the principal stress field is then related to $\Delta\theta_\varepsilon$, by the constant rotation lag as follows:

$$\Delta\theta_\sigma = \begin{cases} \Delta\theta_\varepsilon & for\ |\Delta\theta_\varepsilon| \le \theta^l \\ \left(\Delta\theta_\varepsilon - \theta^l\right) & for\ |\Delta\theta_\varepsilon| > \theta^l \end{cases} \tag{3-63}$$

The orientation of the principal stress field is determined as the sum of the orientation at initial cracking, and the rotation at post-cracking as follows:

$$\theta_\sigma = \theta_{ic} + \Delta\theta_\sigma \tag{3-64}$$

The shear slip strain γ_s^b is obtained by using Mohr's circle of strains.

$$\gamma_s^b = \gamma_{xy} \cdot \cos 2\theta_c + (\varepsilon_y - \varepsilon_x) \cdot \sin 2\theta_\sigma \tag{3-65}$$

Additional details of the formulations for the DSFM can be found in Wong and Vecchio (2002).

3.2.3 Elements and Material Models

Program VecTor2 has a library of constitutive models for three categories of elements: concrete, discrete reinforcement and bond materials. The following is a description of the elements and models used in modelling the shear walls presented herein. Additional details can be found elsewhere (Wong and Vecchio, 2002).

All elements are simple and low powered, with minimal nodes, straight conforming boundaries, and linear displacement functions. Compared to higher powered elements, these lower powered elements are advantageous in two aspects: first, VecTor2 explicitly calculates stiffness coefficients without resorting to numerical integration; and second, low powered elements are not susceptible to spurious behaviours such as zero-energy modes (Wong and Vecchio, 2002).

3.2.3.1 Concrete

Concrete, with or without smeared reinforcement, is modelled with three types of FE's: constant strain triangles, plane stress rectangles, and quadrilaterals. The constant strain triangle is a three-node element with six degrees of freedom; two degrees of freedom at each node. The triangle has constant thickness and may assume any orientation in the X, Y coordinate system (Fig. 3-10). The plane stress rectangle is a four-node element with eight degrees of freedom; two degrees of freedom at each node

(Fig. 3-11). The rectangle has constant thickness and its edges are parallel to the X and Y axes. The quadrilateral is a four-node element with uniform thickness. As each node translates in the X and Y directions, the element has a total of eight degrees of freedom (Fig. 3-12). The quadrilateral may assume any orientation and shape in the X, Y coordinate system. VecTor2 decomposes the quadrilateral into two constant strain triangles T_A and T_B as illustrated in Fig. 3-12, and analyzes each triangle separately. Rectangular elements with aspect ratio less than 3:2, and avoiding distorted and elongated triangular and quadrilateral elements are suggested. Plane stress rectangles are preferable for modelling reinforced concrete since they can represent linear gradients of strain and stress. Triangular elements should be limited to regions with geometric constraints.

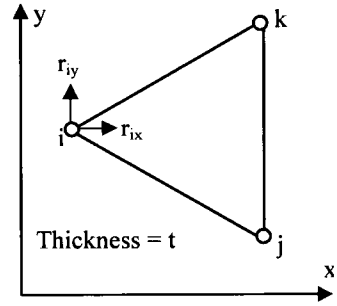

Fig. 3-10 Constant Strain Triangle Element (Wong and Vecchio, 2002)

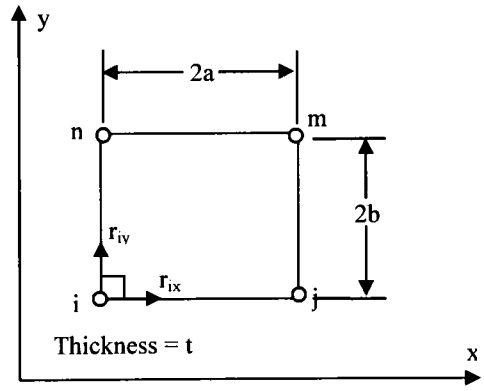

Fig. 3-11 Plane Stress Rectangle Element (Wong and Vecchio, 2002)

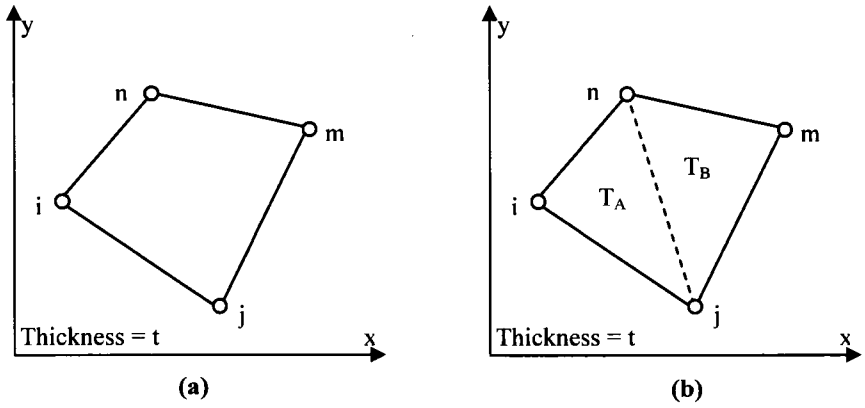

Fig. 3-12 a) Quadrilateral Element; b) Decomposition of Quadrilateral Element into Two Constant Strain Triangle Elements (Wong and Vecchio, 2002)

The constitutive models for concrete are nonlinear empirical functions of stress and strain that describe the primary response as well as secondary effects in concrete behaviour. Whereas primary models such as pre-peak and post-peak response pertain to plain concrete, some models for secondary effects such as confinement pertain to reinforced concrete.

Default models in VecTor2 for primary and secondary effects of concrete are: Hognestad's Parabola for the compressive pre-peak response; modified Park-Kent for the post-peak response; Vecchio's 1992-A model for compression softening; modified Bentz tension stiffening model for tension stiffening effects; linear model for tension softening; Kupfer/Richard model for confined strength effect; modified Kupfer for lateral expansion or dilatation of concrete; Mohr-Coulomb stress model for cracking criterion; Vecchio-Collins 1986 for crack slip check; 20% of the aggregate size limit for crack width check; Vecchio-Lai for slip distortion; and nonlinear with plastic offset model for concrete hysteretic response. Figure 3-13 illustrates typical concrete response in compression and tension.

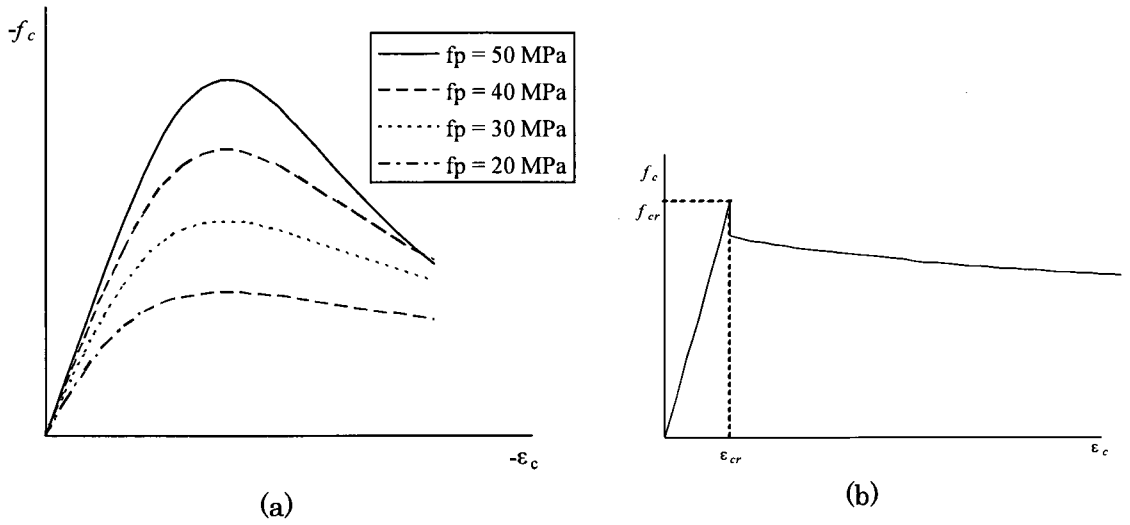

Fig. 3-13 Typical Concrete Response: a) Pre-Peak and Post-Peak Compression Response; b) Tension Response (Wong and Vecchio, 2002)

3.2.3.2 Reinforcement

Two-node truss bar elements with uniform cross-sectional area (Fig. 3-14) are used for modelling internal and external reinforcement for cases where the reinforcement is not modelled as smeared into the concrete element. The truss bar element has four degrees of freedom; displacement in X and Y directions at each node, and can assume any orientation in the X, Y coordinate system. Three types of reinforcement materials are available in VecTor2, which are applicable to this study: ductile steel reinforcement (Fig. 3-7), tension only reinforcement, and externally bonded FRP reinforcement. Conversely, for the latter, the tension only model can be used; however, crack stresses are more accurately calculated when the externally bonded FRP element is used. Other reinforcement elements include compression only reinforcement and prestressing steel.

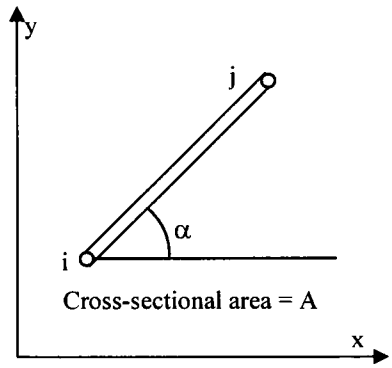

Fig. 3-14 Truss Bar Element (Wong and Vecchio, 2002)

The default models for reinforcement incorporated in VecTor2 include: Seckin model with Bauschinger effect to capture the hysteretic response of the reinforcement; Tassio crack-slip model for dowel action, which arises from crack slip occurring transversely to the axes of the reinforcement; and Asatsu model for buckling of reinforcement. Note that the MCFT does not explicitly evaluate crack shear-slip deformations and, therefore, does not include dowel action of the reinforcement. To account for buckling, the reinforcement is discretely model with truss bars connected to the concrete elements by means of link-bond or contact-bond elements.

3.2.3.3 Bonding Interface

VecTor2 includes two types of bond-slip elements to represent the bonding interface between the reinforcement (steel and FRP) and the concrete: a double-node non-dimensional link-bond element and a two-double-node one-dimensional contact-bond element. Prior to slippage, one of the double nodes of the bond-slip element is connected to the discrete reinforcement element, while the second node is connected to the concrete element. Figure 3-15 and Fig. 3-16 depict the link-bond and contact-bond elements. The link-bond element contains two orthogonal springs connecting the nodes of the reinforcement and concrete elements located at the same coordinates; this allows for transferring of shear and normal stresses to the reinforcement. The bond stress-slip can be described by a multilinear relation for a maximum of three bond

stresses τ_1, τ_2, and τ_3, and corresponding slips $\Delta_1<\Delta_2<\Delta_3$ as illustrated in Fig. 3-17. The default bond model in VecTor2 is the Eligehausen for confined and unconfined bond stress-slip relationships.

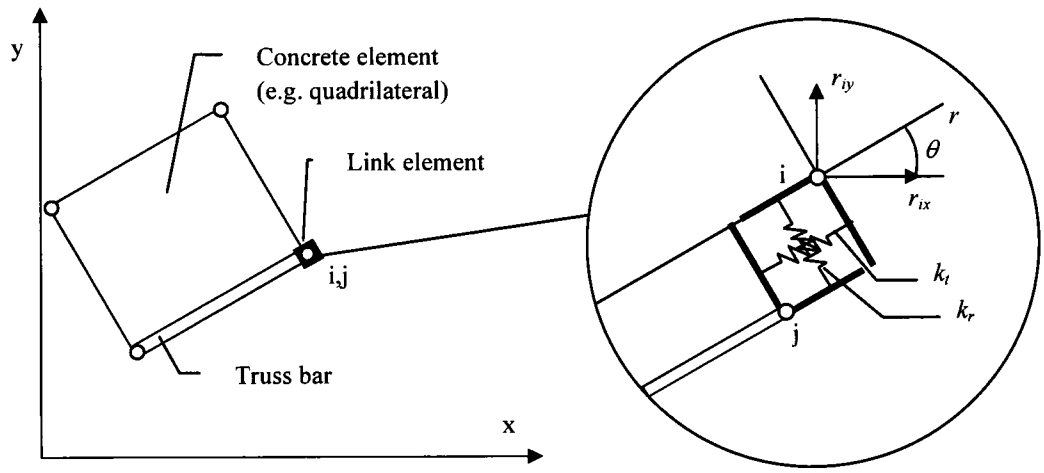

Fig. 3-15 Link-Bond Element (Wong and Vecchio, 2002)

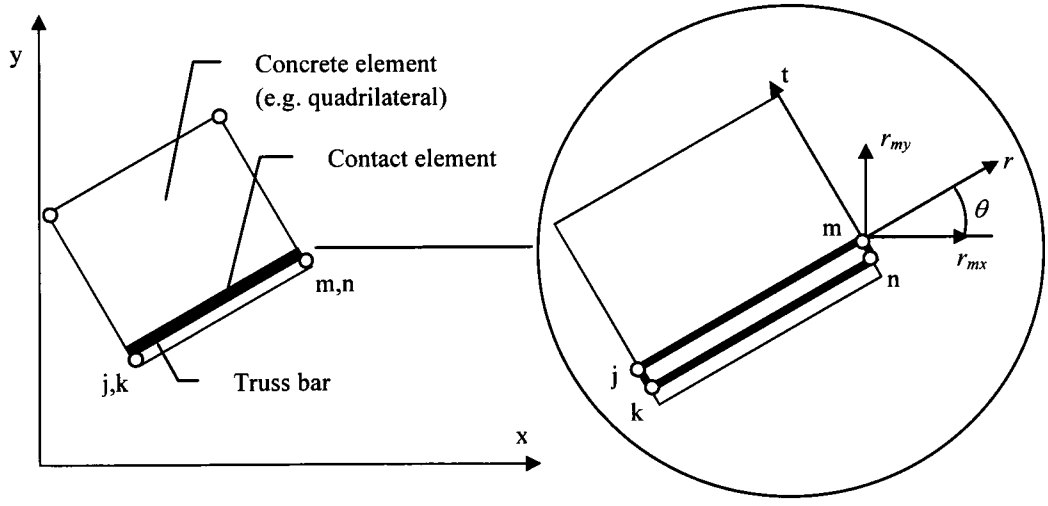

Fig. 3-16 Contact-Bond Element (Wong and Vecchio, 2002)

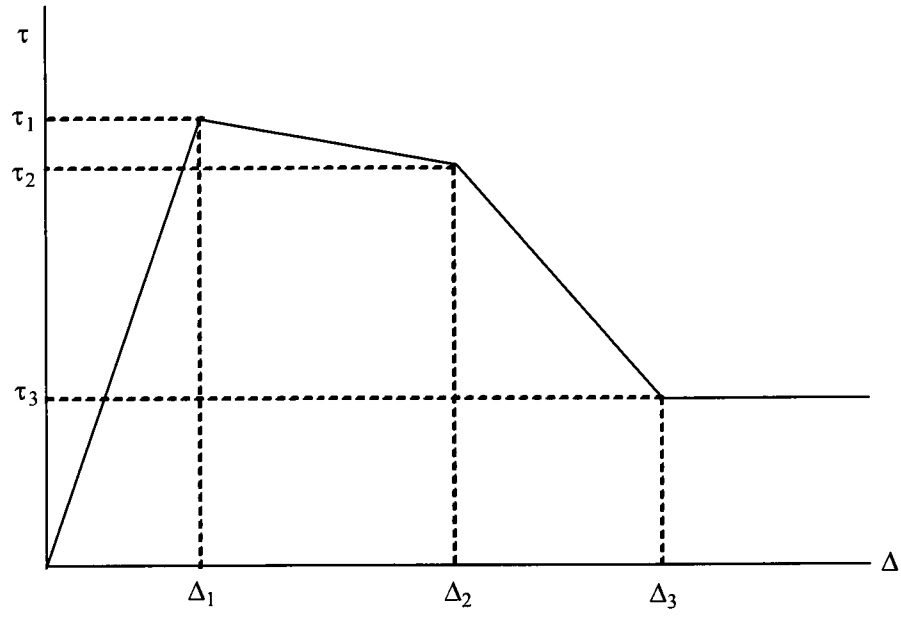

Fig. 3-17 Bond Stress-Slip Response for Externally Bonded Plates or Sheets (Wong and Vecchio, 2002)

3.3 Analysis Methodology

The analysis methodology for repaired/retrofitted shear walls is illustrated in Fig. 3-18. The methodology includes the repair and/or retrofitting construction sequence, which is simulated through the engaging-disengaging of elements approach incorporated in Program VecTor2. As described by Vecchio and Bucci (1999), the engaged elements represent portions of the structure that are currently present. They contribute to the strength and stiffness of the structure. Conversely, disengaged elements represent portions of the structure that are currently absent. They do not contribute to the strength and stiffness of the structure. A typical repair and/or retrofitting procedure consists of replacing damaged material from the original structure with new material in the repaired and/or retrofitted structure.

Analysis Methodology

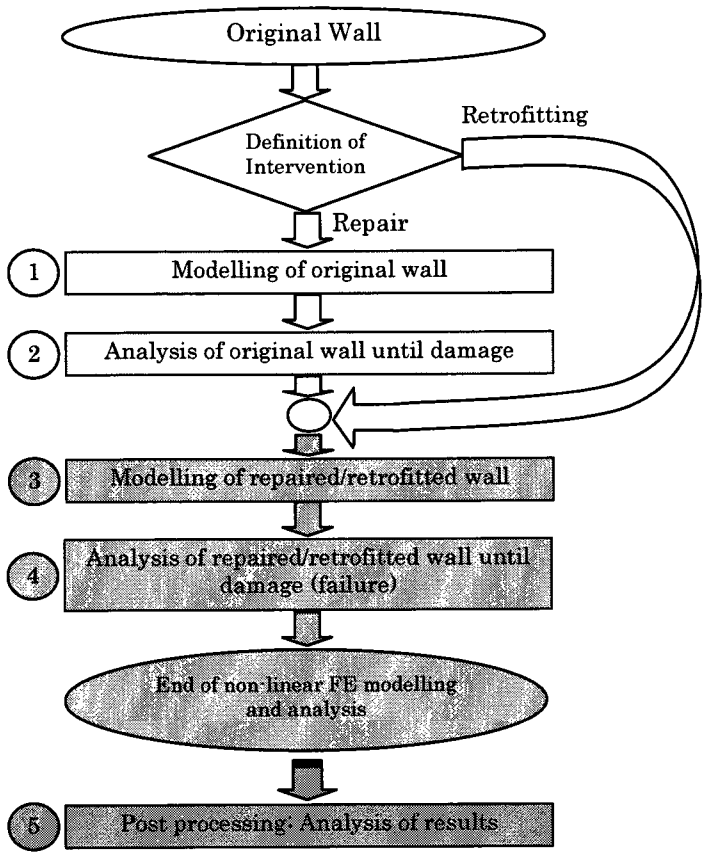

Fig. 3-18 Finite Element Modelling and Analysis Process

The engaging-disengaging process for modelling repaired and/or retrofitted structures is illustrated in Fig. 3-19, Fig. 3-20 and Table 3-1, assuming zero initial elastic offset strains (thermal, pre-strain, shrinkage, and lateral expansion effects), and zero slippage strains. $\varepsilon_{\_ori}$ and $\varepsilon_{\_rep}$ are the total strains of the original and repaired elements, respectively; ε_{i_ori} and ε_{i_rep} are the net strains of the original and repaired elements, respectively; and $\varepsilon^{p}_{\_rep}$ is the plastic offset of the repaired element. In Fig. 3-19 and Fig. 3-20, point 1 corresponds to the initial condition of the original element in which both the stress and strain are zero. Point 2 corresponds to the stress and strain at the predefined level of damage of the original element, where the element sustains a total strain of ε_{2_ori}. From point 2 to point 3, the element is unloaded to zero stress to proceed with the repair and/or retrofitting simulation by using the engaging-disengaging procedure. Therefore, point 3 corresponds to the end of analysis of the original element in which the total strain $\varepsilon_{\_ori}$ is equal to ε_{3_ori}. In the engaging-

disengaging process, the total strain of the original element, $\varepsilon_{\_ori}$, is retained as a plastic offset strain $\varepsilon^{p}_{\_rep}$ for the analysis of the repaired/retrofitted element. Therefore, at point 3, the repair/retrofitting element starts contributing to strength from a zero stress-strain condition, which reflects the actual behaviour of the new materials. The repaired and/or retrofitted element is then analyzed from point 3 to 4 and the net strains of the repaired/retrofitted element ε_{i_rep} are calculated as the total strain of the element $\varepsilon_{\_rep}$ minus the plastic offset strain ε_{p_rep}. Point 4 corresponds to the ultimate condition of the repaired and/or retrofitted element.

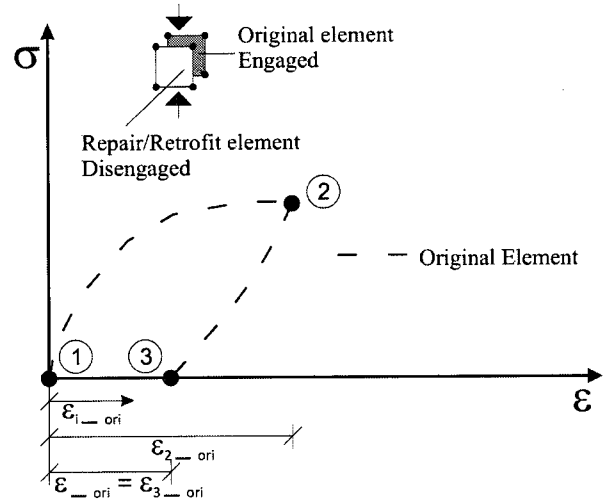

Fig. 3-19 Strain-Stress Relationship of Original Element

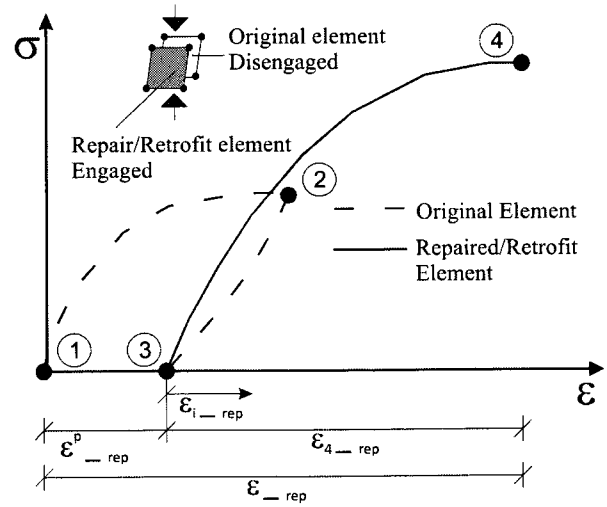

Fig. 3-20 Strain-Stress Relationship of Repaired/Retrofitted Element

Table 3-1 Engaging-Disengaging Process of a Repaired and/or Retrofitted Element

Stage	*Strain Calculation*	
1) Unloaded original element.	$\varepsilon_{\_ori} = 0$	
	$\varepsilon_{\_rep} = 0$	
2) Loaded original element.	$\varepsilon_{\_ori} = \varepsilon_{2\_ori}$	Contribution Stiffness, strength
	$\varepsilon_{\_rep} = \varepsilon_{\_ori}$	No Contribution Stiffness, strength
3) Repair/Retrofitting.		
a) Unloaded original element.	$\varepsilon_{\_ori} = \varepsilon_{3\_ori}$	Contribution Stiffness, strength
	$\varepsilon_{\_rep} = \varepsilon_{\_ori}$	No Contribution Stiffness, strength
b) Unloaded repaired/retrofitted element.	$\varepsilon_{\_ori} = \varepsilon_{\_rep}$	No Contribution Stiffness, strength
	$\varepsilon^{p}_{\_rep} = \varepsilon_{3\_ori}$	Contribution Stiffness, strength
	$\varepsilon_{\_rep} = \varepsilon^{p}_{\_rep}$	
4) Loaded repaired/retrofitted element.	$\varepsilon_{\_ori} = \varepsilon_{\_rep}$	No Contribution Stiffness, strength
	$\varepsilon_{\_rep} = \varepsilon^{p}_{\_rep} + \varepsilon_{4\_rep}$	Contribution Stiffness, strength

3.3.1 Modelling of Original Shear Walls

Modelling of the original shear walls begins with selecting the constitutive models, which are defined for concrete, reinforcement (steel and FRP), and bonding interface. Then, the geometry and the finite element mesh are created to represent the original shear wall including the elements that will be replaced and added during the repair/retrofitting simulation. The model is divided into homogeneous concrete zones according to the internal reinforcement and geometry. In these zones, the model is discretized with rectangle concrete elements with smeared internal reinforcement and aspect ratio no greater than 3:2. Rectangle elements are preferable to triangle elements since they better describe the strain gradient along the elements and are less

susceptible to stress locking; however, triangle elements can be used in zones with geometrical constrains. Internal reinforcement is modelled with discrete truss bar elements where the internal reinforcement is not well distributed or is clearly localized in the structural element.

There are two alternatives to model the externally bonded repair/retrofitting material: the first with superimposed concrete elements with smeared repair/retrofitting material, and the second with truss elements connected to the concrete elements with bond-slip elements. Note that the truss elements representing the externally bonded repair/retrofitting material can also be connected directly to the concrete elements without bond-slip elements when perfect bonding conditions are assumed. The first alternative in which the repair/retrofitting material is smeared into concrete elements inherently results in a very small stiffness, which can lead to numerical instability. In addition, this modelling technique assumes perfect bonding between the repair/retrofitting material and the concrete, which is not always valid and can overestimate the contribution of the externally bonded material. The second alternative is more suitable for modelling externally bonded materials; truss elements with or without bond-slip elements better represent the nonlinear or linear behaviour of the material without including unnecessary concrete properties. The discrete truss elements should represent the continuous bonded material to avoid coarse meshing, which can result in erroneous numerical predictions.

Modelling of the original wall includes the simulation of the repair/retrofitting construction sequence by the engaging/disengaging procedure even though repair/retrofitting is not performed during construction of the original wall. Therefore, the model can be represented by two layers of materials, the first corresponding to the original materials, which are engaged; and the second corresponding to the repair/retrofitting material, which are disengaged as schematized in Fig. 3-21. The two engaged and disengaged elements share the same position in the coordinate system.

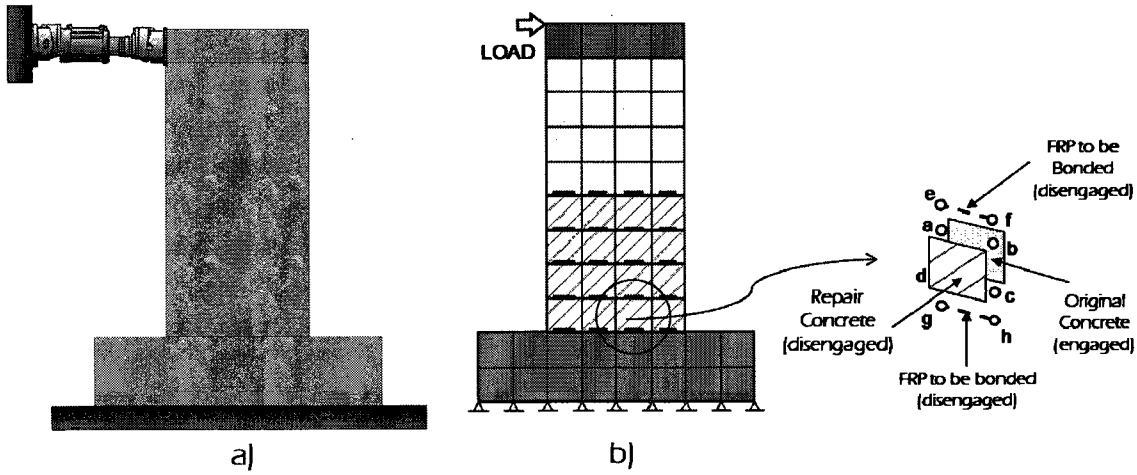

Fig. 3-21 Modelling of Original Shear Wall: a) Specimen; b) FE Model

3.3.2 Analysis of Original Shear Walls

Analysis of a FE model using Program VecTor2 is an iterative process for each load step, in which internal strains and stresses are calculated until convergence, based on secant moduli, reactions, or displacements, is achieved. The analysis is terminated at the onset of failure of the shear wall. During the analysis, the elements representing the original materials are engaged, while the elements representing the repair/retrofitting materials are disengaged as illustrated in Fig. 3-22. As part of the conceptual model, the total strain, ε_i, at any load stage in both the engaged and disengaged elements should be compatible.

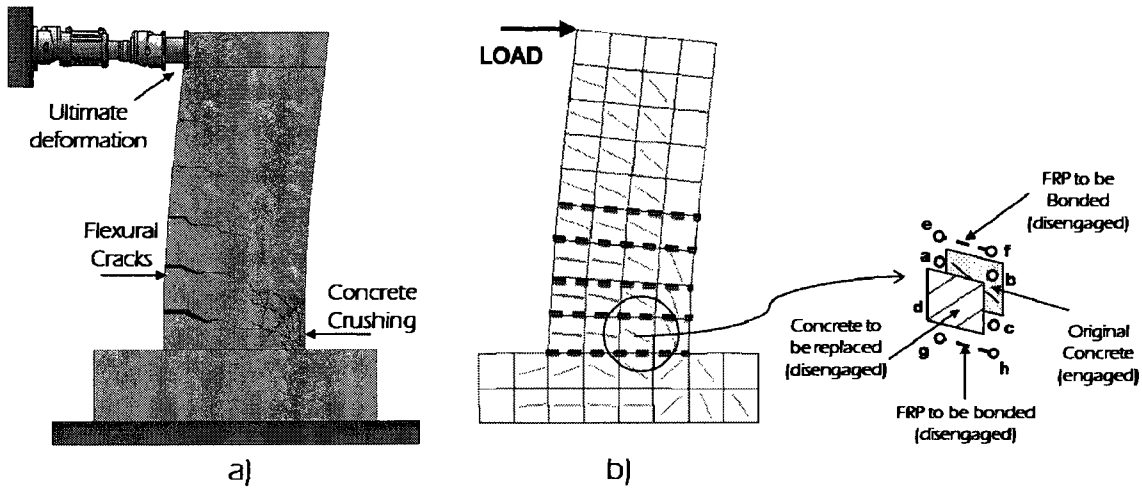

Fig. 3-22 Analysis of Original Shear Wall: a) Testing; b) FE Analysis

3.3.3 Modelling of Repaired and/or Retrofitted Shear Walls

Modelling of repaired and/or retrofitted walls is a process in which distressed elements of the original damaged wall are disengaged and elements representing the new materials are engaged (Fig. 3-23). Engaged elements represent portions of the structure that are active and contribute to the strength and stiffness of the structure. Conversely, disengaged elements represent portions of the structure that are not active and do not contribute to the strength and stiffness of the structure. In cases where regions of a structure will be replaced by repair materials, engaged and disengaged elements occupy the same space in the mesh, resulting in a double meshed region (Vecchio and Bucci, 1999). The total strain of the disengaged element is compatible with the surrounding elements, and the total strain is retained as a plastic offset strain. Once engaged, the element begins to contribute to the strength and stiffness of the structure from a zero elastic strain.

The effectiveness of the repair procedure depends on the load sharing between the original and newly added portions of the structure. In turn, this depends not only on the final configuration of the structure, but also the extent of damage prior to repair

and the strain differentials between the original and repair materials at the time of repair (Wong and Vecchio, 2002).

Similar to the original walls, modelling of the repaired/retrofitted shear wall includes definition of the constitutive models.

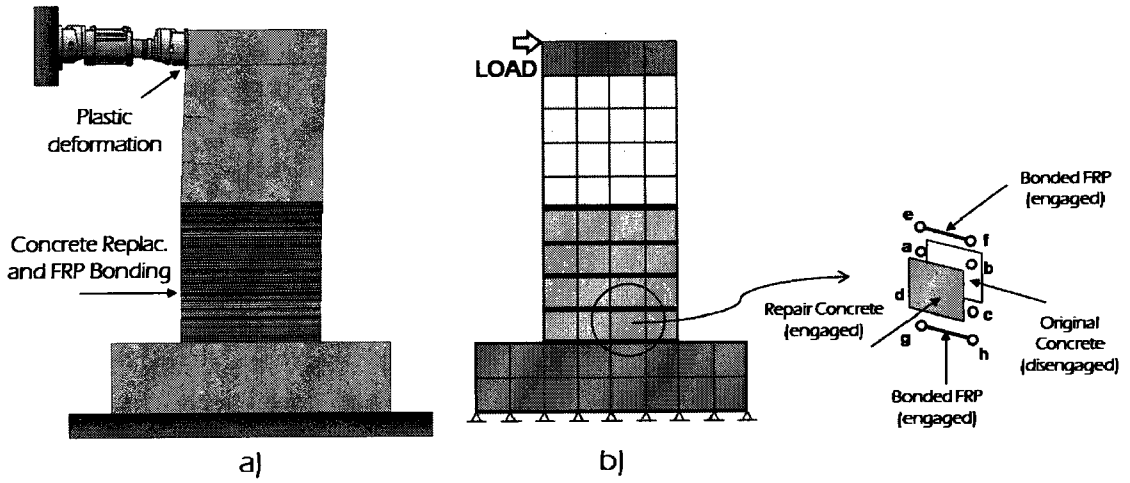

Fig. 3-23 Modelling of Repaired/Retrofitted Shear Wall: a) Specimen; b) FE Model

3.3.4 Analysis of Repaired and/or Retrofitted Shear Walls

The same iterative loading process described for the original walls is used for the analysis of the repaired and/or retrofitted walls. Furthermore, a seed file parameter is included in the analysis of the repaired and/or retrofitted wall. This parameter ensures that the new analysis starts from the previous damage state of the original wall allowing proper simulation of the loading history and repair/retrofitting process. After analysis of the original structure, the total strain, $\varepsilon_{\_ori}$, of the disengaged element is retained as a plastic offset strain, $\varepsilon^{p}_{\_rep}$, which is carried forward in the analysis of the repaired and/or retrofitted structure. The net strain, however, of the newly engaged element, representing the repair/retrofitting material is zero, reflecting the actual repair/retrofitting condition of placing a new material with no stress. Subsequently, in the analysis of the repaired/retrofitted structural model, the newly

engaged elements contribute to the strength and stiffness, whereas the disengaged elements do not. Figure 3-24 illustrates the analysis of a repaired/retrofitted shear wall in which engaged repair/retrofitting elements are stressed and cracked.

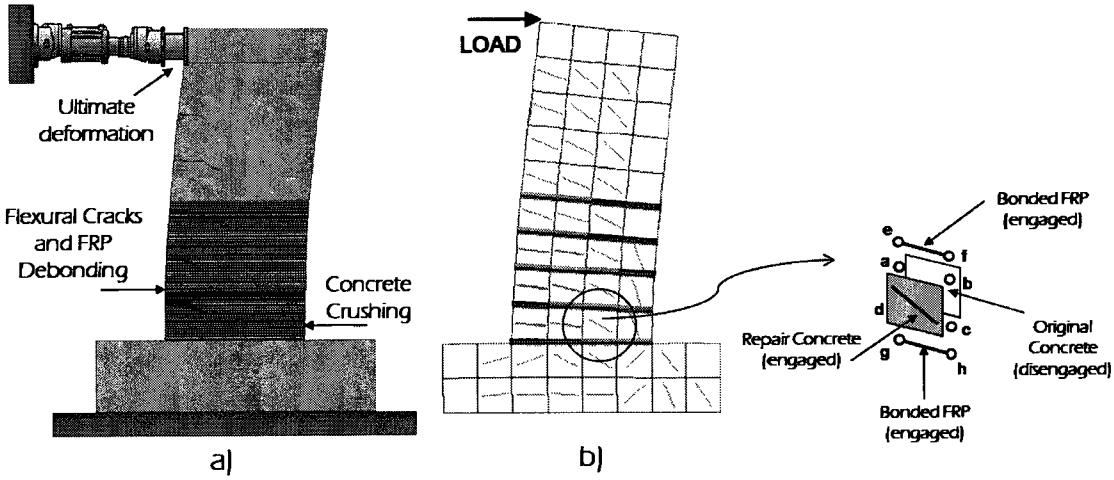

Fig. 3-24 Analysis of Repaired/Retrofitted Shear Wall: a) Testing; b) FE Analysis

3.3.5 Post-Processing

During the post-processing stage, nodal displacements and element stresses are evaluated and further analyses are performed. Salient features of seismic behaviour such as strength, ductility (displacement), energy dissipation, hysteretic behaviour, and failure modes are assessed.

Chapter 4

4 Parametric Study

4.1 Introduction

The parametric study presented herein aims to assess the constitutive models for reinforced concrete, which are implemented in the finite element (FE) program VecTor2. The main objective is to select the models that best describe the behaviour of shear walls. Furthermore, the study aims to corroborate FE techniques presented elsewhere (Palermo and Vecchio, 2007) for the modelling of shear walls subjected to reverse cyclic loading.

The parametric study is divided in two parts: part 1, which is an assessment of the models for the compression pre-peak and post-peak response of plain concrete; and part 2, which assesses the models for slip distortion and the hysteretic response of reinforced concrete. Part 2 depends on part 1, and requires definition of the most appropriate compression response for plain concrete. These models were judged to have significant influence on behaviour. The study does not include models for secondary effects of reinforced concrete, such as tension stiffening and confinement, or models for reinforcement. The default constitutive models in VecTor2 were selected for

all other models not considered in the parametric study. Subsections 4.3 and 4.4 provide details of part 1 and part 2 of the parametric study, including the selected constitutive models.

The benchmarks for the parametric study included six slender shear walls, PCA Walls (Fiorato et al., 1983; Oesterle et al., 1976), and two squat shear walls, DP Walls (Palermo and Vecchio, 2002). Each shear wall is modelled according to its geometry and reinforcement layout. Thereafter, each wall is analyzed following the same loading pattern used during testing, and the results are compared with the experimental results. Failure of PCA Walls was governed by ductile flexural-related mechanisms, while failure of DP Walls was governed by brittle shear-related mechanisms. Therefore, the PCA and DP series of walls provide different challenges to the finite element method (FEM) in predicting the response of reinforced concrete shear walls. This, in turn, provides confidence in the assessment of the constitutive models.

4.2 Shear Walls

4.2.1 PCA Walls

PCA Walls (B1, B2, B3, B5, B9, and B11) were tested by Fiorato et al., (1983) and Oesterle et al. (1976, 1979) in the Portland Cement Association (PCA) laboratories. The walls were approximately 1/3-scale models of full-size walls with height-to-length ratio of approximately 2.4. The web portion of the walls was 4570 mm high, 1910 mm long, and 102 mm thick; the boundary column cross section was 305 mm x 305 mm. Furthermore, the walls were provided with stiff foundation and top slabs for anchoring and loading of the wall, respectively. Fig. 4-1 illustrates the geometry of the walls as well as the reinforcement layout. Table 4-1 lists the material properties of the test specimens, including the reinforcement ratios.

Parametric Study

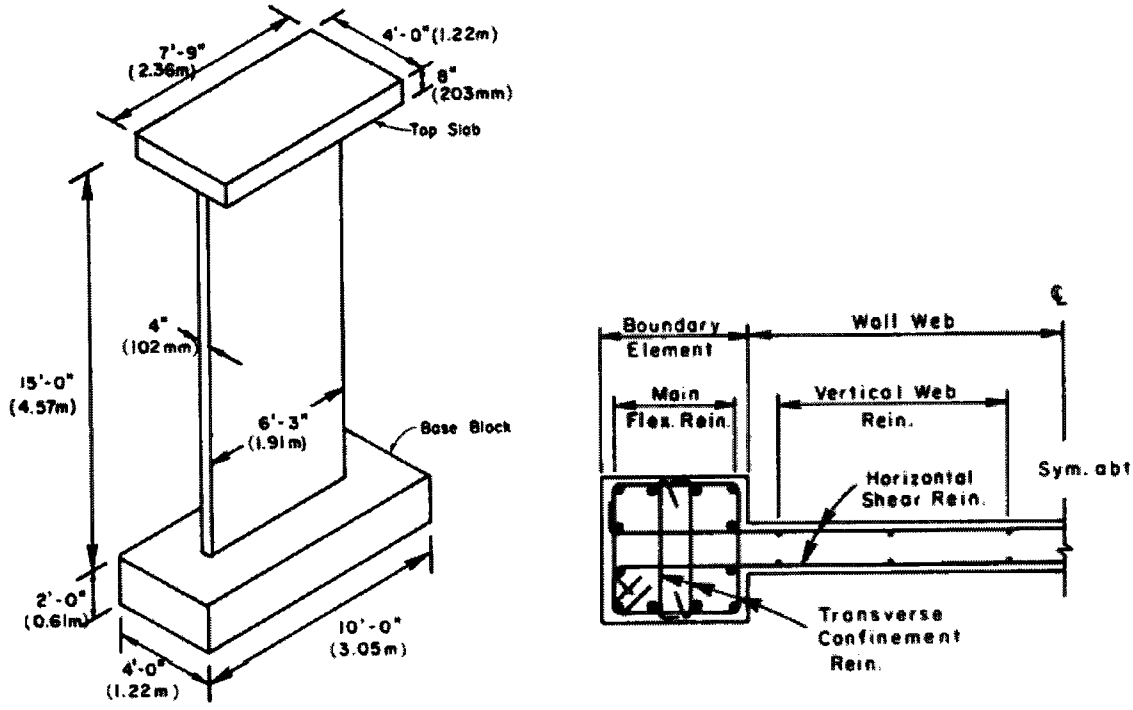

Fig. 4-1 Nominal Test Specimens; PCA Walls (Fiorato et al., 1983)

Table 4-1 Material Properties of PCA Walls

Wall	Zone	Concrete	Reinforcement					
			Horizontal		Vertical		Confinement	
		$f'c$ [MPa]	ρ_h [%]	fy [MPa]	ρ_v [%]	fy [MPa]	ρ_{cf} [%]	fy [MPa]
B1	Web	53.6	0.31	521	0.29	521	—	—
	Boundary	53.6	0.31	521	1.11	405	0.09	474
B2	Web	53.6	0.63	532	0.29	532	—	—
	Boundary	53.6	0.63	532	3.67	410	0.12	474
B3	Web	47.3	0.31	479	0.29	479	—	—
	Boundary	47.3	0.31/1.00	479	1.11	438	0.13/1.00	479
B5	Web	45.3	0.63	502	0.29	502	—	—
	Boundary	45.3	1.35/0.33	502	3.67	444	1.35/0.13	502
B9	Web	44.0	0.63	460	0.29	460	—	—
	Boundary	44.0	1.35/0.33	460	3.67	429	1.35/0.13	460
B11	Web	53.8	0.63	501	0.29	501	—	—
	Boundary	53.8	1.35/0.33	501	3.67	429	1.35/0.13	501

Parametric Study

Walls B1, B2, B3 and B5 were loaded with three repetitions of incremental reverse cyclic lateral displacement of 25 mm to failure. Wall B9 was cycled with single (one repetition) lateral displacements to 13 mm, 133 mm, 38 mm, 121 mm and 108 mm. Loading of Wall B9 included an axial load of 3.76 MPa, applied over the top slab. Wall B11 was loaded with initial small amplitude cycles followed by loading up to 102 mm of lateral displacement. Thereafter, three repetitions of loading were imposed from 51 mm of lateral displacement to failure, which corresponded to 152 mm of lateral displacement.

In general, PCA Walls behaved in a ductile manner, governed by yielding of vertical reinforcement and followed by crushing of the concrete, as evident from Fig. 4-2 to Fig. 4-7. The reported lateral strength capacity of the walls ranged from 271 kN in Wall B1 to 977 kN in Wall B9, while the reported maximum lateral displacement ranged from 102 mm in Walls B1 and B2 to 178 mm in Wall B3. Differences in the strength and lateral displacement capacities were associated with the variation of the reinforcement layout and the loading regime. Failure of Walls B1 and B3 was reported as crushing of concrete in the boundary elements preceded by buckling of the vertical concentrated reinforcing steel. The walls also experienced crushing and shear distortion in the web portion. The observed failure of Wall B2 was characterized by concrete deterioration of the boundary elements, which led to buckling of the vertical reinforcing bars. Subsequently, the concrete in the web portion of the wall crushed and triggered shear sliding along the boundary elements. The reported failure of Walls B5, B9, and B11 consisted of concrete crushing of the lower portion of the web, specifically in the vicinity with the boundary elements. The boundary elements were in good condition and did not experience any fractured or buckled vertical reinforcement. Table 4-2 summarizes the observed strength, maximum displacement and failure of PCA Walls.

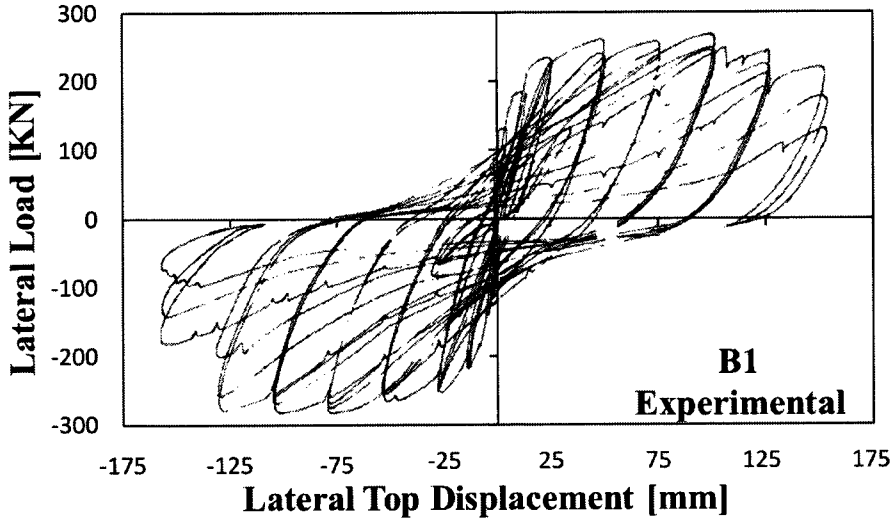

Fig. 4-2 Experimental Response for Wall B1 (Modified from Oesterle et al., 1976)

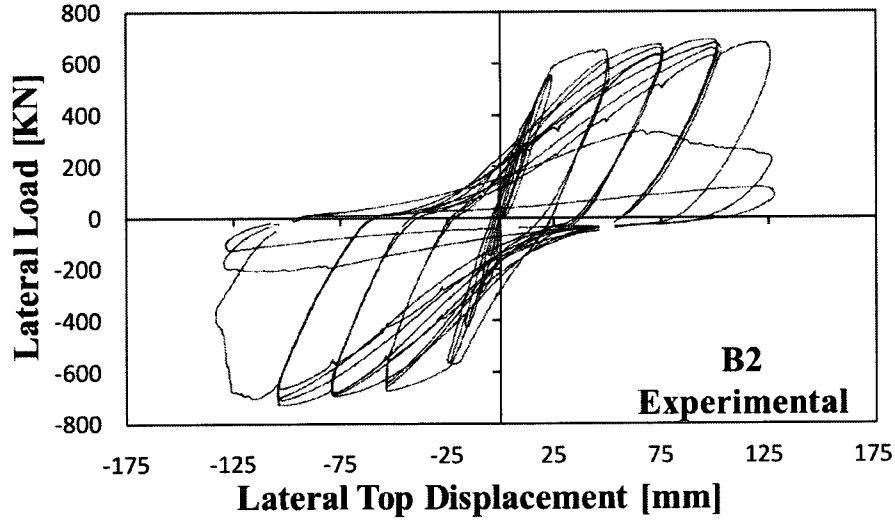

Fig. 4-3 Experimental Response for Wall B2 (Modified from Oesterle et al., 1976)

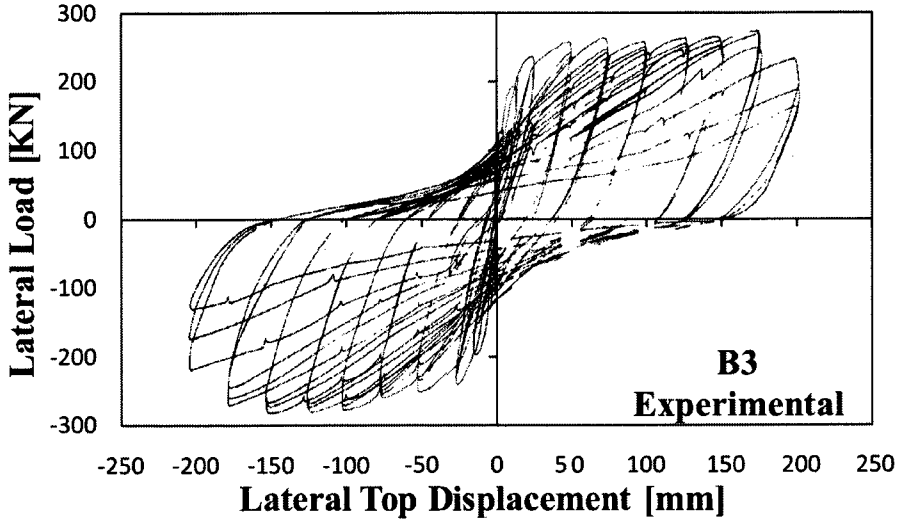

Fig. 4-4 Experimental Response for Wall B3 (Modified from Oesterle et al., 1976)

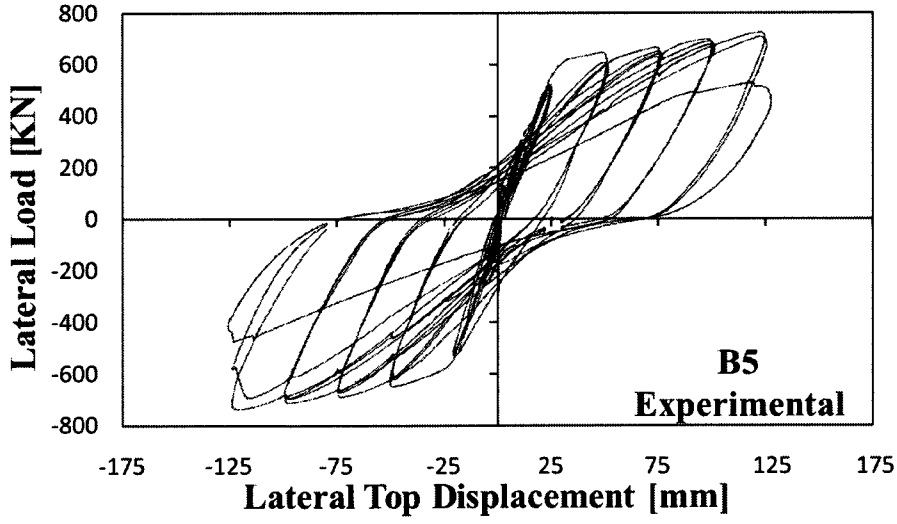

Fig. 4-5 Experimental Response for Wall B5 (Modified from Oesterle et al., 1979)

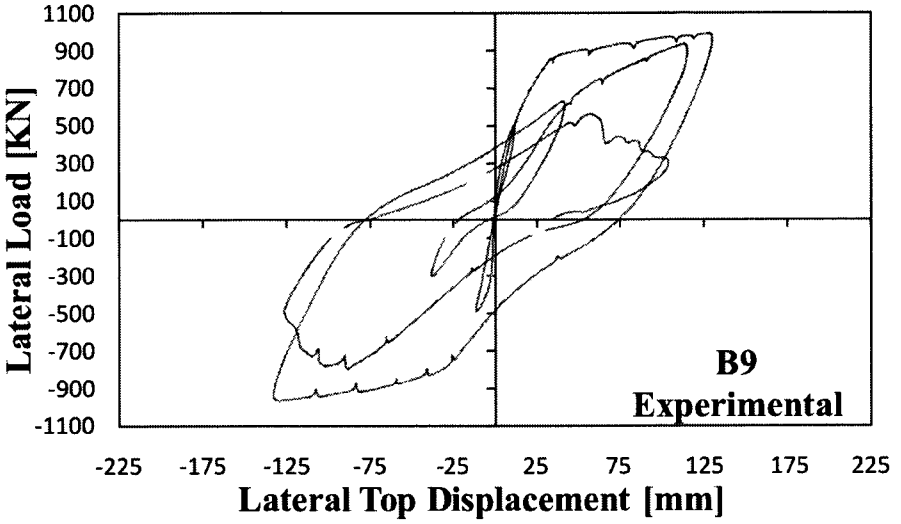

Fig. 4-6 Experimental Response for Wall B9 (Modified from Oesterle et al., 1979)

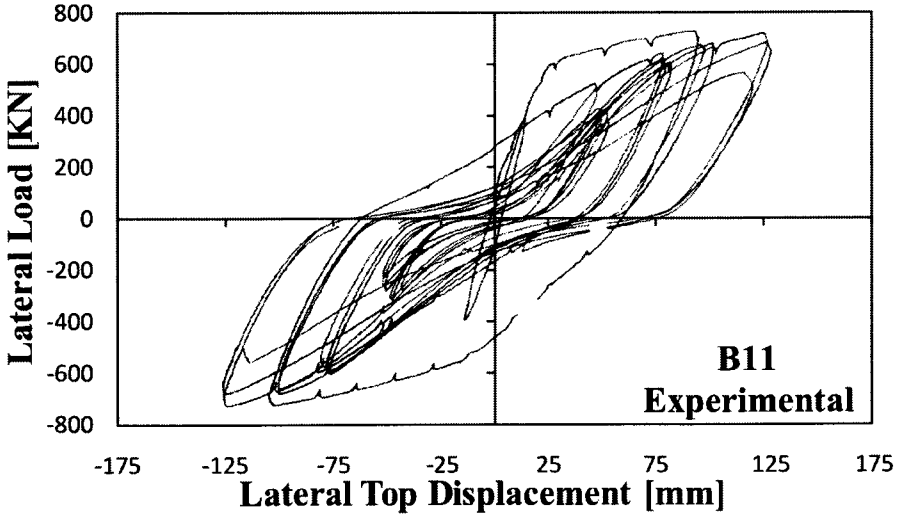

Fig. 4-7 Experimental Response for Wall B11 (Modified from Fiorato et al., 1983)

Parametric Study

Table 4-2 PCA Walls: Experimental Observations

Shear Wall	Strength [kN]	Max. Disp. [mm]	Failure Mode
B1	271	127	Crushing of concrete in the boundary elements preceded by buckling of the vertical reinforcing steel.
B2	704	102	Crushing of concrete in the boundary elements and web, followed by shear sliding along the boundary elements.
B3	276	178	Buckling and rupture of the vertical reinforcing steel.
B5	762	127	Crushing of concrete in the web, specifically in the vicinity with the boundary elements.
B9	977	136	Crushing of concrete in the web, specifically in the vicinity with the boundary elements.
B11	726	127	Crushing of concrete in the web, specifically in the vicinity with the boundary elements.

Walls B1 and B2 were modelled with three homogeneous concrete zones with smeared reinforcement, according to the geometry and material properties of the specimen: the first corresponding to the web; the second corresponding to the boundary elements; and the third corresponding to the foundation (fully restrained horizontally and vertically at the base) and top beams (Fig. 4-8). The mesh, excluding the foundation and top beams, consisted of 14 rectangular elements horizontally and 24 rectangular elements vertically.

Likewise, Walls B3, B5, B9 and B11 were modelled with four homogeneous concrete zones with smeared reinforcement: the first corresponding to the web; the second and third corresponding to the upper and lower portion of the boundary columns (the latter with more transverse and confinement reinforcement); and the fourth corresponding to the foundation (fully restrained horizontally and vertically at the base) and top beams (Fig. 4-9). The mesh, excluding the foundation and top beams, consisted of 14 rectangular elements horizontally and 30 rectangular elements vertically.

Parametric Study

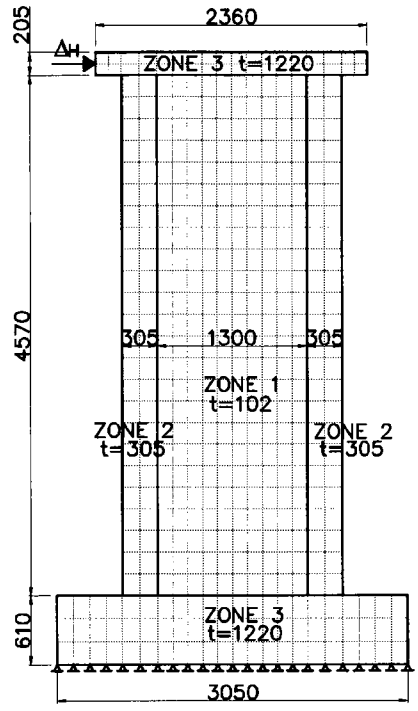

Fig. 4-8 Finite Element Mesh of Walls B1 and B2. All Dimensions in mm

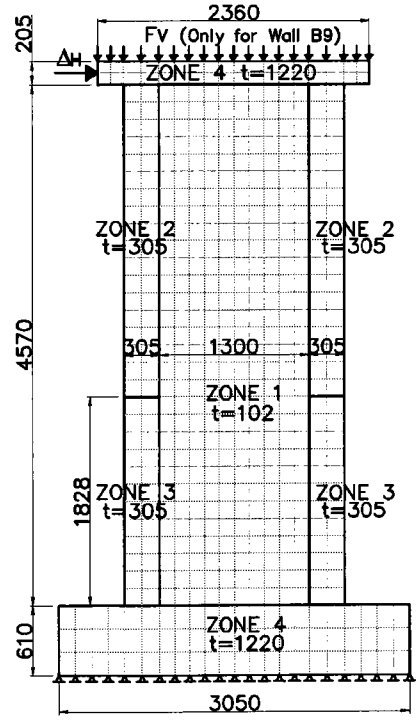

Fig. 4-9 Finite Element Mesh of Walls B3, B5, B9 and B11. All Dimensions in mm

4.2.2 DP Walls

Walls DP1 and DP2 were tested by Palermo and Vecchio (2002) as part of an experimental investigation of flanged concrete shear walls subjected to reversing cyclic loads. The web portion of Walls DP1 and DP2 was 2020 mm high, 2885 mm long and 75 mm thick. The flanges of Wall DP1 were 3045 mm wide and 95 mm thick, while the flanges of Wall DP2 were 3045 mm wide and 100 mm thick. In addition, the walls were built with a stiff foundation and top slab. Details of the geometry are given in Fig. 4-10. Table 4-3 lists the material properties of the walls, including the reinforcement ratios.

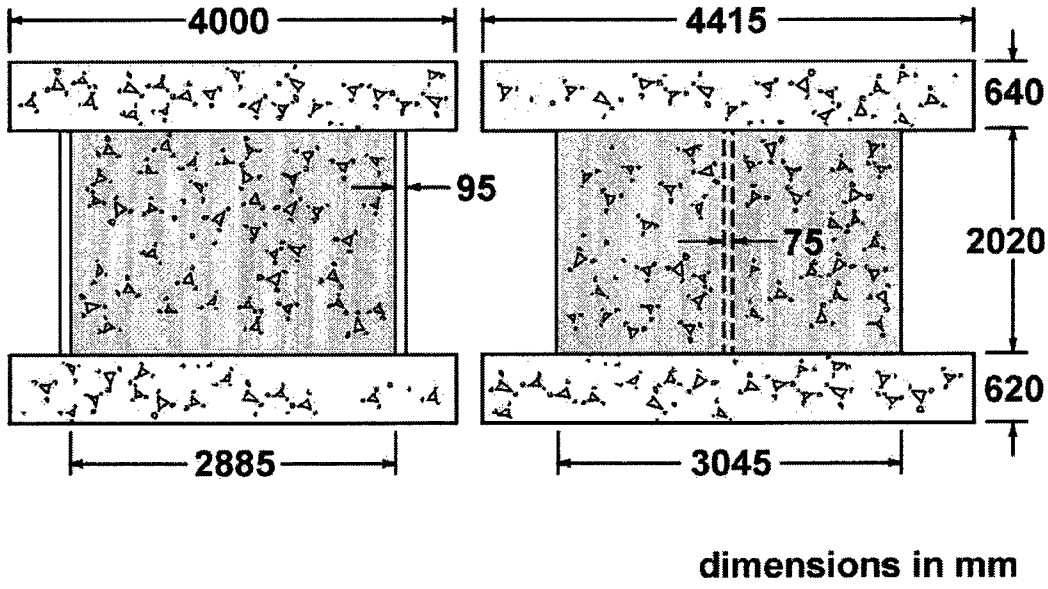

Fig. 4-10 DP Walls (Palermo and Vecchio, 2002)

Table 4-3 Material Properties of DP Walls

Wall	Zone	Concrete	Reinforcement			
			Horizontal		Vertical	
		$f'c$ [MPa]	ρ_h [%]	fy [MPa]	ρ_v [%]	fy [MPa]
DP1	Web	21.7	0.74	605	0.79	605
	Flanges	21.7	0.58	605	0.38	605
DP2	Web	18.8	0.74	605	0.79	605
	Flanges	18.8	0.58	605	0.38	605

Cyclic displacements in increments of 1 mm, repeated two times at each displacement, and a total axial load of 1200 kN and 260 kN for DP1 and DP2, respectively, were applied to the specimens along the top slab.

The pinched responses of Walls DP1 and DP2, observed in Fig. 4-11 and Fig. 4-12, indicate behaviour of the walls governed by concrete shear-related mechanisms with low energy dissipation capacity. Wall DP1 sustained a lateral strength of 1298 kN at approximately 11 mm of displacement. Beyond 11 mm of displacement, the strength of Wall DP1 degraded until failure due to crushing of concrete along six vertical planes in the web wall, which was first observed at 11 mm of displacement. Wall DP2 sustained a lateral strength of 904 kN corresponding to a lateral displacement of 9 mm. Failure of Wall DP2 occurred in the second excursion to 9 mm displacement in the form of shear sliding along the web wall near the top slab.

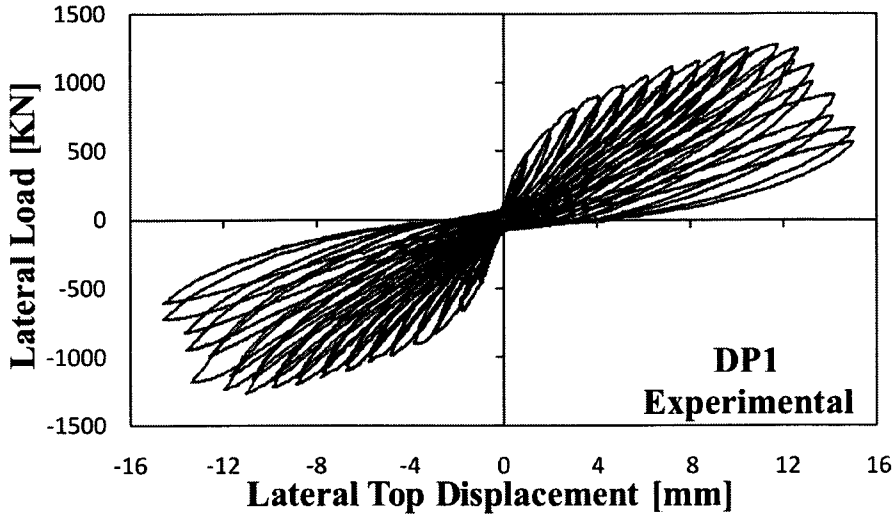

Fig. 4-11 Experimental Response for Wall DP1 (Modified from Palermo and Vecchio, 2002)

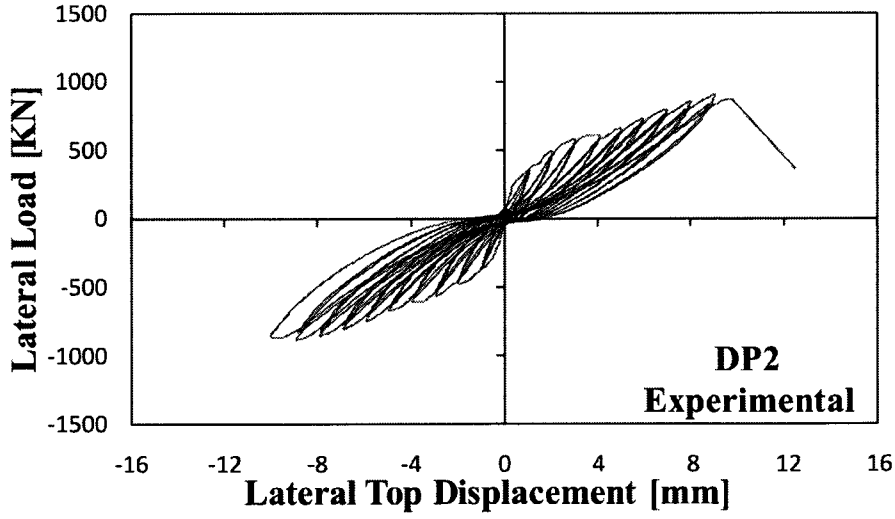

Fig. 4-12 Experimental Response for Wall DP2 (Modified from Palermo and Vecchio, 2002)

Four concrete zones with smeared reinforcement were defined in the model of Walls DP1 and DP2: web portion of the wall, flanges, foundation slab (fully restrained horizontally and vertically at the base), and top slab (Fig. 4-13). The FE mesh consisted of 20 elements horizontally and 16 elements vertically for the web portion of the wall, and 2 elements horizontally and 16 elements vertically for the flanges.

Parametric Study

Meshing of the foundation and top slabs was controlled by the mesh of the web and flanges of the walls.

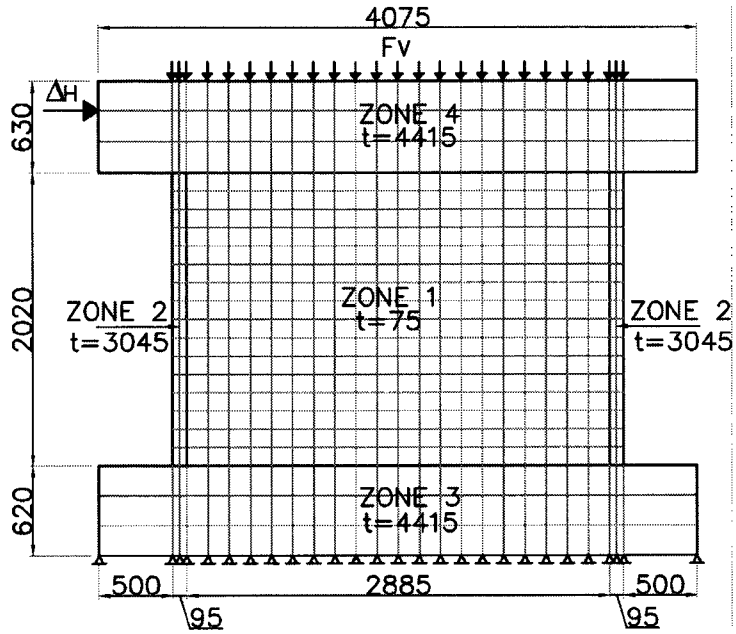

Fig. 4-13 Finite Element Mesh of Walls DP1 and DP2. All Dimensions in mm

4.3 Part 1: Concrete Models

4.3.1 Models

Three compression pre-peak models: Smith-Young, Popovics normal strength concrete (Popovics NSC), and Popovics high strength concrete (Popovics HSC); and two compression post-peak models: base curve, and modified Park-Kent were included in the parametric study of concrete models.

The Smith-Young, Popovics NSC, and Popovics HSC compression pre-peak models compute the principal compressive stress, f_{ci}, when the compressive principal strain, ε_{ci}, is smaller than the peak strain, ε_p, corresponding to the peak compressive stress, f_p. The models include a descending post-peak branch.

Parametric Study

The Smith-Young compression pre-peak model, shown in Fig. 4-14, is expressed by the following exponential function (Smith and Young, 1955).

$$f_{ci} = K\varepsilon_{ci}^{\ m} \qquad K = E_c \tag{4-1}$$

Where f_{ci} is the stress in the concrete; K is a constant taken as the initial tangent stiffness of concrete, E_c; ε_{ci} is the compressive strain corresponding to f_{ci}; and m is an exponent, which defines the shape of the stress-strain curve. The value of m is obtained according to the concrete cylinder compressive stress, f'_c.

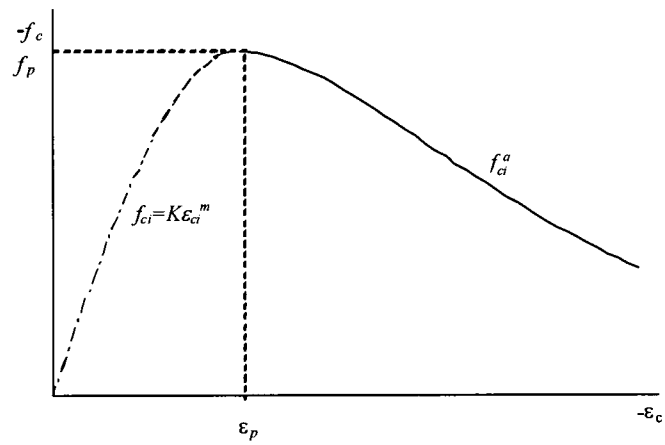

Fig. 4-14 Smith-Young Pre- and Post-Peak Concrete Compression Response (Modified from Wong and Vecchio, 2002)

The compression post-peak stress, f_{ci}^a, is computed as follows (Wong and Vecchio, 2002):

$$f_{ci}^a = -f_p\left(\frac{\varepsilon_{ci}}{\varepsilon_p}\right)\cdot exp\left\{1-\left(\frac{\varepsilon_{ci}}{\varepsilon_p}\right)\right\} \tag{4-2}$$

The Popovics NSC stress-strain curve (Wong and Vecchio, 2002), shown in Fig. 4-15, is given by the following equation:

$$f_{ci} = -\left(\frac{\varepsilon_{ci}}{\varepsilon_p}\right)f_p\frac{n}{n-1+\left(\varepsilon_{ci}/\varepsilon_p\right)^n} \qquad for\ \varepsilon_{ci} < 0 \tag{4-3}$$

Parametric Study

Where f_{ci} is the concrete compressive stress, ε_{ci} is the compressive strain corresponding to f_{ci}, and ε_p is the concrete compressive strain corresponding to the peak concrete compressive stress f_p. Furthermore, n is the curve fitting parameter to capture the greater linearity of higher strength concrete by considering the difference between the initial tangent stiffness of concrete, E_c, and the secant stiffness of concrete, E_{sec}, The fitting parameter, and the secant stiffness of concrete are computed as follows:

$$n = \frac{E_c}{E_c - E_{sec}} \tag{4-4}$$

$$E_{sec} = \frac{f_p}{|\varepsilon_p|} \tag{4-5}$$

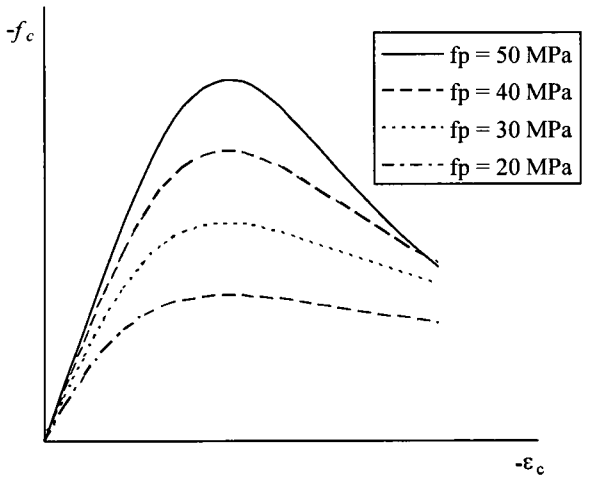

Fig. 4-15 Popovics NSC Pre- and Post-Peak Concrete Compression Response (Wong and Vecchio, 2002)

The Popovics HSC model (Wong and Vecchio, 2002), shown in Fig. 4-16, provides more rapid post-peak stress decay for higher strength concretes, and is defined by the following equation.

$$f_{ci} = -\left(\frac{\varepsilon_{ci}}{\varepsilon_p}\right) f_p \frac{n}{n - 1 + \left(\varepsilon_{ci}/\varepsilon_p\right)^{nk}} \quad for\ \varepsilon_{ci} < 0 \tag{4-6}$$

Parametric Study

The curve fitting parameter, n, which captures the greater linearity of higher strength concrete, is computed by the following equation:

$$n = 0.80 + \frac{f_p}{17} \quad (f_p \text{ in MPa}) \tag{4-7}$$

The parameter k increases the post-peak decay in stress and is calculated as follows:

$$k = \begin{cases} 1.0 & \text{for } \varepsilon_p < \varepsilon_{ci} < 0 \\ 0.67 + \frac{f_p}{62} \geq 1.0 & \text{for } \varepsilon_{ci} < \varepsilon_p < 0 \ (f_p \text{ in MPa}) \end{cases} \tag{4-8}$$

Popovics HSC model predefines the initial tangent stiffness, Ec, as follows:

$$E_c = \frac{f_p}{|\varepsilon_p|} \cdot \frac{n}{n-1} \tag{4-9}$$

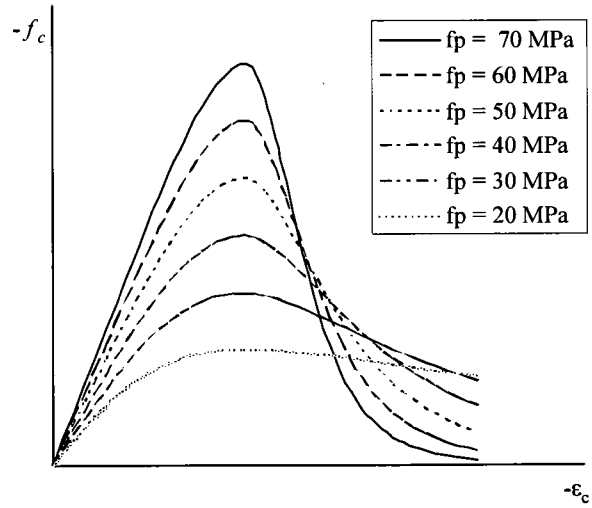

Fig. 4-16 Popovics HSC Pre- and Post-Peak Concrete Compression Response (Wong and Vecchio, 2002)

The base curve and modified Park-Kent compression post-peak models compute the principal compressive stress, f_{ci}, beyond the peak strain, ε_p. The base curve compression post-peak model is defined by the equations of the descending post-peak branch of the selected compression pre-peak model. The modified Park-Kent model is

formulated specifically to account for confined concrete. If the model is selected and the concrete is not significantly confined, an alternative formulation is used to compute the post-peak response based on a combination of the modified Park-Kent model and the post-peak branch of the Smith-Young model for unconfined concrete. In addition, the post-peak response (Fig. 4-17) is assumed to have a sustaining branch equal to 20% of the concrete compressive peak strength, f_p.

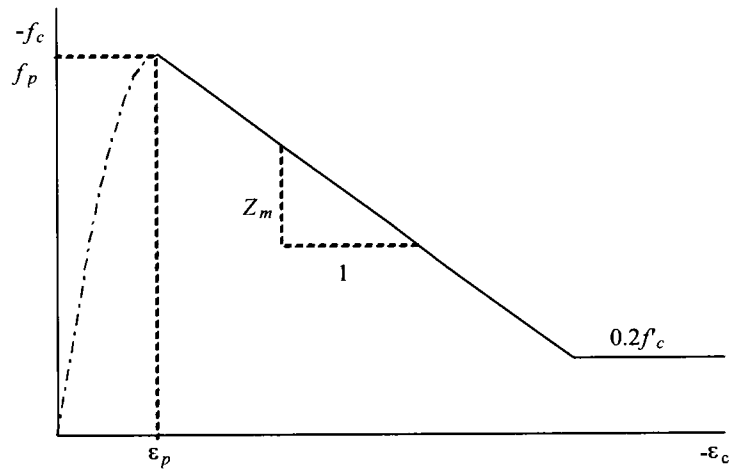

Fig. 4-17 Modified Park-Kent Post-Peak Concrete Compression Response (Wong and Vecchio, 2002)

The linearly descending branch of the modified Park-Kent stress-strain curve is adapted for VecTor2 as follows (Wong and Vecchio, 2002):

$$f_{ci}^{b} = -\left[f_p + Z_m f_p(\varepsilon_{ci} - \varepsilon_p)\right] < 0 \text{ or } -0.2f_p \quad \text{for } \varepsilon_{ci} < \varepsilon_p < 0 \tag{4-10}$$

Where:

$$Z_m = \frac{0.5}{\frac{3 + 0.29|f'_c|}{145|f'_c| - 1000} \cdot \left(\frac{\varepsilon_o}{-0.002}\right) + \left(\frac{|f_{lat}|}{170}\right)^{0.9} + \varepsilon_p} \quad (f'_c \text{ and } f_{lat} \text{ in MPa}) \tag{4-11}$$

ε_o is the concrete compressive strain corresponding to f_c, and f_{lat}, is the summation of principal stresses, acting transversely to the direction under consideration:

Parametric Study

$$f_{lat} = f_{c1} + f_{c2} + f_{c3} - f_{ci} \leq 0 \quad i = 1 \text{ or } 2 \tag{4-12}$$

The parametric study included a combination of two of the three compression pre-peak models and both compression post-peak models, resulting in four FE models for each wall. The first compression pre-peak model is selected according to recommendations by Palermo and Vecchio (2007) based on the cylinder compressive strength, f'_c, of the shear walls. Thus, the Smith-Young model is used for shear walls with f'_c less than 22 MPa; the Popovics NSC model is used for shear walls with f'_c between 22 MPa and 45 MPa; and the Popovics HSC is used for shear walls with f'_c greater than 45 MPa. The second compression pre-peak model is selected arbitrarily depending on the proximity of f'_c of the shear wall to the limits of the aforementioned criterion. For example, the first and second pre-peak models for a wall with f'_c= 44 MPa are the Popovics NSC and the Popovics HSC, respectively. The name of each FE model follows the codification provided in Fig. 4-18.

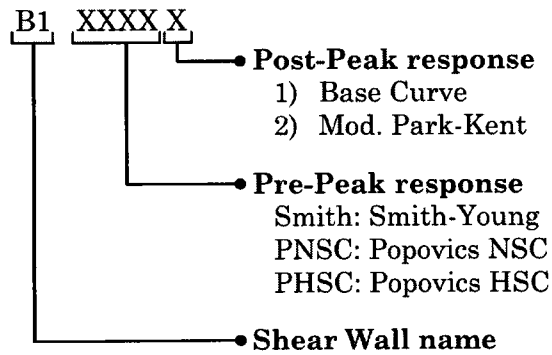

Fig. 4-18 FE Model Codification for Concrete Compression Models

Table 4-4 lists the concrete compression models used in the modelling of the shear walls in the parametric study.

Parametric Study

Table 4-4 Concrete Compression Models

Shear Wall	Compression Pre-Peak	Compression Post-Peak	FE Model
B1	Popovics HSC	Base Curve	PHSC1
	Popovics HSC	Modified Park-Kent	PHSC2
	Popovics NSC	Base Curve	PNSC1
	Popovics NSC	Modified Park-Kent	PNSC2
B2	Popovics HSC	Base Curve	PHSC1
	Popovics HSC	Modified Park-Kent	PHSC2
	Popovics NSC	Base Curve	PNSC1
	Popovics NSC	Modified Park-Kent	PNSC2
B3	Popovics HSC	Base Curve	PHSC1
	Popovics HSC	Modified Park-Kent	PHSC2
	Popovics NSC	Base Curve	PNSC1
	Popovics NSC	Modified Park-Kent	PNSC2
B5	Popovics HSC	Base Curve	PHSC1
	Popovics HSC	Modified Park-Kent	PHSC2
	Popovics NSC	Base Curve	PNSC1
	Popovics NSC	Modified Park-Kent	PNSC2
B9	Popovics NSC	Base Curve	PNSC1
	Popovics NSC	Modified Park-Kent	PNSC2
	Popovics HSC	Base Curve	PHSC1
	Popovics HSC	Modified Park-Kent	PHSC2
B11	Popovics HSC	Base Curve	PHSC1
	Popovics HSC	Modified Park-Kent	PHSC2
	Popovics NSC	Base Curve	PNSC1
	Popovics NSC	Modified Park-Kent	PNSC2
DP1	Smith-Young	Base Curve	Smith1
	Smith-Young	Modified Park-Kent	Smith2
	Popovics NSC	Base Curve	PNSC1
	Popovics NSC	Modified Park-Kent	PNSC2
DP2	Smith-Young	Base Curve	Smith1
	Smith-Young	Modified Park-Kent	Smith2
	Popovics NSC	Base Curve	PNSC1
	Popovics NSC	Modified Park-Kent	PNSC2

Other relevant concrete behavioural models were selected as default: Vecchio's 1992-A model for compression softening, modified Bentz tension stiffening model for tension stiffening effects, linear model for tension softening, Kupfer/Richard model for

confinement of concrete, modified Kupfer for the lateral expansion or dilatation of concrete, Mohr-Coulomb stress model for cracking criterion, Vecchio-Collins 1986 model for crack slip check, 20% aggregate size limit for crack width check, Vecchio-Lai model for slip distortion, and nonlinear with plastic offset model for concrete hysteretic response. Additional details of the models can be found elsewhere (Wong and Vecchio, 2002).

4.3.2 Results

4.3.2.1 PCA Walls

The analyses provided satisfactory responses for the PCA Walls. For all the concrete compression models, the analysis predicted similar behavioural response. However, some models were more accurate, specifically in terms of lateral strength and displacement. Results of part 1 of the parametric study for the PCA Walls are summarized in Table 4-5 and Table 4-6.

Table 4-5 Concrete Models: Observed and Calculated Maximum Lateral Strength for PCA Walls

Max. Lateral Strength [kN]									
Wall	**Analytical**				**Exp.**	**Comparison (Ana./Exp.)**			
	PNSC1	**PNSC2**	**PHSC1**	**PHSC2**		**PNSC1**	**PNSC2**	**PHSC1**	**PHSC2**
B1	257	254	243	242	271	0.948	0.937	0.897	0.893
B2	656	658	630	620	704	0.932	0.935	0.895	0.881
B3	257	268	262	257	276	0.931	0.971	0.949	0.931
B5	680	687	660	659	762	0.892	0.902	0.866	0.865
B9	979	979	959	962	977	1.002	1.002	0.982	0.985
B11	735	735	721	720	726	1.012	1.012	0.993	0.992

Table 4-6 Concrete Models: Observed and Calculated Maximum Lateral Displacement for PCA Walls

Max. Lateral Disp. [mm]									
Wall	**Analytical**				**Exp.**	**Comparison (Ana./Exp.)**			
	PNSC1	**PNSC2**	**PHSC1**	**PHSC2**		**PNSC1**	**PNSC2**	**PHSC1**	**PHSC2**
B1	152	152	127	127	127	1.197	1.197	1.000	1.000
B2	127	127	102	102	127	1.000	1.000	0.803	0.803
B3	228	228	152	228	178	1.281	1.281	0.854	1.281
B5	127	127	76	76	127	1.000	1.000	0.598	0.598
B9	182	182	133	133	133	1.368	1.368	1.000	1.000
B11	127	151	102	102	127	1.000	1.189	0.803	0.803

The PCA walls, except Wall B9, were better simulated in terms of strength and ductility with the Popovics normal strength compression pre-peak model (PNSC), although the cylinder compressive strength, f'c, was greater than 45 MPa. This trend does not comply with the recommendations of Palermo and Vecchio (2007) mainly due to the compression softening of the concrete, which lowered the peak strength and reduced the rapid post-peak stress decay of the concrete. Wall B9 was better predicted with Popovics high strength compression pre-peak model (PHSC), although the concrete strength of Wall B9 (44 MPa) was considered as normal strength concrete. The axial load and the confining reinforcement present in Wall B9 increased the compressive strength of the concrete, resulting in a more brittle post-peak response.

In Walls B1 and B2, the normal strength concrete models in combination with the base curve compression post-peak model, PNSC1, provided accurate predictions of the maximum top displacement, and an underestimation of the lateral load capacity between 5% and 7%. The post-peak response of Walls B1 and B2 (no confinement reinforcement) was similarly captured with the base curve and the modified Park-Kent compression post-peak model. Therefore, the base curve post-peak model is sufficient for the analysis of walls without confinement detailing. The analyses of Walls B1 and B2 predicted concrete degradation of the boundary elements as observed during testing; however, this prediction was preceded by crushing of the web wall. The

actual failure of Wall B1 was reported as crushing of concrete in the boundary elements preceded by buckling of the vertical reinforcing steel, while failure of Wall B2 was reported as crushing of concrete in the boundary elements followed by shear sliding. Predicted responses of Walls B1 and B2 are given in Fig. 4-19 and Fig. 4-20.

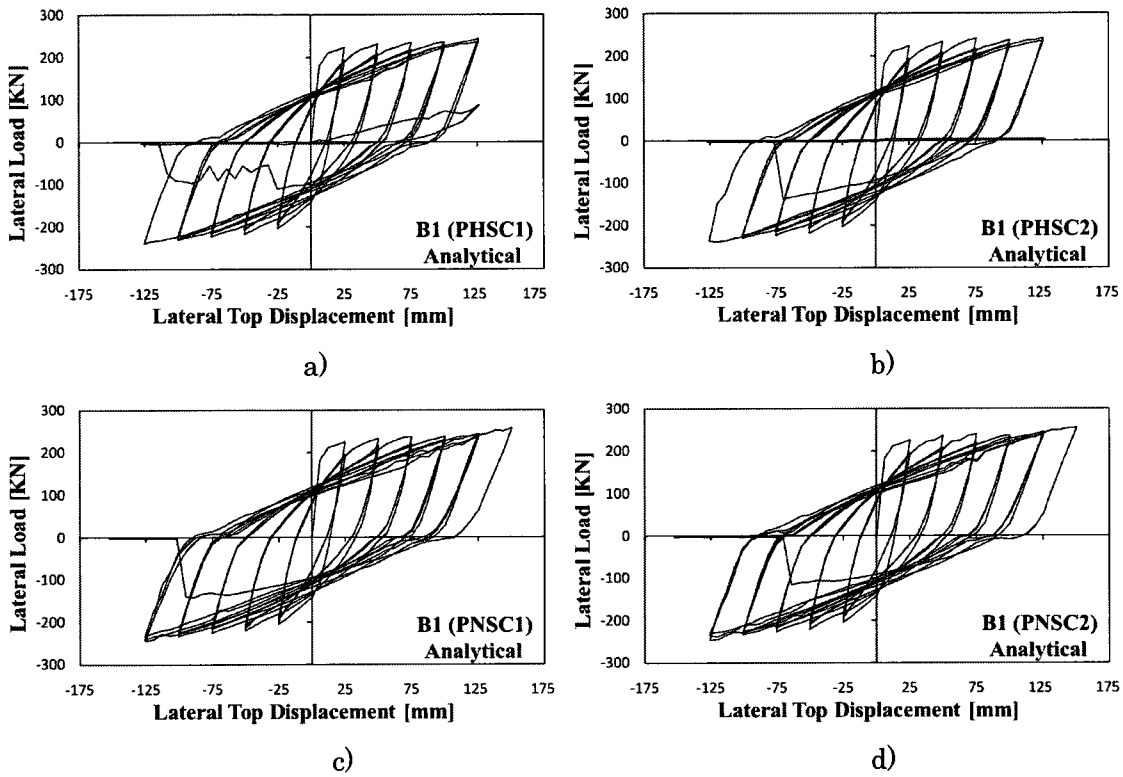

Fig. 4-19 Predicted Response for Wall B1: a) B1 (PHSC1); b) B1 (PHSC2); c) B1 (PNSC1); and d) B1 (PNSC2)

Parametric Study

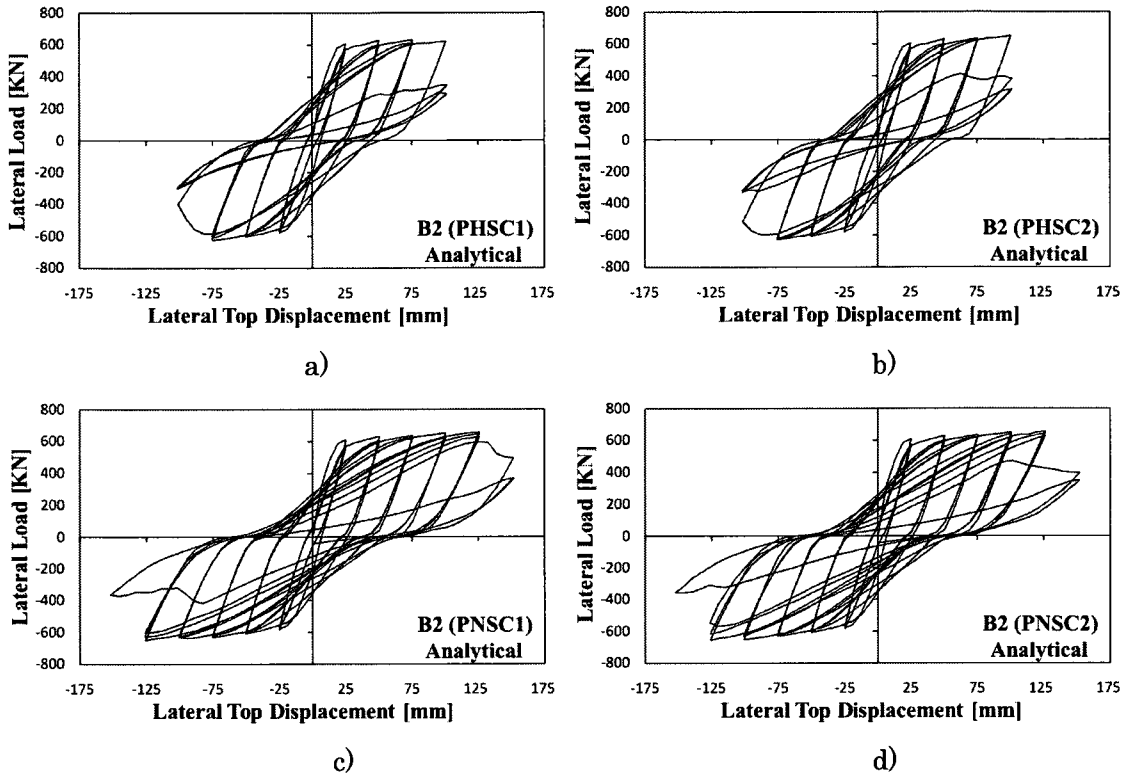

Fig. 4-20 Predicted Response for Wall B2: a) B2 (PHSC1); b) B2 (PHSC2); c) B2 (PNSC1); and d) B2 (PNSC2)

The normal strength and high strength models predicted similar lateral load capacity for Wall B3; however, the models did not capture the rupture of the vertical reinforcement in the boundary elements. The PHSC1 model predicted premature shear sliding at approximately 1000 mm above the foundation beam during the second excursion to 152 mm. Conversely, the PHSC2, PNSC1, and PNSC2 models predicted concrete crushing in the web with high shear distortion, specifically near the boundary elements at 178 mm of lateral displacement. After crushing of the concrete in the web, the PHSC2, PNSC1, and PNSC2 models sustained the load capacity up to 229 mm of lateral displacement due to yielding of the flexural reinforcement.

The PNSC2 model better predicted the strength; therefore, it was selected for the second part of the parametric study. Predicted responses of Wall B3 are given in Fig. 4-21.

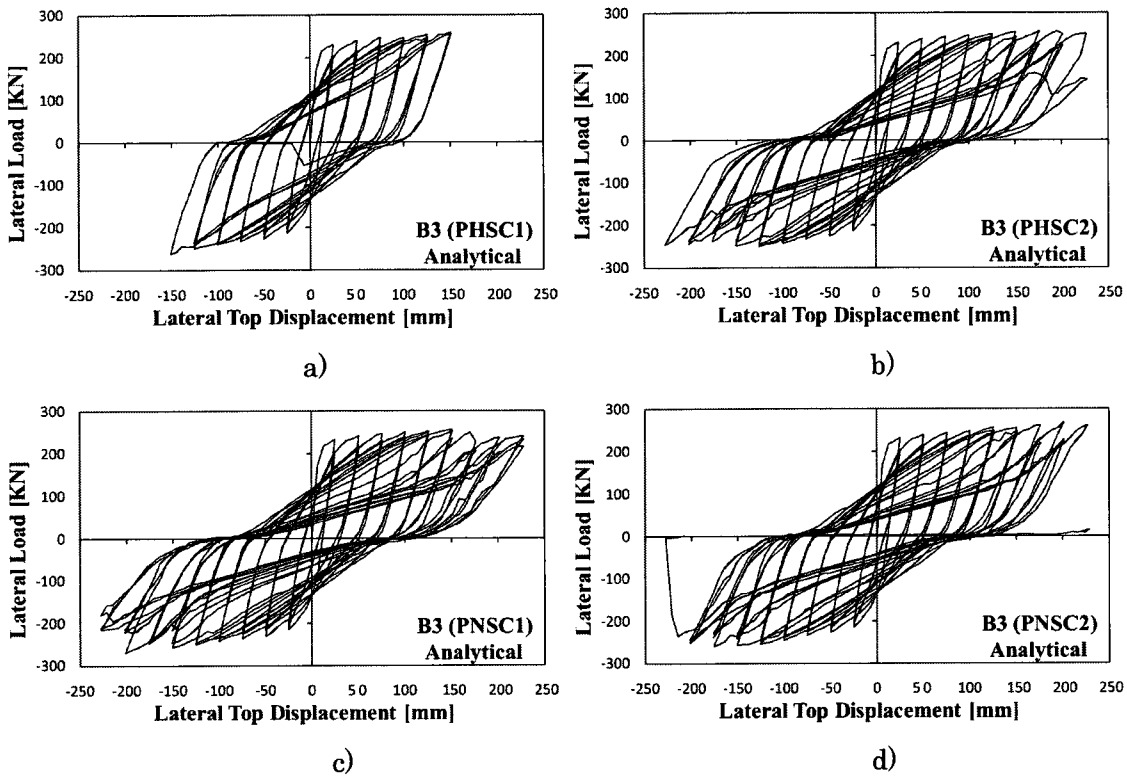

Fig. 4-21 Predicted Response for Wall B3: a) B3 (PHSC1); b) B3 (PHSC2); c) B3 (PNSC1); and d) B3 (PNSC2)

The Popovics normal strength compression pre-peak models, PNSC2 and PNSC1, accurately captured the response of Walls B5 and B11, respectively. These models accurately predicted the lateral load capacity, top displacement, and failure mode. For Wall B5, the modified Park-Kent and the base curve compression post-peak model predicted similar response; however, the response with the former was slightly closer to that reported. On the other hand, for Wall B11, the modified Park-Kent compression post-peak model delayed the failure of the wall one cycle. Similarities in the predicted response using the base curve and modified Park-Kent compression models indicated marginal improvement in the strength of the concrete due to confinement. This fact was corroborated with the predicted compressive strength of the concrete elements, which were always lower than the cylinder compressive strength, f'_c, of the walls. Failure for Walls B5 and B11 were predicted as concrete crushing in the web with high shear distortion near the boundary elements, which

corresponded to that observed during testing. Predicted responses of Walls B5 and B11 are given in Fig. 4-22 and Fig. 4-23, respectively.

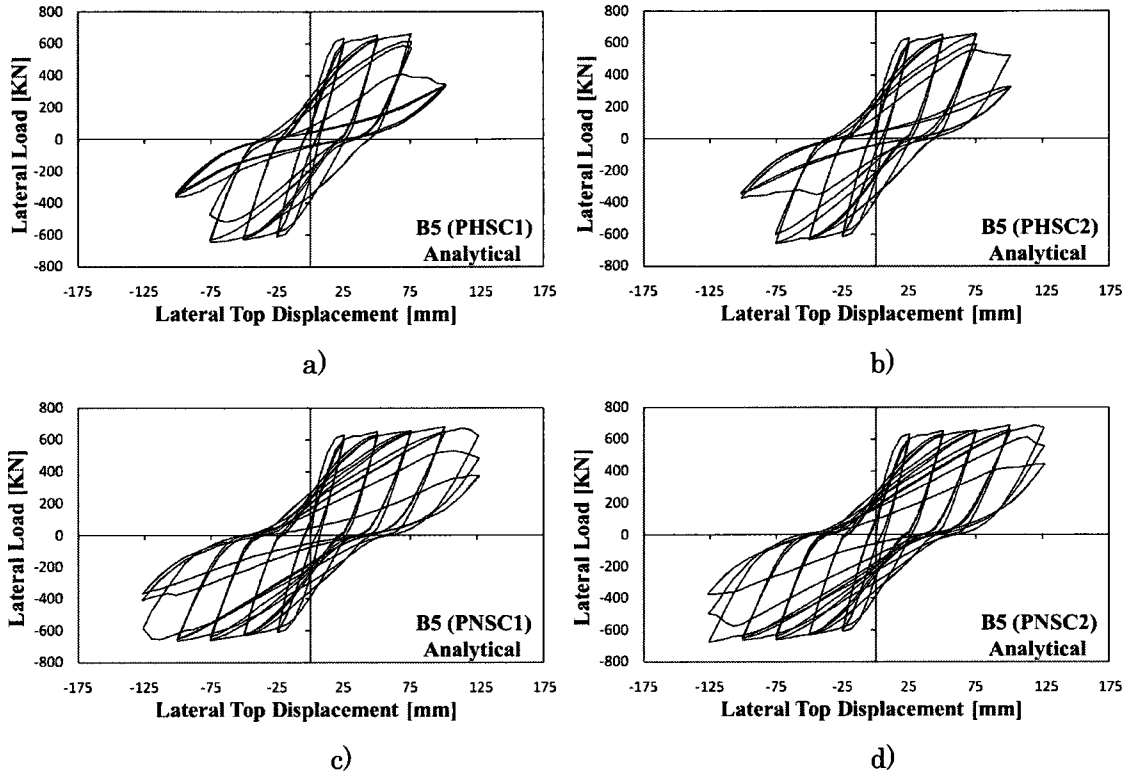

Fig. 4-22 Predicted Response for Wall B5: a) B5 (PHSC1); b) B5 (PHSC2); c) B5 (PNSC1); and d) B5 (PNSC2)

Parametric Study

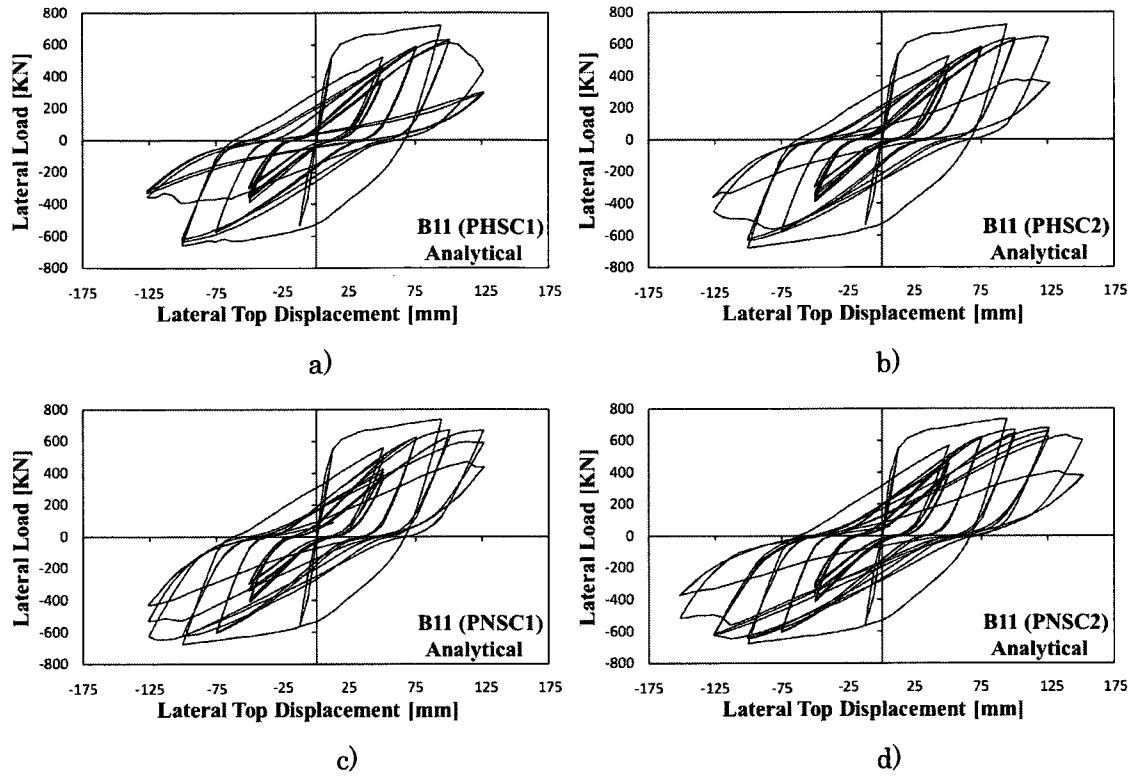

Fig. 4-23 Predicted Response for Wall B11: a) B11 (PHSC1); b) B11 (PHSC2); c) B11 (PNSC1); and d) B11 (PNSC2)

The high strength concrete model with modified Park-Kent model, PHSC2, permitted the best predictions for Wall B9, specifically in terms of ductility. The modified Park-Kent compression post-peak model predicted similar load capacity compared to the compression post-peak base curve. Normal strength concrete models PNSC1 and PNSC2 better predicted the load capacity of Wall B9; however, the predicted strength corresponded to a larger lateral displacement. Crushing of concrete in the web was adequately predicted with all models, which included high shear distortion near the boundary elements. Predicted responses of Wall B9 are given in Fig. 4-24.

Parametric Study

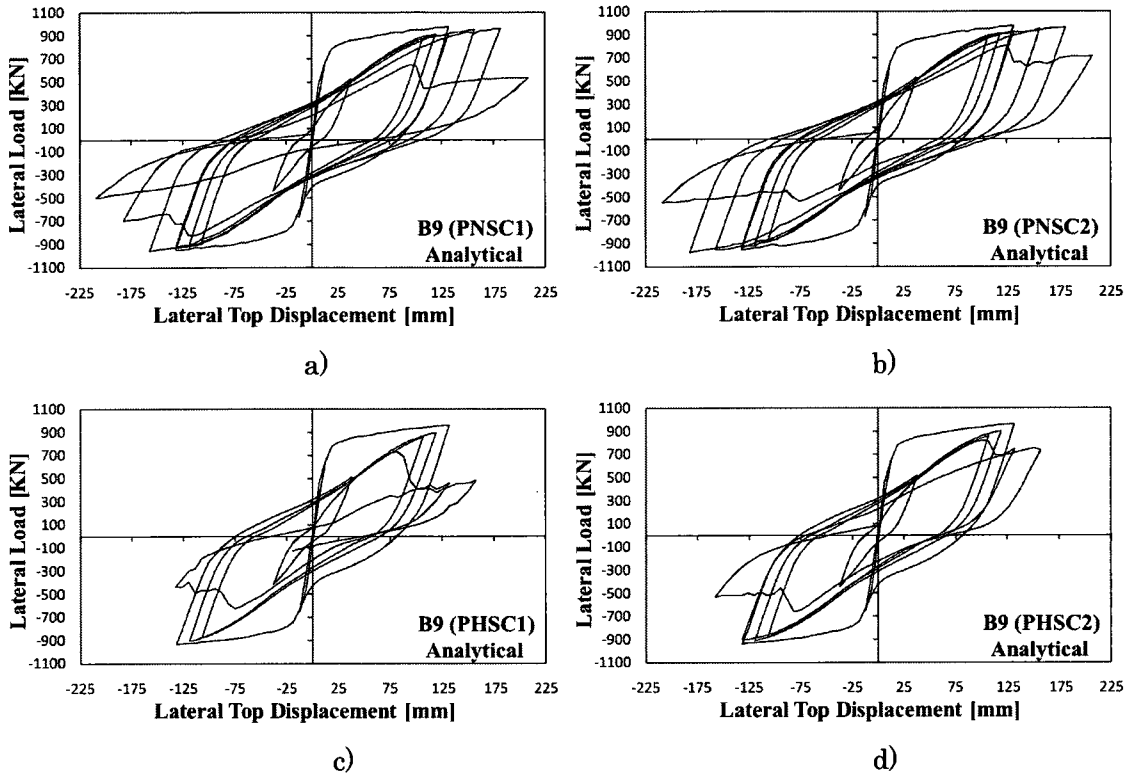

Fig. 4-24 Predicted Response for Wall B9: a) B9 (PNSC1); b) B9 (PNSC2); c) B9 (PHSC1); and d) B9 (PHSC2)

Given the results of the analysis of the PCA Walls, the models presented in Table 4-7 were selected to be used in the second part of the parametric study.

Table 4-7 Selected Concrete Compression Models for PCA Walls

Shear Wall	Compression Pre-Peak	Compression Post-Peak
B1	Popovics NSC	Base Curve
B2	Popovics NSC	Base Curve
B3	Popovics NSC	Modified Park-Kent
B5	Popovics NSC	Modified Park-Kent
B9	Popovics HSC	Modified Park-Kent
B11	Popovics NSC	Base Curve

Parametric Study

4.3.2.2 DP Walls

Results of part 1 of the parametric study for DP Walls are summarized in Table 4-8 and Table 4-9.

Table 4-8 Concrete Models: Observed and Calculated Maximum Lateral Strength for DP Walls

Max. Lateral Strength [kN]									
Wall	**Analytical**				**Exp.**	**Comparison (Ana./Exp.)**			
	Smith1	**Smith2**	**PNSC1**	**PNSC2**		**Smith1**	**Smith2**	**PNSC1**	**PNSC2**
DP1	1451	1451	1615	1609	1298	1.118	1.118	1.244	1.240
DP2*	1136	1135	1142	1144	904	1.257	1.256	1.263	1.265
DP2(2)**	1120	1124	1181	1179	904	1.239	1.243	1.306	1.304

* Results at the 2nd excursion to 9 mm where there was a sudden failure at the top of the web wall during testing.

** Analysis with concrete f'c reduced at the top four rows of elements in the web and flanges.

Table 4-9 Concrete Models: Observed and Calculated Maximum Lateral Displacement for DP Walls

Max. Lateral Disp. [mm]									
Wall	**Analytical**				**Exp.**	**Comparison (Ana./Exp.)**			
	Smith1	**Smith2**	**PNSC1**	**PNSC2**		**Smith1**	**Smith2**	**PNSC1**	**PNSC2**
DP1	11	15	15	15	14	0.786	1.071	1.071	1.071
DP2*	9	9	9	9	9	1.000	1.000	1.000	1.000
DP2(2)**	10	10	11	11	9	1.111	1.111	1.222	1.222

* Results at the 2nd excursion to 9mm where there was a sudden failure at the top of the web wall during testing.

** Analysis with concrete f'c reduced at the top four rows of elements in the web and flanges.

The analyses of the DP walls, DP1 and DP2, with the Smith-Young compression pre-peak model predicted better responses in terms of lateral load capacity and top displacement compared to the Popovics normal strength compression pre-peak model. However, the strength was overestimated between 12% and 30%. For both walls, DP1 and DP2, the Smith-Young models, Smith1 and Smith2, predicted failure in the form of shear sliding along the web wall preceded by crushing of the compression struts. The Popovics normal strength models, PNSC1 and PNSC2, overestimated the load

capacity and ductility, and underestimated the damage in the concrete. Analysis conducted with PNSC1 and PNSC2 did not predict failure before 15 mm of lateral displacement.

Wall DP1 was similarly predicted with models Smith1 and Smith2, corresponding to the Smith-Young compression pre-peak model in combination with the base curve and modified Park-Kent compression post-peak model, respectively. Both combinations predicted the same lateral load capacity, ductility and failure mode. However, the Smith2 model combination predicted better post-peak response. Although the analysis with the Smith2 model did not indicate improvement of the compressive strength of the concrete due to confinement, the modified Park-Kent model predicted better stiffness and strength degradation in the post-peak range compared to the base curve. The predicted crushing of concrete, which led to shear sliding failure, was more localized than observed during testing. Predicted responses of Wall DP1 are given in Fig. 4-25.

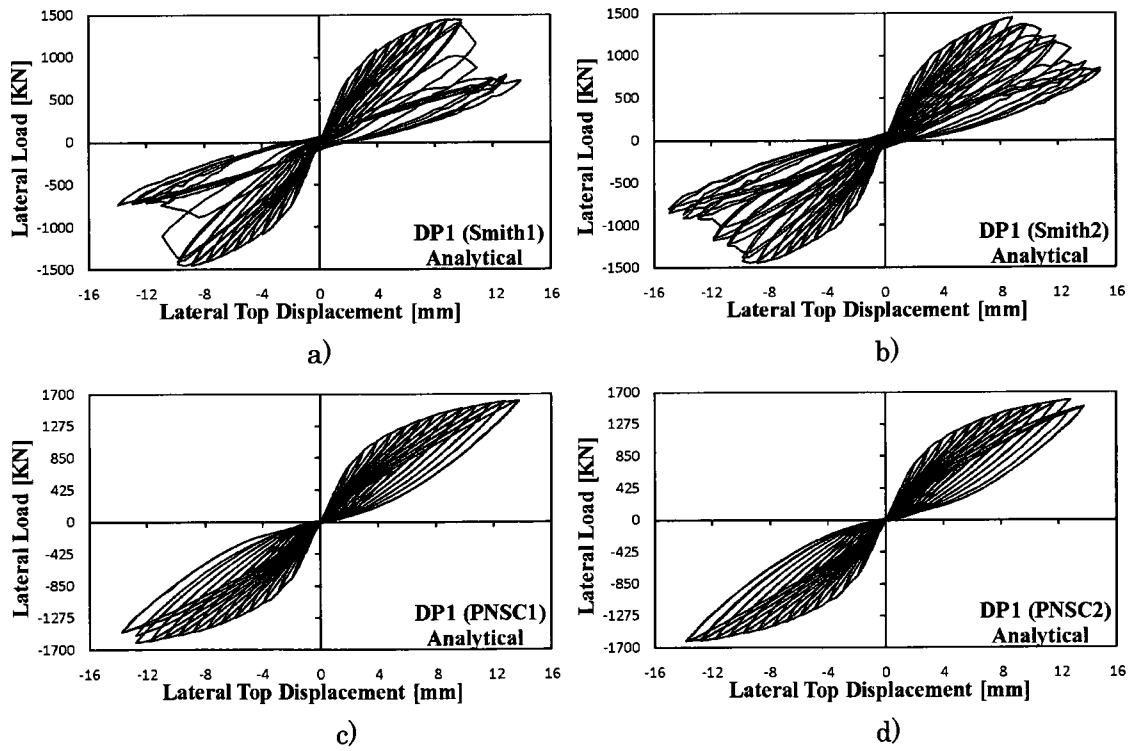

Fig. 4-25 Predicted Response for Wall DP1: a) DP1 (Smith1); b) DP1 (Smith2); c) DP1 (PNSC1); and d) DP1 (PNSC2)

Parametric Study

Response of Wall DP2 was adequately captured to 9 mm of displacement by the Smith-Young compression pre-peak models, Smith1 and Smith2. Beyond 9 mm, the analytical responses demonstrated an increase in load capacity until reaching the peak load, which was followed by a sudden post-peak decay. These predictions were in contrast with that observed during testing where Wall DP2 suddenly failed during the second excursion to 9 mm due to shear sliding in the web near the top slab. Palermo and Vecchio (2002) attributed the failure of the specimen to a probable zone of weakness created by weaker concrete near the top of the wall. For better comparison, the predicted response up to 9 mm was evaluated. In this displacement range, the predicted response was independent of the compression post-peak model since the wall did not reach the post-peak range. However, the modified Park-Kent post-peak model predicted better post-peak response. The Smith-Young compression pre-peak model combined with the modified Park-Kent compression post-peak model, Smith2, was selected for the second part of the parametric study. Predicted responses of Wall DP2 are given in Fig. 4-26.

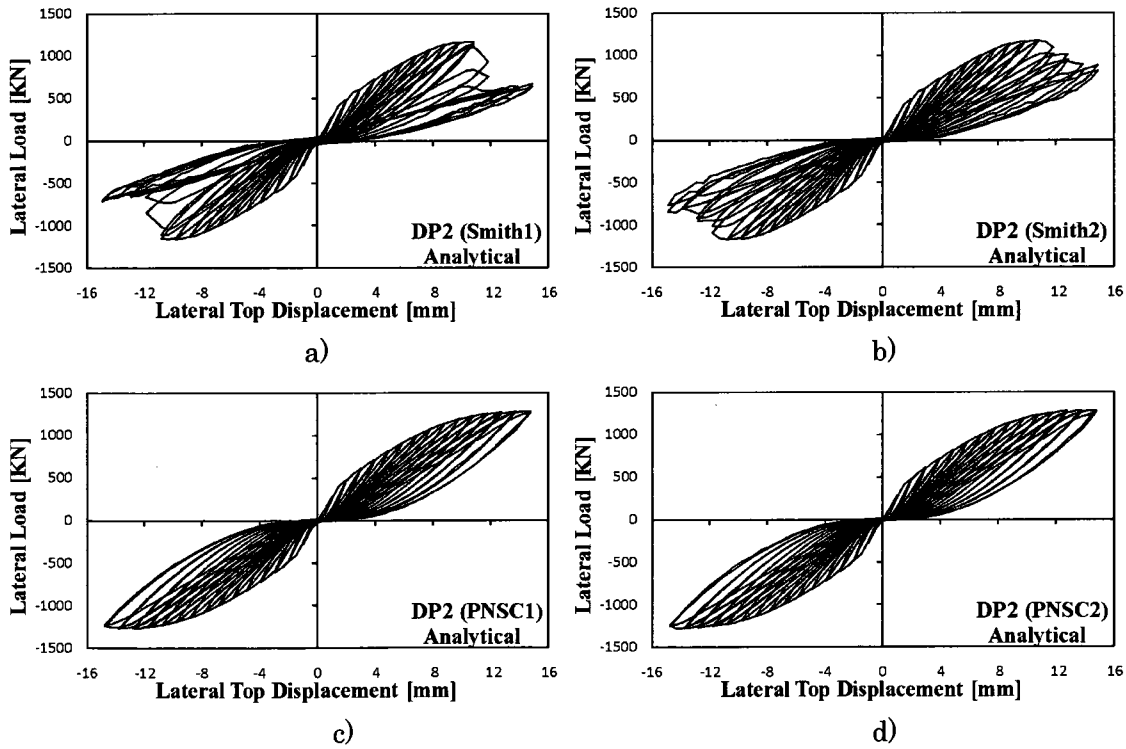

Fig. 4-26 Predicted Response for Wall DP2: a) DP2 (Smith1); b) DP2 (Smith2); c) DP2 (PNSC1); and d) DP2 (PNSC2)

Parametric Study

Further analyses of Wall DP2, with reduced concrete compressive strength of 70% of the cylinder strength in the top four rows of elements, were performed to capture the actual failure of the specimen, following the procedure described by Palermo and Vecchio (2004). The modified FE model, named DP2(2), predicted similar load capacity to DP2 model at 9 mm of displacement; however, the maximum displacement was better predicted. Furthermore, DP2(2) accurately predicted the shear sliding failure in the web wall near the top slab. Predicted responses of DP2(2) model are presented in Fig. 4-27.

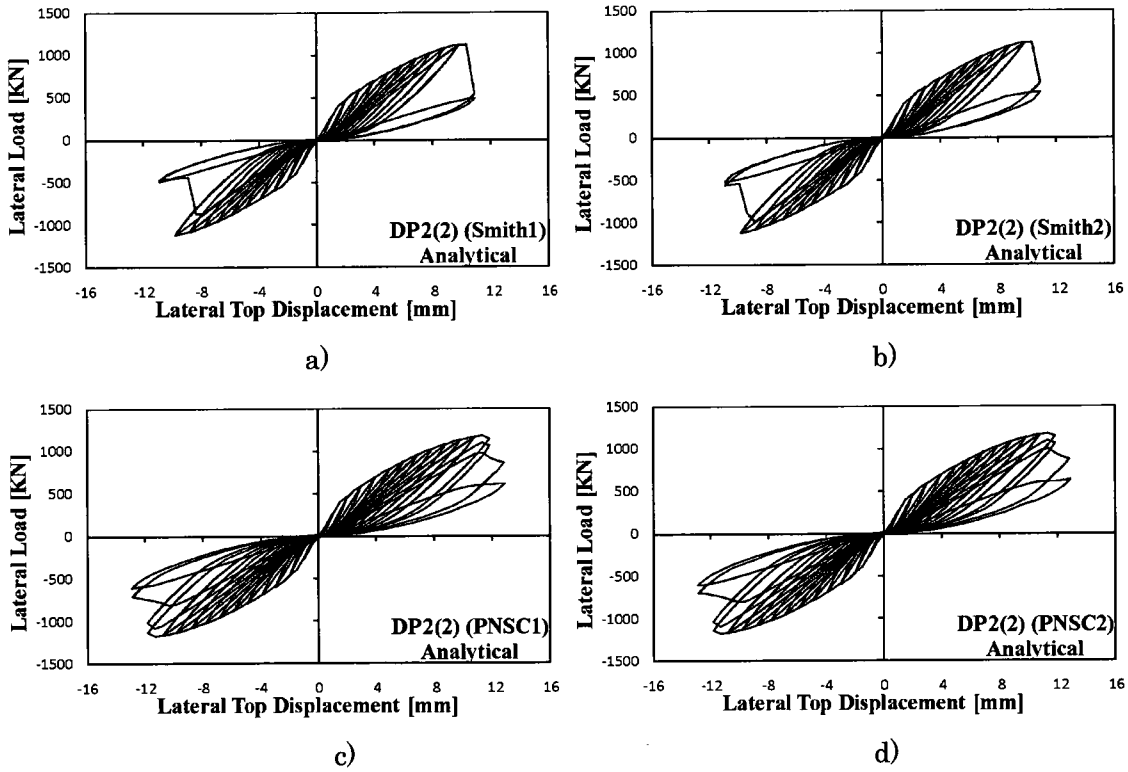

Fig. 4-27 Predicted Response for Wall DP2(2): a) DP2(2) (Smith1); b) DP2(2) (Smith2); c) DP2(2) (PNSC1); and d) DP2(2) (PNSC2)

The models selected for the analysis of DP Walls in the second part of the parametric study are listed in Table 4-10.

Table 4-10 Selected Compression Concrete Models for DP Walls

Shear Wall	Compression Pre-peak	Compression Post-peak
DP1	Smith-Young	Mod. Park-Kent
DP2	Smith-Young	Mod. Park-Kent
DP2(2)	Smith-Young	Mod. Park-Kent

4.4 Part 2: Slip Distortion and Hysteretic Response

4.4.1 Models

The second part of the parametric study is performed on four models for each shear wall resulting from the combination of two slip distortion models (Vecchio-Lai and not considered) and two concrete hysteretic models (nonlinear with plastic offset and nonlinear with cyclic decay). The models are codified according to the scheme given in Fig. 4-28 and summarized in Table 4-11.

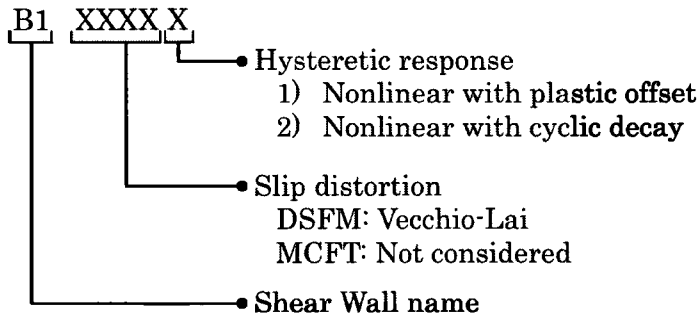

Fig. 4-28 FE Model Codification for Slip Distortion and Concrete Hysteretic Models

Table 4-11 Slip Distortion and Concrete Hysteretic Models

Model	Slip Distortion	Hysteretic Response	FE Model
DSFM1	Vecchio-Lai	Nonlinear with plastic offset	DSFM1
DSFM2	Vecchio-Lai	Nonlinear with cyclic decay	DSFM2
MCFT1	Not considered	Nonlinear with plastic offset	MCFT1
MCFT2	Not considered	Nonlinear with cyclic decay	MCFT2

The study of the slip distortion parameter involves the analysis of the shear walls with and without explicit consideration for strains due to shear slip along the crack. The Vecchio-Lai model is used when the shear slip along the crack is considered according to the Disturbed Stress Field Model (DSFM). The Vecchio-Lai slip distortion model is a stress-based model that relates the shear slip, δ_s, along the crack to the local shear stress, v_{ci}, along the crack. The shear slip strain, γ_s, is computed as the shear slip divided by the crack spacing, s. Conversely, when slip distortion is not considered, the shear slip, δ_s, is set equal to zero as in the Modified Compression Field Theory (MCFT).

Furthermore, two nonlinear loading/reloading hysteretic responses for concrete are considered: nonlinear with plastic offset, and nonlinear with cyclic decay. Both responses account for plastic offset strains resulting from concrete damage; however, the nonlinear with cyclic decay response (Palermo and Vecchio, 2002) extends the nonlinear with plastic offset response to simulate damage during reloading. In addition, the nonlinear with cyclic decay response modifies the nonlinear with plastic offset response in other aspects, such as partial unloading and reloading, shape of the unloading curve, and calculations of the instantaneous plastic offset strains, in both the compression and tension domains.

The nonlinear with plastic offset hysteretic model follows the nonlinear Ramsberg-Osgood formulations (Wong and Vecchio, 2002). Unloading in compression to a strain of ε_c results in concrete stress, f_c, as follows:

Parametric Study

$$f_c = f_{cm} + E_c\left(\varepsilon_c - \varepsilon_{cm}\right) + \frac{E_c\left(\varepsilon_c - \varepsilon_{cm}\right)^{N_c}}{N_c\left(\varepsilon_c^p - \varepsilon_{cm}\right)^{N_c-1}} \qquad for\ 1 \le N_c \le 20 \tag{4-13}$$

$$f_c = E_c\left(\varepsilon_c - \varepsilon_c^p\right) \quad for\ N_c \le 1\ or\ 20 \le N_c \tag{4-14}$$

Where ε_c^p is the current plastic offset strain, ε_{cm} is the maximum previously attained compressive strain, and f_{cm} is the corresponding stress. N_c is the Ramsberg-Osgood power term representing the deviation from linear elasticity.

$$N_c = \frac{E_c \cdot \left(\varepsilon_c^p - \varepsilon_{cm}\right)}{f_{cm} + E_c\left(\varepsilon_c^p - \varepsilon_{cm}\right)} \tag{4-15}$$

Unloading in tension results in concrete stress, f_c, as follows:

$$f_c = f_{tm} - E_c\left(\varepsilon_{tm} - \varepsilon_c\right) + \frac{E_c\left(\varepsilon_{tm} - \varepsilon_c\right)^{N_t}}{N_t\left(\varepsilon_{tm} - \varepsilon_c^p\right)^{N_t-1}} \qquad for\ 1 \le N_t \le 20 \tag{4-16}$$

$$f_c = E_c\left(\varepsilon_c - \varepsilon_c^p\right) \quad for\ N_t \le 1\ or\ 20 \le N_t \tag{4-17}$$

Where ε_c^p is the current plastic offset strain, ε_{tm} is the maximum previously attained tensile strain, and f_{tm} is the corresponding stress. N_t is computed as follows such that the initial unloading modulus is equal to the initial tangent stiffness of concrete, E_c:

$$N_t = \frac{E_c \cdot \left(\varepsilon_{tm} - \varepsilon_c^p\right)}{E_c\left(\varepsilon_{tm} - \varepsilon_c^p\right) - f_{tm}} \tag{4-18}$$

The nonlinear with cyclic decay response in compression and tension are illustrated in Fig. 4-29 (Wong and Vecchio, 2002).

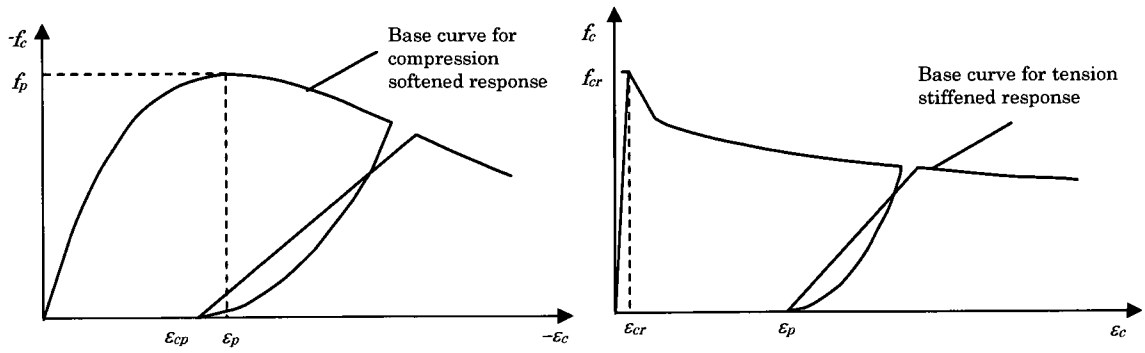

Fig. 4-29 Nonlinear with Cyclic Decay Response in: a) Compression; b) Tension (Wong and Vecchio, 2002)

When reloading in the compression domain to a compressive strain of ε_c, the concrete compressive stress, f_c, is computed as follows:

$$f_c = f_{ro} + E^+_{cm}(\varepsilon_c - \varepsilon_{ro}) \tag{4-19}$$

$$E^+_{cm} = \frac{\beta_d \cdot f_{cm} - f_{ro}}{\varepsilon_{cm} - \varepsilon_{ro}} \tag{4-20}$$

Where ε_{ro} is the strain at load reversal in the current hysteretic loop corresponding to a stress of f_{ro}, ε_{cm} is the unloading strain in the current hysteretic loop corresponding to a stress of f_{cm}, and E^+_{cm} is the reloading modulus in compression.

The damage indicator, β_d, is a function of the strain recovered in unloading of the current hysteretic loop, ε_{rec}.

$$\beta_d = \begin{cases} \dfrac{1}{1 + 0.10(\varepsilon_{rec}/\varepsilon_p)^{0.5}} & for\ |\varepsilon_c| < |\varepsilon_p| \\ \dfrac{1}{1 + 0.175(\varepsilon_{rec}/\varepsilon_p)^{0.6}} & for\ |\varepsilon_c| > |\varepsilon_p| \end{cases} \tag{4-21}$$

$$\varepsilon_{rec} = \varepsilon_{cm} - \varepsilon_{ro} \tag{4-22}$$

Parametric Study

Where ε_p is the strain corresponding to the peak stress in the base-curve.

The instantaneous plastic strain, ε_c^p, for the compression domain is computed with following equation:

$$\varepsilon_c^{p\,'} = \varepsilon_p \left[0.166 \left(\frac{\varepsilon_{cm}}{\varepsilon_p} \right)^2 + 0.132 \left(\frac{\varepsilon_{cm}}{\varepsilon_p} \right) \right] \tag{4-23}$$

If $\varepsilon_c^{p'}$ is more compressive than ε_c^p, then ε_c^p is updated as $\varepsilon_c^{p'}$.

Unloading in compression to a strain of ε_c results in concrete stress, f_c, as follows:

$$f_c = f_{cm} + E_c(\varepsilon_c - \varepsilon_{cm}) + \frac{E_c(0.071-1)(\varepsilon_c - \varepsilon_{cm})^{N_c}}{N_c(\varepsilon_c^p - \varepsilon_{cm})^{N_c-1}} \tag{4-24}$$

Where ε_c^p is the current plastic offset strain, ε_{cm} is the maximum previously attained compressive strain corresponding to a stress of f_{cm}. N_c is the Ramsberg-Osgood power term representing the deviation from linear elasticity.

$$N_c = \frac{E_c(1-0.071)(\varepsilon_c^p - \varepsilon_{cm})}{f_{cm} + E_c(\varepsilon_c^p - \varepsilon_{cm})} \tag{4-25}$$

When reloading in the tensile domain to a tensile strain of ε_c, the concrete tensile stress, f_c, is computed as follows:

$$f_c = \beta_t \cdot f_{tm} - E_{tm}^{+}(\varepsilon_{tm} - \varepsilon_c) \tag{4-26}$$

$$E_{tm}^{+} = \frac{\beta_t \cdot f_{tm} - f_{ro}}{\varepsilon_{tm} - \varepsilon_{ro}} \tag{4-27}$$

Where ε_{tm} is the unloading strain in the current hysteretic loop corresponding to a stress of f_{tm}, E^{+}_{tm} is the reloading modulus in tension, and β_t is the damage indicator.

$$\beta_t = \frac{1}{1 + 1.15(\varepsilon_{rec})^{0.25}} \tag{4-28}$$

$$\varepsilon_{rec} = \varepsilon_{tm} - \varepsilon_{ro} \tag{4-29}$$

The instantaneous plastic strain, $\varepsilon_c^{p'}$, for the tension domain is computed with the following equation:

$$\varepsilon_c^{p\,\prime} = 146\varepsilon_{tm}^{\ 2} + 0.523\varepsilon_{tm} \tag{4-30}$$

Unloading in tension results in concrete stress, f_c, as follows:

$$f_c = f_{tm} - E_c\left(\varepsilon_{tm} - \varepsilon_c\right) + \frac{\left(E_c - E_c^f\right)\left(\varepsilon_{tm} - \varepsilon_c\right)^{N_t}}{N_t\left(\varepsilon_{tm} - \varepsilon_c^p\right)^{N_t - 1}} \tag{4-31}$$

Where ε_c^p is the current plastic offset strain, ε_{tm} is the maximum previously attained tensile strain corresponding to a stress of f_{tm}. N_t is computed such that the unloading modulus is equal to the initial tangent stiffness of concrete, E_c, at the beginning of the unloading branch, and equal to E_c^f at the end of the unloading branch.

$$N_t = \frac{\left(E_c - E_c^f\right)\cdot\left(\varepsilon_{tm} - \varepsilon_c^p\right)}{E_c\left(\varepsilon_{tm} - \varepsilon_c^p\right) - f_{tm}} \tag{4-32}$$

$$E_c^f = \begin{cases} 0.071 \cdot E_c\left(0.001/\varepsilon_{tm}\right) & for\ \varepsilon_{tm} < 0.001 \\ 0.053 \cdot E_c\left(0.001/\varepsilon_{tm}\right) & for\ \varepsilon_{tm} < 0.001 \end{cases} \tag{4-33}$$

4.4.2 Results

4.4.2.1 PCA Walls

Table 4-12 and Table 4-13 summarize the results for the second part of the parametric study for the PCA walls. The tables show similar results for the slip distortion and concrete hysteretic response models, which indicates marginal sensitivity of the analysis for these parameters.

Parametric Study

Table 4-12 Slip Distortion and Hysteretic Models: Observed and Calculated Maximum Lateral Strength for PCA Walls

Max. Lateral Load (kN)									
Wall	**Analytical**				**Exp.**	**Comparison (Ana./Exp.)**			
	DSFM1	**DSFM2**	**MCFT1**	**MCFT2**		**DSFM1**	**DSFM2**	**MCFT1**	**MCFT2**
B1	257	243	246	239	271	0.948	0.897	0.908	0.882
B2	656	658	659	661	704	0.932	0.935	0.936	0.939
B3	268	251	260	254	276	0.971	0.909	0.942	0.920
B5	687	683	683	674	762	0.902	0.896	0.896	0.885
B9	962	958	954	951	977	0.985	0.981	0.976	0.973
B11	735	734	725	726	726	1.012	1.011	0.999	1.000
					Mean	0.958	0.938	0.943	0.933
					COV [%]	4.122	5.093	4.157	5.089

Table 4-13 Slip Distortion and Hysteretic Models: Observed and Calculated Maximum Lateral Displacement for PCA Walls

Max. Lateral Disp. (mm)									
Wall	**Analytical**				**Exp.**	**Comparison (Ana./Exp.)**			
	DSFM1	**DSFM2**	**MCFT1**	**MCFT2**		**DSFM1**	**DSFM2**	**MCFT1**	**MCFT2**
B1	151	126	126	126	127	1.189	0.992	0.992	0.992
B2	126	126	126	126	127	0.992	0.992	0.992	0.992
B3	227	176	151	151	178	1.275	0.989	0.848	0.848
B5	126	126	126	126	127	0.992	0.992	0.992	0.992
B9	132	132	132	132	133	0.992	0.992	0.992	0.992
B11	126	151	151	151	127	0.992	1.189	1.189	1.189
					Mean	1.072	1.024	1.001	1.001
					COV [%]	11.832	7.870	10.848	10.848

Predictions in terms of lateral strength and maximum lateral displacement for the PCA Walls differed slightly from one model to the other. Table 4-12 shows a difference of less than 3% in the mean analytical-to-experimental ratio for strength. Similarly, Table 4-13 shows a difference of approximately 7% in the mean analytical-to-experimental ratio for the maximum lateral displacement. Given these small

differences, Table 4-12 and Table 4-13 are not conclusive. A qualitative assessment of the predicted responses, specifically in terms of prediction of damage, indicated that the Vecchio-Lai slip distortion model with nonlinear with decay hysteretic model (DSFM2) captured better the hysteretic response of the PCA Walls.

In general, the lateral strength calculated with the Vecchio-Lai slip distortion models (DSFM1 and DSFM2) were slightly higher than that calculated without considering the slip distortion (MCFT1 and MCFT2).

The DSFM models better predicted the lateral strength. Furthermore, the damage calculated with the nonlinear with decay hysteresis model was slightly greater than that calculated with the nonlinear with plastic offset model. The prediction of more damage using the nonlinear with decay hysteretic model resulted in reduced displacement capacity for some shear walls, specifically Walls B1, B3 and B9. Conversely, the nonlinear with decay predicted higher lateral displacement for Wall B11.

Similar responses were predicted with the DSFM and the MCFT models for Walls B1 and B2. However, the MCFT models predicted more damage and less hysteretic cycles. All the models underestimated the pinching phenomenon mostly due to the modelling, which did not consider buckling of the vertical reinforcement. This caused an underestimation of the shear distortion of the concrete in the boundary elements. Although the analyses did not capture buckling of the reinforcement, the high compressive strains in the elements indicated this phenomenon. VecTor2 can simulate buckling of reinforcement by using link-bond elements between truss bar elements and concrete elements; however, this results in a significant increase of computational time. The predicted failure for all the models was crushing of the concrete in the web, followed by crushing of the concrete in the boundary elements, which led to shear sliding. Predicted responses of Walls B1 and B2 are given in Fig. 4-30 and Fig. 4-31, respectively.

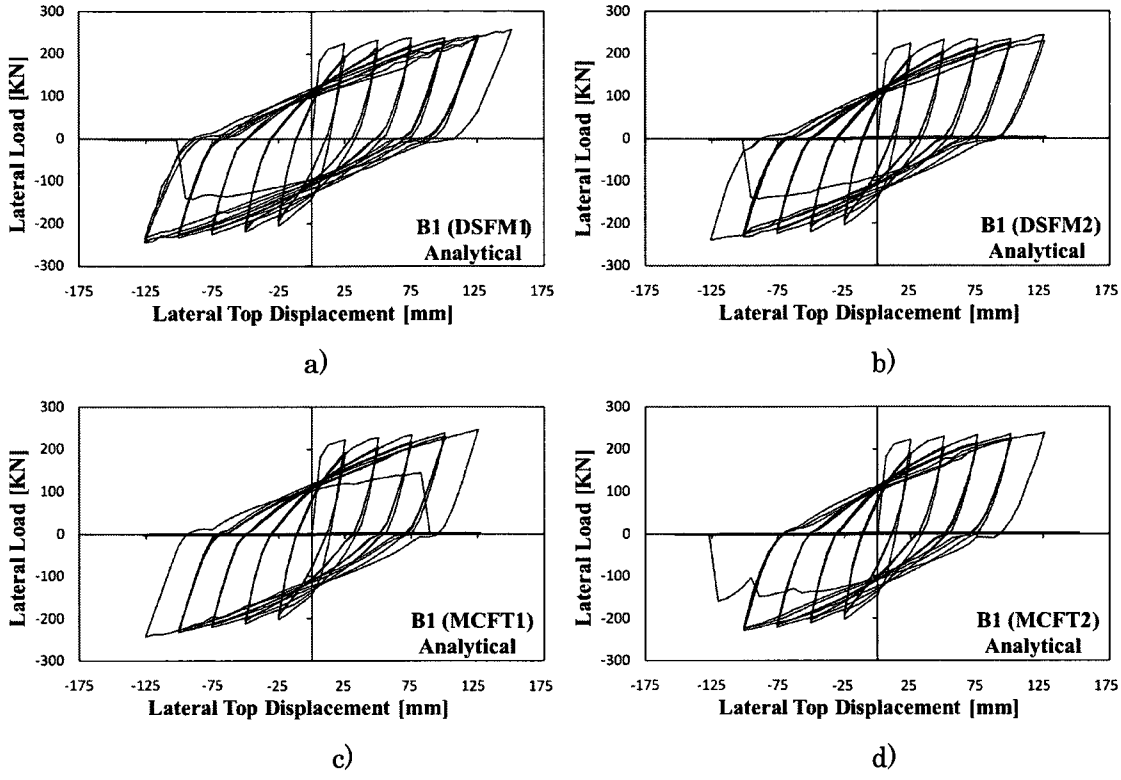

Fig. 4-30 Predicted Response for Wall B1: a) B1 (DSFM1); b) B1 (DSFM2); c) B1 (MCFT1); and d) B1 (MCFT2)

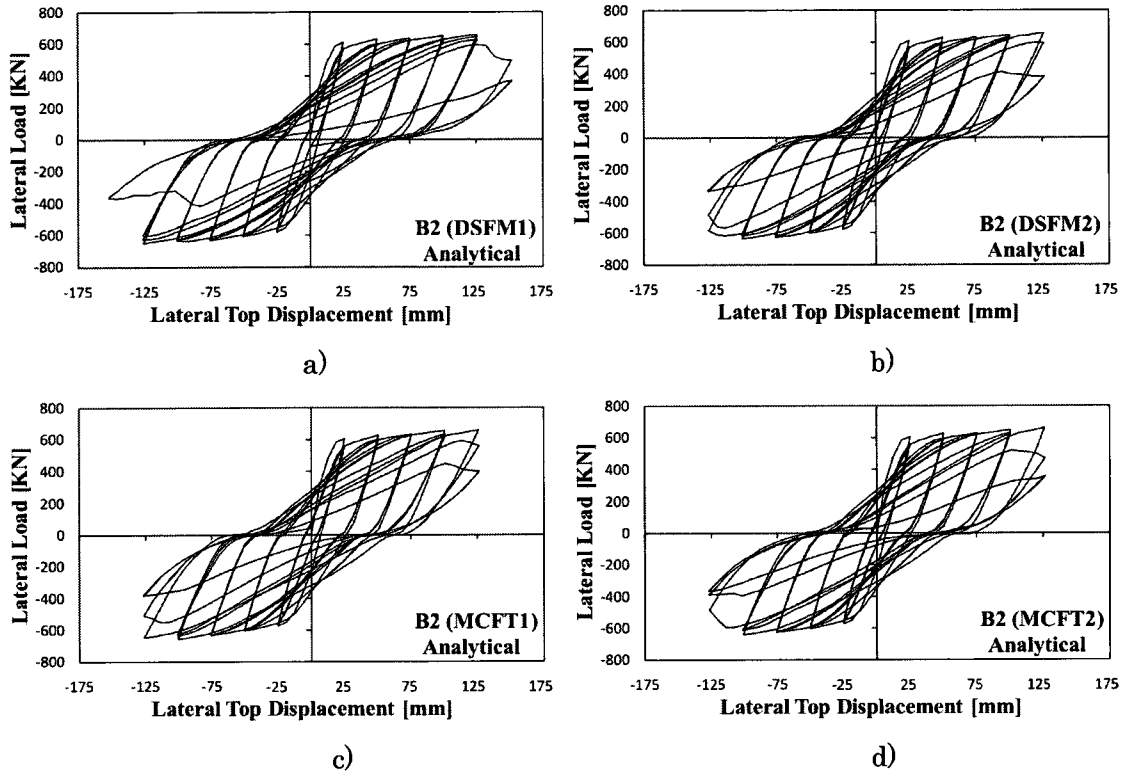

Fig. 4-31 Predicted Response for Wall B2: a) B2 (DSFM1); b) B2 (DSFM2); c) B2 (MCFT1); and d) B2 (MCFT2)

For Wall B3, the DSFM models predicted higher lateral displacement than the MCFT models (Fig. 4-32); however, both analyses predicted similar failure in the form of crushing of concrete in the web. The MCFT models predicted more damage in the boundary elements, which triggered shear sliding failure during loading to 175 mm of displacement. None of the models predicted buckling and rupture of the vertical reinforcement; however, the models predicted crushing of the concrete with high shear distortion, which followed the bar buckling observed during testing. The DSFM model with both nonlinear hysteretic models captured the substantial stiffness degradation and degree of pinching after buckling of the vertical reinforcement, which was observed at 203 mm of displacement. Stiffness degradation was better captured by the DSFM model with the nonlinear with decay hysteretic model, which predicted a drop of strength of approximately 10% at 203 mm of displacement. Beyond this displacement, the wall was considered to have failed given the high predicted web

crushing with significant shear distortion. Predicted responses of Walls B3 are given in Fig. 4-32.

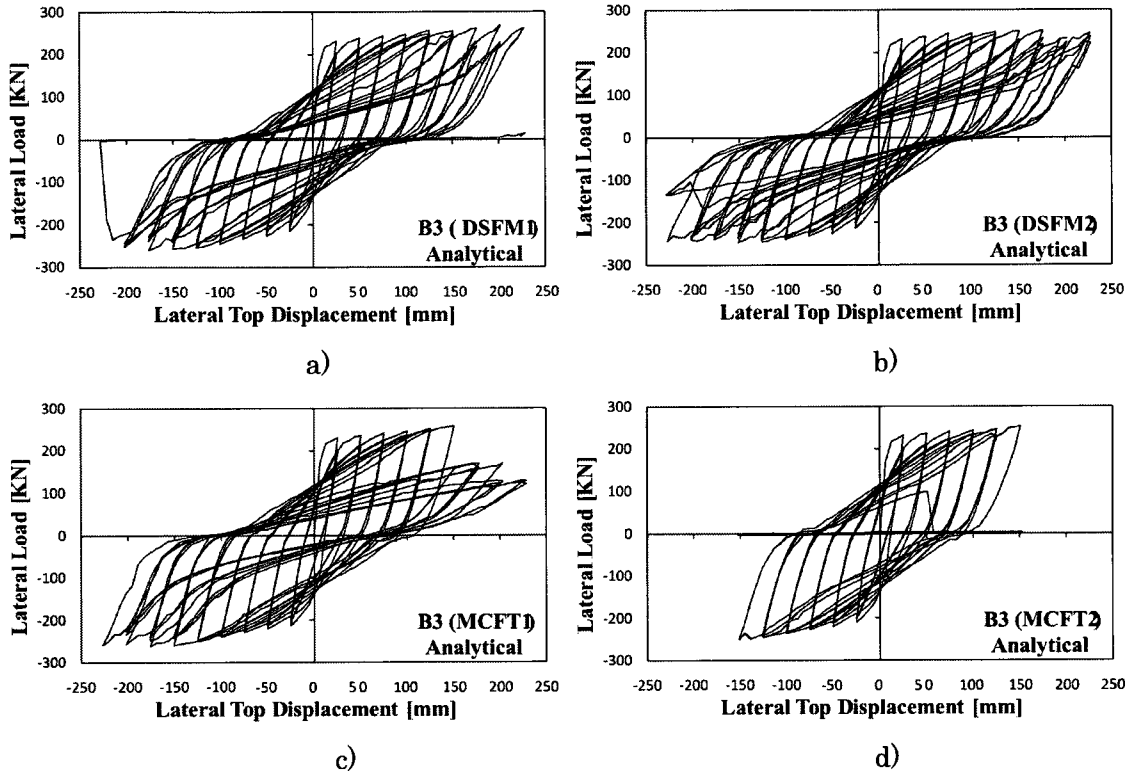

Fig. 4-32 Predicted Response for Wall B3: a) B3 (DSFM1); b) B3 (DSFM2); c) B3 (MCFT1); and d) B3 (MCFT2)

Wall B5 was similarly predicted with the DSFM and MCFT models. All the models adequately predicted the lateral strength, lateral displacement, failure mode, and other behavioural aspects such as pinching and energy dissipation. In general, the lateral strength was underestimated approximately 10%, and the difference in mean lateral strength among the models was less than 2%. The maximum displacement was accurately predicted, and some minor differences were obtained in the last cycle to 127 mm of displacement, depending on the employed models. Predicted responses of Wall B5 are given in Fig. 4-33.

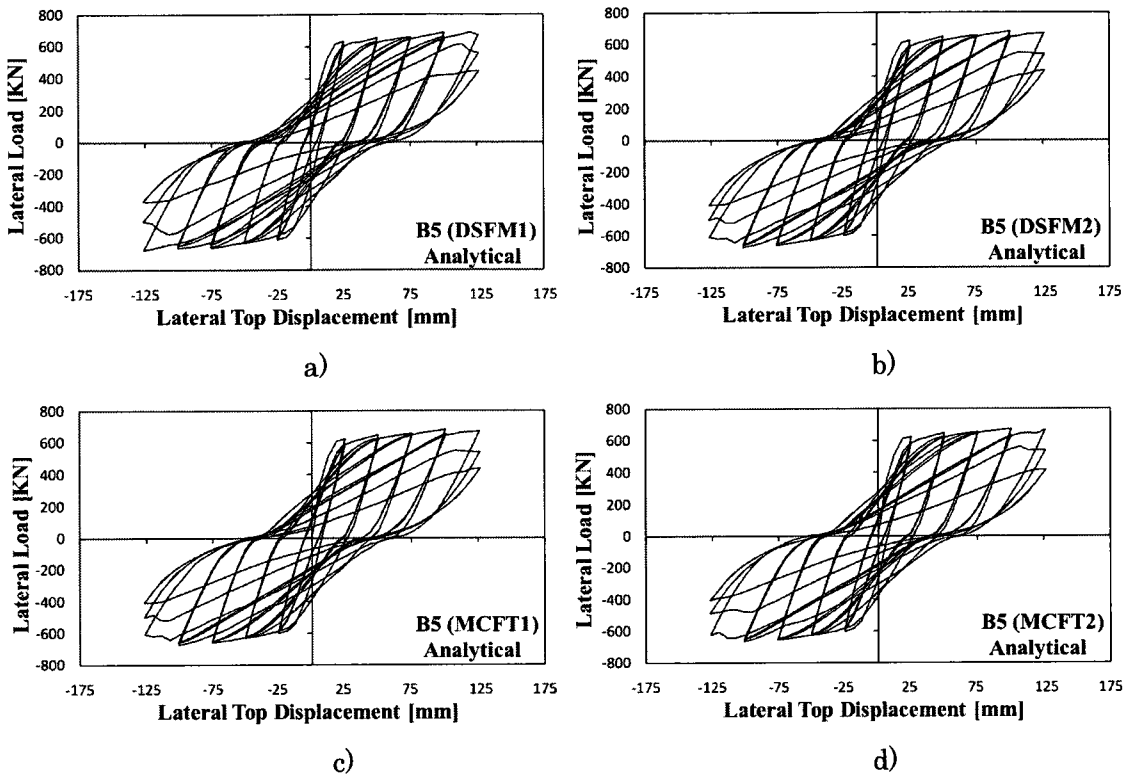

Fig. 4-33 Predicted Response for Wall B5: a) B5 (DSFM1); b) B5 (DSFM2); c) B5 (MCFT1); and d) B5 (MCFT2)

The DSFM and MCFT models predicted similar lateral strength for Wall B9 as shown in Fig. 4-34, although the latter sustained more hysteretic cycles after the first excursion to 125 mm. The predicted response with the Vecchio-Lai slip distortion model and nonlinear with decay model (DSFM2) closely matched the reported response, and captured the damage in the web that led to the failure of the wall during loading to 108 mm of displacement. All the models adequately predicted the failure mode, which consisted of crushing of the concrete in the web portion of the wall.

Parametric Study

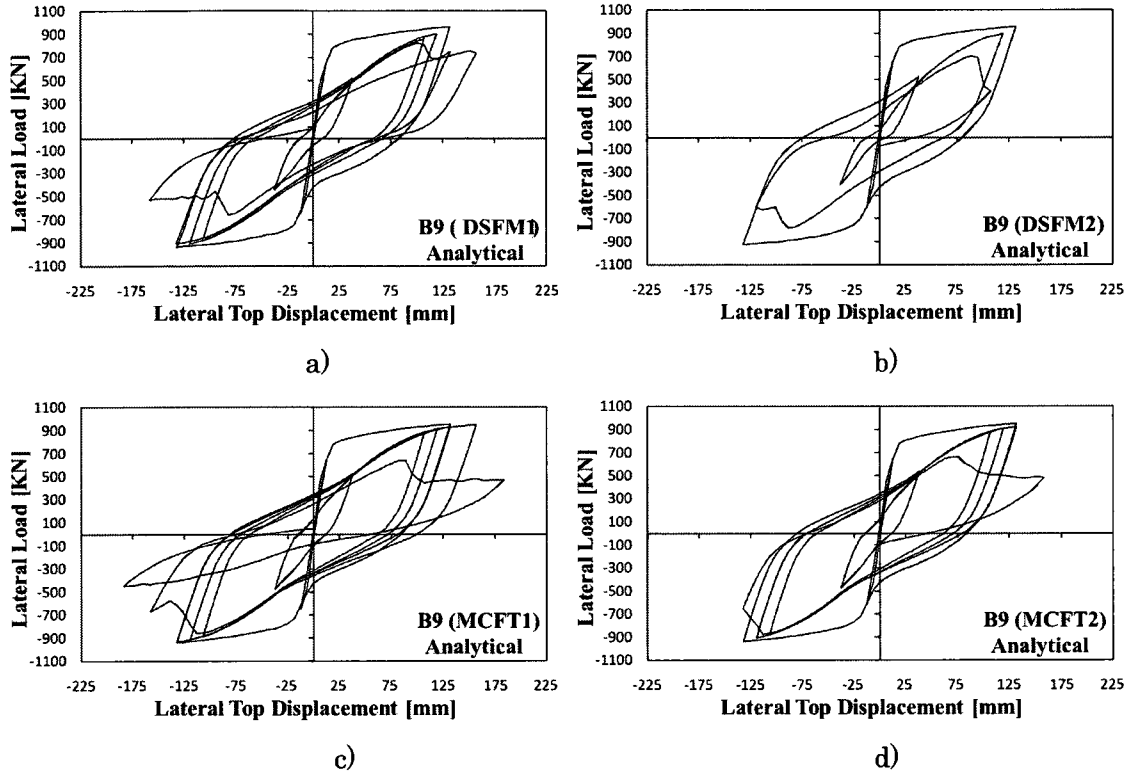

Fig. 4-34 Predicted Response for Wall B9: a) B9 (DSFM1); b) B9 (DSFM2); c) B9 (MCFT1); and d) B9 (MCFT2)

In general, the Vecchio-Lai slip distortion model with nonlinear with plastic offset hysteretic model, DSFM1, predicted better response for Wall B11, specifically in terms of maximum displacement. The analyses without considering slip distortion of the elements, MCFT models, slightly better predicted the lateral strength. However, the MCFT overestimated the maximum lateral displacement approximately by 19% (one extra cycle). All the analyses predicted similar loading, reloading, pinching, and energy dissipation, as well as failure mode, which consisted of crushing of the concrete with high shear distortion in the web. Predicted responses of Wall B11 are given in Fig. 4-35.

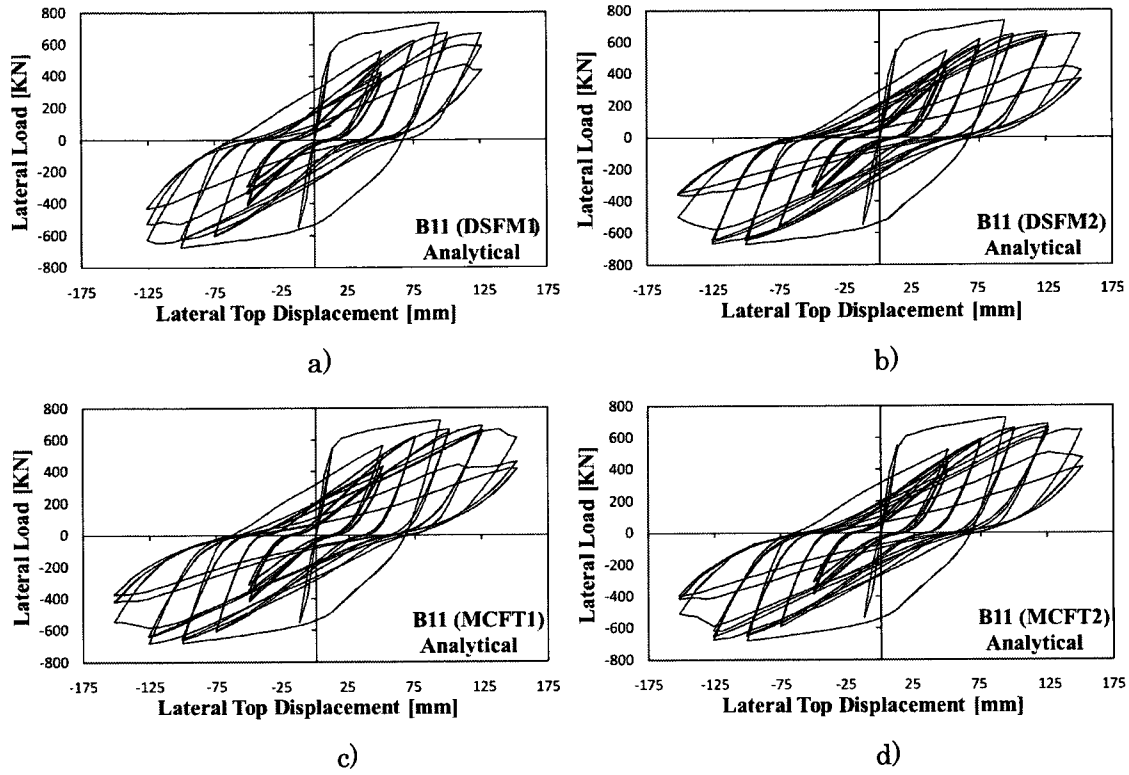

Fig. 4-35 Predicted Response for Wall B11: a) B11 (DSFM1); b) B11 (DSFM2); c) B11 (MCFT1); and d) B11 (MCFT2)

Table 4-14 summarizes the slip distortion and concrete hysteretic response models selected for the PCA Walls.

Table 4-14 Selected Slip Distortion and Hysteretic Response Models for PCA Walls

Shear Wall	Slip Distortion	Hysteretic Response
B1	Vecchio-Lai	Nonlinear with cyclic decay
B2	Vecchio-Lai	Nonlinear with cyclic decay
B3	Vecchio-Lai	Nonlinear with cyclic decay
B5	Vecchio-Lai	Nonlinear with cyclic decay
B9	Vecchio-Lai	Nonlinear with cyclic decay
B11	Vecchio-Lai	Nonlinear with plastic offset

Parametric Study

4.4.2.2 DP Walls

Results of the analyses of DP Walls for the second part of the parametric study are presented in Table 4-15 and Table 4-16.

Table 4-15 Slip Distortion and Concrete Hysteretic Models: Observed and Calculated Maximum Lateral Strength for DP Walls

Max. Lateral Load (kN)									
Wall	**Analytical**				**Exp.**	**Comparison (Ana./Exp.)**			
	DSFM1	**DSFM2**	**MCFT1**	**MCFT2**		**DSFM1**	**DSFM2**	**MCFT1**	**MCFT2**
DP1	1449	1390	1379	1335	1298	1.116	1.071	1.062	1.029
DP2*	1135	1098	1052	991	904	1.256	1.215	1.164	1.096
DP2(2)**	1124	1077	1015	946	904	1.243	1.191	1.123	1.046
					Mean	1.205	1.159	1.116	1.057
					COV [%]	6.397	6.657	4.566	3.320

Table 4-16 Slip Distortion and Concrete Hysteretic Models: Observed and Calculated Maximum Lateral Displacement for DP Walls

Max. Lateral Disp. (mm)									
Wall	**Analytical**				**Exp.**	**Comparison (Ana./Exp.)**			
	DSFM1	**DSFM2**	**MCFT1**	**MCFT2**		**DSFM1**	**DSFM2**	**MCFT1**	**MCFT2**
DP1	13	14	13	13	14	0.929	1.000	0.929	0.929
DP2*	9	9	9	9	9	1.000	1.000	1.000	1.000
DP2(2)**	10	11	9	10	9	1.111	1.222	1.000	1.111
					Mean	1.013	1.074	0.976	1.013
					COV [%]	9.079	11.945	4.225	9.079

According to the results presented in Table 4-15 and Table 4-16, the analysis without accounting for the slip distortion with the nonlinear with decay hysteretic model, MCFT2, predicted the best response in terms of lateral strength and maximum lateral displacement for the DP Walls. Conversely to the PCA predictions, the difference between models is evident, specifically the hysteretic models, which allowed better

prediction of damage between repetitions to the same lateral displacement. The Vecchio-Lai slip distortion model with the nonlinear with decay hysteretic response, DSFM2, better captured the rounded post-peak response; however, this model predicted more lateral strength than the analysis without considering the slip distortion phenomenon (MCFT1 and MCFT2). Overestimation of the lateral strength is probably due to the overestimation of the stiffness of the flanges. A more accurate analysis could be performed with either a three-dimensional model or a two-dimensional model with modified properties of the flanges.

The MCFT2 model more accurately predicted the lateral strength for Wall DP1 compared to that reported during testing. This model, however, predicted a sudden loss of strength of approximately 500 kN during loading to 13 mm of displacement, which was not observed during testing. The DSFM2 predicted better post-peak response and better captured the progressive stiffness and strength degradation. The nonlinear with decay hysteretic model predicted better loading and reloading of the cycles, and adequately predicted the damage and stiffness degradation in the second repetitions of the cycles. All the models adequately predicted the maximum lateral displacement; however, the Vecchio-Lai slip distortion model with the nonlinear with plastic offset response, DSFM1, underestimated the displacement corresponding to the peak strength. Selection of the slip distortion and hysteretic models did not affect the predicted failure, which consisted of crushing of concrete in the web and subsequent shear sliding. Predicted responses of Wall DP1 are given in Fig. 4-36.

Parametric Study

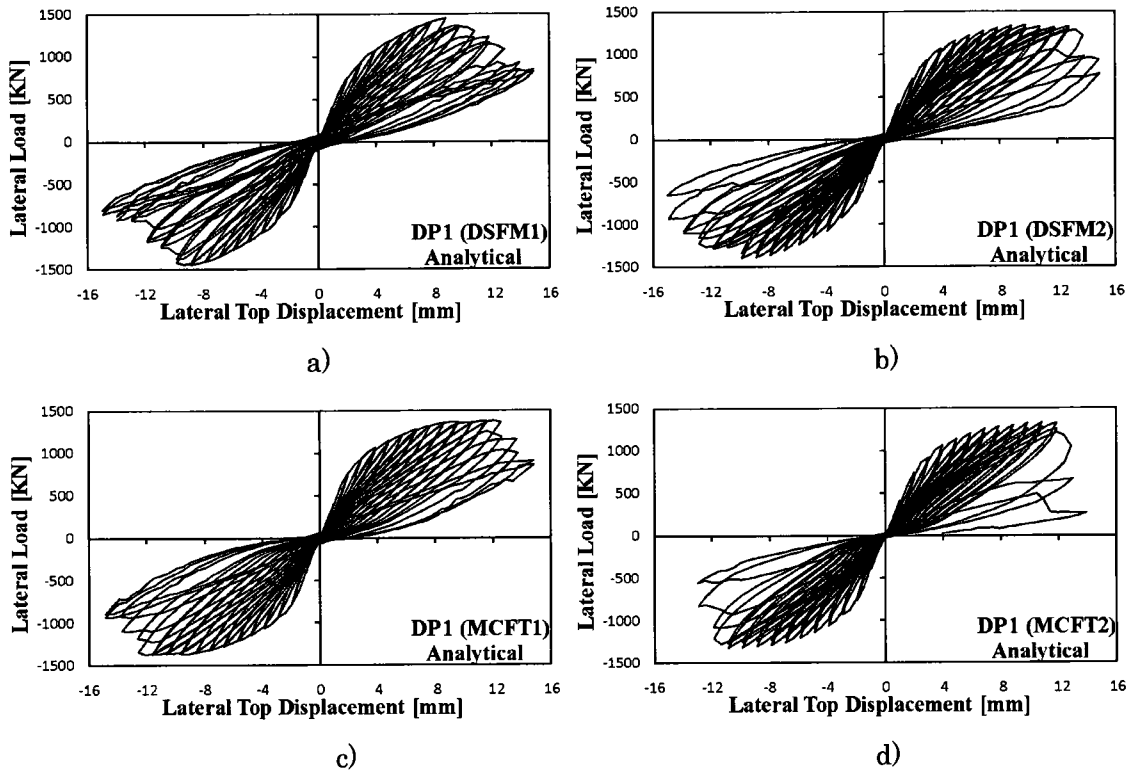

Fig. 4-36 Predicted Response for Wall DP1: a) DP1 (DSFM1); b) DP1 (DSFM2); c) DP1 (MCFT1); and d) DP1 (MCFT2)

Prediction of the lateral strength in Wall DP2 was assessed at 9 mm of displacement, where the actual failure was observed, to conduct a better comparison. During the second excursion to 9 mm of displacement, the specimen failed by shear sliding due to a probable zone of weakness created by weaker concrete near the top of the wall. Similar to DP1, the best prediction of the lateral strength was obtained with the MCFT2 model. The nonlinear with decay hysteretic model better captured the cyclic damage and predicted better the loading and reloading branches of the hysteretic behaviour. Predicted responses of Wall DP2 are given in Fig. 4-37.

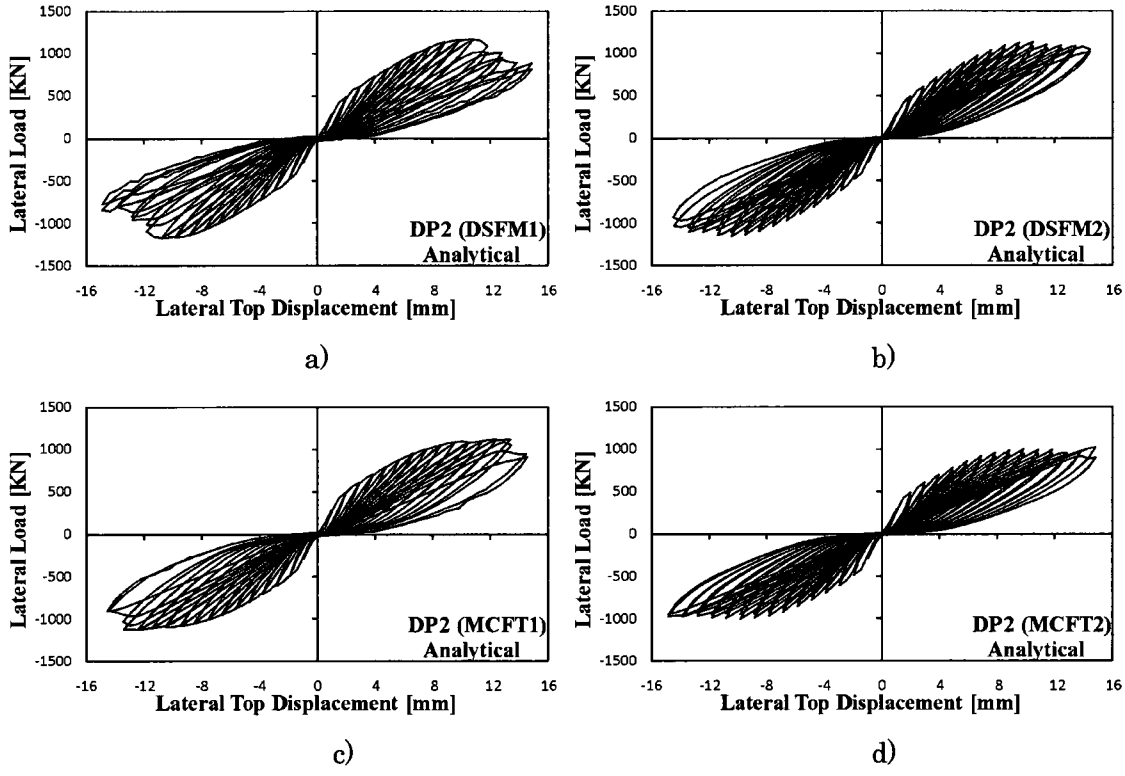

Fig. 4-37 Predicted Response for Wall DP2: a) DP2 (DSFM1); b) DP2 (DSFM2); c) DP2 (MCFT1); and d) DP2 (MCFT2)

The modified finite element model DP2(2), described in part 1 of the parametric study, predicted similar lateral strength and improved the prediction of the maximum lateral displacement relative to the DP2 model. Specifically, the MCFT2 model predicted the best response in terms of lateral strength, loading and reloading, and stiffness degradation. All the slip distortion and hysteretic models in DP2(2) predicted failure in the form of shear sliding near the top slab, which was preceded by crushing of concrete in the web. Predicted responses of DP2(2) models are presented in Fig. 4-38.

Table 4-17 summarizes the slip distortion and concrete hysteretic response models selected for the DP Walls.

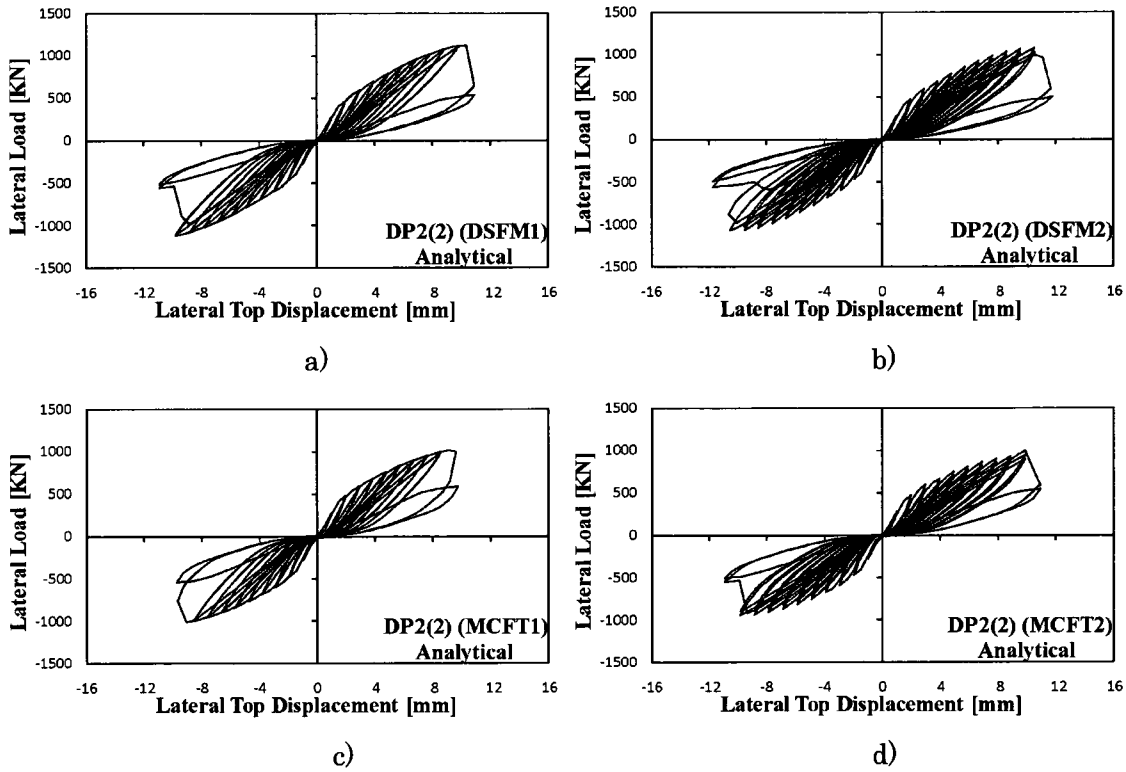

Fig. 4-38 Predicted Response for Wall DP2(2): a) DP2(2) (DSFM1); b) DP2(2) (DSFM2); c) DP2(2) (MCFT1); and d) DP2(2) (MCFT2)

Table 4-17 Selected Slip Distortion and Hysteretic Response Models for DP Walls

Shear Wall	Slip Distortion	Hysteretic Response
DP1	Not considered	Nonlinear with cyclic decay
DP2	Not considered	Nonlinear with cyclic decay
DP2(2)	Not considered	Nonlinear with cyclic decay

4.5 Conclusions

The parametric study was conducted to select the most suitable models for the reverse cyclic analysis of shear walls and was divided in two parts. Part 1 studied the compression models for concrete, while part 2 investigated the slip distortion and concrete hysteretic models.

Part 1 of the parametric study focused on the compression pre-peak and post-peak response of plain concrete, where three models were studied: Popovics normal strength concrete, Popovics high strength concrete, and Smith-Young. The compression models were initially selected according to recommendations of Palermo and Vecchio (2007), based on the cylinder strength of plain concrete. However, further analyses based on the calculated compression peak strength, after accounting for the compression softening, provided additional information.

Shear walls with confined boundary elements, specifically PCA Walls, were similarly predicted with the base curve and modified Park-Kent compression post-peak response. However, the latter slightly improved the response of Walls B3, B5, and B9. This trend indicates that the predicted responses of PCA Walls were independent of the compression post-peak response model, mostly due to the failure mechanism and amount of confining reinforcement. The predicted failure of the PCA Walls depended more on the damage of the unconfined concrete in the web than the damage of the confined concrete in the boundary elements.

The modified Park-Kent compression post-peak response better simulated the post-peak response of the DP Walls. The wide flanges of Walls DP1 and DP2 could introduce some confinement effect in the web near the flanges, which the base curve post-peak response model underestimated. The predicted sudden failure with the compression base curve post-peak response could be due to some overestimation of the stiffness of the flanges, which could induce excessive damage to the web elements. Three-dimensional analyses with more realistic prediction of the damage of the flanges would improve the responses of Walls DP1 and DP2.

Parametric Study

Part 2 of the parametric study focused on the slip distortion parameter and the concrete hysteretic response. Two types of analyses were performed to study the slip distortion parameter. The first analysis accounted for the slip distortion of elements by using the Vecchio-Lai model as in the DSFM, while the second analysis did not account for slip distortion of elements as in the MCFT. On the other hand, the concrete hysteretic response was studied using two hysteretic models: nonlinear with plastic offset, and nonlinear with decay (Palermo and Vecchio, 2007).

In general, the PCA Walls, which were governed by yielding of the vertical steel, were slightly better predicted with the Vecchio-Lai slip distortion model along with the nonlinear with cyclic decay model (DSFM2). The DSFM2 better predicted the damage of the walls, which led to closer predictions of the maximum lateral displacement in most of the walls (B1, B2, B3 and B9). However, the other models provided satisfactory predictions, specifically in terms of lateral strength and failure mode. Similarities in the mean results for all the models showed that shear walls governed by flexural mechanisms depend more on the constitutive models for the reinforcement than the concrete.

On the other hand, the DP Walls, which were governed by crushing of concrete with shear distortion, were better predicted without accounting for slip distortion along with the nonlinear with cyclic decay model (MCFT2). Predicted responses with MCFT models were in good agreement with that reported during testing, specifically in terms of lateral strength, loading and reloading, and stiffness degradation. However, the post-peak response was better predicted by the DSFM2 model. Further analyses with three-dimensional finite element models would be necessary to confirm the MCFT2 model as the most suitable model for the analysis of the DP Walls. The results presented for the DP Walls indicated that shear walls governed by shear mechanisms are more challenging to analyse and, therefore, need careful selection of the constitutive models that affect concrete behaviour.

Table 4-18 summarizes the final constitutive models for reinforced concrete selected in the parametric study for PC Walls and DP Walls.

Parametric Study

Table 4-18 Selected Constitutive Models for DP Walls and PCA Walls

Shear Wall	Compression Pre-peak	Compression Post-peak	Slip Distortion	Hysteretic Response
B1	Popovics NSC	Base Curve	Vecchio-Lai	Nonlinear with cyclic decay
B2	Popovics NSC	Base Curve	Vecchio-Lai	Nonlinear with cyclic decay
B3	Popovics NSC	Modified Park-Kent	Vecchio-Lai	Nonlinear with cyclic decay
B5	Popovics NSC	Modified Park-Kent	Vecchio-Lai	Nonlinear with cyclic decay
B9	Popovics HSC	Modified Park-Kent	Vecchio-Lai	Nonlinear with cyclic decay
B11	Popovics NSC	Base Curve	Vecchio-Lai	Nonlinear with plastic offset
DP1	Smith-Young	Mod. Park-Kent	Not considered	Nonlinear with cyclic decay
DP2	Smith-Young	Mod. Park-Kent	Not considered	Nonlinear with cyclic decay
DP2(2)	Smith-Young	Mod. Park-Kent	Not considered	Nonlinear with cyclic decay

Chapter 5

5 Nonlinear Analysis of Repaired/Retrofitted Shear Walls

5.1 Introduction

This chapter presents nonlinear analysis of repaired and/or retrofitted shear walls using the finite element method (FEM) program VecTor2. The analyses were based on information available in the literature: geometry, materials and load history; however, some assumptions were required in those cases where the information was insufficient. For the shear walls where repairing was instituted, results of the analysis of the original undamaged walls are included. The success of the analyses of repaired and retrofitted shear walls depends on the ability of the analysis tool to capture the response of the original walls, particularly the level of damage and the failure mode before repair.

The repair and retrofitting techniques (summarized in Table 5-1) include replacement of concrete for Walls B5/B5R and B9/B9R (Fiorato et al., 1983), Walls DP1/DP1R (Vecchio et al., 2002), and Walls LSW3/RLSW3 (Antoniades et al., 2003); addition of

steel reinforcing bars for Walls B11/B11R (Fiorato et al., 1983); external bonding of steel plates for Walls IC-SW24/IC-SWR24, IC-SW32, and IC-SW35/IC-SWR35 (Elnashai and Salama, 1992; Elnashai and Pinho, 1998); addition of unbonded steel rods and plates with a slip-delay mechanism for Walls IC-SW31 and IC-SW34 (Elnashai and Salama, 1992; Elnashai and Pinho, 1998); and external bonding of FRP sheets for Walls LSW1/FRPLSW1 and MSW1/FRPMSW1 (Antoniades et al., 2003, 2005). Other procedures such as local replacement of concrete for Walls SW31/SW31R, SW32/SW32R, and SW33/SW33R (Lefas and Kotsovos, 1990); and bolting of external steel plates for Walls W11/W11RP and W11R (Taghdi et al., 2000) were also simulated. The walls reported by Elnashai and Salama (1992) and Elnashai and Pinho (1998) are denoted with the subscript IC- to avoid confusion with the walls reported by Lefas and Kotsovos, (1990).

Table 5-1 Repair and Retrofitting Techniques

Shear Wall	Technique
B5/B5R	Replacement of Concrete (concrete in the web)
B9/B9R	Replacement of Concrete (concrete in the web)
B11/B11R	Addition of Reinforcing Bars (diagonal bars)
DP1/DP1R	Replacement of Concrete (concrete in the web)
IC-SW24/IC-SWR24	External Bonding of Steel Plates (staggered horizontal plates)
IC-SW31	Addition of Unbonded Steel Rods with Delay Mechanism
IC-SW32	External Bonding of Steel Plates (u-shaped plates)
IC-SW34	Addition of Unbonded Steel Plates with Delay Mechanism
IC-SW35/IC-SWR35	External Bonding of Steel Plates (vertical plates)
SW31/SW31R	Local Concrete Replacement (lower portion in boundary element)
SW32/SW32R	Local Concrete Replacement (lower portion in boundary element)
SW33/SW33R	Local Concrete Replacement (lower portion in boundary element)
LSW1/FRPLSW1	External Bonding of FRP Sheets (horizontal and vertical FRP) and Concrete Replacement (lower portion of the web)
LSW3/RLSW3	Concrete Replacement (lower portion of the web)
MSW1/FRPMSW1	External Bonding of FRP Sheets (horizontal and vertical FRP) and Concrete Replacement (lower portion of the web)
W11/W11RP	Bolting of Steel Plates (vertical plates; repair)
W11R	Bolting of Steel Plates (vertical and diagonal plates; retrofitting)

5.2 Modelling of Materials

Based on previous research conducted by Palermo and Vecchio (2007) and results from the parametric study presented in Chapter 4, the following criterion was adopted for the selection of the compression pre-peak response of concrete according to the cylinder concrete strength. For low-strength concrete, $f'c$ lower than 22 MPa, the Smith-Young model was selected. For concrete with strength ranging from 22 MPa to 45 MPa, the Popovics normal-strength model was selected, and for high strength concrete, $f'c$ greater than 45 MPa, the Popovics high-strength model was selected. The latter is a modification of the Popovics normal-strength model and accounts for a greater linear pre-peak response and more brittle post-peak response. For the post-peak response, the base curve used for the pre-peak response was selected and demonstrated satisfactory agreement with the experimental responses. However, the modified Park-Kent model was utilized for the post-peak for those walls in which an increase in the concrete compressive strength due to confinement was observed. Table 5-2 provides the properties of the materials used in the repaired and/or retrofitted shear walls. Concrete cylinder strength of Walls IC-SW24/IC-SWR24, IC-SW31, IC-SW32, IC-SW34, and IC-SW35/IC-SWR35 was assumed as 77% of the reported cubic strength based on a correlation between cube and cylinder strength presented elsewhere (Lefas, 1988). Table 5-3 lists the compression pre-peak and post-peak response models used for modelling the repaired and/or retrofitted walls.

Table 5-2 Material Properties of Repaired/Retrofitted Walls

Wall	Zone	Concrete	Reinforcement					
			Horizontal		Vertical		Confinement	
		Old/New $f'c$ [MPa]	ρ_h [%]	fy [MPa]	ρ_v [%]	fy [MPa]	ρ_{cf} [%]	fy [MPa]
B5/B5R	Web	45.3/42.8	0.63	502	0.29	502	—	—
	Boundary	45.3/—	1.35/0.33	502	3.67	444	1.35/0.13	502
B9/B9R	Web	44/51.7	0.63	460	0.29	460	—	—
	Boundary	44/—	1.35/0.33	460	3.67	429	1.35/0.13	460
B11/B11R*	Web	53.8/42.6	0.63	501	0.29	501	—	—
	Boundary	53.8/—	1.35/0.33	501	3.67	429	1.35/0.13	501
DP1/DP1R	Web	21.7/44	0.74	605	0.79	605	—	—
	Flanges	21.7/—	0.58	605	0.38	605	—	—
IC-SW24/	Web	37.9	0.56	400	0.63	545	—	—
IC-SWR24**	Boundary	37.9	2.79/0.56	400	5.10	545	1.12/0.22	400
IC-SW31***	Web	37.9	1.09	450	0.63	545	—	—
	Boundary	37.9	2.18/1.09	450	2.23	450	0.87/0.44	450
IC-SW32†	Web	37.9	1.09	450	0.63	545	—	—
	Boundary	37.9	1.09	450	2.23	450	0.44	450
IC-SW34††	Web	37.9	1.09	450	0.63	545	—	—
	Boundary	37.9	2.18/1.09	450	2.23	450	0.87/0.44	450
IC-SW35/	Web	37.3	1.09	450	2.52/0.63	545	—	—
IC-SWR35†††	Boundary	37.3	2.18/1.09	450	3.49/2.23	450	0.87/0.44	450
MSW1/	Web	26.1/75	0.57	585	0.57	585	0.06	575
FRPMSW1‡	Boundary	26.1/75	0.66	575	1.68	585	0.55	575
LSW1/	Web	22.2/75	0.57	585	0.57	585	0.06	575
FRPLSW1‡	Boundary	22.2/75	1.03	575	1.68	585	0.64	575
LSW3/	Web	23.9/75	0.28	575	0.28	575	0.06	575
RLSW3	Boundary	23.9/75	1.03	575	1.26	585	0.86	575
SW31/	Web	27.1/—	0.36	520	1.50	470	—	—
SW31R	Boundary	27.1/26.9	0.30	420	3.30	470	0.13	420
SW32/	Web	41.6/—	0.36	520	1.50	470	—	—
SW32R	Boundary	41.6/29.4	0.30	420	3.30	470	0.13	420
SW33/	Web	37/—	0.36	520	1.50	470	—	—
SW33R	Boundary	37/29.3	0.30	420	3.30	470	0.13	420
W11/W11RP‡‡	Web	29	0.24	480	0.24	480	—	—
	Boundary	—	—	—	—	—	—	—

Wall	Zone	Concrete	Reinforcement					
			Horizontal		Vertical		Confinement	
		Old/New $f'c$ [MPa]	ρ_h [%]	fy [MPa]	ρ_v [%]	fy [MPa]	ρ_{cf} [%]	fy [MPa]
W11R‡‡	Web	29	0.24	480	0.24	480	—	—
	Boundary	—	—	—	—	—	—	—

* Two reinforcing bars No. 5 at 45 deg. in each direction added in the lower 90 cm, fy= 501 MPa.

** Nine staggered horizontal plates (78 x 3.6 mm), fy= 275 MPa; f'c taken as 0.77 fcub.

*** Three 6-mm steel rods in each edge of the wall, fy= 545 MPa; f'c taken as 0.77 fcub.

† Six U-shaped plates (480 x 120 x 3.6 mm), fy= 275 MPa; f'c taken as 0.77 fcub.

†† One 1200 x 50 x 3.6 mm steel plate in each edge of the wall, fy= 275 MPa; f'c taken as 0.77 fcub.

††† Four plates (1100 x 190 x 3.6 mm), fy= 275 MPa; f'c taken as 0.77 fcub.

‡ Three layers tf=0.45 mm vertical CFRP, fu= 1100 MPa; one layers tf=0.60 mm horizontal GFRP, fu= 550 MPa.

‡‡ Two vertical steel plates (160 x 4.76 mm) near each end face of the wall.

‡‡‡ Two diagonal steel plates (220 x 3.81 mm) in each side, fy= 227 MPa; two vertical steel plates (80 x 3.81 mm) in each side, fy= 248 MPa.

Table 5-3 Compression Response Models Used for Modelling the Repaired and/or Retrofitted Walls

	Pre-peak Response	Post-peak Response
B5/B5R	Popovics (NSC)	Modified Park-Kent
B9/B9R	Popovics (HSC)	Modified Park-Kent
B11/B11R	Popovics (NSC)	Modified Park-Kent
DP1/DP1R	Smith-Young	Modified Park-Kent
IC-SW24/IC-SWR24	Popovics (NSC)	Base Curve
IC-SW31	Popovics (NSC)	Modified Park-Kent
IC-SW32	Popovics (NSC)	Modified Park-Kent
IC-SW34	Popovics (NSC)	Modified Park-Kent
IC-SW35/IC-SWR35	Popovics (NSC)	Base Curve
MSW1/FRPMSW1	Popovics (NSC)/Popovics (HSC)	Base Curve
LSW1/FRPLSW1	Popovics (NSC)/Popovics (HSC)	Base Curve
LSW3/RLSW3	Popovics (NSC)/Popovics (HSC)	Base Curve
SW31/SW31R	Popovics (NSC)	Base Curve
SW32/SW32R	Popovics (NSC)	Base Curve
SW33/SW33R	Popovics (NSC)	Base Curve
W11/W11RP	Smith-Young	Base Curve
W11R	Smith-Young	Base Curve

Other models to account for secondary effects were selected as default: Vecchio's 1992-A model for compression softening; modified Bentz tension stiffening model for tension stiffening effect; linear model for tension softening; Kupfer/Richard model for confined strength effect; modified Kupfer for lateral expansion or dilatation of concrete; Mohr-Coulomb stress model for cracking criterion; Vecchio-Collins 1986 for crack slip check; a limit of 20% of the aggregate size for crack width check; Vecchio-Lai for slip distortion; and Palermo 2002 with decay for concrete hysteretic response, except for Wall B11. The nonlinear with plastic offset hysteretic model was selected for Wall B11.

Three materials were assigned to the reinforcement depending on the type of reinforcement: ductile steel reinforcement, tension only reinforcement and externally bonded FRP reinforcement. Ductile steel reinforcement was used in cases where the internal steel reinforcement was modelled as discrete reinforcement and where external steel plates were bonded as part of the repair or retrofitting process. Tension only truss bars were implemented in the modelling of externally unbonded rods and plates. Finally, the externally bonded FRP was used to model FRP retrofit of walls. Conversely, for the latter, the tension only model can be used; however, crack stresses are more accurately calculated when the externally bonded FRP model is used. The constitutive models for the reinforcement were selected as default: the Seckin model was assigned to capture the hysteretic response; the Bauschinger effect was selected to capture the unloading and reloading response; and the Tassio crack slip model was selected to capture the dowel action. Buckling of reinforcement was not simulated since it requires the use of link-bond elements between truss bar elements and concrete elements. Although such phenomenon can be modelled, it significantly increases the number of elements resulting in increased computational time. The analyses presented herein demonstrate accurate simulations for those walls that experienced buckling during testing; therefore, ignoring buckling did not sacrifice the accuracy of the analyses.

To simulate the effect of bond between external reinforcement (steel and FRP) and concrete, a two node non-dimensional link-bond element was used. The link-bond

element is connected to the truss bar, which represents the external bonded element, and the concrete element. The bond-slip behaviour of the externally bonded steel and FRP plates/sheets was modelled with a linear elastic ascending response, followed by a linear post-peak descending branch (Fig. 5-1) based on the fracture energy method (Sato and Vecchio, 2003). The parameters in this model include the maximum bond stress, U_{max}, and corresponding slip, S_{max}, which constitutes the termination of the ascending branch. The post-peak region begins at the maximum bond stress, U_{max}, and corresponding slip and ends at the slip corresponding to zero bond stress, S_{ult}. In addition to the selection of the relationship for bond-slip, the Eligehausen model was used to capture the hysteretic response of the element. The formulation for the bond stress-slip relationship is based on research on bonded FRP; however, its application for bonded steel plates provided satisfactory analytical results.

$$U_{\max} = (54 f'_c)^{0.19} \tag{5-1}$$

$$G_f = (U_{\max}/6.6)^2 \tag{5-2}$$

$$S_{\max} = 0.057 G_f^{0.5} \tag{5-3}$$

$$S_{ult} = 2G_f / U_{\max} \tag{5-4}$$

Where G_f is the fracture energy of the concrete, and f'_c is the concrete cylinder compressive strength.

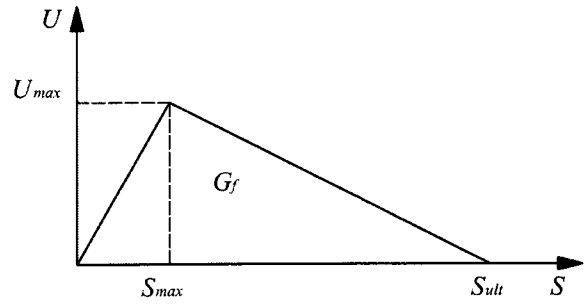

Bond Stress-Slip relationship

Fig. 5-1 Bond Stress-Slip Relationship for Externally Bonded Steel and FRP Plates/Sheets

5.3 Finite Element Meshing

The finite element (FE) mesh of the shear walls consisted of a minimum of 13 rectangular plane stress elements in the short direction, including the boundary elements, and a maximum aspect ratio of 1.5, unless geometric constrains dictated otherwise. In general, the internal reinforcement was modelled as smeared in the concrete rectangular elements. Full replacement of concrete repair method was modelled with a double mesh; permitting the original material to be disengaged and the new repair material to become engaged after damage. External reinforcement used in the repair/retrofitting interventions, including steel plates, steel rods and FRP sheets, were modelled as either perfectly bonded or link-bonded truss elements depending on the retrofitting technique implemented. Meshing of the foundation and top loading beam of the shear walls conformed to the mesh of the web portion of the walls. Nodes at the bottom of the foundation were restrained in the X and Y directions to simulate the fixed support condition of the shear wall.

The mesh used to model the shear walls was sufficiently fine to ensure accurate simulation of the strain and stress gradients across the wall length. The results presented herein corroborate the meshing criterion described by Palermo and Vecchio (2007) in which 14 to 16 elements in the short direction of a shear wall were recommended. Triangular constant strain elements were used only in regions where it was necessary due to geometric constraints.

5.4 Replacement of Concrete

5.4.1 Walls B5/B5R and B9/B9R

Testing

Walls B5/B5R and B9/B9R were tested by Fiorato et al. (1983) as part of an experimental program of slender shear walls. The walls had a barbell section with high-to-length ratio of 2.4. Dimensions of the walls were: 4570 mm in height, 1910 mm

in length, and 102 mm in thickness (Fig. 5-2). Boundary columns were 305 mm x 305 mm. Furthermore, the walls were provided with stiff top and foundation beams. Material properties of the walls are listed in Table 5-2. Wall B5 was repaired (Wall B5R) by removing the concrete in the lower portion of the web up to 2600 mm and replacing it with high strength concrete. The thickness of the web in the repaired zone was maintained at 102 mm. Wall B9 was repaired (Wall B9R) following the same procedure as Wall B5R; however, the thickness of the web was increased to 152 mm. In the boundary columns where spalling of concrete was observed, roughening, removing of loose particles and subsequent hand-packing of a sand-cement mortar was applied. The reinforcement in the original walls was preserved and no new reinforcement was added. The repair was limited to the damaged concrete and did not include retrofitting.

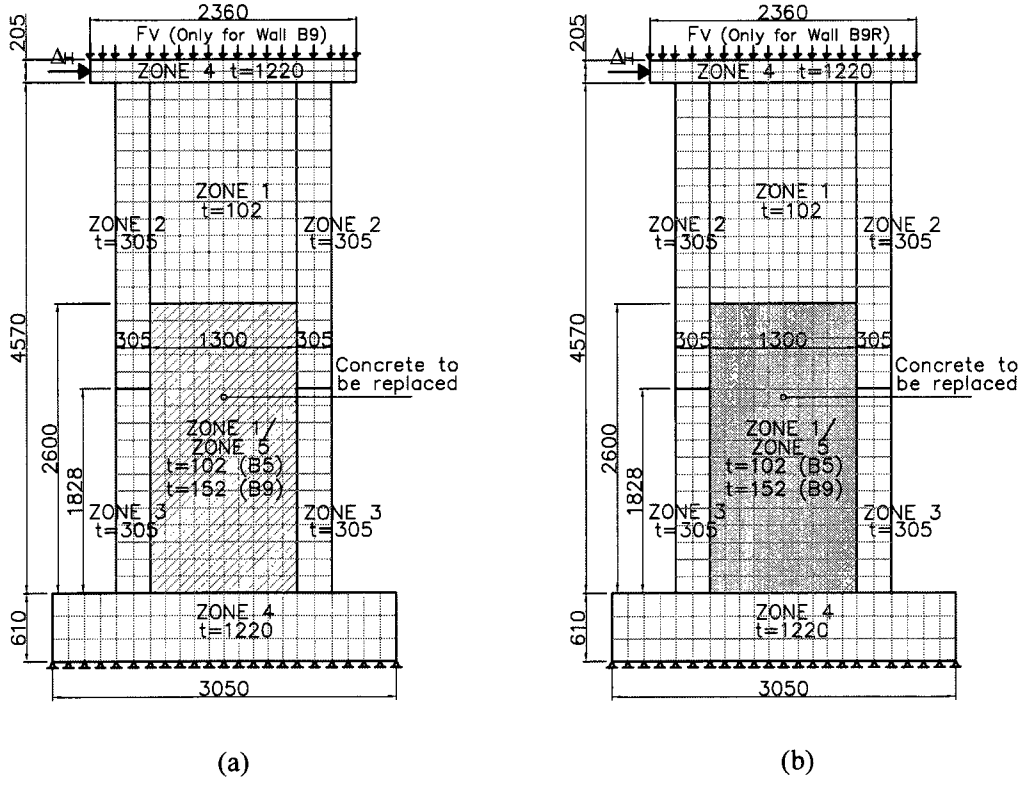

Fig. 5-2 Finite Element Mesh of Walls: (a) B5 and B9; (b) B5R and B9R. All Dimensions in mm

Modelling

The FE model for Walls B5/B5R and B9/B9R consisted of five homogeneous concrete zones: the first corresponding to the web; the second and third corresponding to the upper and lower portion of the boundary elements (the latter with more transverse and confinement reinforcement); the fourth corresponding to the foundation and top beams, which were heavily reinforced to ensure stiff elements; and the fifth zone corresponded to the replacement of concrete in the lower portion of the wall (Fig. 5-2). All the vertical, horizontal and confinement reinforcement was smeared in the concrete zones. The mesh of only the walls consisted of 14 by 30 rectangular elements in the horizontal and vertical directions, respectively.

Concrete zones one to four were engaged; while concrete zone five, representing the repaired concrete, was disengaged prior to the analysis of the original wall. Simulation of the repair procedure involved engaging the concrete elements in zone five, and disengaging the concrete elements in zone one sharing the same position. The simulation of the repair did not include the concrete hand-packing of the slightly damaged boundary elements.

Analysis

Loading of original Wall B5 consisted of reverse cyclic lateral displacements in increments of approximately 25 mm applied along the top beam. Three repetitions were imposed at each displacement level to 126 mm. The loading did not include axial loads. Yielding occurred during the first repetition to 50 mm of displacement. The wall reached a maximum lateral load of 762 kN corresponding to a displacement of 126 mm. As illustrated in Fig. 5-3, the recorded response of the original wall demonstrates wide hysteretic cycles with some degree of pinching, which allowed the wall to dissipate a considerable amount of energy. Figure 5-3 also depicts the stiffness degradation between repetitions to the same lateral displacement. Final failure due to crushing of concrete occurred during the third excursion to 126 mm of displacement in the positive direction. Damage of the wall was mostly localized in the web portion with slight damage in the boundary columns.

The predicted hysteretic response of Wall B5, displayed in Fig. 5-4, was in good agreement with the reported response shown in Fig. 5-3. The predicted response demonstrated slightly less strength degradation at the end of the analysis compared to that recorded. Unloading and reloading of the analytical response was similar to the experimental response, and captured behavioural aspects such as initial stiffness, stiffness degradation and energy dissipation. Pinching in the analytical response was slightly less pronounced than that reported in the experimental response. The predicted lateral load capacity of 703 kN underestimated the observed lateral strength by approximately 8%. The corresponding displacement of 126 mm; and therefore, the ductility was in excellent agreement with the observed displacement. The predicted failure closely matched the observations, which involved crushing of concrete in the web during the third excursion to 126 mm of displacement. The analysis of Wall B5 was terminated at the end of the third repetition to 126 mm.

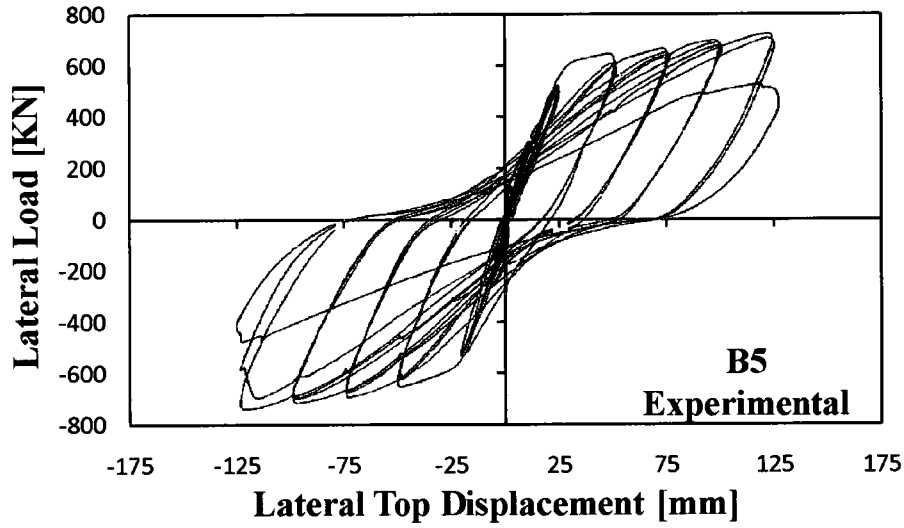

Fig. 5-3 Experimental Load-Deformation Response for Wall B5 (Modified from Fiorato et al., 1983)

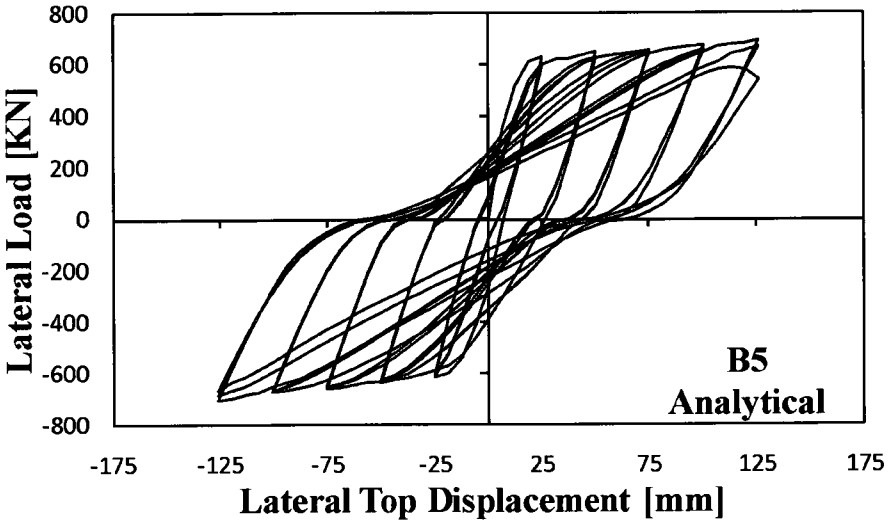

Fig. 5-4 Analytical Load-Deformation Response for Wall B5

After repair, Wall B5R was subjected to the same loading pattern as the original wall. Yielding of the repaired wall occurred approximately at a lateral displacement of 60 mm and the ultimate displacement was 152 mm, which corresponded with extensive crushing of concrete in the web portion of the wall. By replacing the concrete, the lateral strength capacity was restored, reaching a maximum capacity of 746 kN (Fig. 5-5). However, the wall was not capable of restoring its initial stiffness, and the response was more rounded with less energy dissipation than the original wall. Pinching of the repaired wall was similar to the original wall.

Strong correlation in the hysteretic response of the analysis of the repaired wall, Wall B5R, with respect to the recorded behaviour is evident in Fig. 5-6. The predicted response presented a slightly higher initial stiffness than observed. Stiffness and strength degradation were well captured. The pinching effect was well predicted, particularly when reloading from negative displacement; the analysis predicted slightly less pinching when reloading from positive displacement. The analytical maximum lateral strength was approximately 685 kN, which underestimated the observed lateral strength by approximately 8%. The corresponding displacement of 151 mm was in excellent agreement with the recorded displacement, and corresponded to the displacement level where failure ultimately occurred. The failure mode was well

simulated, which was characterized by crushing of concrete in the web. The predicted wide hysteretic loops in Fig. 5-6 compared very well with the recorded hysteretic loops in Fig. 5-5; therefore, the energy dissipation of the repaired wall was well captured.

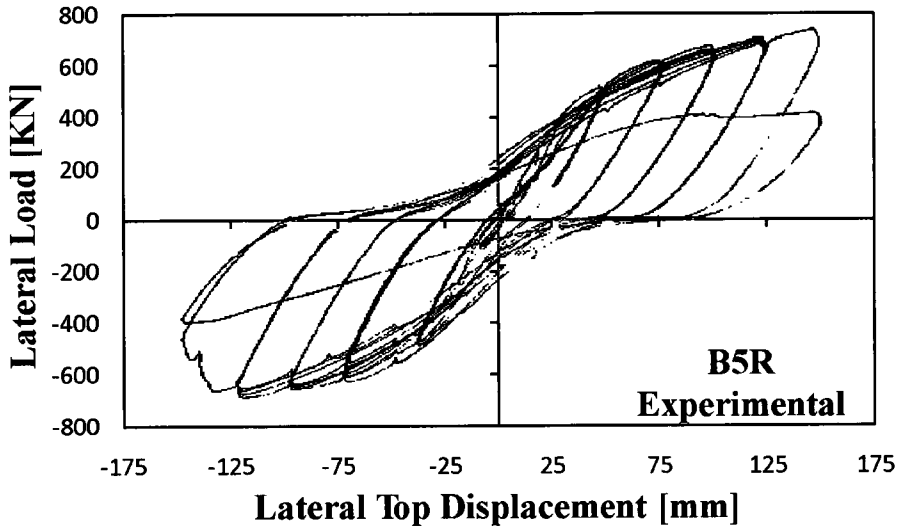

Fig. 5-5 Experimental Load-Deformation Response for Wall B5R (Modified from Fiorato et al., 1983)

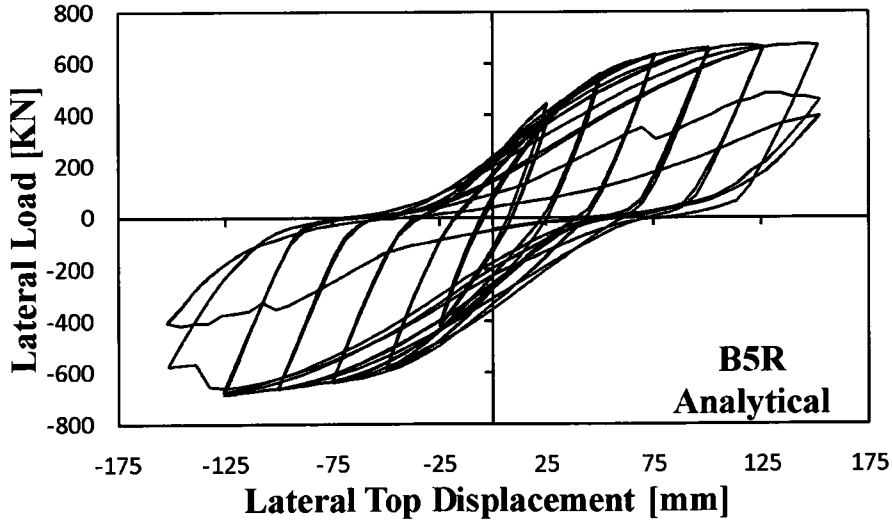

Fig. 5-6 Analytical Load-Deformation Response for Wall B5R

Original Wall B9 was loaded with five alternating small and long single (one repetition) displacements to 13 mm, 133 mm, 38 mm, 121 mm and 108 mm. In

addition, the wall was subjected to axial loading of 3.76 MPa. Wall B9 responded with wide hysteretic cycles and little pinching as illustrated in Fig. 5-7, reflecting ductile behaviour with high energy dissipation capacity. Yielding occurred during the second cycle, corresponding to a lateral displacement of 132 mm. During this cycle, the wall reached its maximum strength capacity of 977 kN. Thereafter, the wall sustained stiffness and strength degradation until failure, which was recorded in the negative direction of the cycle to 127 mm. Failure was reported as widespread crushing of concrete in the web portion of the wall. Slight damage was also observed in the boundary columns.

The predicted response of the original Wall B9 (Fig. 5-8) closely matched the recorded response. The initial stiffness was slightly overestimated in the positive direction; however, it was accurately captured in the negative direction. Yield strength of 811 kN was predicted at 25 mm during the cycle to 132 mm and corresponded to that recorded during testing. The analysis predicted maximum strength of 958 kN at a displacement of 132 mm, which was in excellent agreement with that reported. Unloading and reloading of the hysteretic loops were well predicted; therefore, the stiffness degradation, degree of pinching, and energy dissipation were adequately captured. The final reverse cycle to 120 mm captured the failure mechanisms, which involved crushing of concrete in the web with high shear distortion. The analysis of Wall B9 was terminated at the end of the cycle to 120 mm.

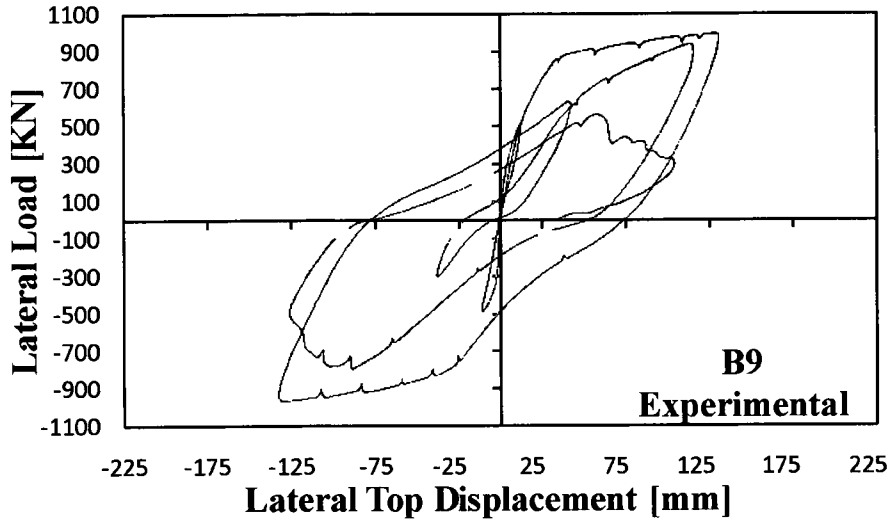

Fig. 5-7 Experimental Load-Deformation Response for Wall B9 (Modified from Fiorato et al., 1983)

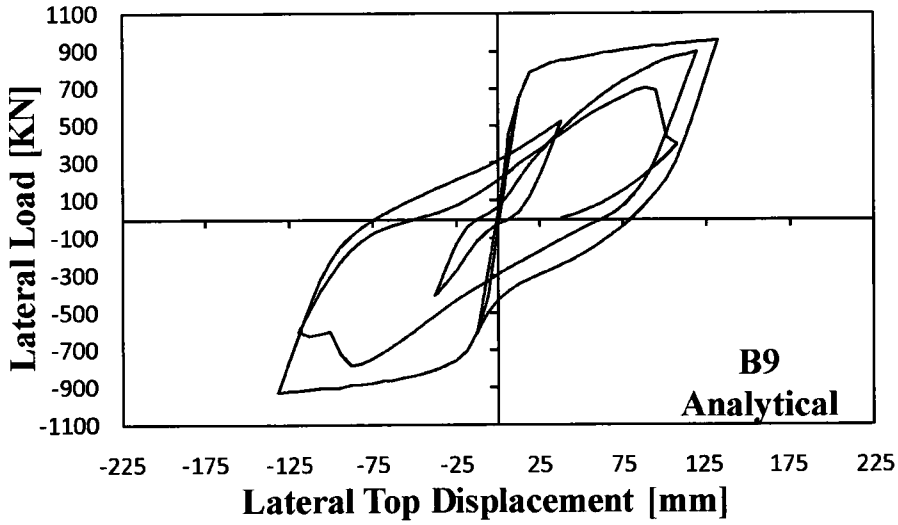

Fig. 5-8 Analytical Load-Deformation Response for Wall B9

Repaired Wall B9R was subjected to a similar loading regime as the original wall; however, the wall was cycled further owing to the improved ductility. Axial loading was maintained, but it was modified to 3.10 MPa. The initial stiffness of Wall B9R was lower than that reported for the original wall, resulting in a more rounded response as evident in Fig. 5-9. Unloading and reloading of the initial cycles corresponded to that reported in the final cycles of the original wall prior failure. The wall recovered its

strength of 977 kN during loading to 133 mm. Subsequent cycles up to 184 mm displayed marginal stiffness and strength degradation. The wall failed due to crushing of the concrete in the web at 184 mm of displacement. Pinching of the repaired wall was similar to the original wall; however, the repaired wall was capable of dissipating more energy owing to the improved ductility.

The analytical response of the repaired shear wall, Wall B9R, (Fig. 5-10) compared very well to the rounded experimental response, Fig. 5-9, specifically in terms of strength and ductility. Other behavioural aspects such as unloading and reloading of the hysteretic cycles, pinching phenomenon and energy dissipation were adequately captured. The analysis predicted peak strength of 951 kN, which was similar to that observed, and was noted during loading to the first repetition to 169 mm. However, the predicted peak strength was reached at a higher lateral displacement. The analytical maximum lateral displacement of 170 mm underestimated that recorded during testing by 9% and 4% in the positive and negative directions, respectively. The analysis captured crushing of concrete in the web with significant shear distortion, specifically near the interface of the web and boundary columns.

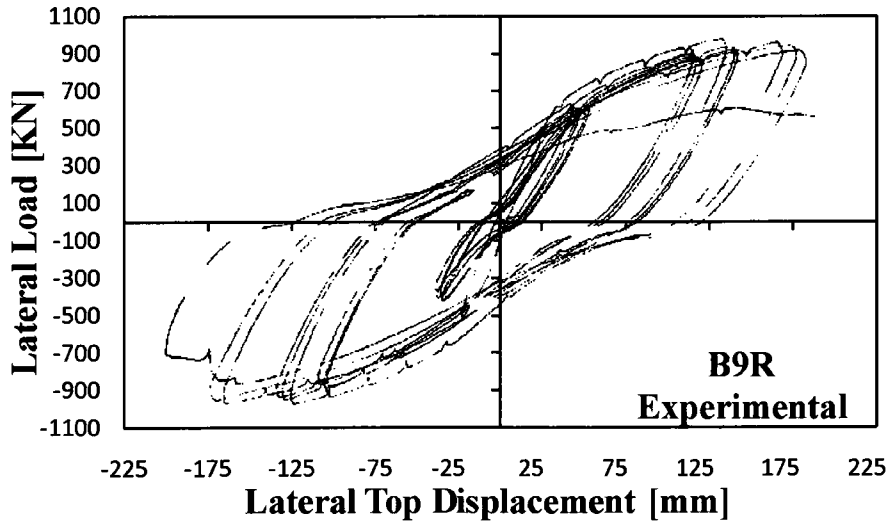

Fig. 5-9 Experimental Load-Deformation Response for Wall B9R (Modified from Fiorato et al., 1983)

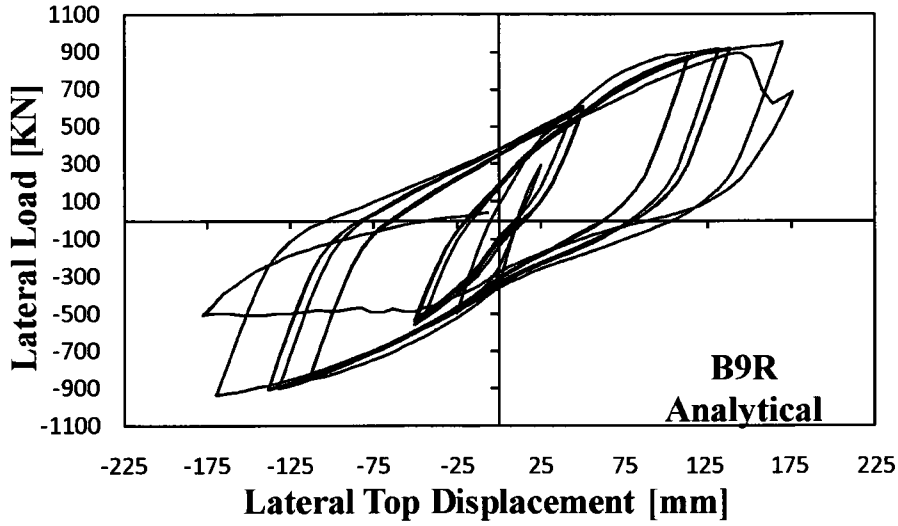

Fig. 5-10 Analytical Load-Deformation Response for Wall B9R

The marginal discrepancy in strength in both the original walls, Wall B5 and Wall B9, and repaired walls, Wall B5R and Wall B9R, can be attributed to the strain hardening modulus assumed in the analysis. Improved results could be obtained by increasing the slope of the strain hardening branch; however, this information was not clear in the literature.

5.4.2 Walls DP1/DP1R

Testing

Wall DP1R (Vecchio et al., 2002), referred as DP1 (Palermo and Vecchio, 2002) before repair, was tested as part of an experimental investigation on repair of squat concrete shear walls subjected to reverse cyclic loads. The repair consisted of replacing damage concrete and did not include retrofitting. Walls DP1/DP1R were 2020 mm high and 2885 mm long, with web thickness of 75 mm as illustrated in Fig. 5-11. The walls contained end flanges measuring 3045 mm in width. The thickness of the flanges was 95 mm. The walls were provided with stiff foundation and top slabs; the former to

allow clamping of the wall to the strong floor in the laboratory, and the latter to transfer the load from the actuators to the web wall.

At the end of testing of the original wall, the concrete in the web was removed and replaced. The vertical and horizontal reinforcement was left intact since no damage was observed and yielding was not evident. Vecchio et al. (2002) reported no significant damage in the flanges; therefore, no treatment of these elements was necessary. The strength of the new concrete was approximately two times the strength of the original concrete in the web. The new concrete was applied up to a height of 180 mm from the soffit of the top slab, and a non-shrinkage high strength epoxy was used in the top 180 mm of the web. Once repaired, the wall was designated DP1R and was tested following the same protocol used for the undamaged wall.

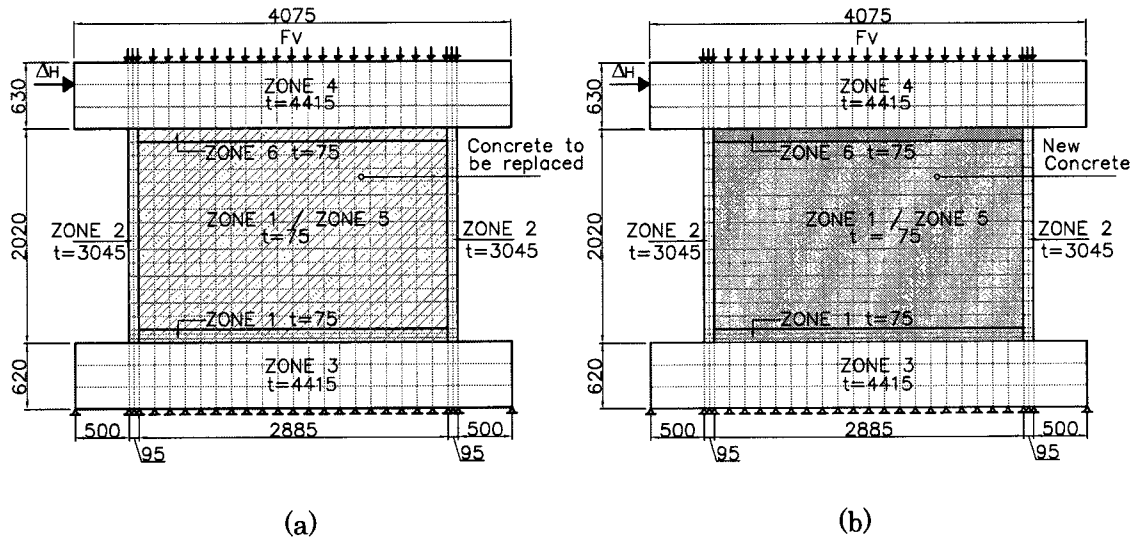

Fig. 5-11. Finite Element Mesh of Walls: (a) DP1; (b) DP1R. All Dimensions in mm

Modelling

The modelling of Walls DP1/DP1R required definition of six concrete zones with smeared reinforcement; four corresponding to the original wall including the web, flanges, foundation slab and top slab; and two to model the new concrete in web and epoxy grout in the top 180 mm of the web. The foundation slab, as well as the top slab, was modelled with elements containing high steel ratios to simulate rigid members. In

total, 888 rectangular elements were used in the FE mesh, including the additional 300 double-meshed elements in the web. The mesh, without accounting for the slabs, had 24 elements horizontally and 18 elements vertically. The bottom three horizontal rows of the web and flanges were smaller in comparison with the rest of the wall in order to better capture the failure mode. Figure 5-11 depicts the meshing used to model Walls DP1/DP1R.

Prior to analysis of the original wall, zones one to four, corresponding to the original concrete, were engaged, while zones five and six, corresponding to the repaired concrete, were disengaged. After analysis of the original wall, elements in zones five and six were engaged, while elements in zone 1 located in the same position as zones five and six were disengaged.

Analysis

A total axial load of 1200 kN, including the self weight of the top slab was applied during testing to the original wall, Wall DP1. The reverse cyclic lateral load consisted of displacement increments of 1 mm, with two repetitions per increment.

The observed response of DP1 included maximum peak strength of 1298 kN at 11 mm of displacement, and a post-peak decay to 545 kN at 15 mm displacement at which point the test was terminated. Failure consisted of crushing of concrete localized in six vertical planes in the web. The response was governed by the concrete behaviour, as indicated by the pinched load-displacement response and rounded envelope of the load-displacement response (Fig. 5-12). Unloading and reloading of the hysteretic cycles exhibited stiffness and strength degradation, which was more evident during the post-peak response. No yielding of the steel was recorded; therefore, the wall behaved predominantly in shear. Furthermore, the narrow hysteretic loops with low energy dissipation capacity reflected the non-ductile behaviour of the wall.

Comparison between Fig. 5-13 and Fig. 5-12 indicates good agreement between the analytical and experimental response of the original wall, Wall DP1. Although the analytical response was slightly more rounded, it showed adequate prediction of behavioural characteristics such as initial stiffness, lateral strength and energy

dissipation. Predicted lateral load strength of 1297 kN at 10 mm matched the observed lateral strength of 1298 kN at 11 mm. The predicted post-peak response presented similar strength and stiffness degradation as the observed response, and a lateral load of approximately 900 kN was predicted at the end of the analysis. Unloading, reloading and pinching of the hysteretic cycles were satisfactory predicted, and despite some differences in the post-peak response, similar low energy dissipation was captured. Failure of the FE model initiated with crushing of concrete in two vertical planes in the web wall near the flanges. This was followed by concrete crushing of additional elements in the web, leading to a horizontal failure plane at the bottom of the web. This horizontal failure plane promoted shear sliding of the web. The analysis captured the crushing of the concrete in the web; however, it overestimated the shear distortion that led to the final failure of the wall.

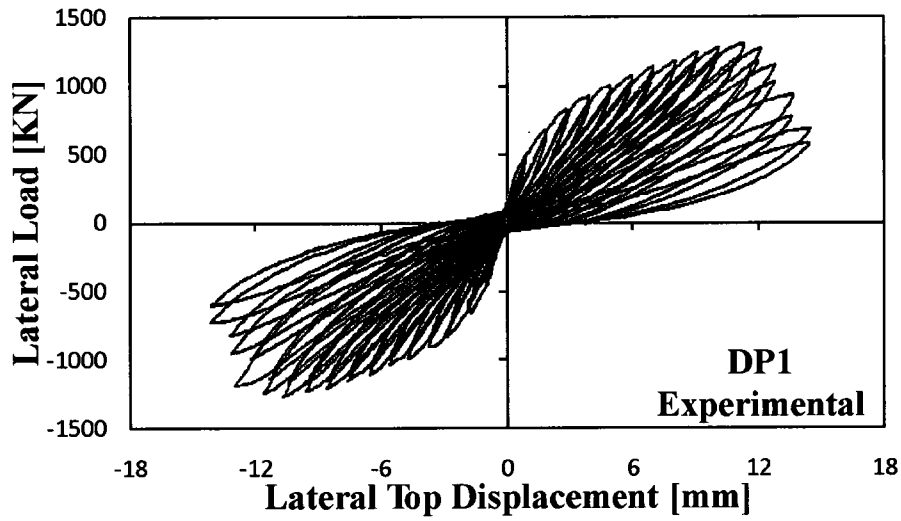

Fig. 5-12 Experimental Load-Deformation Response for Wall DP1 (Modified from Vecchio et al., 2002)

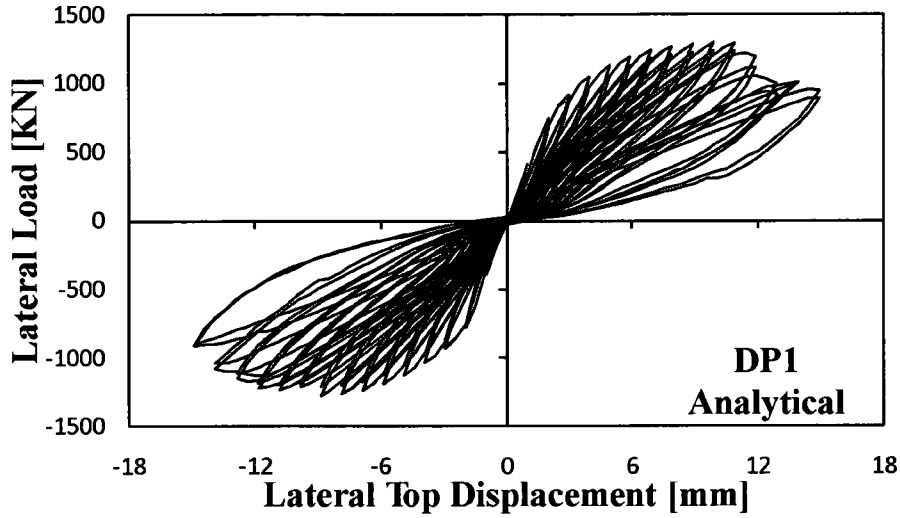

Fig. 5-13 Analytical Load-Deformation Response for Wall DP1

The behaviour of the repaired wall, Wall DP1R, was similar to the original wall and 92% of the lateral load-carrying capacity was restored. Maximum strength of 1192 kN was attained during the first repetition to 11 mm of displacement. Unloading and reloading of the hysteretic cycles displayed the same response characteristics as the original wall (Fig. 5-14). During the post-peak, the wall experienced significant stiffness and strength degradation resulting in a lateral load capacity of 350 kN at 17 mm displacement. The behaviour of the repaired wall was controlled by shear; post-peak decay, pinching, and energy dissipation capacity were similar to that displayed in the original wall. The repaired wall failed by shear sliding along the base of the web, coupled with punching of the web through the flanges.

The analysis of the repaired wall, Wall DP1R, did not achieve the same success as the analysis of the original wall. The predicted response (Fig. 5-15) was stiffer, stronger, and less ductile than the observed response (Fig. 5-14). The strength was overestimated approximately 20% (1426 kN), and corresponded to a lateral displacement of 5 mm. Maximum lateral displacement of 11 mm at which final failure took place was lower than observed in testing. Overestimation of the stiffness was significant in the first 9 mm of displacement. However, during cycles to 10 mm and 11 mm of displacement, unloading and reloading of the hysteretic loops were similar to

that reported. Both experimental and analytical hysteretic responses presented the same degree of pinching as a consequence of the non-ductile behaviour of the wall. At 11 mm when damage of the wall was predicted, the analytical energy dissipation capacity was higher than reported. The stiffer analytical response is attributed to the two-dimensional model of a three-dimensional wall with wide flanges. The entire flanges were lumped at the end of the web wall leading to an overestimation of strength and stiffness contribution of the flanges. Furthermore, the predicted damage in the flanges of the original wall, Wall DP1, was underestimated, leading to an overestimated initial stiffness of the repaired wall. Although the strength was overestimated and the displacement capacity underestimated, the failure mechanism, which was initiated by shear sliding between the web wall and base foundation at 11 mm of displacement, was well simulated

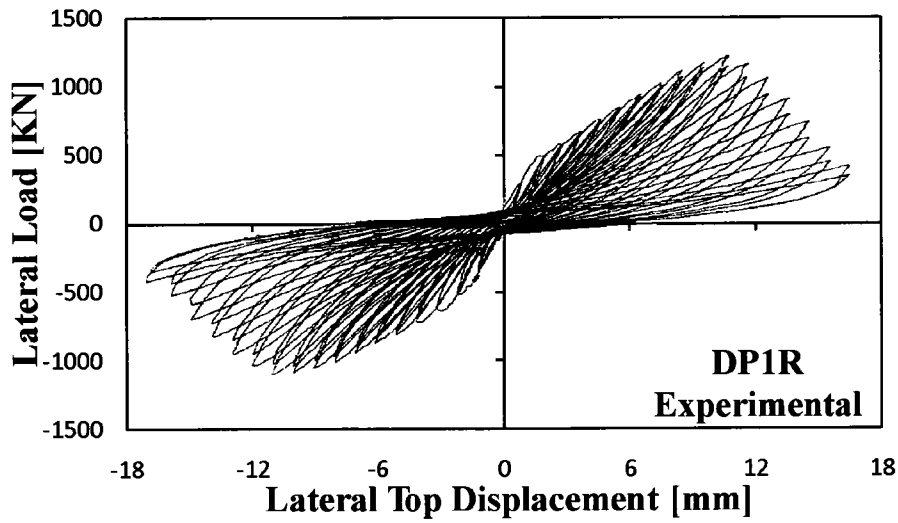

Fig. 5-14 Experimental Load-Deformation Response for Wall DP1R (Modified from Vecchio et al., 2002)

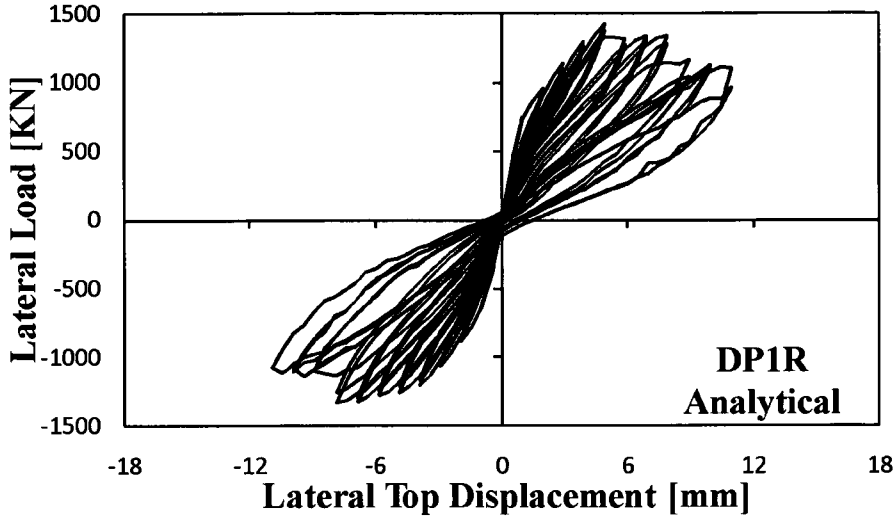

Fig. 5-15 Analytical Load-Deformation Response for Wall DP1R

5.4.3 Walls LSW3/FRPLSW3

Testing

Antoniades et al. (2003) reported on the testing of Walls LSW3/RLSW3 as part of a program on previously damaged 1:2.5 scaled squat reinforced concrete walls with aspect ratio of 1.0 (1200 mm x 1200 mm x 100 mm) as illustrated in Fig. 5-16. The original specimen, Wall LSW3, was cyclically loaded to failure, and then repaired by replacing concrete in the lower portion of the wall. After repairing, the wall was renamed RLSW3. Material properties and reinforcement ratios are listed in Table 5-2.

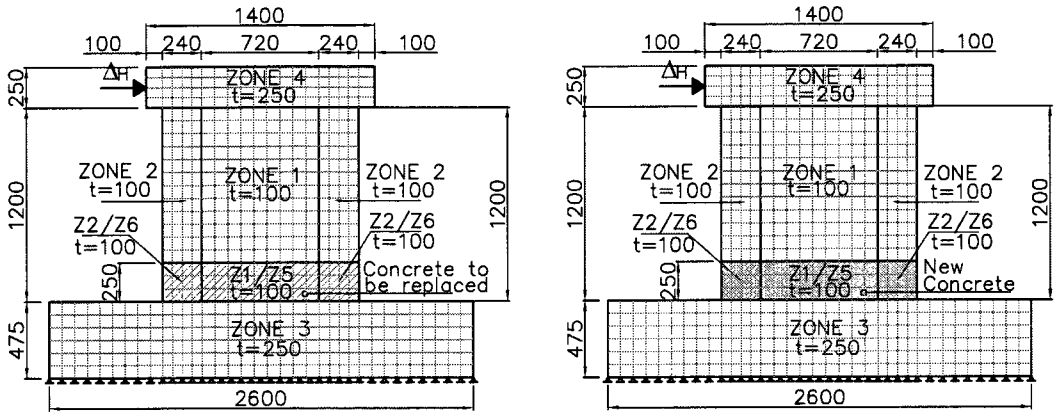

Fig. 5-16. Finite Element Mesh of Walls: (a) LSW3; (b) RLSW3. All Dimensions in mm

Repair of Wall RLSW3 involved removing the heavily damaged concrete within the lower 250 mm of the wall, including the boundary elements; replacing damaged vertical reinforcement and hoops; and casting of new high strength concrete. Damaged vertical reinforcement was cut and replaced with new reinforcing bar segments through lap welding.

Modelling

Walls LSW3/RLSW3 were modelled with a total of 626 concrete elements with smeared reinforcement, where 68 elements were double meshed to simulate the replacement of concrete procedure. The finite element model was divided into six homogeneous concrete zones corresponding to the web portion, boundary elements, foundation beam, top loading beam, and new concrete in the lower 250 mm of the web and boundary elements. Meshing of the web portion and boundary elements consisted of 17 elements in the horizontal direction and 16 elements in the vertical direction. Elements in the concrete zones for the web, boundary elements, foundation beam and top beam were initially engaged, while the concrete elements representing the replaced concrete were disengaged prior to the analysis of the original wall. At the end of the analysis of the original wall, removing concrete in the lower 250 mm of the web and boundary elements was simulated by disengaging the originally engaged elements

present in the repair zone. Casting of the new high strength concrete was simulated by engaging the elements defining the repaired concrete, assuming complete replacement of the damaged concrete.

Analysis

The loading history of the original wall, Wall LSW3, consisted of three repetitions of incremental cyclic displacements of 2 mm to failure, applied along the top loading beam. Furthermore, the wall was subjected to constant axial loading of 200 kN, corresponding to $0.07f'_cA_g$, where f'_c is the cylinder strength of the concrete and A_g is the gross area of the wall section. After failure of Wall LSW3, the wall was repaired. Thereafter, the repaired wall was tested to failure following the loading pattern used for the original wall.

Figure 5-17 illustrates the rounded response of the original wall, Wall LSW3, where the wall sustained stiffness and strength degradation until failure. Peak strength of 268 kN was reported at a lateral displacement of 4 mm, and was maintained until the subsequent cycle to 6 mm displacement. Thereafter, the wall experienced a gradual reduction in strength capacity to approximately 200 kN at 8 mm; this strength was maintained until failure. The failure mode was reported at 15 mm displacement in the form of shear sliding at the base of the wall. Prior to shear sliding, the wall displayed signs of crushing of concrete, specifically in the boundary elements. The original wall responded with good energy dissipation capacity owing to the ductility of the wall, although the hysteretic response indicated some degree of pinching, which was a consequence of shear stiffness degradation in the post-peak regime.

The predicted response of the original wall, LSW3, (Fig. 5-18) accurately captured the pre-peak response; however, the analysis underestimated the stiffness and strength degradation in the post-peak range. The predicted initial stiffness, and yield point at 4mm closely matched that reported, specifically in the positive direction. The predicted peak strength of 282 kN was in good agreement with the recorded peak strength, although the corresponding lateral displacement of 14 mm did not agree with the reported peak displacement of 4 mm. The analysis did not capture the concrete

softening in the post-peak range, which resulted from probable buckling of the vertical reinforcement. This discrepancy, however, did not affect the satisfactory prediction of pinching, but it resulted in overestimation of the total energy dissipation capacity. A model with link-bond elements to simulate buckling would improve the post-peak response of the wall. Shear sliding failure at the base of the wall was predicted at 14 mm, and correlated to that observed during testing, which was recorded at 15 mm.

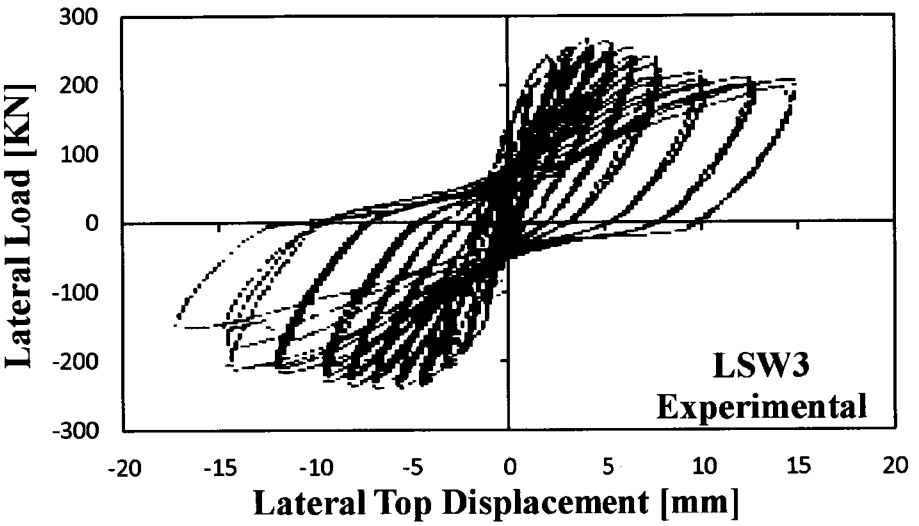

Fig. 5-17 Experimental Load-Deformation Response for Wall LSW3 (Modified from Antoniades et al., 2003)

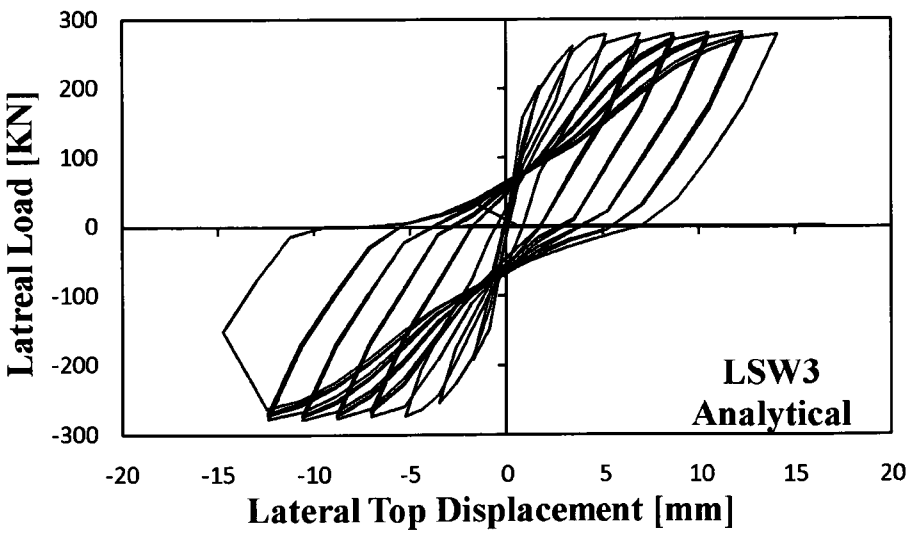

Fig. 5-18 Analytical Load-Deformation Response for Wall LSW3

Nonlinear Analysis of Repaired/Retrofitted Shear Walls

Response of the repaired wall, Wall RLSW3, (Fig. 5-19) displayed smaller initial stiffness, strength capacity and ductility than that of the original wall. Furthermore, the energy dissipation was not recovered and the hysteretic loops were more pinched. The wall attained peak strength of 179 kN at a displacement of 6 mm, which was sustained for one extra cycle to 8 mm displacement. Beyond 8 mm displacement, the wall responded with strength degradation of more than 20% along with high stiffness degradation and was considered to have failed. However, the test continued until 14 mm of displacement, where the wall sustained less than 50 kN of lateral strength capacity. Although Antoniades et al. (2003) did not explicitly state the failure mode, they suggested failure in the form of crushing of concrete with high shear distortion (shear sliding).

Analytical response of Wall RLSW3, presented in Fig. 5-20, overestimated the strength capacity by 17% and the ductility by 75% compared to the reported response. Furthermore, the analysis overestimated the initial stiffness and did not capture the significant stiffness and strength degradation in the post-peak range. The predicted failure initiated with crushing of concrete, which led to shear sliding at the base of the wall, was similar to that observed during testing. The unloading branch of the hysteretic loops displayed the same shape as that recorded, but the reloading branch displayed less stiffness degradation. Underestimation of the stiffness degradation resulted in less predicted pinching and less predicted energy dissipation capacity. Discrepancies in the predictions, particularly in terms of initial stiffness and stiffness degradation, suggest partial replacement as shown in Fig. 5-21 instead of complete replacement of the damaged concrete. Note that Antoniades et al. (2003) did not provide a complete description of the repair construction process. A second analysis, named RLSW3(2), with a triple mesh in the repair zone to account for 50% of previously damaged concrete and 50% new high strength concrete was performed to simulate the partial replacement of concrete. Figure 5-22 provides a schematic of the modelling strategy for the simulation of partial replacement of concrete.

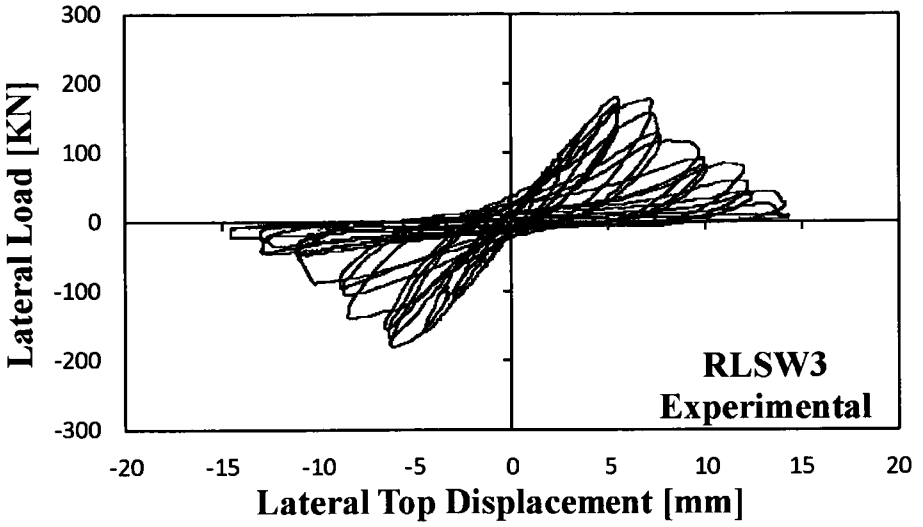

Fig. 5-19 Experimental Load-Deformation Response for Wall RLSW3 (Modified from Antoniades et al., 2003)

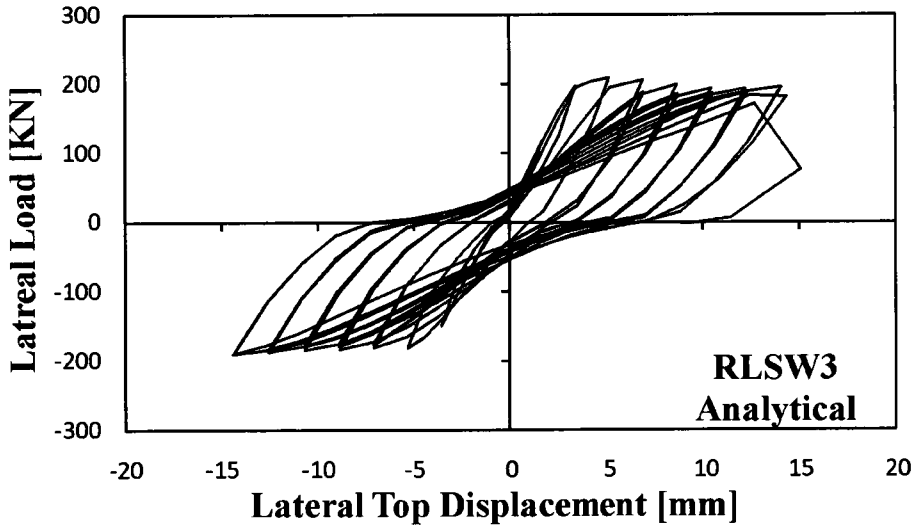

Fig. 5-20 Analytical Load-Deformation Response for Wall RLSW3

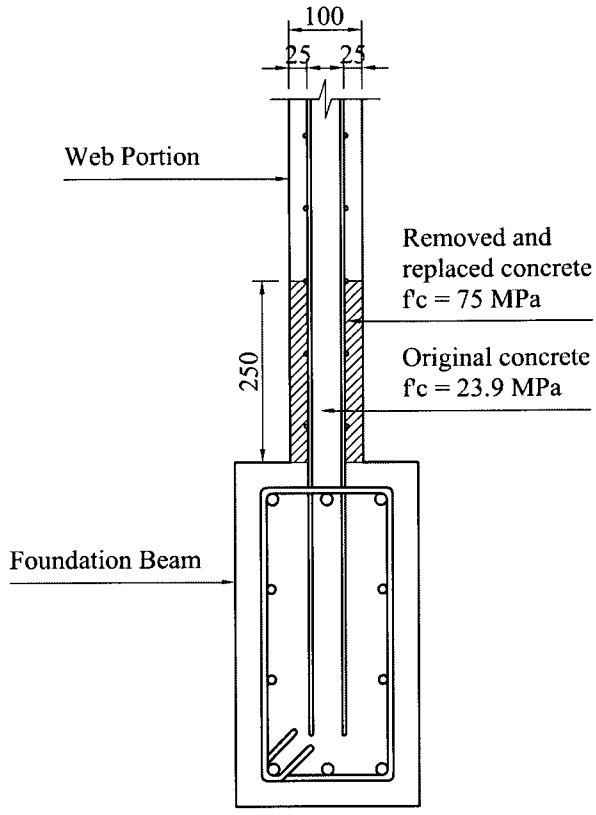

Fig. 5-21 Partial Replacement of Concrete. All Dimensions in mm

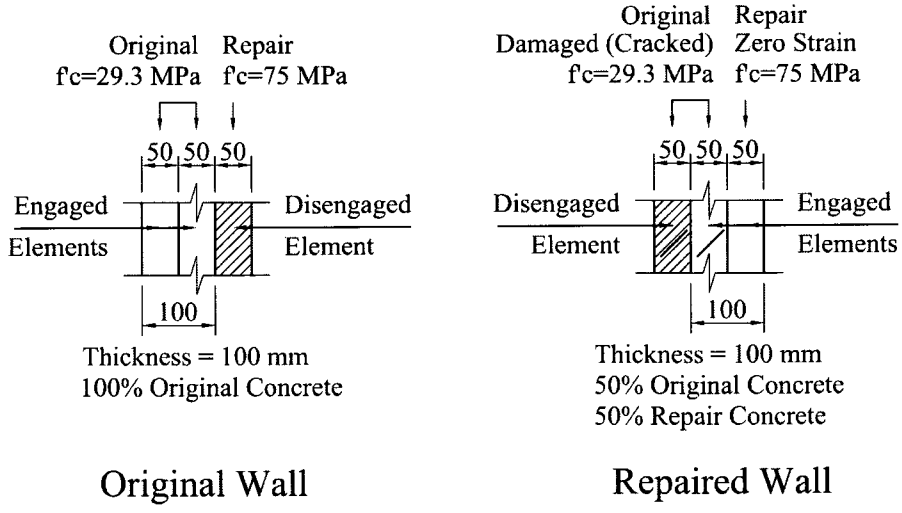

Fig. 5-22 Modelling of Partial Replacement of Concrete. All Dimensions in mm

Generally, the proposed modelling strategy for partial replacement of concrete provided better response of the repaired wall, RLSW3, as shown in Fig. 5-23. The analysis with this strategy improved the initial stiffness, the peak strength (199 kN) and the ductility (maximum displacement of 11 mm); however, the stiffness and strength degradation in the post-peak range were underestimated, which consequently overestimated the energy dissipation capacity.

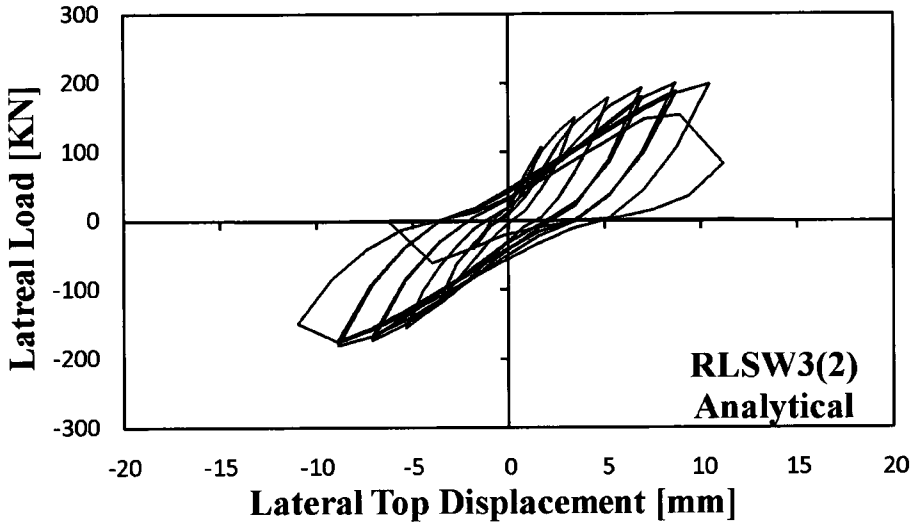

Fig. 5-23 Analytical Load-Deformation Response for Wall RLSW3(2)

5.5 Addition of Reinforcing Bars

5.5.1 Walls B11/B11R

Testing

Wall B11 (Fiorato et al., 1983) was tested to damage and repaired (B11R) by replacing the concrete in the web from the base slab up to 2600 mm in height. In addition, the wall was retrofitted with four diagonal reinforcing bars (two in each direction), which were placed near the base of the wall as shown in Fig. 5-24. Wall B11 was subjected to an alternating cyclic load history.

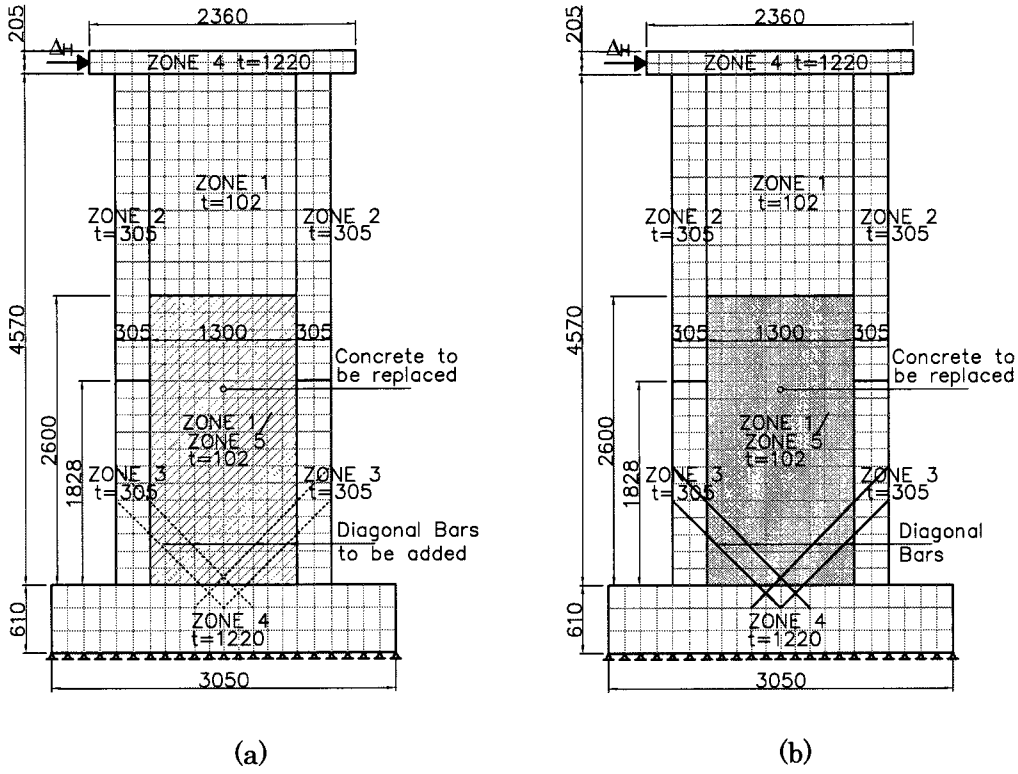

Fig. 5-24 Finite Element Mesh of Walls: (a) B11; (b) B11R. All Dimensions in mm

Modelling

Walls B11/B11R were modelled similarly to Walls B5/B5R, with the exception of the four additional diagonal bars included in the repair/retrofitting technique. The diagonal bars were modelled as truss bars, and assumed perfectly bonded to the foundation and boundary elements. Elements corresponding to the repaired concrete and retrofitting diagonal truss bars were initially disengaged during modelling of the original wall. The repair and retrofitting simulation consisted of engaging the repaired concrete and diagonal truss bars, and disengaging the elements representing the removed concrete. Figure 5-24 illustrates the finite element model of Walls B11/B11R.

Analysis

Loading of the original wall, Wall B11, included an initial single reverse cycle to approximately 13 mm, followed by a single reverse cycle to 95 mm; thereafter, three

repetitions of displacements from 51 mm to 126 mm were imposed. Wall B11R was subjected to the same loading pattern as the original wall; however, it was subjected to an extra cycle to 152 mm. Damage of the original wall, Wall B11, was characterized by inclined cracks in both directions as well as crushing of the concrete in the web, specifically near the boundary elements. Significant shear distortion was observed near the base of the wall at the end of testing.

The observed hysteretic response of the original wall, Wall B11, is illustrated in Fig. 5-25. The wall reached yielding at 25 mm of displacement, corresponding to approximately 600 kN of lateral loading, which occurred during the long cycle to 95 mm of displacement. After yielding, the lateral load capacity of the wall continued to increase to approximately 725 kN in the positive direction. During unloading from the positive displacement and reloading to the negative displacement, the wall did not experience significant shear stiffness degradation as corroborated by the absence of pinching in the hysteretic response. However, during the same cycle, the wall sustained some shear stiffness degradation during unloading in the negative displacement regime as indicated by the pinching in the response. During subsequent cycles, the wall experienced considerable stiffness degradation. In addition, the hysteretic cycles were more pinched than prior cycles. During the third repetition to 126 mm, prior to failure, the wall attained the maximum lateral load strength of 725 kN, which was similar to the lateral load capacity experienced during the cycle to 95 mm of displacement. Failure was characterized by significant crushing of concrete in the web portion of the wall. The wide hysteretic cycles in the observed response indicates that the wall dissipated significant energy. Furthermore, the displacement ductility of approximately 5.0 indicates ductile behaviour.

The predicted response of the original wall, Wall B11, (Fig. 5-26) was in good agreement with the observed response (Fig. 5-25). Behavioural aspects such as lateral strength, ductility, and energy dissipation were accurately captured. Maximum strength capacity of 735 kN was accurately predicted in the positive direction during loading to the long cycle of 95 mm of displacement. The unloading curve at this cycle was slightly wider than observed. Subsequent cycles captured adequately the stiffness

degradation, unloading and reloading branches, and the pinching effect; however, the lateral strength predicted in cycles to displacements of 100 mm and 126 mm were slightly lower than reported. The analysis correctly predicted failure in form of crushing of concrete during the third repetition to 126 mm of displacement. In general, the analysis predicted slightly less pinching; however, the energy dissipation was still well captured.

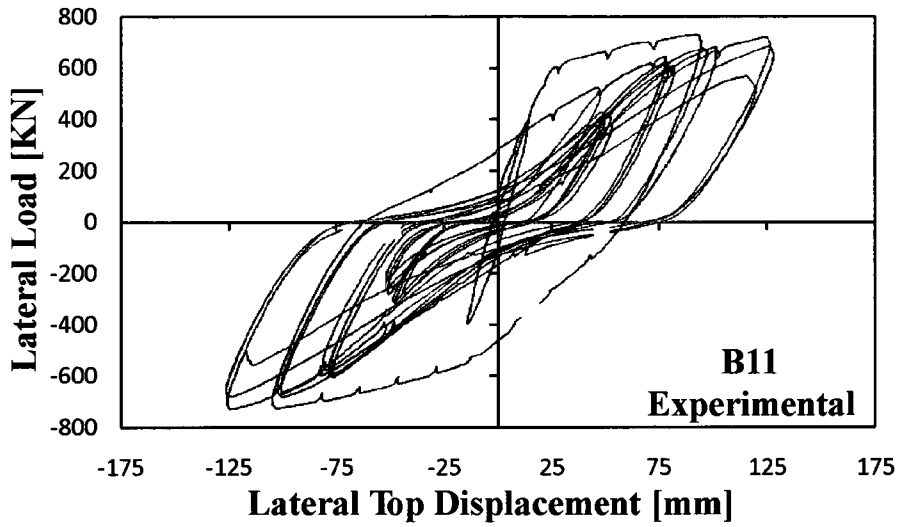

Fig. 5-25 Experimental Load-Deformation Response for Wall B11 (Modified from Fiorato et al., 1983)

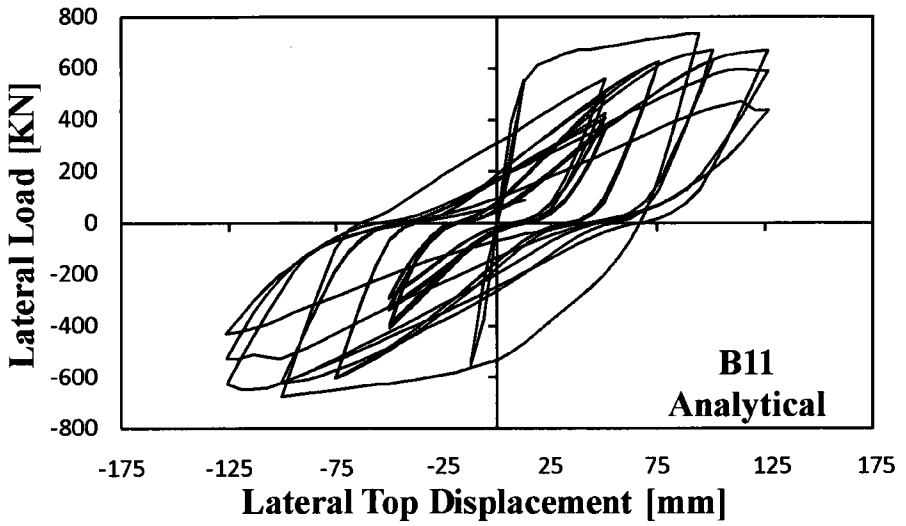

Fig. 5-26 Analytical Load-Deformation Response for Wall B11

By replacing the damaged concrete and adding diagonal reinforcing bars in Wall B11R, the peak strength and displacement capacity were increased relative to the original wall as illustrated in Fig. 5-27. The improvements in strength and ductility were mainly due to the bi-diagonal bars, which increased the shear capacity of the section and, therefore, delayed failure.

Good agreement between the analytical and experimental responses of the repaired wall, Wall B11R, is observed in Fig. 5-28 and Fig. 5-27. The analytical maximum strength of 672 kN slightly underestimated the recorded strength of 761 kN. This discrepancy is probably due to the strain hardening modulus used in the analysis. Failure was predicted during the first excursion to 155 mm, whereas failure was reported at the same displacement but after multiple repetitions. The predicted unloading, reloading, and pinching effect compared well with the observations. The predicted wide cycles with little pinching reflected significant energy dissipation of the wall and was in agreement with the actual energy dissipation of the wall. The failure mode was well simulated; concrete crushing in web near the interface with the boundary elements, along with significant shear distortion.

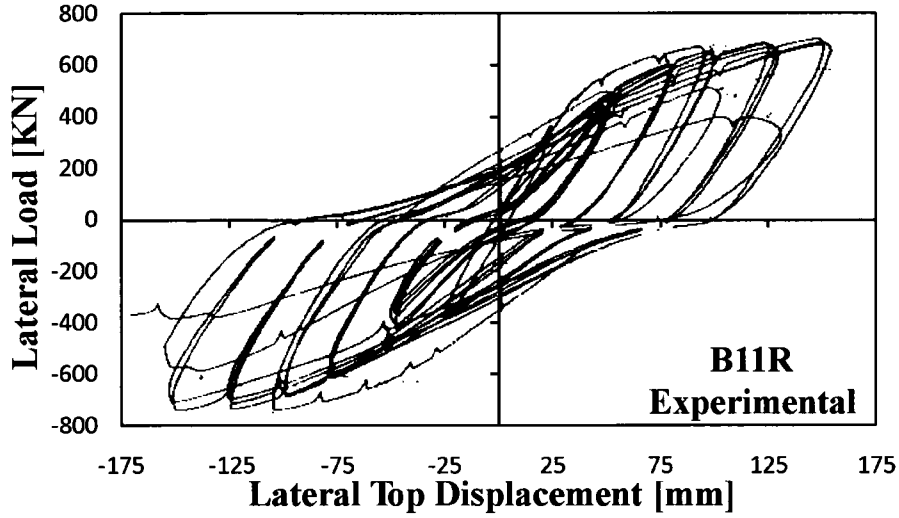

Fig. 5-27 Experimental Load-Deformation Response for Wall B11R (Modified from Fiorato et al., 1983)

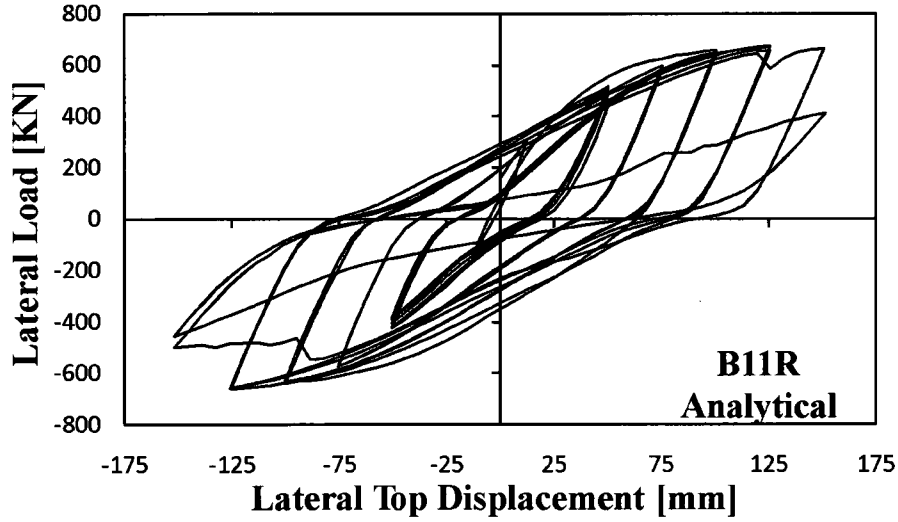

Fig. 5-28 Analytical Load-Deformation Response for Wall B11R

5.6 External Bonding of Steel Plates

5.6.1 Walls IC-SW24/IC-SWR24

Testing

Elnashai and Salama (1992), and Elnashai and Pinho (1998) tested Walls IC-SW24/IC-SWR24 to investigate a shear-strength technique to improve the ductility of a shear wall governed by shear-related mechanisms. Figure 5-29 depicts the geometry of the walls, which were 1200 mm high, 600 mm long, and 60 mm thick, and had an aspect ratio of 2.0. Table 5-2 lists the properties of the materials. The walls included asymmetrical vertical reinforcement in each boundary element to improve the ductility; larger bars were concentrated at the edges of the walls.

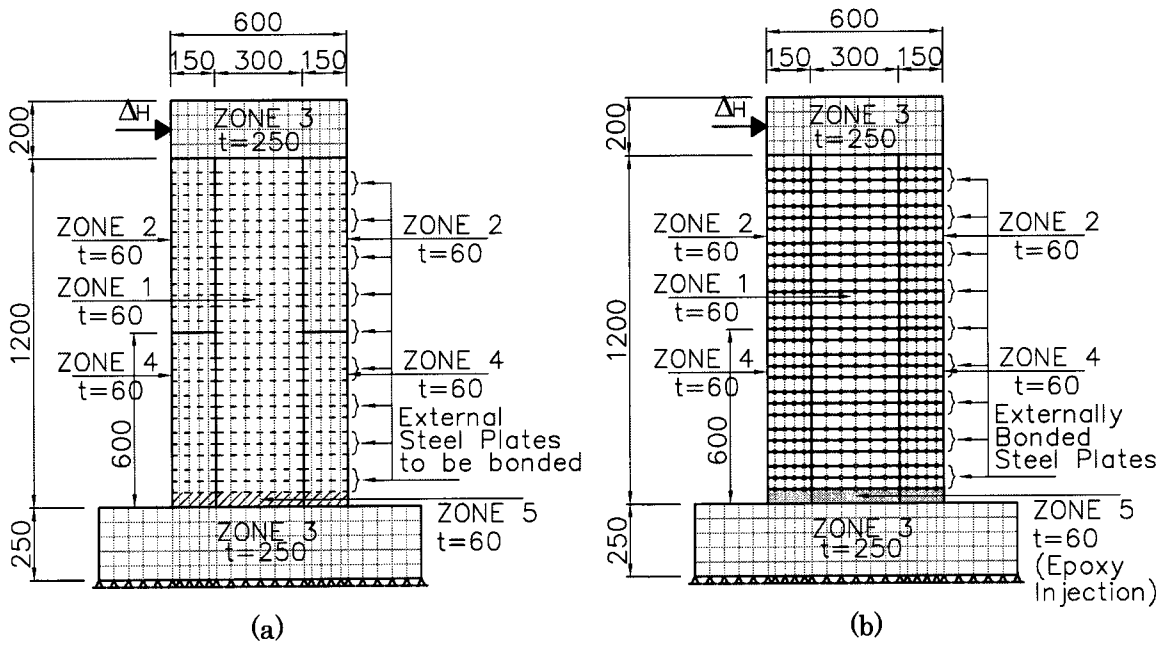

Fig. 5-29 Finite Element Mesh of Walls: (a) IC-SW24; (b) IC-SWR24. All Dimensions in mm

Repair of the damaged wall involved injection of the cracks with a high strength epoxy. Retrofitting consisted of bonding of horizontal steel plates, 78 mm x 3.6 mm, by means of epoxy resin on both sides of the wall in a staggered manner. The plates were bent at the extremities and bonded to the edge of the wall to prevent end splitting.

After repair and retrofitting, the wall was renamed IC-SWR24 and retested to failure following the same loading regime as the original wall.

Modelling

The finite element model illustrated in Fig. 5-29 was constructed with 658 smeared concrete elements defining five homogeneous concrete zones. The first zone corresponded to the web portion of the wall. The second zone corresponded to the upper half of the unconfined boundary elements. The third zone corresponded to the foundation and top beams. The fourth zone corresponded to the lower half of the confined boundary elements, and the fifth zone corresponded to the bottom row of concrete elements in the wall to simulate the epoxy injection of the cracks near the foundation beam. The web portion of the wall and the boundary elements consisted of 16 elements in the horizontal direction and 28 elements in the vertical direction. Internal vertical reinforcement of the boundary elements was modelled with perfectly bonded truss bars. Externally bonded steel plates were modelled with three horizontal rows of truss bars connected to the concrete with link-bond elements to simulate the effect of bond slip. The link-bond elements were attached to the concrete nodes and the truss bar nodes at the same coordinate position, except for the extremities of the steel plates, where the plates were bent to avoid end splitting. At this location, the truss bars where modelled as perfectly bonded to the nodes shared with the concrete elements, thus link-bond elements were not necessary. Figure 5-30 provides a detail of the simulation of the externally bonded steel plates with link-bond elements. The concrete elements defining the web, boundary elements and foundation and top beams, as well as the truss bars defining the internal reinforcement were engaged during the analysis of the original wall. Truss bars to simulate the externally bonded steel plates and concrete elements to simulate the crack injection were disengaged. After damage, the originally disengaged elements defining the repair and retrofitting materials were engaged, and the concrete elements near the foundation beam sharing the same position as the newly engaged concrete elements (epoxy injection) were disengaged. Note that epoxy injection was simulated with complete replacement of the damaged elements, thus assuming perfect sealing of the cracks. The remainder of

elements defining the web, boundary elements and foundation and top beams remained engaged as in the original analysis.

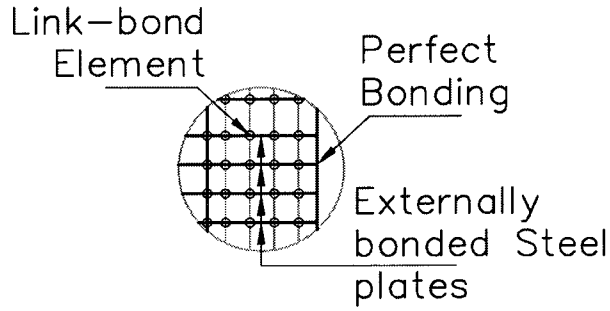

Fig. 5-30 Detail of Modelling of Externally Bonded Steel Plates

Analysis

Original Wall IC-SW24 was subjected to incremental cyclic displacements of 2 mm to failure, and then repaired and retrofitted. Non-ductile behaviour of the wall is evident in Fig. 5-31. The recorded response was asymmetrical and displayed stiffer hysteretic loops in the negative direction. Existing damage prior testing, due to transportation problems, resulted in a softening of the response in the positive direction. The wall sustained a maximum strength of 110 kN at 18 mm of displacement in the positive direction, and 125 kN at 12 mm of displacement in the negative direction. In the post-peak range, the wall responded with stiffness and strength degradation, specifically in the negative direction. The response displayed significant pinching, which reflected the shear stiffness degradation of the wall; and low energy dissipation capacity, in addition to low ductility. Failure was observed during the first repetition of loading to 21 mm displacement and involved crushing of concrete of the web.

The predicted response of the original wall, Wall IC-SW24, (Fig. 5-32) was in good agreement with the observed response, specifically in terms of strength and ductility. However, the analysis predicted higher initial stiffness in both directions. This discrepancy is due to the damage in the wall prior to testing, which was not considered in the analysis. Peak strength of 121 kN was predicted at 9 mm, which compared well

to the peak strength of 125 kN recorded during testing. In the post-peak range, the analysis predicted slight stiffness and strength degradation until failure, which was associated with shear-related behavioural mechanisms. The analytical unloading and reloading of the hysteretic loops was stiffer, particularly in the positive direction, resulting in higher energy dissipation compared to the observed response. Furthermore, the analysis predicted less pinching, which is associated with less damage due to shear stiffness degradation. Failure in the form of shear sliding was simulated during the first repetition to 16 mm of displacement. Note that shear sliding was preceded by crushing of the concrete at the bottom of the wall, which corresponded to the actual failure.

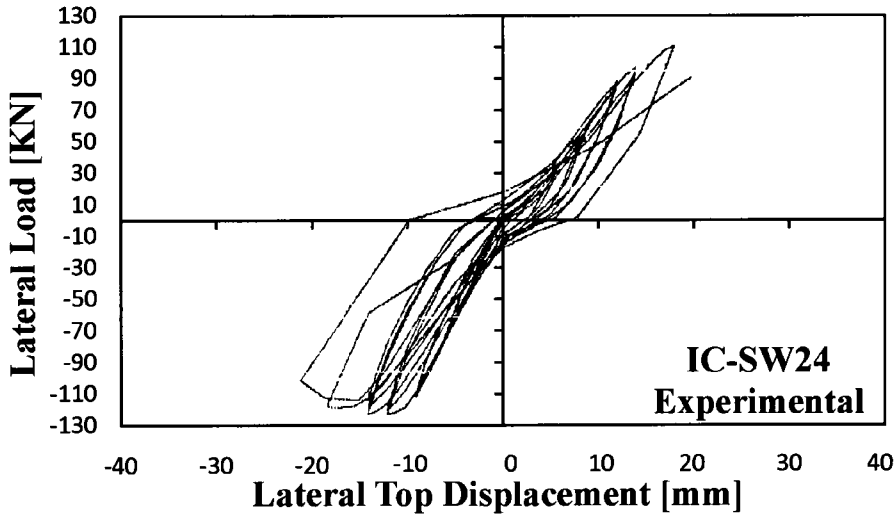

Fig. 5-31 Experimental Load-Deformation Response for Wall IC-SW24 (Modified from Elnashai and Salama, 1992)

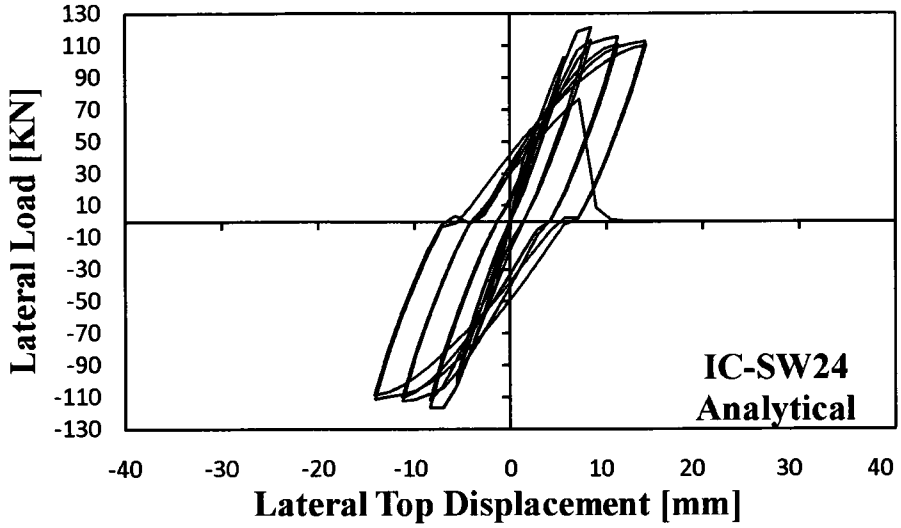

Fig. 5-32 Analytical Load-Deformation Response for Wall IC-SW24

The repair of Wall IC-SWR24 improved the ductility and the energy dissipation capacity relative to the original wall. However, the recorded rounded response displayed signs of shear-related mechanisms governing the behaviour (Fig. 5-33). Yield strength of 110 kN and peak strength of 125 kN were recorded at 8 mm and 10 mm of displacement, respectively. During the post-peak range, the wall sustained significant stiffness and strength degradation, leading to crushing of concrete with high shear distortion, specifically in the boundary elements. The first steel plate, near the foundation beam, debonded at 20 mm of displacement. Continual damage of the concrete was sustained until termination of the testing at 32 mm of displacement.

Figure 5-34 shows the predicted response of the repaired and retrofitted wall, IC-SWR24. The simulation of the repair and retrofitting procedure predicted a recovery of the stiffness and lateral strength. Yield strength of 114 kN at 9 mm displacement was in excellent agreement with that recorded. The peak strength, 119 kN, was slightly underestimated; however, the corresponding displacement did not agree with the experimental response. The analysis predicted a displacement corresponding to the peak strength of 19 mm, while the testing recorded a displacement of 10 mm. The response flattened in the post-peak range and sustained the peak strength to failure. The analysis did not capture the stiffness and strength degradation in the post-peak

range. However, unloading of the hysteretic loops was accurately captured. Failure to capture the stiffness degradation resulted in underestimation of pinching and overestimation of the total energy dissipation capacity. These discrepancies are probably due to an overestimation of the stiffness of the concrete elements which simulated the epoxy injection of cracks. Replacement of concrete to simulate epoxy injection of cracks captured the recovery of the initial stiffness; however, it did not capture the shear stiffness degradation associated with re-opening of sealed cracks. Failure as a result of shear sliding was predicted at 22 mm of displacement, and was preceded by crushing of the concrete at the bottom of the wall.

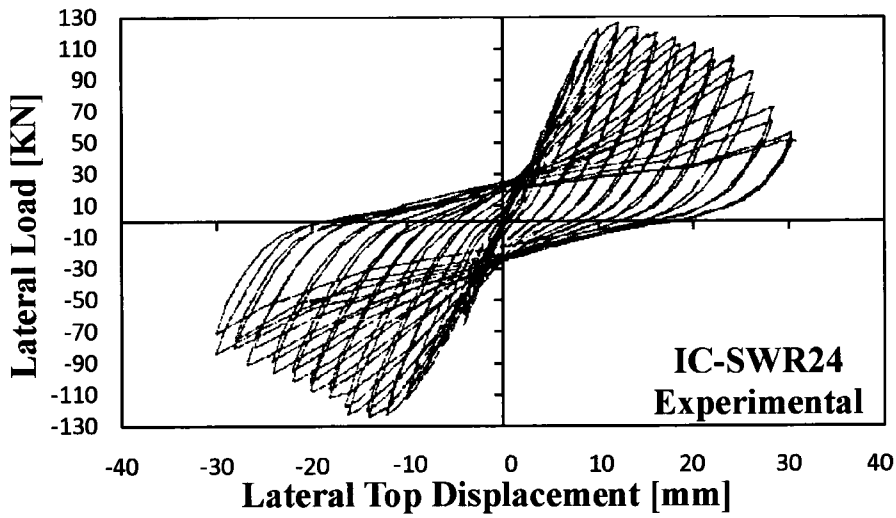

Fig. 5-33 Experimental Load-Deformation Response for Wall IC-SWR24 (Modified from Elnashai and Salama, 1992)

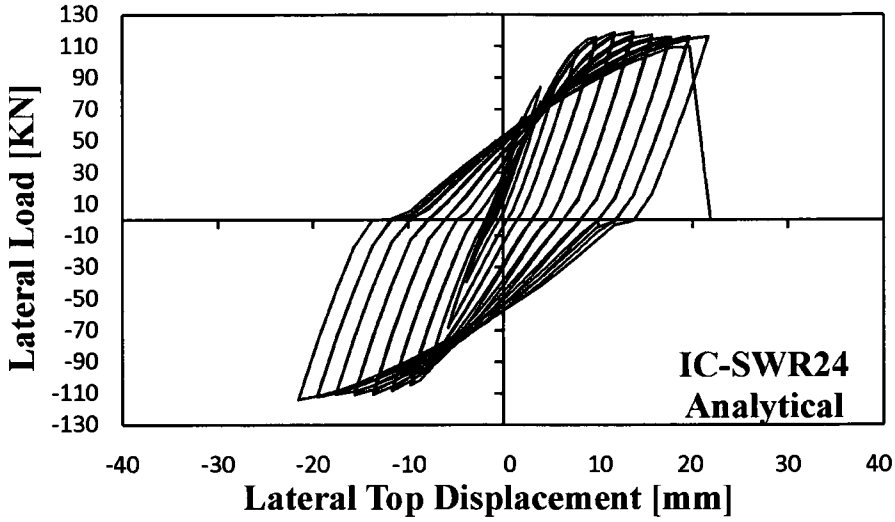

Fig. 5-34 Analytical Load-Deformation Response for Wall IC-SWR24

5.6.2 Wall IC-SW32

Testing

Wall IC-SW32 was part of an experimental program conducted and reported by Elnashai and Salama (1992), and Elnashai and Pinho (1998). The objective was to investigate the feasibility of ductility-only techniques to retrofit shear walls. The wall was scaled at 1:2.5 with aspect ratio of two, and height and length of 1200 mm and 600 mm, respectively, as shown in Fig. 5-35. Properties of the materials are listed in Table 5-2.

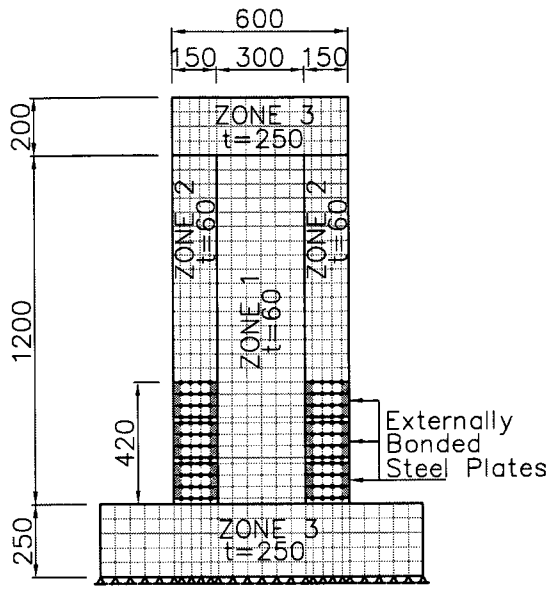

Fig. 5-35 Finite Element Mesh of Wall IC-SW32. All Dimensions in mm

Wall IC-SW32 was retrofitted by means of U-shaped external confinement steel plates in the boundary elements, which were fastened to the lower portion of the wall. This method was used to assess a ductility-only intervention of existing walls. The plates were bonded with high strength epoxy and fastened with pre-stressed bolts. The dimensions of the U-shaped plates were 480 mm x 120 mm x 3.6 mm. A gap of 20 mm between the plates and foundation was necessary to avoid any enhancement in the strength of the wall.

Modelling

The finite element mesh was defined with three homogeneous concrete zones according to the nominal dimensions and material properties of the wall: the first for the web, the second for the boundary elements and the third for the foundation and top beams. A total of 16 elements were used across the length of the wall, whereas 28 elements were used in the vertical direction as shown in Fig. 5-35. The U-shaped externally bonded steel plates were modelled with truss bars connected to the concrete with link-bond elements to simulate the effect of bond slip. The link-bond elements were attached to the concrete nodes and the truss bar nodes at the same coordinate position. An exception was at the extremities of the U-shaped steel plates, which were

wrapped around the wall. At this location, the truss bars where modelled as perfectly bonded to the nodes shared with the concrete elements, thus link-bond elements were not necessary. The confining effect of the leg of the plates in the out-of-plane direction of the wall (parallel to the thickness) and the bolts used to fasten the plates were modelled as additional confinement reinforcement. This reinforcement was smeared in the concrete elements in the vicinity of the end of the truss elements as illustrated in Fig. 5-36. Note that all the elements, including the retrofitting elements, were engaged prior the analysis to simulate the retrofitting of the wall.

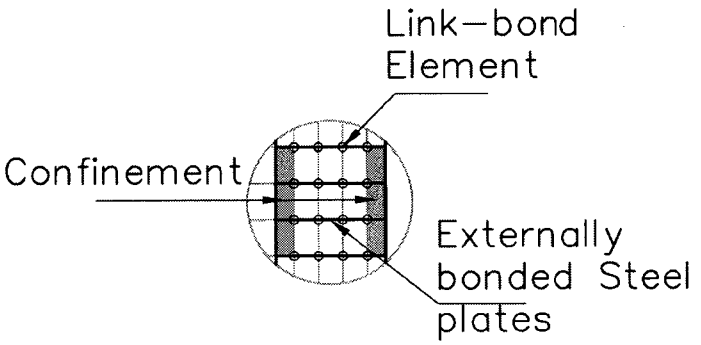

Fig. 5-36 Detail of Modelling of Externally Bonded Steel Plates with Confinement

Analysis

The loading protocol of the retrofitted wall, Wall IC-SW32, consisted of two repetitions of incremental cyclic lateral displacement from 2 mm to failure.

The observed behaviour of Wall IC-SW32 is illustrated in Fig. 5-37. Yield strength of 54 kN was attained at approximately 6 mm of displacement, and maximum strength of 62 kN was recorded at 8 mm of displacement. The lateral strength capacity was maintained to 18 mm of displacement. Beyond 18 mm of displacement, the wall sustained strength degradation and failed at a displacement of 24 mm. Failure was initiated by severe concrete damage leading to shear sliding. The hysteretic response, characterized by wide cycles with little pinching demonstrated the ductile behaviour and the energy dissipation capacity of the wall.

Nonlinear Analysis of Repaired/Retrofitted Shear Walls

Figure 5-38 demonstrates that the response of Wall IC-SW32 was well simulated. Yield strength of 50 kN at 6 mm of displacement was predicted. The strength gradually increased following a near-flat plateau up to 33 mm where the maximum strength of 57 kN was reached. At this point, most of the vertical reinforcement fractured and the wall failed. Unloading and reloading of the hysteretic cycles were well captured, and similar stiffness degradation was predicted between the first and second repetitions to the same lateral displacement. The predicted and observed hysteretic loops were similar in shape. However, the observed strength degradation beyond a displacement of 18 mm was not captured. Although the FEM was able to capture the flexural behaviour of the wall, the ductility as well as the failure mode differed from the observed behaviour. A probable cause was the reporting of the material properties. The concrete strength was given in terms of cubic strength, which is higher than the cylinder strength typically required in FEM programs. Note that an assumed cylinder compressive strength of 77% of the cubic strength was used in the analysis. Lower compressive cylinder strength could alter the predicted mode of failure to that observed (shear sliding). Furthermore, the properties of the steel were not clear, specifically for the 6 mm diameter vertical rebar used in the walls, which was reported with an uncharacteristic low ultimate strain. An increase in the ultimate strain could delay rupturing of the steel and promote shear sliding. This reasoning is probable since rupturing of the reinforcement was not observed during testing. Furthermore, the assumed confinement of the steel plate through bolts may have been excessive leading to more ductility than observed. Although a number of modelling assumptions led to some discrepancies in behaviour, the general response was satisfactorily simulated.

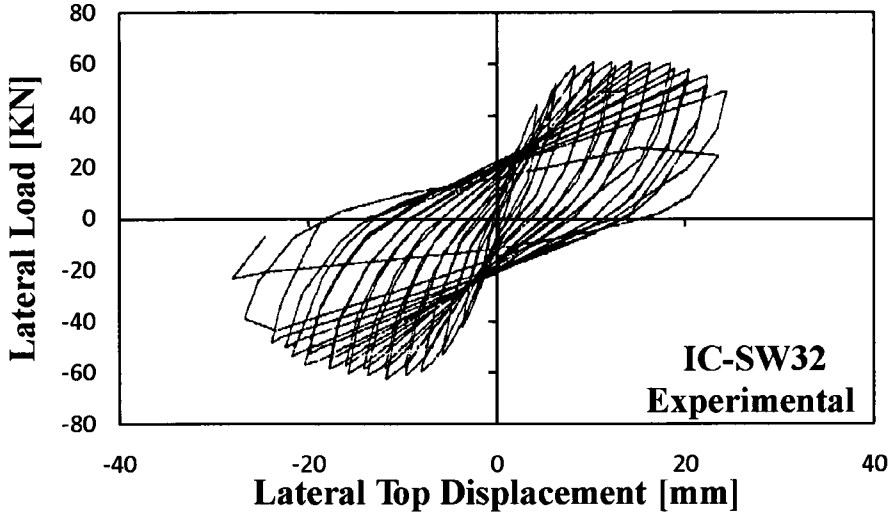

Fig. 5-37 Experimental Load-Deformation Response for Wall IC-SW32 (Modified from Elnashai and Salama, 1992)

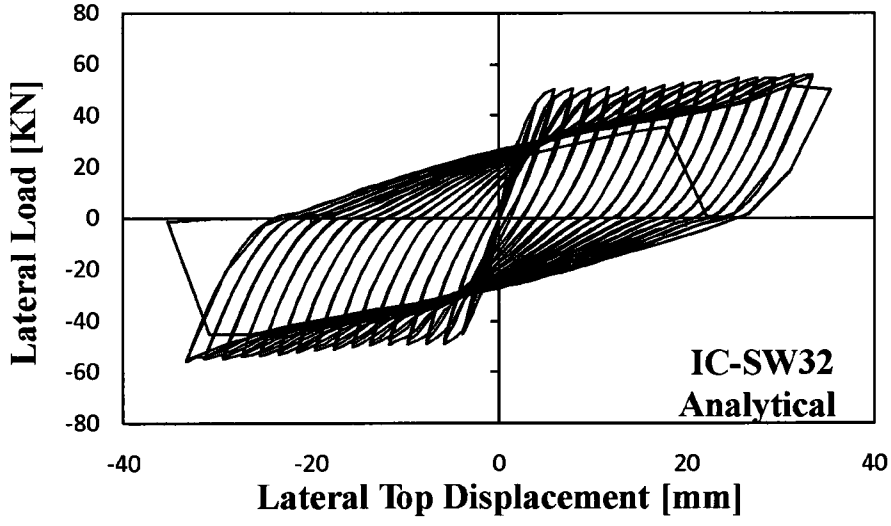

Fig. 5-38 Analytical Load-Deformation Response for Wall IC-SW32

5.6.3 Walls IC-SW35/IC-SWR35

Testing

Walls IC-SW35/IC-SWR35 were tested and reported by Elnashai and Salama (1992), and Elnashai and Pinho (1998). The walls had an aspect ratio of 2.0, were 1200 mm high, 600 mm long, and 60 mm thick. Figure 5-39 illustrates the geometry of the walls, and properties of the materials are listed in Table 5-2. In addition to the vertical reinforcement present in the boundary elements and the web, the wall was constructed with five-12 mm diameter starter reinforcing bars in the lower 250 mm of the wall to prevent shear sliding. To investigate a stiffness only intervention, the retrofitting consisted of bonding four steel plates (1100 mm x 190 mm x 3.6 mm) with epoxy near the edges of the wall, without any repair to the concrete. Wide cracks were treated with emulsion paint as a protection from corrosion. The steel plates were placed 50 mm above and below the foundation and top beams, respectively, to avoid contribution to the overall strength of the wall.

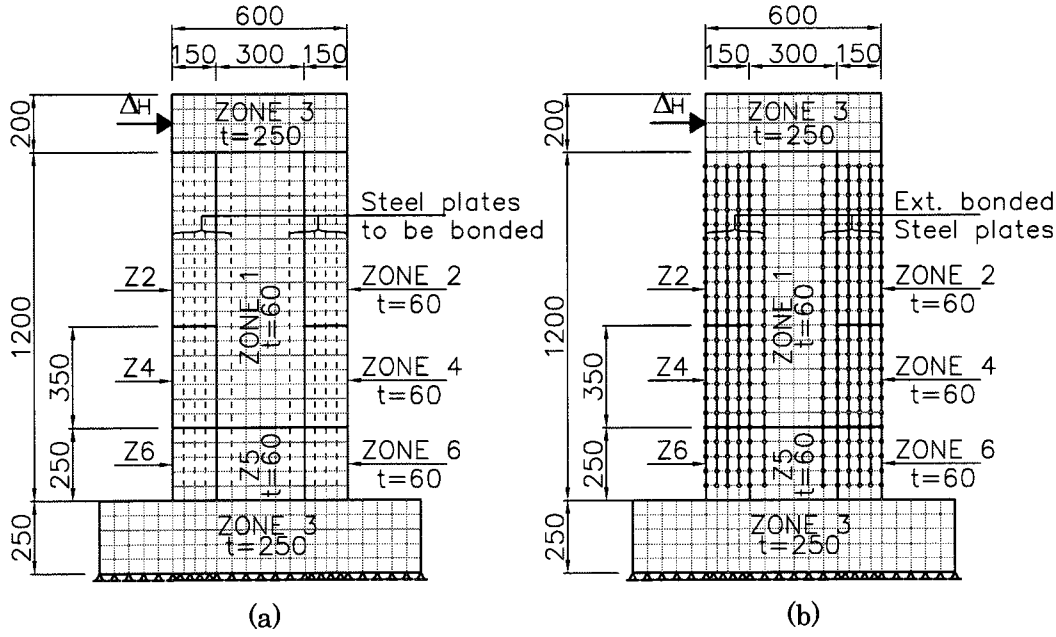

Fig. 5-39 Finite Element Mesh of Walls: (a) IC-SW35; (b) IC-SWR35. All Dimensions in mm

Modelling

Walls IC-SW35/IC-SWR35 were modelled with six homogeneous concrete zones: the first for the web, not including the lower 250 mm near the base foundation; the second for the upper half of the boundary elements; the third for the foundation and top beams; the forth for the lower half of the boundary elements less the 250 mm section above the foundation; and the fifth and sixth for the lower 250 mm of the wall from the foundation where starter bars were used to control shear sliding. The area of the vertical smeared reinforcement in zones five and six was reduced in the first five rows of elements to simulate the development length of the starter bars. Additionally, the first row above the starter bars was double meshed to simulate probable sealing of the cracks due to the epoxy used to bond the steel plates to the wall during retrofitting. It was observed during preliminary analyses of the wall without the aforementioned double mesh that excessive crack widths caused a premature debonding of the steel plates on one of the sides of the walls. A total of 344 elements were used in the web, including the boundary elements, corresponding to a mesh of 14 by 24 elements and eight double meshed elements. Figure 5-39 shows details of the mesh and zones of the model. Simulation of the externally bonded steel plates consisted of truss bars attached to the concrete elements by link-bond elements. Before the analysis of the original wall, the concrete elements, except the additional elements in the first row above the starter bars, were engaged, and the retrofitting elements were disengaged. After damage of the original wall, the retrofitting was simulated and the wall was renamed as IC-SWR35. Originally engaged elements and disengaged elements in the double mesh to simulate sealing of the cracks were disengaged and engaged, respectively. Furthermore, the truss bars and link-bond elements representing bonding of the external steel plates were engaged.

Analysis

The original wall, Wall IC-SW35, was tested under cyclic displacements to 14 mm, corresponding to a displacement ductility of 2.0 to simulate partial damage induced by a moderate earthquake.

Nonlinear Analysis of Repaired/Retrofitted Shear Walls

The original wall reached its yield capacity of 65 kN at approximately 7 mm of displacement. Yielding was reported just above the starter bars indicating a shift of the critical section from the bottom of the wall. The observed response, as illustrated in Fig. 5-40, was rounded and did not present a clear yield plateau. The wall attained a lateral strength of 75 kN at the end of testing (14 mm displacement). Damage included cracking above the starter bars without significant concrete deterioration or spalling of concrete cover. The hysteretic cycles were slightly pinched, and marginal stiffness degradation between first and second repetitions of cycling to the same displacement level was observed. After failure, the wall was retrofitted (IC-SWR35) and retested to failure under incremental reverse cycles of 2 mm.

The predicted response was in agreement with the observed response of the original wall as shown in Fig. 5-41. Initial stiffness, yielding, unloading and reloading, and pinching were accurately captured, specifically during the four first cycles up to 8 mm of displacement. From 8 mm to 14 mm of displacement, the predicted response was flatter, and the maximum lateral strength of 69 kN underestimated the reported strength by approximately 9%. The level of energy dissipation was similar between predicted and observed responses. The predicted damage was similar to that observed, and included cracking above the starter bars. At the end of the cycle to 14 mm of displacement, the analysis was terminated and the retrofitting procedure was simulated. After retrofitting, Wall IC-SWR35 was analyzed to failure following the same loading regime used in the testing.

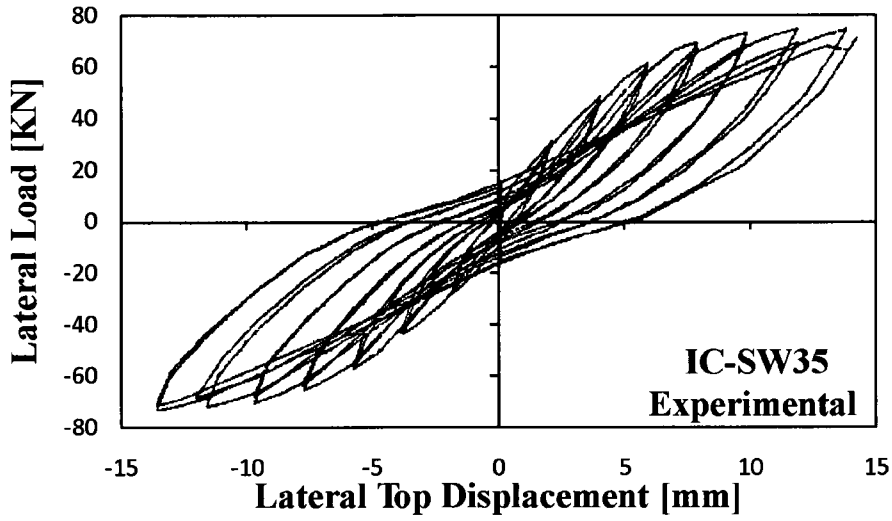

Fig. 5-40 Experimental Load-Deformation Response for Wall IC-SW35 (Modified from Elnashai and Salama, 1992)

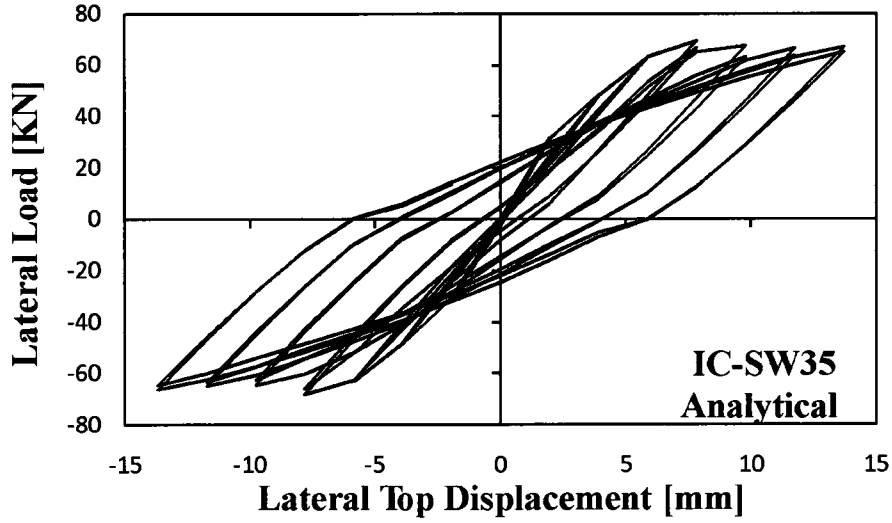

Fig. 5-41 Analytical Load-Deformation Response for Wall IC-SW35

The retrofitted wall, IC-SWR35, reached its yield strength of 70 kN at 6 mm of displacement, which was sustained until a displacement of 20 mm. At larger displacements, the stiffness compared very well with that of the original wall. At each increment of displacement, debonding of the steel plates was observed and cracks reopened leading to delamination of the interface between the epoxy and the concrete.

Nonlinear Analysis of Repaired/Retrofitted Shear Walls

After delamination of the bonding interface, failure of the wall occurred at 24 mm of displacement due to concrete crushing just above the starter bars and between the plates. Information regarding the hysteretic cycles was lacking, and only the envelope of the observed response of Wall IC-SWR35 was available (Fig. 5-42).

The analytical response of the retrofitted wall, IC-SWR35, was in agreement with the experimental response (Fig. 5-43), specifically during the first 4 mm of loading where the initial stiffness was restored. The strength was well captured; however, the displacement capacity was overestimated. During the analysis beyond 4 mm of displacement, a drop in the strength occurred in the pushing direction due to debonding of the steel plates leading to widening of cracks and reopening of the cracks in the double meshed concrete elements above the starter bars. After debonding of the plates, the wall behaved as if it was not retrofitted; therefore, no increase of stiffness was achieved. In the post-peak phase, the wall gained marginal strength and reached a maximum predicted lateral load capacity of 71 kN at a corresponding displacement of 34 mm. At the ultimate load, significant concrete degradation in the first 200 mm above the starter bars and between the steel plates was predicted and similar to that observed. The analysis predicted failure due to shear sliding at a height of 400 mm above the foundation. Note that the shear sliding was initiated due to damage in the concrete, which was the triggering failure mechanism as observed in the test. A probable cause for the discrepancy in the ultimate displacement was the simulation of the externally bonded steel plates, which did not fully capture the delamination of concrete. A photograph of the retrofitted wall after testing (Elnashai and Pinho, 1998) revealed a sizeable portion of the concrete being removed from the wall during the delamination of the plates. A reduction in the thickness of the concrete due to delamination could reduce the contribution of concrete to the lateral capacity and potentially anticipate failure of the wall by concrete crushing.

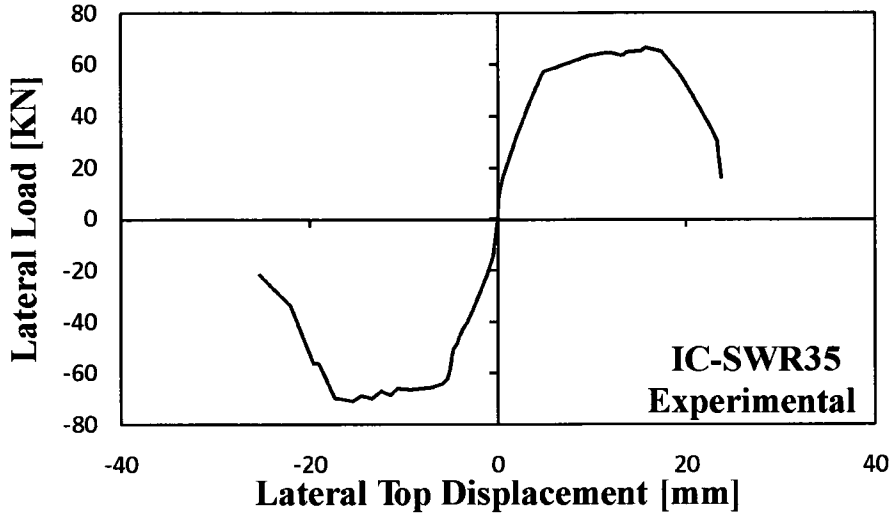

Fig. 5-42 Experimental Load-Deformation Response for Wall IC-SWR35 (Modified from Elnashai and Salama, 1992)

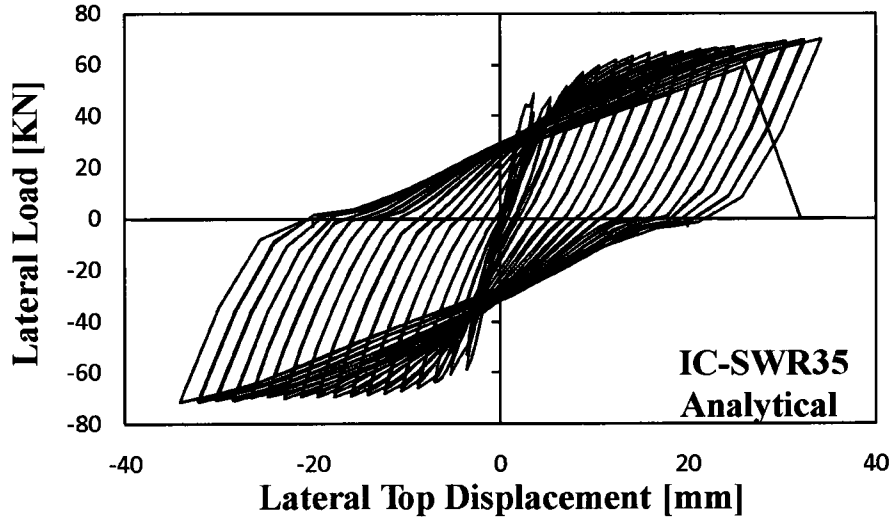

Fig. 5-43 Analytical Load-Deformation Response for Wall IC-SWR35

5.7 Addition of Unbonded Steel Rods and Plates with Delay Mechanism

5.7.1 Walls IC-SW31 and IC-SW34

Testing

Walls IC-SW31 and IC-SW34 (Elnashai and Salama,1992; Elnashai and Pinho, 1998) were constructed with three-6 mm diameter external steel rods, and one external unbonded steel plate (1200 mm x 50 mm x 3.6 mm) at each edge of the walls, respectively. The rods and plates were provided with a delay mechanism as shown in Fig. 5-44 and Fig. 5-45 to promote a strength-only retrofit scheme. The steel rods in Wall IC-SW31 were fastened with a high strength epoxy mortar to the foundation beam and connected with a steel assembly to the soffit of the top beam. The delay mechanism in Wall IC-SW31 consisted of mechanical couplers with a gap located between the steel rods and the steel assembly near the mid height of the wall. The couplers allowed initial free displacement of the rods with no contribution to the stiffness or strength of the wall. The steel plates in Wall IC-SW34 were connected to the side of the wall by steel gusset plates at the foundation beam and slotted steel plates at the top loading beam. The delay mechanism in Wall IC-SW34 consisted of slotted steel plates with grooves that allowed 3 mm of free vertical movement.

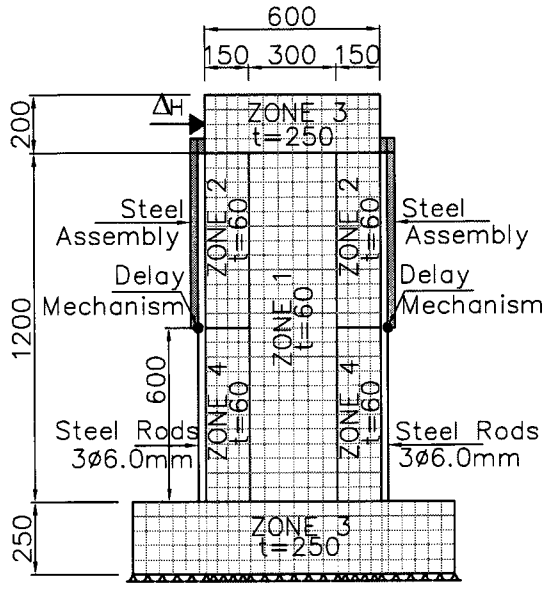

Fig. 5-44 Finite Element Mesh of Wall IC-SW31. All Dimensions in mm

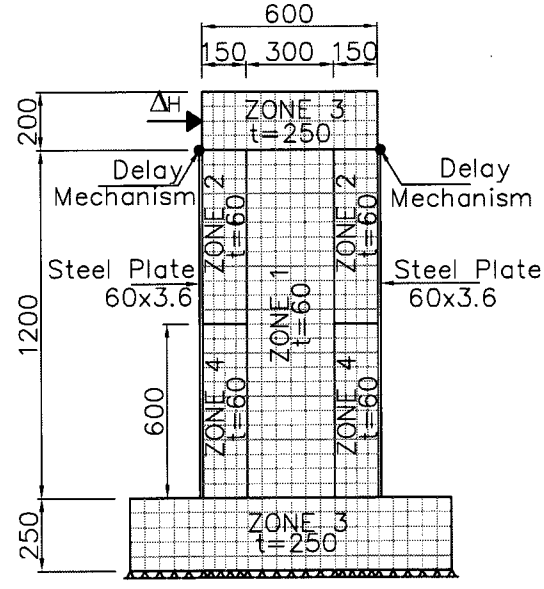

Fig. 5-45 Finite Element Mesh of Wall IC-SW34. All Dimensions in mm

Modelling

Walls IC-SW31 and IC-SW34 were discretized with 512 rectangular elements distributed in four concrete zones: web wall; upper half of the boundary elements;

foundation and top beams; and lower half of the boundary elements, which contained closer hoop spacing to improve shear resistance and confinement. The mesh of the wall (excluding foundation and top beams) consisted of 14 elements in the horizontal direction and 24 elements in the vertical direction. Two truss bar elements were used to model the steel rods and steel plates for Walls IC-SW31 and IC-SW34, respectively. The steel rods and plates were perfectly connected to the foundation; therefore, the truss bar elements were directly connected to the concrete nodes at the same coordinate position. The delay mechanisms were simulated with link-bond elements having zero shear stress for the first 3 mm of vertical displacement, which corresponded to the actual gap. In Wall IC-SW31, the delay mechanism was located at the middle of the wall at the end of the stiff rectangular elements representing the steel assembly connected to the soffit of the top beam. In Wall IC-SW34, the delay mechanism was simulated at the top of the wall at the soffit of the top beam. Figure 5-44 and Fig. 5-45 illustrate the finite element model used for Walls IC-SW31 and IC-SW34, respectively. A trilinear bond stress-slip relationship similar to the steel strain-stress relationship of the reinforcement was used after the gap was exhausted as shown in Fig. 5-46. Yield bonding stress, U_y, was set equal to the yield stress, f_y, of the steel rods and steel plates. Similarly, maximum bonding strength, U_{ult}, was set equal to the ultimate steel stress, f_u, of the steel rods and steel plates. Initial slip, S_o, was selected to correspond to the actual vertical gap. Yield slip, S_y, corresponded to the yield deformation of the steel rods and steel plates. Lastly, ultimate slip, S_{ult}, corresponded to the ultimate deformation of the steel rods and steel plates. Therefore, once the rods or plates were engaged, the reinforcing steel and bond material were coupled. The area of the bond material was assumed equal to the area of the steel rods and steel plates to ensure accurate stress in the delay mechanism. Furthermore, the Fujii bond-slip model was selected to better capture the hysteretic behaviour of the delay mechanism.

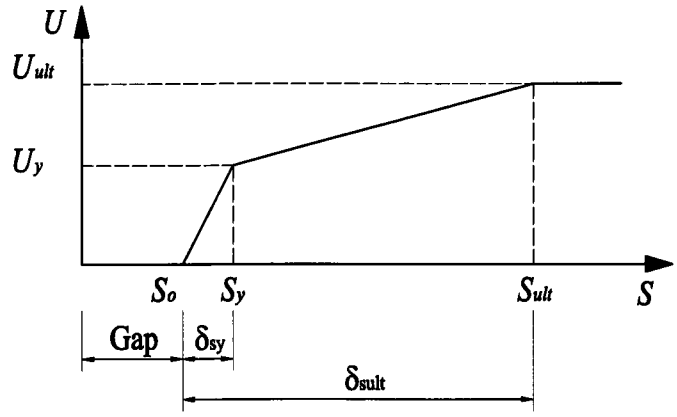

Fig. 5-46 Delay Mechanism Bond Stress-Slip Relationship

Analysis

Retrofitted Walls IC-SW31 and IC-SW34 were tested to failure with incremental reverse cycles of 2 mm. The walls performed well and accomplished the objective of the strength-only retrofit.

Wall IC-SW31 reached yield strength of 56 kN during the third cycle of loading corresponding to an approximate displacement of 6 mm. During the fifth cycle to approximately 10 mm of displacement, one of the steel rods became engaged and started to contribute to the strength of the wall. The delay mechanism ensured that the rods would not alter the initial stiffness of the wall, and prevented buckling of the rods under compression. The full contribution of the rods was achieved at 14 mm of displacement, resulting in a maximum strength of 90 kN, which was sustained until a displacement of 24 mm. At this displacement, the rods were physically disconnected and the wall behaved as if it was not retrofitted. The wall failed at 30 mm of displacement due to concrete crushing in the boundary elements. The pinching effect was evident in the experimental response of Wall IC-SW31 (Fig. 5-47).

The analytical predictions of Wall IC-SW31 closely matched the experimental behaviour, specifically in terms of strength as observed in Fig. 5-48. The behaviour of the delay mechanism was well captured and demonstrated the success of the

modelling technique. Yield strength of approximately 48 kN was predicted at approximately 5 mm of displacement. During the fourth cycle to 8 mm, the delay mechanism was activated (one cycle before that observed in the test) and the steel rods contributed to lateral strength, which rapidly increased to 78 kN at a corresponding displacement of 15 mm at which point yielding of the rods occurred. Beyond this point, the envelope of the response flattened and the wall sustained its strength capacity of 82 kN at 23 mm displacement where the delay mechanism was deactivated in accordance with the actual testing. During the subsequent cycle to 25 mm, the strength capacity of the wall decayed to 61 kN. Thereafter, the wall gained marginal strength up to 34 mm displacement prior to failure. Failure consisted of rupturing of the vertical reinforcement in the web and boundary elements along the base of the wall. Unloading and pinching of the hysteretic cycles were well captured.

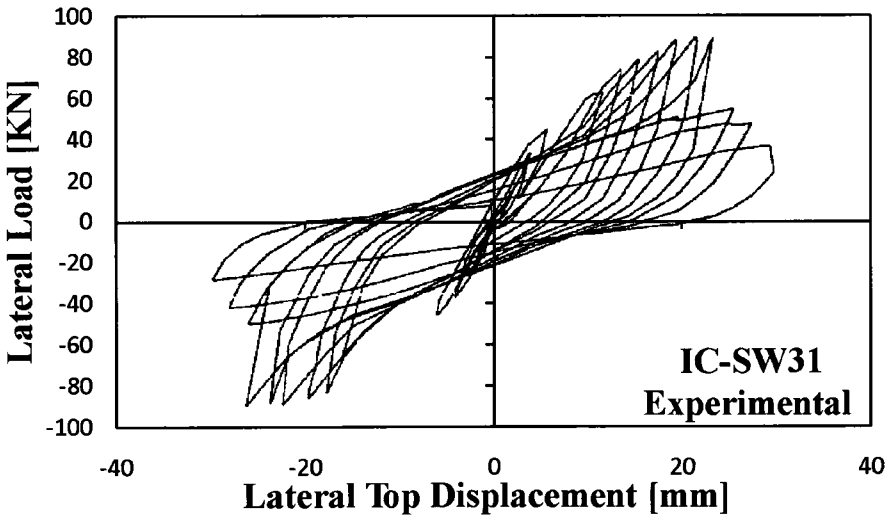

Fig. 5-47 Experimental Load-Deformation Response for Wall IC-SW31 (Modified from Elnashai and Salama, 1992)

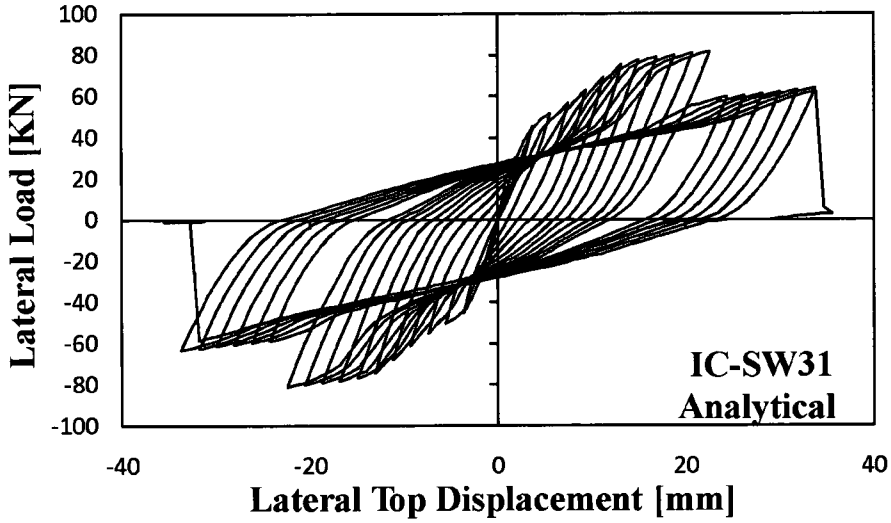

Fig. 5-48 Analytical Load-Deformation Response for Wall IC-SW31

Wall IC-SW34 had yield strength of 60 kN at a corresponding displacement of 6 mm. The steel plates became engaged at 8 mm of displacement when the 3 mm vertical gap was exhausted, allowing strength contribution from the plate. The retrofitting scheme did not affect the initial stiffness of the wall, and prevented buckling of the steel plates in compression. Maximum strength of 90 kN was recorded at 22 mm of displacement, and thereafter, strength degradation was observed until the second excursion to 26 mm of displacement when failure of the wall occurred due to crushing of the concrete in the boundary elements. Figure 5-49 displays the hysteretic response of Wall IC-SW34, which was subjected to two repetitions to each cycle. Unloading and reloading between first and second repetitions demonstrated marginal stiffness degradation in the pre-peak response; stiffness degradation substantially increased in the post-peak response.

The hysteretic response of Wall IC-SW34 was adequately captured and the strength-only intervention was successfully simulated. Specifically, behaviour of the steel plates was in excellent agreement with the reported response as demonstrated by the correct prediction of hysteretic characteristics such as unloading and reloading and the pinching effect. Furthermore, the analysis accurately predicted the engagement of the steel plates. The analytical predictions compared very well with the experimental

results in terms of strength as provided in Fig. 5-50. Yield strength of 56 kN was predicted at 6 mm of displacement. At 8 mm of displacement, the delay mechanism was activated and the steel plates contributed to the response of the wall. The strength subsequently increased rapidly to 78 kN at a corresponding displacement of 16 mm when yielding of the plates occurred. Beyond 14 mm, the envelope of the response flattened and the wall sustained ultimate strength of 86 kN at 30 mm of displacement. The predicted failure mechanism of the wall was similar to IC-SW31, which involved rupturing of the vertical reinforcement. The energy dissipation up to 24 mm displacement was approximately the same as that recorded.

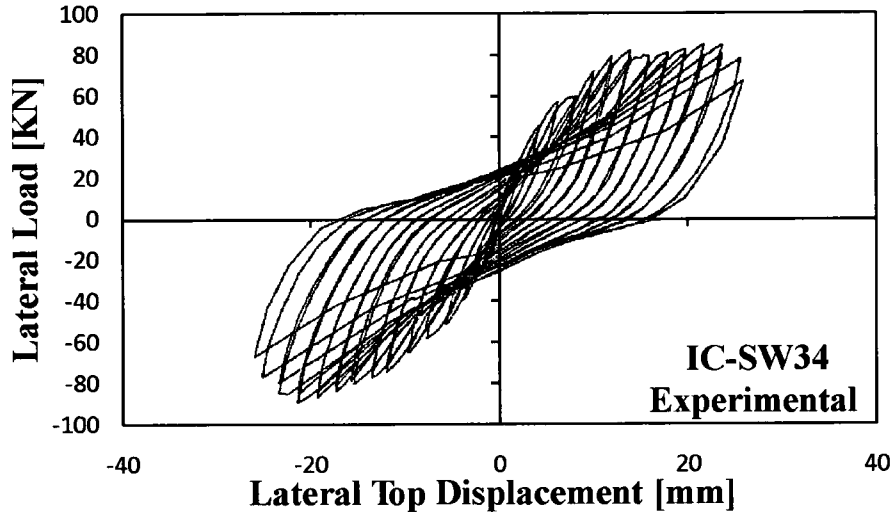

Fig. 5-49 Experimental Load-Deformation Response for Wall IC-SW34 (Modified from Elnashai and Salama, 1992)

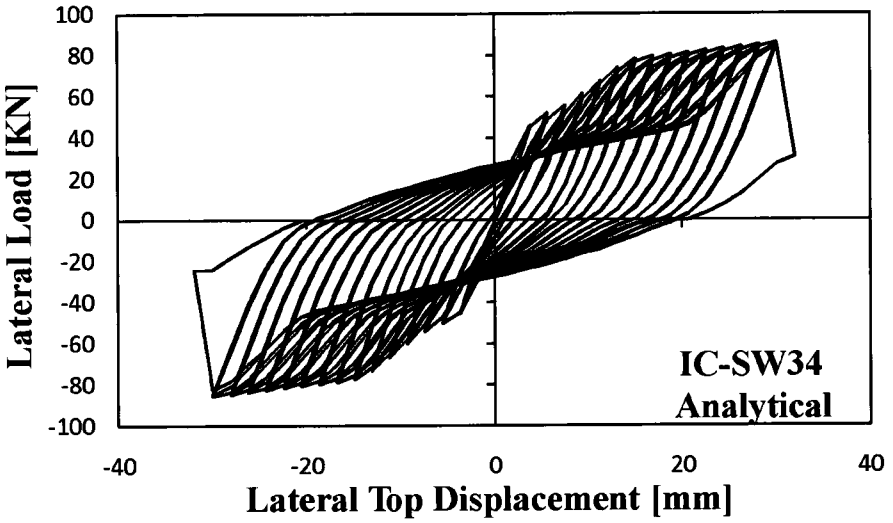

Fig. 5-50 Analytical Load-Deformation Response for Wall IC-SW34

Discrepancies in the prediction of the ultimate displacement as well as in the failure mode in both walls, IC-SW31 and IC-SW34, were similar and attributed to the assumptions in the material properties as described previously for Walls IC-SW32, and IC-SW35/IC-SWR35. The concrete strength was given in terms of cubic strength, which is higher than the cylinder strength typically required in FEM programs. Note that an assumed cylinder compressive strength of 77% of the cubic strength was used in the analysis. Furthermore, the properties of the steel were not clear, specifically for the 6 mm diameter vertical rebar used in the walls, which was reported with an uncharacteristic low ultimate strain. An increase in the ultimate strain could delay rupturing of the steel and promote shear sliding.

5.8 External Bonding of FRP Sheets

5.8.1 Walls LSW1/FRPLSW1 and MSW1/FRPMSW1

Testing

Walls LSW1/FRPLSW1 and MSW1/FRPMSW1 were part of a series of tests conducted by Antoniades et al. (2003, 2005) on previously damaged 1:2.5 scaled squat and squat-slender reinforced concrete walls, respectively.

Walls LSW1/FRPLSW1 had an aspect ratio of 1.0 (1200 mm x 1200 mm x 100 mm) and Walls MSW1/FRPMSW1 had an aspect ratio of 1.5 (1200 mm x 1800 mm x 100 mm) as illustrated in Fig. 5-51 and Fig. 5-52, respectively. The original specimens, Walls LSW1 and MSW1, were cyclically loaded to failure, repaired and retrofitted, and renamed FRPLSW1 and FRPMSW1, respectively. Material properties and reinforcement ratios are listed in Table 5-2.

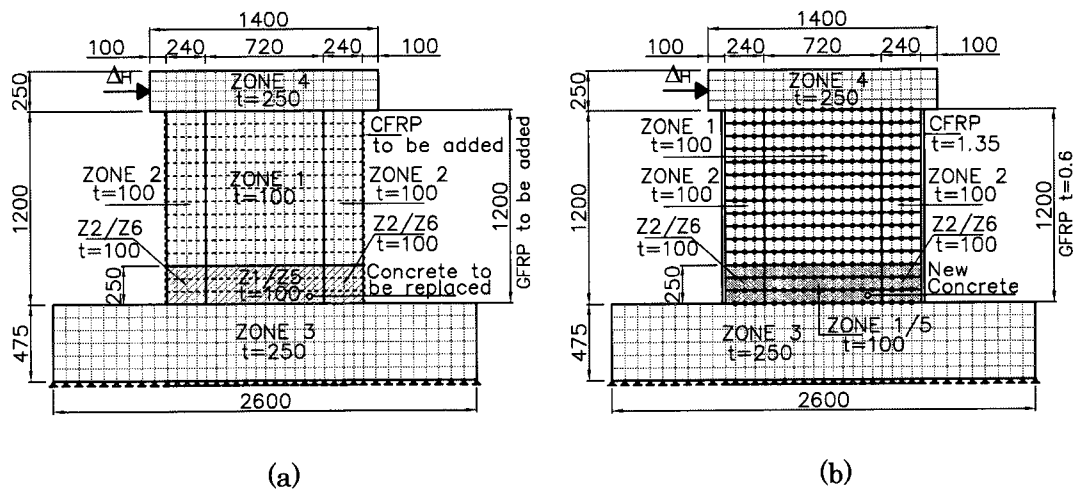

Fig. 5-51 Finite Element Mesh of Walls: (a) LSW1; (b) FRPLSW1. All Dimensions in mm

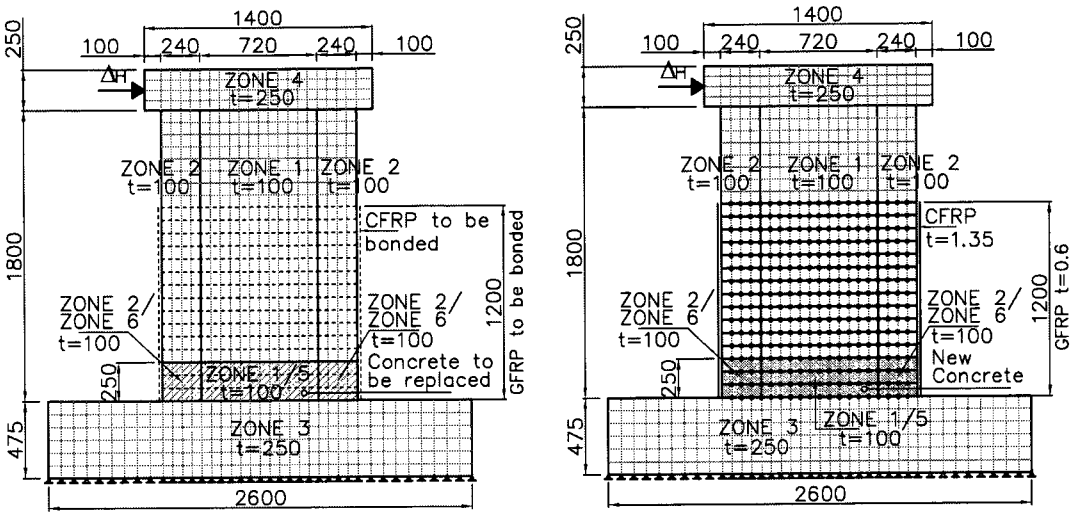

Fig. 5-52 Finite Element Mesh of Walls: (a) MSW1; (b) FRPMSW1. All Dimensions in mm

Repair and retrofitting of Walls FRPLSW1 and FRPMSW1 began with removing heavily damaged concrete within the lower 250 mm of the wall, including the boundary elements. In addition, damaged vertical reinforcement was cut and replaced with new reinforcing bar segments through lap welding, and damaged hoops were also replaced. New concrete was then cast in the lower section of the wall. Flexural and shear cracks were sealed with an epoxy resin in the remainder of the wall. The retrofit involved application of three layers of 0.45 mm thick and 100 mm wide carbon fibre reinforced polymer (CFRP) strips at the edges of the wall with fibres oriented in the vertical direction. This was followed by wrapping of the wall with 0.6 mm thick glass fibre reinforced polymer (GFRP) sheets along a height of 1200 mm (total height of Wall FRPLSW1). Finally, the edge FRP strips were anchored to the foundation with a combination of inverted U-shaped GFRP and 20 mm thick steel plates glued with an epoxy resin.

Modelling

The finite element model of Walls LSW1/FRPLSW1 and MSW1/FRPMSW1 contained five homogeneous concrete zones for the web portion of the web, boundary elements,

foundation beam, top loading beam and new concrete in the lower 250 mm of the wall. The total number of rectangular concrete elements used in the model of Walls LSW1/FRPLSW1 and MSW1/FRPMSW1 were 592 and 728, respectively. Meshing of the web portion and boundary elements consisted of 17 x 15 concrete elements for Walls LSW1/FRPLSW1 and 17 x 23 concrete elements for Walls MSW1/FRPMSW1. Furthermore, the model included 51 concrete elements for a double mesh used in the simulation of the replacement of concrete. Vertical CFRP strips were modelled with 30 perfectly bonded truss elements (15 in each edge) based on an assumed rigid anchoring system. Wrapping of the wall with GFRP was simulated with 16 rows of 17 truss elements horizontally oriented along the lower 1200 mm of the wall (total height of Wall FRPLSW1). These elements were connected to the concrete by means of link-bond elements, except the extreme nodes at the wall edges, which were simulated as perfectly bonded (Fig. 5-51 and Fig. 5-52). Concrete elements in the web portion, boundary elements, foundation beam, and top loading beam were initially engaged, while the truss elements simulating the FRP and the concrete elements representing the replacement of concrete were disengaged prior the analysis of the original wall. At the end of the initial analysis, the repair and retrofitting was simulated by engaging the elements corresponding to the vertical and horizontal FRP, including link-bond elements, and the elements defining the repaired concrete. Removing of concrete in the lower 250 mm of the web and boundary elements was simulated by disengaging the originally engaged elements present in this zone.

Analysis

The loading history of the original walls, LSW1 and MSW1, consisted of three repetitions of incremental cyclic displacement of 2 mm to failure, applied along the top loading beam. After repair and retrofitting, the walls, FRPLSW1 and FRPMSW1, were tested following the same loading pattern as the original walls.

The reported hysteretic response of the original wall, LSW1, was rounded without a clear yield plateau and displayed significant stiffness and strength degradation in the post-peak range (Fig. 5-53). The wall reached its maximum lateral strength of 262 kN during the loading cycle to 8 mm of displacement. Thereafter, the wall sustained

additional cyclic displacements to failure, which occurred at 11 mm. Failure of Wall LSW1 was reported as shear sliding at the base of the wall just above the foundation beam. The reported hysteretic loops were narrow with significant pinching, which reflected shear stiffness degradation during the course of testing. The wall was capable of dissipating substantial energy; however, shear-related mechanisms limited the energy dissipation capacity.

The analysis of the original wall, LSW1, predicted satisfactory hysteretic response (Fig. 5-54), specifically in terms of stiffness and strength degradation in the positive direction. Predicted strength degradation in the post-peak range was associated with concrete softening, which led to the predicted crushing of the concrete elements followed by shear sliding. Initial stiffness and ductility was accurately captured; however, the lateral strength was somewhat overestimated. Peak lateral strength of 293 kN was predicted at a lateral displacement of 7 mm. Predicted maximum lateral displacement of 11 mm corresponded to that recorded. Unloading and reloading of the hysteretic cycles were in good agreement with the reported response. The analysis predicted slightly less pinching of the hysteretic loops, which did not affect the prediction of the energy dissipation.

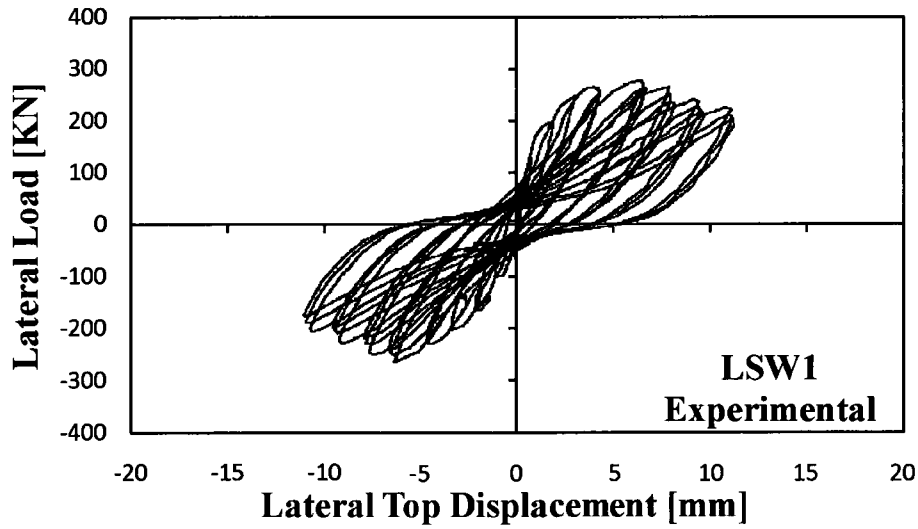

Fig. 5-53 Experimental Load-Deformation Response for Wall LSW1 (Modified from Antoniades et al., 2003)

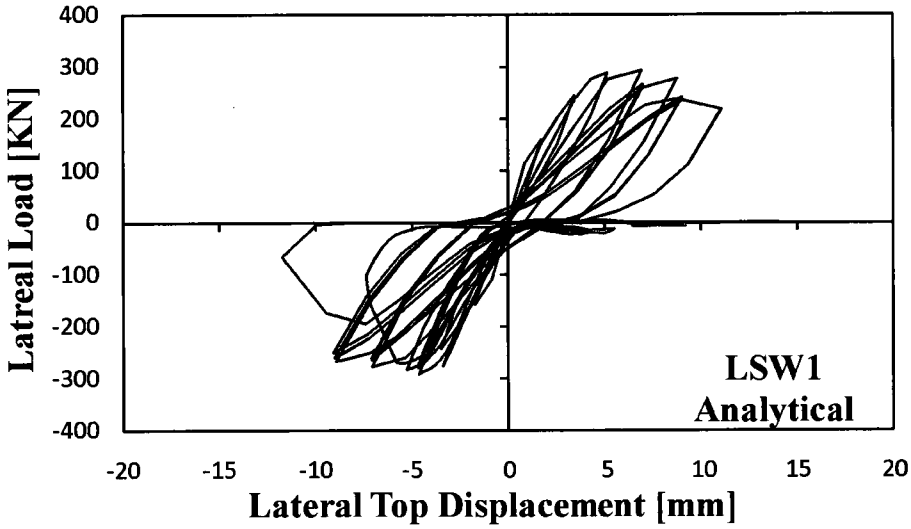

Fig. 5-54 Analytical Load-Deformation Response for Wall LSW1

The repair and retrofitting procedure permitted Wall FRPLSW1 to recover the initial stiffness and ductility, and improved upon the lateral strength experienced by the original wall. However, the wall responded asymmetrically as illustrated in Fig. 5-55. Peak lateral strength of 325 kN was recorded at 10 mm in the positive direction and 6 mm in the negative direction. Wall FRPLSW1 sustained stiffness and strength degradation in the post-peak range until failure, similar to the original wall. Actual failure of the wall consisted of peeling off of the FRP used in the anchorage of the vertical FRP strips at 12 mm of displacement. Less pinching and slightly more energy dissipation was recorded compared to the original wall.

Predicted response of Wall FRPLSW1 (Fig. 5-56) captured behavioural aspects such as initial stiffness, strength capacity, ductility and energy dissipation, specifically in the negative direction. In this direction, the analysis predicted a strength capacity of 290 kN at a corresponding displacement of 7 mm. Furthermore, the predicted unloading and reloading, and energy dissipation in the negative direction were in good agreement with that reported. In the positive direction, the predicted response was stiffer and reached higher peak strength at a lower displacement compared to the experimental response. The analysis underestimated the stiffness and strength degradation observed during testing. The positive peak strength of 387 kN was

predicted at a displacement of 7 mm, while the positive peak strength of 325 kN was reported at a displacement of 5 mm during testing. The predicted failure mechanism did not capture the failure of the anchor of the vertical CFRP observed during testing. However, rupture of the vertical reinforcement along with crushing of concrete after failure of the CFRP anchor was properly simulated during the second excursion to 7 mm. Noteworthy is that the CFRP anchorage was not simulated.

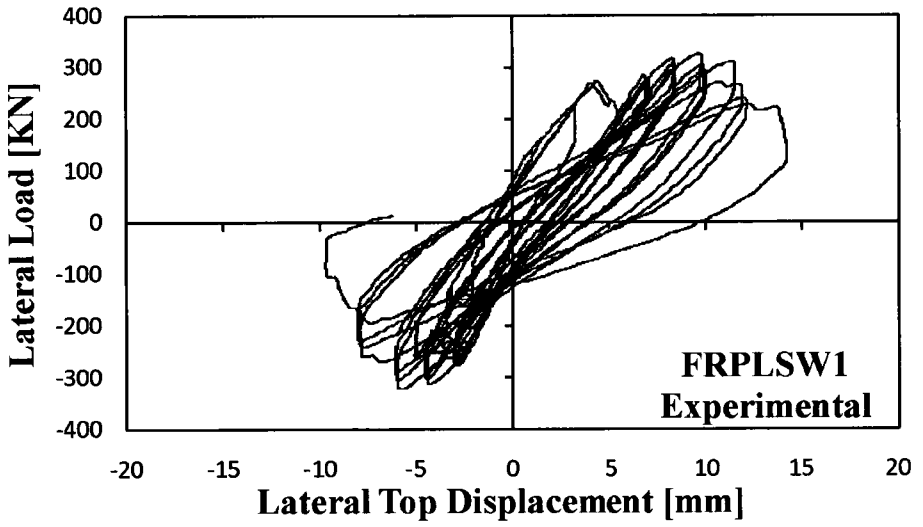

Fig. 5-55 Experimental Load-Deformation Response for Wall FRPLSW1 (Modified from Antoniades et al., 2003)

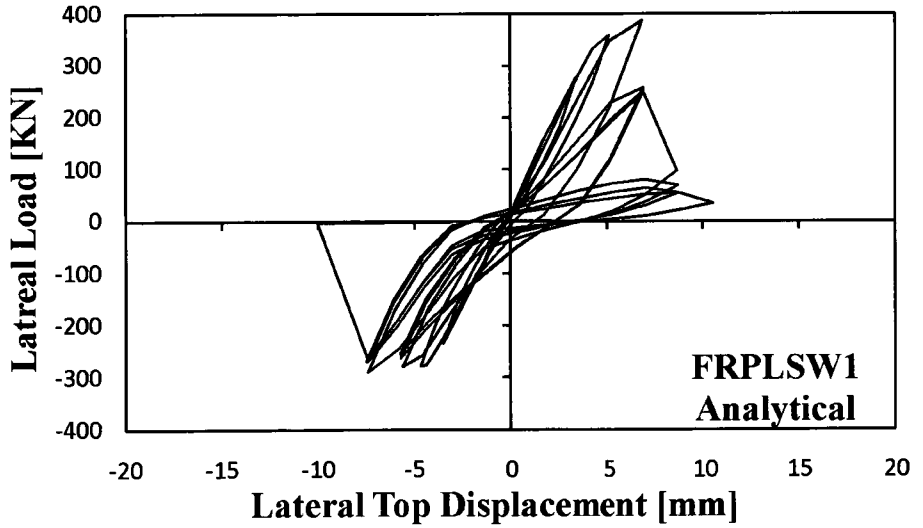

Fig. 5-56 Analytical Load-Deformation Response for Wall FRPLSW1

Nonlinear Analysis of Repaired/Retrofitted Shear Walls

The original wall, MSW1, displayed a rounded hysteretic response without a clear yield plateau (Fig. 5-57). During the first cycles to 11 mm of displacement, the hysteretic response showed insignificant stiffness degradation between repetitions to the same displacement. The wall reached maximum lateral load capacity of 197 kN during the first repetition to 11 mm of displacement, which was sustained to 15 mm. During the post-peak, the wall experienced stiffness and strength degradation up to a maximum displacement of 26 mm, which corresponded to a displacement ductility of approximately 3.0. During the second repetition to 26 mm of displacement, the wall failed by shear sliding at the base foundation beam. The hysteretic loops exhibited some pinching; however, energy dissipation capacity was evident. The pinching effect was the result of the shear stiffness degradation at the base of the wall.

The predicted response of the original wall, MSW1, (Fig. 5-58) compared very well with the observed response. Characteristics of the response such as initial stiffness, unloading and reloading, and pinching were accurately captured. The analysis predicted a lateral strength of 203 kN at 9 mm of displacement, which was 3% higher than the reported lateral load capacity. Beyond 15 mm, the predicted response maintained the lateral load strength to approximately 25 mm of displacement, while strength degradation was more evident in the observed behaviour. This difference can be attributed to the assumed strain hardening of the vertical steel, which was not reported by Antoniades et al. (2005). However, the displacement corresponding to the ultimate lateral load capacity (26 mm) was in agreement with the reported displacement. Failure in the form of shear sliding was adequately predicted, although it was delayed one additional cycle to 30 mm of displacement. The predicted energy dissipation, although slightly higher than the observed energy dissipation as result of the strength overestimation in the post-peak response, was satisfactorily captured.

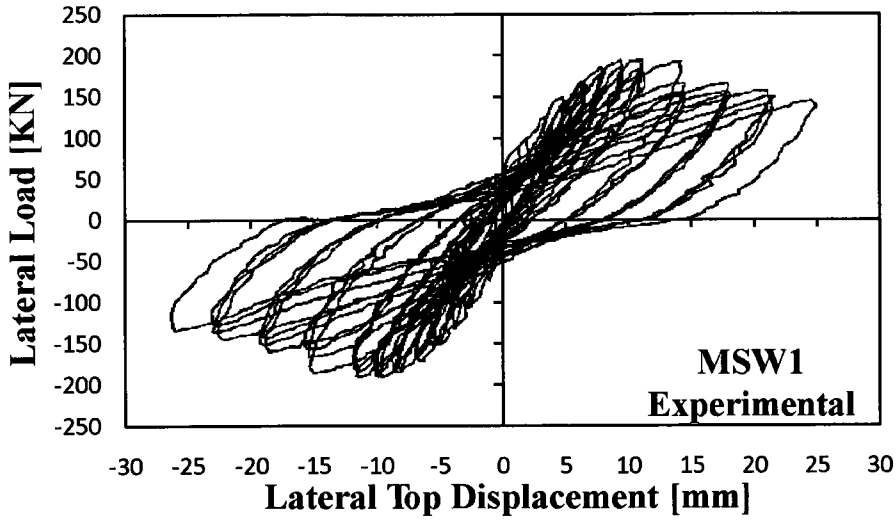

Fig. 5-57 Experimental Load-Deformation Response for Wall MSW1 (Modified from Antoniades et al., 2005)

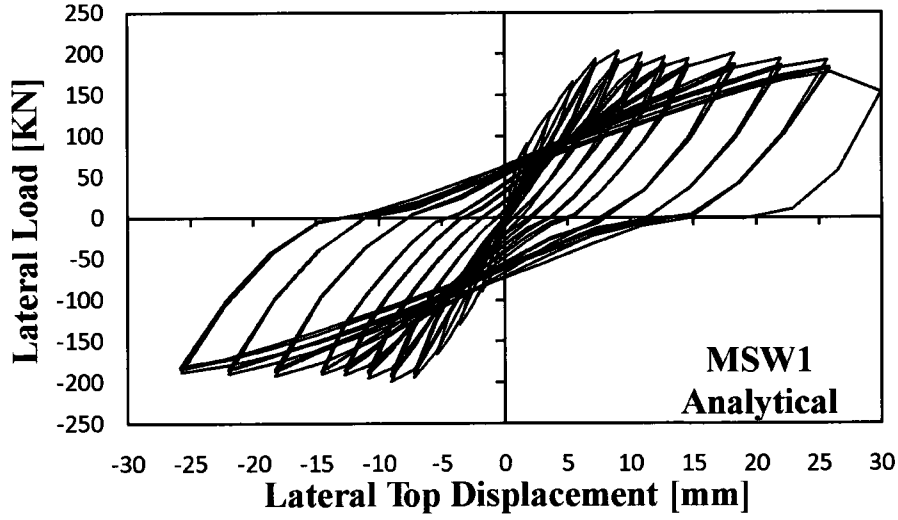

Fig. 5-58 Analytical Load-Deformation Response for Wall MSW1

The repaired and retrofitted wall, Wall FRPMSW1, responded with enhanced strength and similar initial stiffness relative to the original wall; however, with less ductility and energy dissipation (Fig. 5-59). A maximum lateral load capacity of approximately 245 kN was reached at 12 mm of displacement, followed by strength degradation mainly due to concrete softening. The failure mechanism involved rupturing of the

vertical FRP strip anchors at a lateral displacement of 15 mm. Subsequently, a complete loss of lateral load capacity resulted.

During preliminary analysis of the repaired/retrofitted wall, FRPMSW1, the strength was overestimated since failure as a consequence of the anchoring system of the vertical CFRP was not modelled. An improvement was obtained by disconnecting the vertical CFRP from the foundation beam during the third repetition of loading to 15 mm of displacement. The modified model predicted failure as rupturing of the vertical reinforcing bars. A more detailed model of the anchor would provide a more accurate prediction of the failure mode. The ultimate strength of 251 kN was predicted at a displacement of 15 mm. Figure 5-60 provides the analytical load-deformation responses of Wall FRPMSW1. Given the simplified model to represent rupturing of the anchoring system, the predicted response was in good agreement with the observed response.

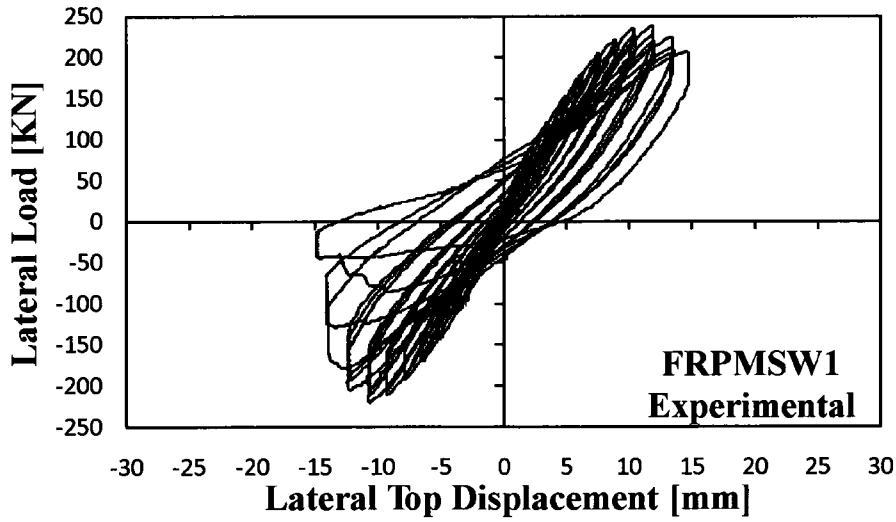

Fig. 5-59 Experimental Load-Deformation Response for Wall FRPMSW1 (Modified from Antoniades et al., 2005)

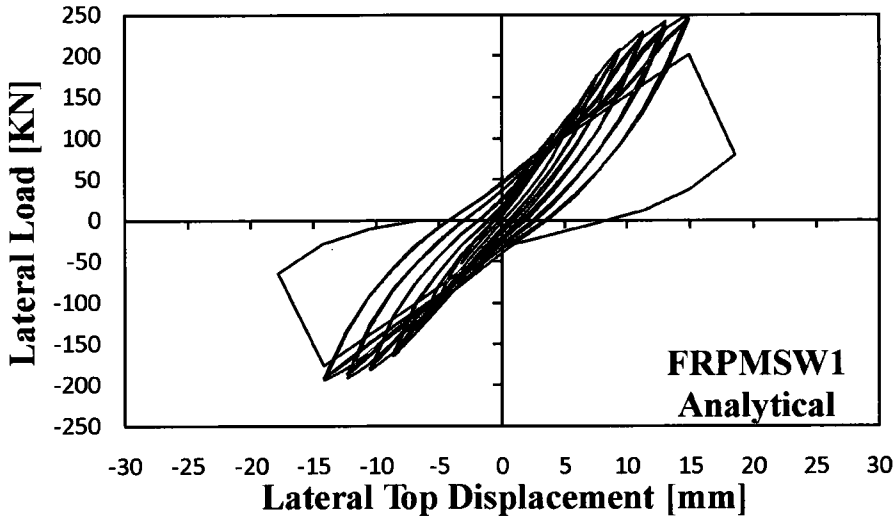

Fig. 5-60 Analytical Load-Deformation Response for Wall FRPMSW1

5.9 Other Techniques

5.9.1 Local Replacement of Concrete

5.9.1.1 Walls SW31/SW31R, SW32/SW32R, and SW33/SW33R

Testing

Lefas and Kotsovos (1990) tested Walls SW31/SW31R, SW32/SW32R, and SW33/SW33R as part of an investigation of repairing of shear walls. The walls were 650 mm wide, 1300 mm high and 65 mm thick (Fig. 5-61). Reinforcement comprised of 8 mm and 6.25 mm reinforcing bars in the vertical and horizontal directions, respectively. Additionally, boundary elements were provided with 4 mm diameter hoops for confinement. Material properties are listed in Table 5-2. Repair of the walls involved removing the lower 150 mm x 200 mm portion of concrete subjected to high compressive stress in the boundary element and replacing with new concrete of similar properties.

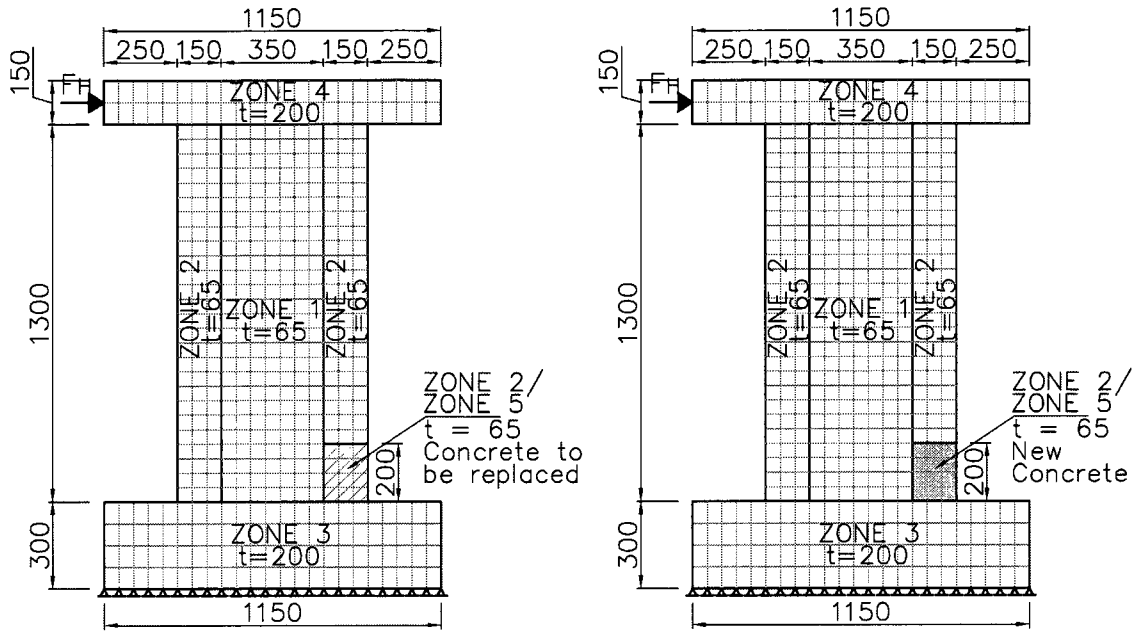

Fig. 5-61 Finite Element Mesh of Wall: (a) SW31, SW32, and SW33; (b) SW31R, SW32R, and SW33R. All Dimensions in mm

Modelling

In the FE model, the wall was divided into four homogeneous concrete zones with smeared steel: web, boundary elements, foundation beam, and top beam as illustrated in Fig. 5-61. The original concrete in the web and boundary elements was modelled with 338 rectangular elements: 13 horizontally and 26 vertically. In addition, the repair zone in the lower 150 mm x 200 mm contained 12 double meshed elements to represent the zone where concrete was removed and replaced with new concrete (zone 5 in Fig. 5-61). Removing of concrete was simulated by disengaging the 12 elements in the repair zone, which originally were engaged to simulate the original concrete. Placing of new concrete was then simulated by engaging the initially disengaged 12 elements, which represented the new concrete after repair.

Analysis

The loading history of the original walls, SW31 and SW32, and the repaired wall, SW32R, consisted of initial reverse cyclic loading, followed by monotonic loading. Conversely, the loading history of the repaired wall, SW31R, was monotonic.

The originals walls, SW31 and SW32, responded similarly as evident in Fig. 5-62 and Fig. 5-63. They sustained similar initial stiffness and rounded response during yielding of the vertical reinforcement. First yield was recorded at approximately 4 mm, which corresponded to a strength capacity of 65 kN. Wall SW31 reached its peak strength of 116 kN at an ultimate displacement of 23 mm, while Wall SW32 reached its peak strength of 111 kN at an ultimate displacement of 24 mm. Observed failure of both walls involved crushing of concrete in the lower zone of the compressive boundary element. Walls SW31 and SW32 displayed similar unloading and reloading with stiffness degradation between repetitions and pinching of the hysteretic loops. However, the hysteretic loops for Wall SW32 were wider owing to the differences in the loading history.

The analysis predicted similar response for the original walls, SW31 and SW32 (Fig. 5-64 and Fig. 5-65). The predicted initial stiffness of both walls was adequately captured; however, the analysis predicted a clear yield point, which was in contrast with the recorded rounded yielding response. The analysis captured the hysteretic response of the initial cyclic loading, although the analysis overestimated the degree of pinching. Lateral strength was underestimated, and the maximum displacement was overestimated. The analysis predicted maximum lateral strength of 104 kN at the ultimate displacement of 30 mm for Wall SW31, and maximum lateral strength of 110 kN at the ultimate displacement of 33 mm for Wall SW32. At ultimate, the analysis predicted failure due to crushing of concrete in the lower zone of the compressive boundary element. Differences in the response at yielding are attributable to the constitutive model for the reinforcement, which assumes perfect tri-linear response.

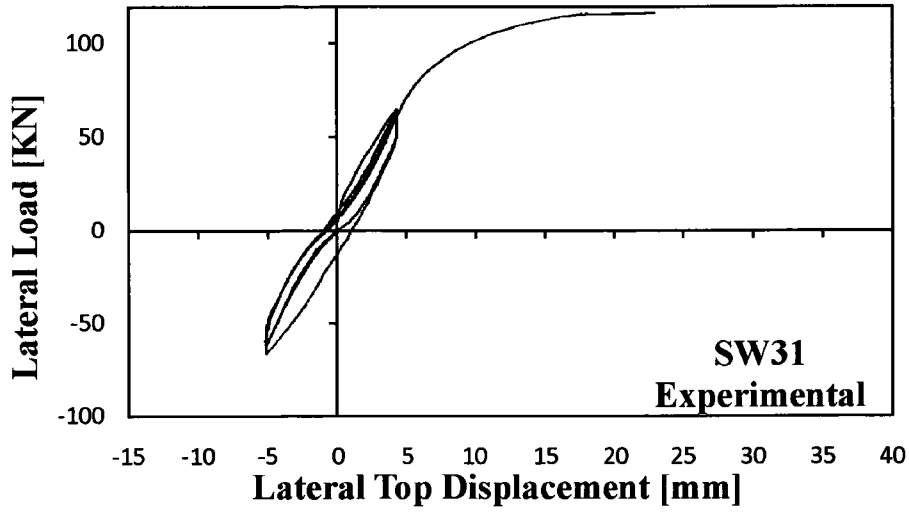

Fig. 5-62 Experimental Load-Deformation Response for Wall SW31 (Modified from Lefas and Kotsovos, 1990)

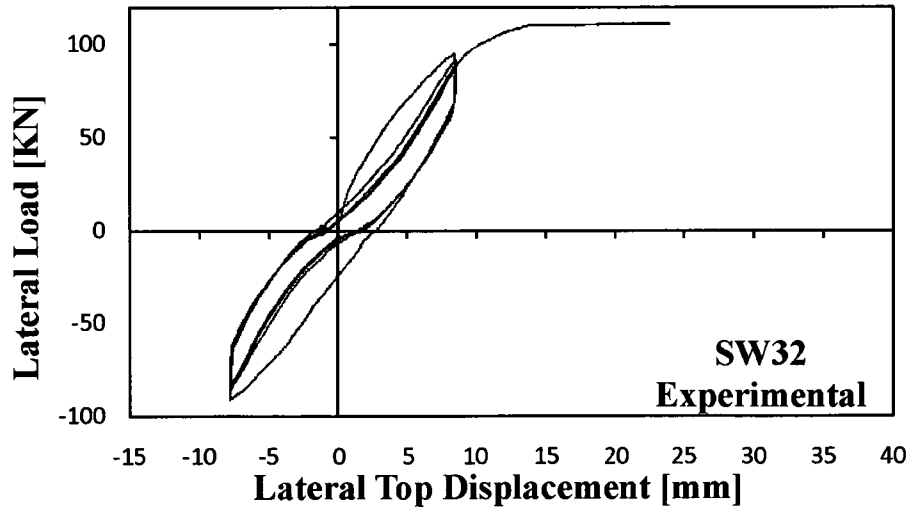

Fig. 5-63 Experimental Load-Deformation Response for Wall SW32 (Modified from Lefas and Kotsovos, 1990)

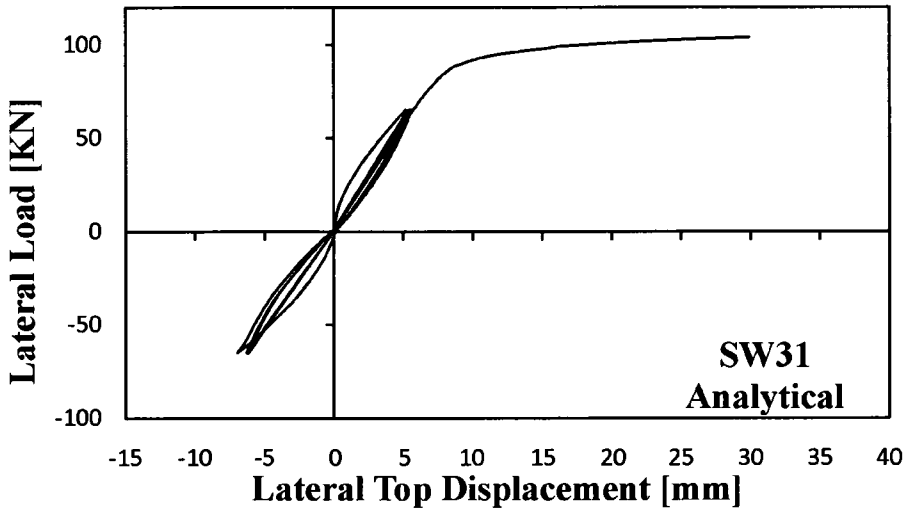

Fig. 5-64 Analytical Load-Deformation Response for Wall SW31

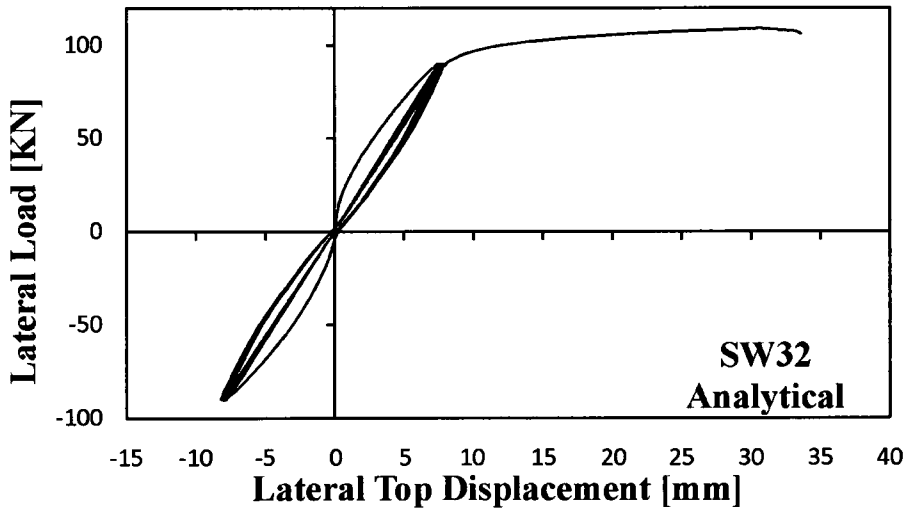

Fig. 5-65 Analytical Load-Deformation Response for Wall SW32

The repaired wall, SW31R, exhibited less initial stiffness, and more strength and displacement capacity compared to the original wall (Fig. 5-66). First yielding occurred at approximately 13 mm and corresponded to approximately 120 kN. Similar to the original wall, the wall did not present a clear yield point and displayed a rounded response. The response flattened and reached the maximum strength of 140 kN at approximately 20 mm of displacement. Failure of the wall was reported at 26 mm of

displacement and involved crushing of the concrete in the lower zone of the compressive boundary element. The repaired wall, SW32R, did not completely recover its original behavioural characteristics as shown in Fig. 5-67. The initial stiffness, strength and maximum displacement were lower than those recorded for the original wall. First yielding was recorded at a similar displacement as the original wall. Furthermore, yielding of the vertical reinforcement resulted in a rounded response, which was sustained up to failure at 15 mm. Ultimate strength of 90 kN was recorded at failure, which consisted of crushing of concrete and rupturing of the vertical reinforcement. The recorded hysteretic loops were highly pinched and displayed significant stiffness degradation between repetitions. The testing reported low energy dissipation capacity.

The analysis of the repaired walls, SW31R and SW32R, predicted responses with higher initial stiffness than reported, and with a clear yield point followed by a flat response until failure (Fig. 5-68 and Fig. 5-69). Initial stiffness of the repaired walls corresponded to that of the original walls; therefore, the analysis predicted complete recovery of the initial stiffness. Although the predicted maximum lateral displacement compared well to that recorded, the strength capacity was underestimated by 20% for Wall SW31R, and overestimated by 13% for Wall SW32R. Lateral strength of 112 kN was predicted at 29 mm for Wall SW31R, while lateral strength of 102 kN was predicted at 20 mm for Wall SW32R. Crushing of concrete in the lower zone of the compressive boundary element was accurately predicted. Furthermore, the analysis of Wall SW32R captured the rupture of the vertical reinforcement. Unloading and reloading of the predicted hysteretic loops displayed less stiffness and strength degradation than recorded. Discrepancies in the predictions, specifically in terms of initial stiffness and strength capacity, may be due to premature failure of the interface between the existing and new concrete. Another reason could be underestimation of the damage during the analysis of the original wall.

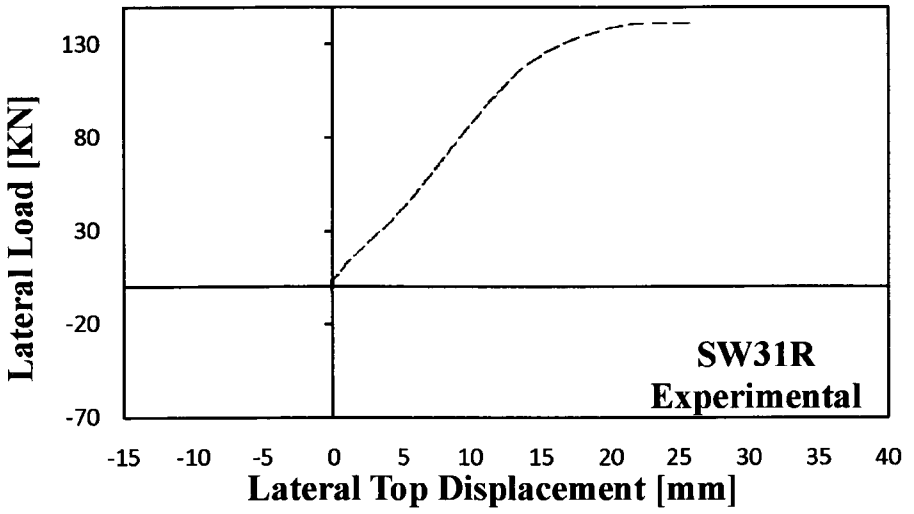

Fig. 5-66 Experimental Load-Deformation Response for Wall SW31R (Modified from Lefas and Kotsovos, 1990)

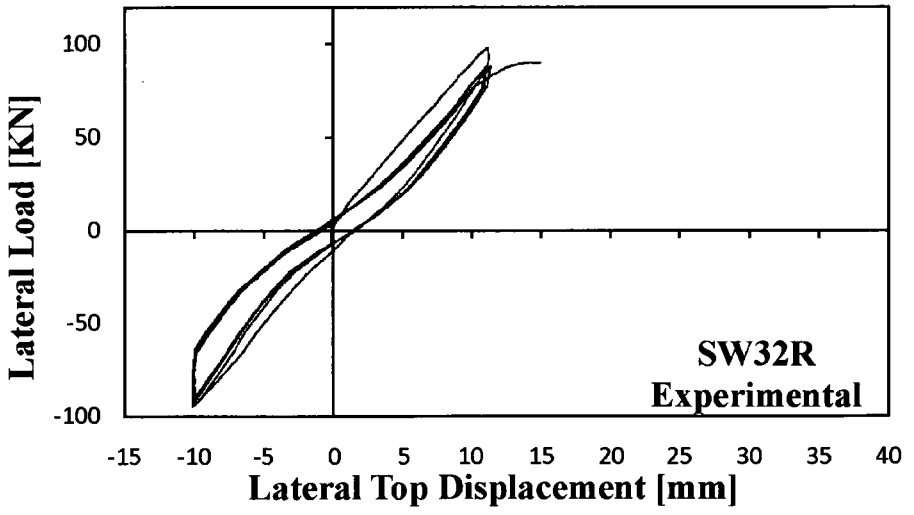

Fig. 5-67 Experimental Load-Deformation Response for Wall SW32R (Modified from Lefas and Kotsovos, 1990)

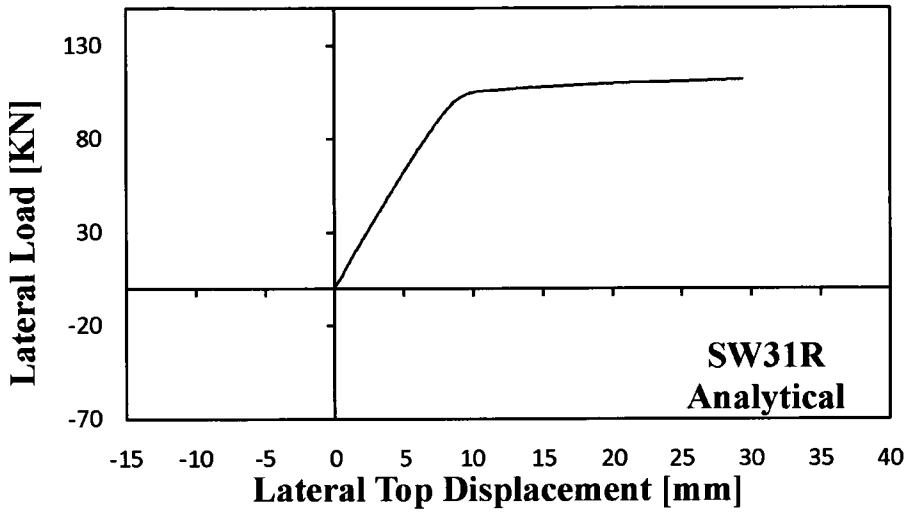

Fig. 5-68 Analytical Load-Deformation Response for Wall SW31R

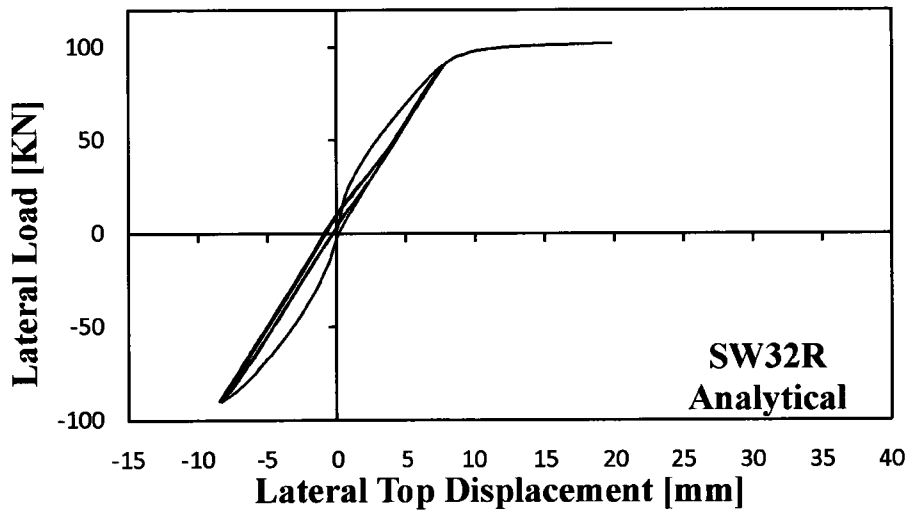

Fig. 5-69 Analytical Load-Deformation Response for Wall SW32R

The load history of the original wall, SW33, and repaired wall, SW33R, was a combination of initial load-controlled reverse cycles to yielding and monotonic loading thereafter.

The observed behaviour of the original wall, SW33, included low ductility and failure at a displacement of 25 mm (Fig. 5-70). Yield strength of 89 kN was reached at approximately 8.5 mm during the first repetition to the second cycle. During the

monotonic loading phase, the wall reached maximum lateral strength of 112 kN corresponding to a displacement of 25 mm. Failure in the form of crushing of concrete was localized in the lower region of the boundary elements in the compressive zone, and was preceded by wide vertical cracks and spalling of the concrete. After concrete crushing at 25 mm of displacement, the original wall was unloaded and repaired.

The predicted response of Wall SW33 (Fig. 5-71) compared well to that reported. The first two cycles to 4.5 mm and 9 mm were in excellent agreement in terms of lateral load capacity; however, the predicted cycles were narrower and less rounded. The lateral displacement corresponding to 105 kN, where the monotonic loading was applied, was overestimated by approximately 5 mm, resulting in more damage. The lateral load capacity of 108 kN, corresponding to a displacement of 37 mm, was accurately predicted; it deviated from the actual lateral load capacity by 4%. Failure due to crushing of concrete was adequately captured; however, it was delayed by 12 mm. The overestimation of the displacement corresponding to failure was, for the most part, caused by the idealized stress-strain relationship of the reinforcing steel, which assumed a flat yield plateau. A non-flat yield plateau would cause an increase in the load capacity and increase the strain in the concrete, resulting in damage of the concrete.

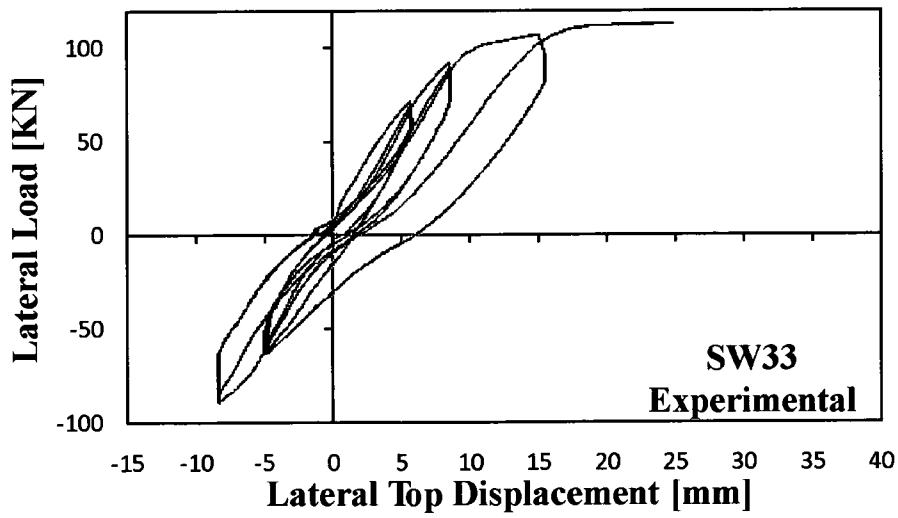

Fig. 5-70 Experimental Load-Deformation Response for Wall SW33 (Modified from Lefas and Kotsovos, 1990)

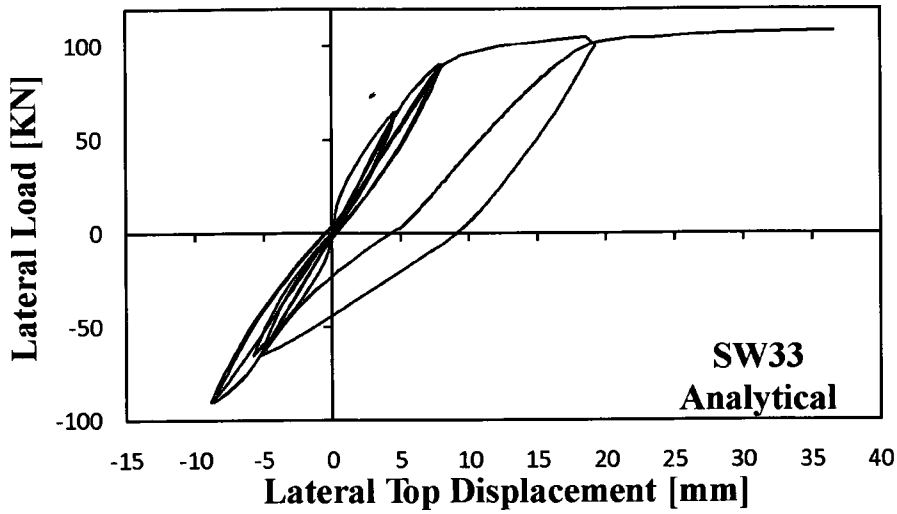

Fig. 5-71 Analytical Load-Deformation Response for Wall SW33

Behaviour of the repaired wall, SW33R, was similar to the original wall and included low ductility and failure due to concrete crushing. However, failure occurred at a displacement of 17 mm, which corresponded to a maximum lateral strength of 94 kN (Fig. 5-72). Repair of the wall did not allow a recovery of the initial stiffness; the initial stiffness of the repaired wall was equal to the residual stiffness of the original wall. Hysteretic cycles were narrow and pinched compared to the original wall.

Figure 5-73 demonstrates excellent agreement between the predicted response and the reported response of the repaired wall, SW33R, specifically the initial stiffness, the lateral load strength, and the displacement of the cyclic loading phase. However, similar to the original wall, the hysteretic cycles were slightly narrower and less rounded. The load capacity (106 kN) and corresponding displacement (22 mm) of the repaired wall were overestimated by 13% and 29%, respectively. The analysis predicted the same failure mode observed in the testing, which was crushing of concrete in the lower compressive zone of the wall. The discrepancies are related to the results of the analysis of the original wall in which lower load capacity and greater displacement capacity were obtained. Therefore, less damage was predicted and retained in the analysis of the original wall, which was subsequently carried forward in the analysis of the repaired wall.

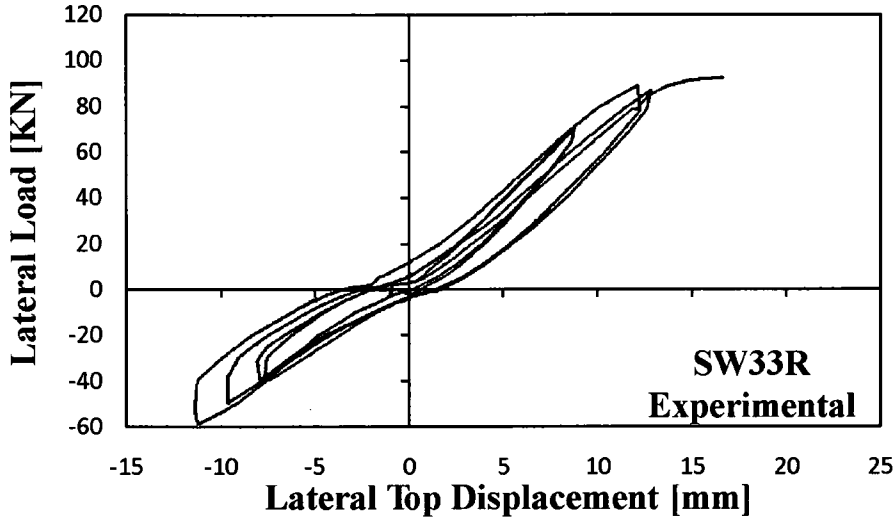

Fig. 5-72 Experimental Load-Deformation Response for Wall SW33R (Modified from Lefas and Kotsovos, 1990)

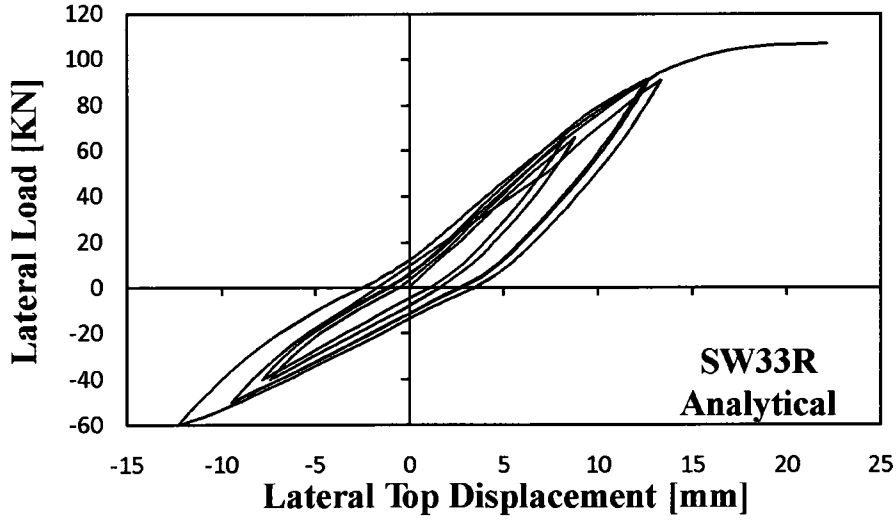

Fig. 5-73 Analytical Load-Deformation Response for Wall SW33R

5.9.2 Bolting of Steel Plates

5.9.2.1 Walls W11/W11RP

Testing

Taghdi et al. (2000) tested to failure the squat reinforced concrete Wall W11, which had an aspect ratio of 1.0. After failure, the wall was repaired and renamed W11RP. Repair consisted of bolting two vertical 160 mm x 4.76 mm steel plates near each end face without treatment of the damaged concrete. Bolt spacing in the vertical steel plates was chosen to prevent elastic buckling. The vertical steel plates were anchored to the foundation by means of 154 mm x 154 mm x 15.9 mm steel angles and 19-mm diameter anchor bolts. The layout of the original and repaired wall is shown in Fig. 5-74, and the material properties are listed in Table 5-2.

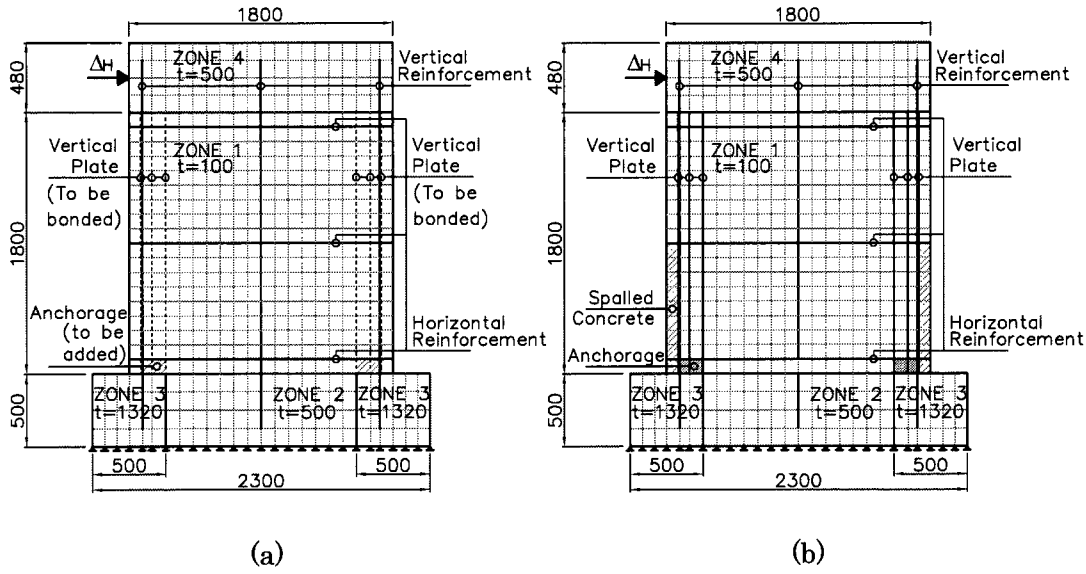

Fig. 5-74 Finite Element Meshing of Walls: (a) W11; (b) W11RP. All Dimensions in mm

Modelling

The FE model consisted of four homogeneous concrete zones as depicted in Fig. 5-74. Zone one corresponded to the plain concrete in the web portion of the wall, which included vertical truss bars to simulate the internal vertical and horizontal

reinforcement. Zones two and three defined the stiff I-shape foundation, where zone three was deeper than zone two. Finally, zone four defined the stiff top beam. Three sets of 18 ductile truss bar elements perfectly bonded along the height of the wall were attached to the concrete elements near each end of the wall to simulate the externally bolted vertical steel plates. A model with link-bond elements was investigated to capture buckling of the plates; however, this phenomenon was not well captured owing, in most part, to the link-bond properties not reflecting the bolting technique used to attach the steel plates to the concrete. Meshing of the wall consisted of a 20 x 18 grid of rectangular concrete elements defining the web, and 184 additional elements defining the foundation and top beam. Furthermore, four stiff concrete elements were defined near the bottom corners of the wall to simulate anchorage of the steel plates to the foundation during the repair process. Prior to the analyses of the original wall, the elements defining the steel plates including the anchorage were disengaged. After damage, the concrete elements remained engaged, except for 18 concrete elements at the ends of the wall to simulate the observed loss of sectional area due to spalling of concrete. Then, the truss bars defining the vertical steel plates, and the concrete elements defining the anchors to the foundation were engaged.

Analysis

Loading of the original wall, Wall W11, consisted of incremental repetitions of lateral cyclic drifts of 0.1% (fraction of the height of the wall) to 1.0% followed by incremental repetitions of lateral cyclic drifts of 0.5% to failure. Likewise, loading of the repaired wall, Wall W11RP, consisted of initial repetitions to 0.1% lateral drift followed by incremental lateral cyclic drifts of 0.5% to failure. Furthermore, the wall was subjected to a total axial load of 121 kN, including the self weight of the top beam and horizontal actuator.

Original wall, Wall W11, reached yield strength of approximately 155 kN during loading to 0.2% lateral drift, according to the reported hysteretic response shown in Fig. 5-75. Thereafter, the wall sustained a clear yield plateau and increased its strength capacity until reaching the ultimate strength of 173 kN at 2.0% lateral drift. Taghdi et al. (2000) reported rigid-body rotation behaviour (rocking) with the vertical

reinforcement controlling the wall rotation. This behaviour promoted crushing of concrete at the end of the walls and elastic buckling of the vertical reinforcing bars. This mechanism resulted in failure due to discontinuity of the construction joint between the web and the foundation, and rupturing of the middle vertical reinforcing bars. Unloading and reloading, and pinching of the hysteretic loops indicated shear stiffness degradation associated with the aforementioned rocking behaviour. Note that the reported response displays an abrupt loss of strength during unloading. Although the wall was controlled by rocking, the wall achieved good ductility with satisfactory energy dissipation capacity.

The analysis of the original wall, Wall W11, accurately captured the initial stiffness as shown in Fig. 5·76. Yield strength of 145 kN at 0.2% lateral drift compared well to that reported. After yielding, the response flattened and gained marginal lateral strength, similar to that displayed in the experimental response. The analysis predicted a maximum strength of 156 kN at 2.0% lateral drift, which underestimated that recorded by 9%. Maximum displacement of 2.0% lateral drift, corresponding to a displacement ductility of approximately 10, was accurately predicted. During the first repetition to 2.5% lateral drift, the analysis predicted failure of the wall due to crushing of concrete at the ends of the wall coupled with high shear distortion. The analysis neither captured buckling nor rupturing of the vertical reinforcement. However, the analysis predicted crushing and cracking of the concrete elements surrounding the vertical reinforcement, which indicated the buckling phenomenon. Cracking of the concrete elements surrounding the extreme vertical reinforcement corresponded to the spalling of concrete observed during buckling. Predicted unloading and reloading of the hysteretic loops differed somewhat to that reported, which led to a slight overestimation of the energy dissipation. The unloading branch displayed gradual strength reduction, not observed in the reported response, and the reloading branch predicted less stiffness degradation, specifically beyond 1.0% lateral drift. This discrepancy may be due to the analysis not accurately capturing the rocking behaviour and the formation of a rigid body after failure of the construction joint. Note that the vertical reinforcement was assumed perfectly bonded to the concrete, thus the anchorage slip leading to the rocking motion was not modelled. Improvements could be

achieved by using bond elements between the vertical internal reinforcement and the concrete elements.

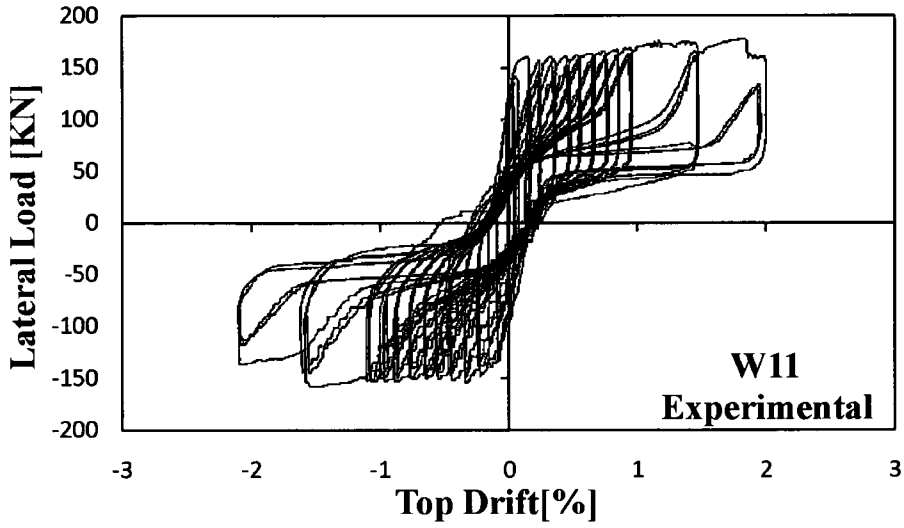

Fig. 5-75 Experimental Load-Deformation Response for Wall W11 (Modified from Taghdi et al., 2000)

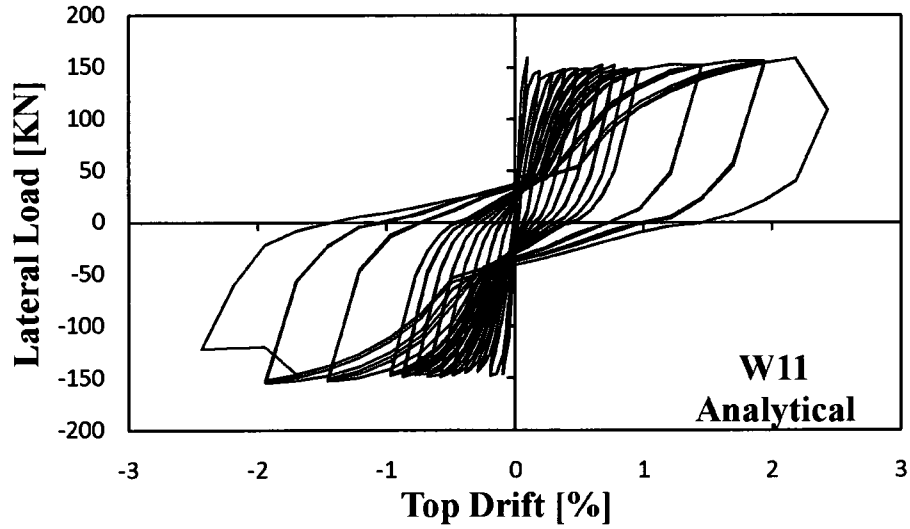

Fig. 5-76 Analytical Load-Deformation Response for Wall W11

Repaired wall, Wall W11RP, recovered the initial stiffness, and improved the strength capacity, ductility, and energy dissipation of the original wall. The hysteretic response

of the repaired wall is shown in Fig. 5-77. The onset of plastic buckling of the steel plates was reported at 1.32% lateral drift, corresponding to a lateral strength of approximately 260 kN. The wall reached its peak strength of 269 kN at 1.5% lateral drift, and was sustained to 2.0% lateral drift. The recorded post-peak response indicated stiffness and strength degradation, particularly in the positive direction. During the course of testing, the wall sustained significant shear sliding at the base, which was related to slippage of the anchor bolts. Failure was reported during the first repetition to 2.5% lateral drift in the positive direction where the wall suffered a sudden drop in strength. However, the wall sustained an additional cycle to 3.0% lateral drift in the negative direction. The cracking pattern at the end of testing consisted of two major wide diagonal cracks in each direction along with the existing horizontal cracks along the construction joint sustained by the original wall.

Before the analysis of the repaired wall, Wall W11RP, rupturing of the middle vertical reinforcing bars was simulated, in addition to bolting of the steel plates, to be consistent with the experimental program. During the simulation, the truss bar element of the middle vertical reinforcement in the web near the foundation was disengaged. As previously stated, bolting of the steel plates was simulated with perfectly bonded truss elements along the height of the wall. The analytical response (Fig. 5-78) of the repaired wall was in good agreement with the reported response in terms of strength capacity, lateral strength and stiffness degradation. However, the analysis underestimated the initial stiffness and overestimated the pinching phenomenon, which resulted in less predicted total energy dissipation. Peak lateral strength was accurately predicted in both directions; 264 kN at 1.5% lateral drift in the positive direction, and 217 kN at 3.0% lateral drift in the negative direction. Stiffness and strength degradation in the post-peak range compared to that reported, specifically in the positive direction. The predicted failure mechanism consisted of crushing of concrete with high shear distortion of the concrete elements representing the left anchorage plate, and shear sliding of the second row of concrete elements between 1.5% and 2.0% lateral drift. Beyond 2.0% lateral drift, the analysis predicted extensive damage in the concrete, and the strength capacity was limited to the contribution of the steel plates. Plastic buckling of the vertical steel plates was not

captured, but the predicted shear distortion of the concrete elements crossing the truss elements defining the steel plates suggested this phenomenon. Note that the simulation of buckling requires bond elements to connect the truss elements to the concrete elements.

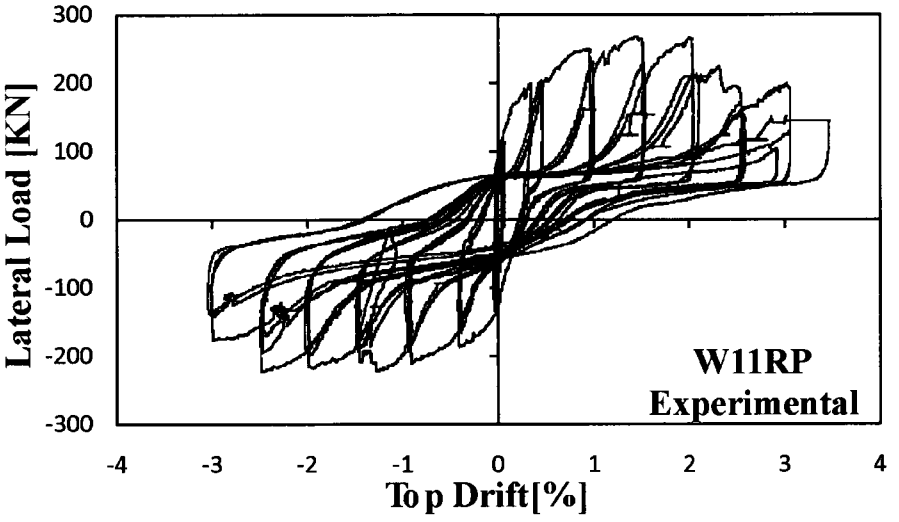

Fig. 5-77 Experimental Load-Deformation Response for Wall W11RP (Modified from Taghdi et al., 2000)

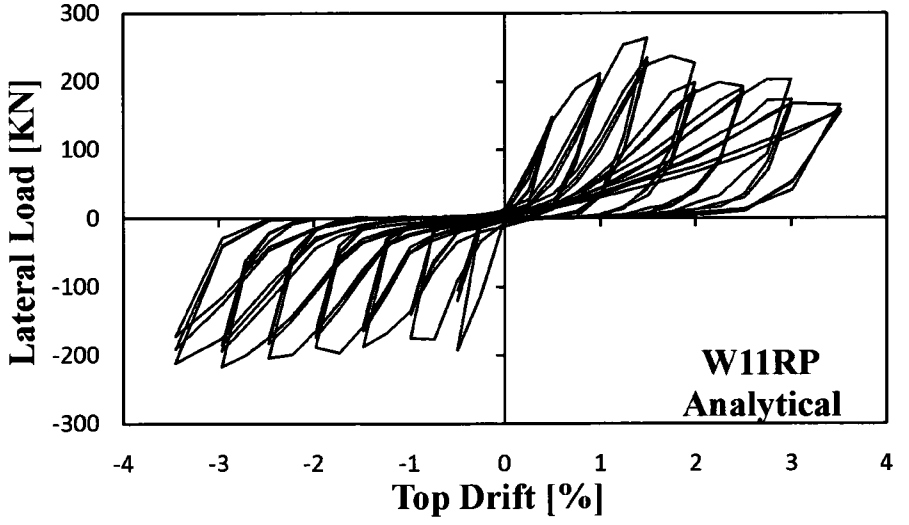

Fig. 5-78 Analytical Load-Deformation Response for Wall W11RP

5.9.2.2 Wall W11R

Testing

Taghdi et al. (2000) tested Wall W11R, which had similar geometrical characteristics as Walls W11 and W11RP. The wall was retrofitted by means of two 220 mm x 3.81 mm diagonal steel plates and two vertical 80 mm x 3.81 mm steel plates bolted near each end face of the wall. The bolt spacing was chosen to prevent elastic buckling of the plates. The diagonal steel plates were welded at the centre of the wall where they intercepted. In addition, both diagonal and vertical plates were welded to 150 mm x 150 mm angles, which were anchored to the foundation. The layout of the retrofitted wall is shown in Fig. 5-79, and the material properties are listed in Table 5-2.

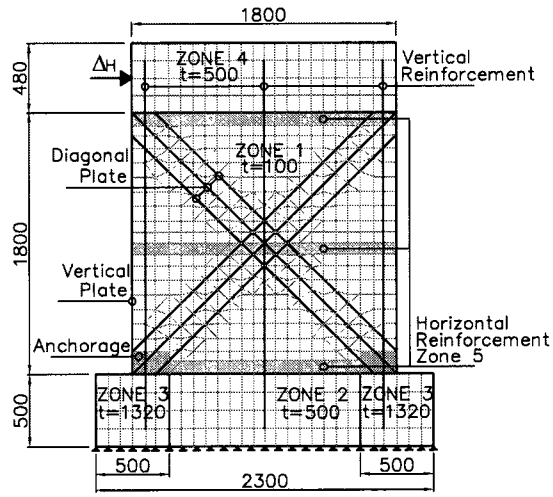

Fig. 5-79 Finite Element Meshing of Wall W11R. All Dimensions in mm

Modelling

The FE model, illustrated in Fig. 5-79, was defined by five homogeneous concrete zones. The first was a plain concrete zone for the web in which three vertical truss bars were included to simulate the internal vertical reinforcement. The second and third were heavily reinforced concrete zones defining the I-shape foundation. (Note that zone 3 is deeper than zone 2.) The fourth zone was used for the top beam, and the fifth concrete zone contained smeared horizontal reinforcement concentrated in

specific bands in the mesh. The use of the horizontal bands for the horizontal reinforcement was preferred to avoid premature shear sliding in the first row of elements adjacent to the foundation. A refined mesh was investigated, which included truss bar elements for the horizontal reinforcement in this zone, however, no improvement was achieved in the response. To simulate the externally bolted diagonal steel plates, three ductile truss bars perfectly bonded along the wall were attached to the concrete elements. The externally bolted vertical steel plates were modelled with perfectly bonded tension-only truss bars attached at the edges of the wall. Although the steel used in the vertical steel plates was ductile, tension-only elements were used since buckling was observed at an early stage of testing. Previous analysis of Wall W11RP using link-bond elements to attach the plates to the concrete did not capture the buckling phenomenon; therefore, link-bond elements were not used for modelling Wall W11R. Finally, an extra zone was defined at the end of the diagonal steel plates to simulate anchorage to the foundation and avoid undesired stress concentration not observed in the experiment.

Meshing of the web was a combination of rectangular and triangular elements totalling 672; equivalent to a grid of 22 by 20 elements. The constant strain triangular elements were necessary due to the geometric constrains imposed by the diagonal truss bars. All elements were active during the simulation of the retrofitted wall.

Analysis

Loading of the retrofitted Wall W11R consisted of three repetitions of reverse cycles to 0.1% lateral drift and 0.2% lateral drift, and subsequent incremental reverse cycles of 0.5% lateral drift to failure.

First yielding of the vertical reinforcing steel of Wall W11R was observed during the first excursion to 0.5 % lateral drift, followed by buckling of both diagonal and vertical steel plates during the second and third excursions to the same displacement level. Yield strength of 450 kN, corresponding to yielding of the diagonal steel plates, was achieved at 0.5% lateral drift. A post-yield load capacity of 496 kN was sustained to 2.0% lateral drift. At this displacement, the steel plates were significantly stressed,

resulting in rupture of one vertical plate. Furthermore, some internal vertical reinforcement buckled. At 2.5% lateral drift, the steel plates continued to rupture and concrete crushed near the mid-height of the wall between the diagonal and vertical plates. At this stage, the test was halted due to the heavy damage and significant loss of strength. The wall demonstrated ductility capacity; however, shear-related mechanisms such as pinching and significant stiffness and strength degradation were evident as demonstrated in Fig. 5-80.

The analytical response (Fig. 5-81) was in close agreement with the experimental response (Fig. 5-80). Initial stiffness was well predicted; however, the first cycles up to 0.5% lateral drift were slightly less rounded than reported. Approximate yield strength of 500 kN at 0.5% lateral drift was predicted, which overestimated the reported strength by approximately 10%. The flat-top envelope of the predicted response beyond yielding was accurately captured. Yield load was sustained to 1.5% lateral drift where crushing of concrete between the diagonal plates and vertical plates around the quarter-height of the wall and some shear sliding in the plate anchorage zone reduced the strength to approximately 470 kN. From 1.5% to 2.5% lateral drift, the strength capacity was slightly reduced to approximately 460 kN. At 3.0% lateral drift, failure of the wall was predicted; the vertical steel plates ruptured and the strength of the wall was reduced to 307 kN. The analysis captured hysteretic characteristics such as unloading, reloading, pinching of the hysteretic cycles, and energy dissipation capacity. Due to the model, buckling of the internal reinforcement and steel plates was not captured; however, the predicted crushing of the adjacent concrete elements indirectly indicated this phenomenon.

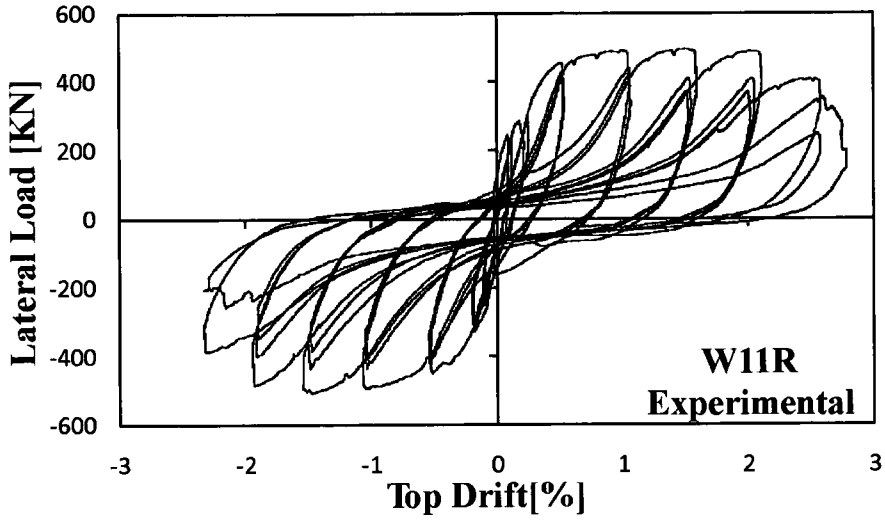

Fig. 5-80 Experimental Load-Deformation Response for Wall W11R (Modified from Taghdi et al., 2000)

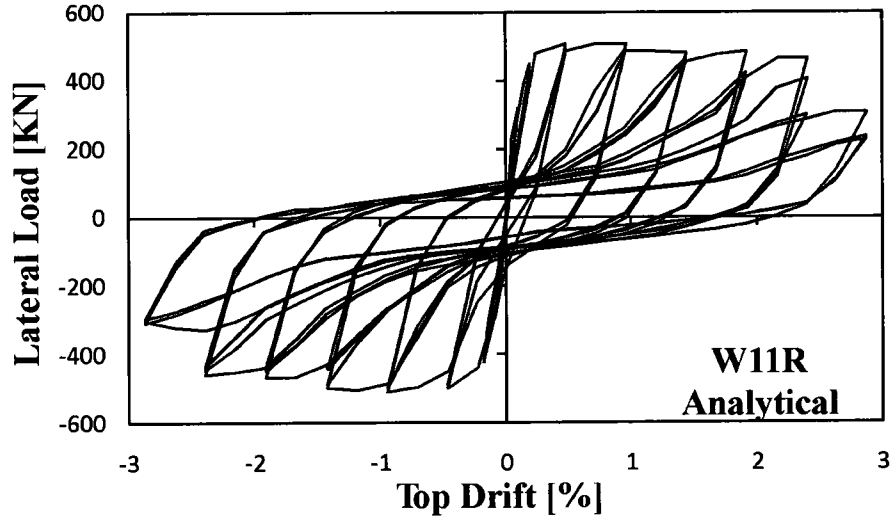

Fig. 5-81 Analytical Load-Deformation Response for Wall W11R

Chapter 6

6 Summary and Conclusions

6.1 Summary and Discussion of Results

The results in Table 6-1 demonstrate the success of the FE method in modelling and assessing seismically repaired and retrofitted reinforced concrete shear walls. The mean strength was slightly underestimated, less than 1%, with a coefficient of variance (COV) of approximately 9%. The mean maximum displacement was overestimated by approximately 8% with a COV of approximately 22%. Table 6-1 also presents the predicted and observed failure modes. Some discrepancies are evident; however, as noted in Chapter 5, these were mainly attributed to uncertainties in the material properties and certain simplifying assumptions in the modelling. Generally, though, the failure modes and preceding mechanisms were well simulated.

Table 6-1 Comparison of Analytical Predictions with Experimental Observations

Wall	Analysis			Experiment			Ana./Exp.	
	Strength [kN]	Max. Disp. [mm]	Failure	Strength [kN]	Max. Disp. [mm]	Failure	Strength	Max. Disp.
Replacement of Concrete								
B5	703	126	Conc. Crushing	762	126	Conc. Crushing	0.923	1.000
B5R	685	151	Conc. Crushing	746	152	Conc. Crushing	0.918	0.993
B9	958	132	Conc. Crushing	977	132	Conc. Crushing	0.981	1.000
B9R	951	170	Conc. Crushing	977	184	Conc. Crushing	0.973	0.924
DP1	1297	14	Shear Sliding	1298	14	Shear Sliding	0.999	1.000
DP1R	1426	11	Shear Sliding	1192	16	Shear Sliding	1.196	0.688
LSW3	282	14	Shear Sliding	268	15	Shear Sliding	1.052	0.933
RLSW3(2)	199	11	Shear Sliding	179	7	Shear Sliding	1.112	1.571
Addition of Reinforcing Bars								
B11	735	126	Conc. Crushing	726	126	Conc. Crushing	1.012	1.000
B11R	672	152	Conc. Crushing	761	155	Conc. Crushing	0.883	0.981
Bonding of Steel Plates								
IC-SW24	121	14	Shear Sliding	125	18	Conc. Crushing	0.968	0.778
IC-SWR24	119	22	Shear Sliding	125	30	Conc. Crushing	0.952	0.733
IC-SW32	57	33	Steel Rupture	62	24	Shear Sliding	0.919	1.375
IC-SW35	69	14	No Failure	75	14	No Failure	0.920	1.000
IC-SWR35	71	34	Shear Sliding	70	24	Conc. Crushing	1.014	1.417
Addition of Steel Rods and Plates with Delay Mechanism								
IC-SW31	82	34	Steel Rupture	90	30	Conc. Crushing	0.911	1.133
IC-SW34	86	30	Steel Rupture	90	26	Conc. Crushing	0.956	1.154
Bonding of FRP Sheets								
LSW1	293	11	Shear Sliding	262	11	Shear Sliding	1.118	1.000
FRPLSW1	387	7	Steel Rupture	325	12	FRP Anchor	1.191	0.583
MSW1	203	26	Shear Sliding	197	26	Shear Sliding	1.030	1.000
FRPMSW1	251	15	Steel Rupture	245	15	FRP Anchor	1.024	1.000
Other Techniques								
SW31	104	30	Conc. Crushing	116	23	Conc. Crushing	0.897	1.304
SW31R	112	29	Conc. Crushing	140	26	Conc. Crushing	0.800	1.115
SW32	110	33	Conc. Crushing	111	24	Conc. Crushing	0.991	1.375
SW32R	102	20	Steel Rupture	90	15	Steel Rupture	1.133	1.333
SW33	108	37	Conc. Crushing	112	25	Conc. Crushing	0.964	1.480
SW33R	106	22	Conc. Crushing	94	17	Conc. Crushing	1.128	1.294
W11	156	2.00%	Shear Sliding	173	2.00%	Reinf. buckl./ conc. crushing	0.902	1.000
W11RP	264	2.00%	Shear Sliding	269	2.00%	Plates buckl./ conc. crushing	0.981	1.000
W11R	507	2.50%	Conc. Crushing	497	2.00%	Plates buckl./ conc. crushing	1.020	1.250
						Mean	0.996	1.081
						COV [%]	9.428	21.922

Summary and Conclusions

The techniques presented in this thesis: replacement of concrete, addition of reinforcing bars, external bonding of steel plates, addition of unbonded steel rods and plates with delay mechanism, external bonding of FRP sheets, and other techniques (local replacement of concrete and bolting of steel plates) were simulated following the engaging-disengaging procedure developed by Vecchio and Bucci (1999).

Modelling of the original shear walls involved definition of the constitutive models of the materials, definition of the geometry and finite element (FE) mesh, and definition of the load patterns. After modelling, the original shear walls were analyzed by means of an iterative process according to the previously defined load pattern. Modelling of repaired/retrofitted shear walls was based on the model of the original wall and included engagement and disengagement of unstressed new materials and damaged elements, respectively. The engagement-disengagement process ensured proper calculation of strains and stresses in the new materials. Analysis of the repaired shear wall was similar to the analysis of the original wall; however, it started at a stage in which the shear wall was already damaged and strains and stresses were carried forward in the elements that remained engaged.

In general, the following constitutive models were selected for the numerical investigation; therefore, they are recommended for analyses of original and repaired/retrofitted shear walls. For the pre-peak compression response of concrete: Smith-Young for low strength concrete, f'_c lower than 22 MPa; Popovics NSC for normal strength concrete, f'_c ranging from 22 MPa to 45 MPa; and Popovics HSC response for high strength concrete, f'_c greater than 45 MPa. For concrete confinement: base curve compression post-peak response for unconfined to lightly confined concrete members; and Modified Park-Kent compression post-peak response for concrete elements with sufficient confinement. Other models include: Vecchio's 1992-A model for compression softening, modified Bentz tension stiffening model for tension stiffening effects, linear model for tension softening, Kupfer/Richard model for confinement of concrete, modified Kupfer for the lateral expansion or dilatation of concrete, Mohr-Coulomb stress model for cracking criterion, Vecchio-Collins 1986

model for crack slip check, 20% aggregate size limit for crack width check, Vecchio-Lai model for slip distortion (DSFM), and nonlinear with cyclic decay model for concrete hysteretic response. Suggested models for reinforcement include: Seckin model for reinforcement hysteretic response; and Tassio crack-slip model for dowel action. The Asatsu model can be used for the simulation of buckling of reinforcement; however, this phenomenon was not considered in the analyses reported in this thesis. The effect of bond can be simulated with: Eligehausen model for bonding of FRP and steel plates/sheets; and Fujii model for delay mechanisms or gap mechanisms for reinforcement.

Replacement of concrete technique was the most straightforward to model. Modelling of the original walls consisted of engaging elements corresponding to the original concrete and disengaging elements corresponding to the repair and retrofitting concrete. After analysis of the original wall, the repair and retrofitting technique was simulated by disengaging the elements representing the replaced concrete, and engaging the elements representing the new concrete. The replacement of concrete technique was assessed with the analysis of Walls B5R, B9R, DP1R and RLSW3. The predictions of the repaired walls (B5R, B9R, DP1R, and RLSW3) and the corresponding original walls (B5, B9, DP1, and LSW3) were in excellent agreement with experimental observations.

Retrofitting through the addition of reinforcing bars included repair of the damaged concrete; therefore, the modelling technique was similar to that implemented for replacement of concrete, in addition to the use of truss bars elements to represent the addition of reinforcing bars. The retrofitting reinforcing bars were modelled with truss bars and assumed perfectly bonded to the concrete elements only at their ends. The truss bars elements were disengaged during the analysis of the original wall. Repair/retrofitting was simulated at the end of the analysis of the original wall by engaging originally disengaged truss bars elements. The technique was successfully applied to Wall B11R.

External bonding of steel plates was modelled with truss bars elements connected to the concrete elements with link-bond elements to simulate the effect of bond slip. The

link-bond elements were attached to the concrete nodes and the truss bar nodes at the same coordinate position. Furthermore, the extremities of the plates were assumed perfectly bonded; therefore, the end nodes of the truss bar elements were directly attached to the concrete elements without link-bond elements. Retrofitting was simulated by engaging previously disengaged truss elements representing the external steel plates and link-bond elements. The external steel plate bonding retrofitting technique was adequately simulated as demonstrated by the predictions of Walls IC-SWR24, IC-SW32 and IC-SWR35. However, the lateral displacement was somewhat overestimated.

Retrofitting with the addition of unbonded steel rods and plates with delay mechanism was modelled with truss bars elements, representing the steel rods and plates, connected to the concrete elements by link-bond elements. The properties of the link-bond elements were developed to permit load transfer from the steel rods or plates to the foundation after an initial gap was exhausted. Analysis of shear walls modelled with this retrofitting technique, Walls IC-SW31 and IC-SW34, captured the strength, displacement and failure mechanism, as well as the displacement corresponding to the engagement of the rods and plates.

Bonding of external FRP as a retrofitting technique was simulated with truss bar elements connected to the concrete elements according to the bonding condition. For perfect bonding of FRP, the truss bar elements were directly attached to the concrete elements without incorporating link-bond elements. For other FRP bonding conditions, the truss bar elements were connected to the concrete elements by means of link-bond elements. The truss and link-bond elements corresponding to the FRP and bonding material, respectively, were disengaged during analysis of the original wall. At the end of the initial analysis, the retrofitting was simulated by engaging the truss and link-bond elements. The analytical results of Walls FRPLSW1 and FRPMSW1 validated the applicability of the model.

Local replacement of concrete repair technique was simulated following the same procedure described for the replacement of concrete technique. Although some minor discrepancies were found in the prediction of the lateral displacement of Walls

Summary and Conclusions

SW31R, SW32R and SW33R, accurate results in terms of lateral strength capacity and failure mode corroborated the simulation technique.

Bolting of external steel plates was modelled with perfectly bonded ductile and tension-only truss bar elements. The latter was used to simulate steel plates that buckled at an early stage of testing. Simulation of the retrofitting technique did not include modelling of the buckling phenomenon; however, the simulation was a success as confirmed by the accurate predictions of Walls W11RP and W11R.

6.2 Conclusions

This study presented results of shear walls modelled with the finite element method using Program Vector2. Modelling procedures were developed for shear walls repaired and or retrofitted with different techniques ranging from conventional replacement of concrete to external bonding of FRP. Salient parameters of seismic response were assessed: maximum strength, maximum lateral displacement, failure mechanism, energy dissipation, stiffness, and hysteretic response. In general, strong correlation between the analytical and experimental results was demonstrated. Some discrepancies were obtained, specifically in those walls where information of the materials properties was either incomplete or not entirely clear. Generally, the response of shear walls with low aspect ratio was more difficult to capture, and this was magnified when a new material was added such as steel plates or FPR sheets. Repaired Wall DP1R was further challenging due to the three dimensional geometry of the wall. The nonlinear FEM program VecTor2 was capable of modelling repair and/or retrofitting of shear walls effectively by using simple finite elements, demonstrating that accuracy of results is not necessarily sacrificed when using FEM programs with low powered levels. Link-bond elements performed well when modelling externally bonded FRP and steel plates/sheets, and also in the simulation of delay mechanisms. This demonstrated the adaptability and versatility of VecTor2, particularly in those cases where new or novel techniques were implemented. Therefore, the research conducted herein demonstrated that FEM procedures can

provide accurate simulations of repaired and/or retrofitted shear walls given a good analysis program and comprehensive models for material and structural behaviour.

Further work is necessary to improve the accuracy of the predictions, specifically in the post-peak range of walls governed by shear-related mechanisms. Additionally, further studies are required to address other emerging materials such as shape memory alloys (SMA) for repair and/or retrofitting of reinforced concrete structures. These studies could include earthquake ground motions and dynamic loading to better simulate the seismic phenomenon.

References

Antoniades, K. K., Salonikios, T. N., and Kappos, A. J. (2003). Cyclic tests on seismically damaged reinforced concrete walls strengthened using fiber-reinforced polymer reinforcement. *ACI Structural Journal, 100*(4), 510-518.

Antoniades, K. K., Salonikios, T. N., and Kappos, A. J. (2005). Tests on seismically damaged reinforced concrete walls repaired and strengthened using fiber-reinforced polymers. *Journal of Composites for Construction, 9*(3), 236-246.

Aprile, A., Spacone, E., and Limkatanyu, S. (2001). Role of bond in RC beams strengthened with steel and FRP plates. *Journal of Structural Engineering, 127*(12), 1445-1452.

Arduini, M., Di Tommaso, A., and Nanni, A. (1997). Brittle failure in FRP plate and sheet bonded beams. *ACI Structural Journal, 94*(4), 363-370.

Bentz, E. C. (2000). Sectional analysis of reinforced concrete members. (Ph.D. Thesis, University of Toronto). Toronto, ON, Canada.

Buyle-Bodin, F., David, E., and Ragneau, E. (2002). Finite element modelling of flexural behaviour of externally bonded CFRP reinforced concrete structures. *Engineering Structures, 24*(11), 1423-1429.

References

Clough, R. W. (1960). The finite element method in plane stress analysis. *Proceedings of Second ASCE Conference on Electronic Computation* (pp. 345-378), Pittsburg, PA, USA: American Society of Civil Engineering.

Courant, R. (1943). Variational methods for the solution of problems of equilibrium and vibrations. *Bull. Amer. Math. Soc., 49*, 1-23.

Desroches, R., and Smith, B. (2004). Shape memory alloys in seismic resistant design and retrofit: A critical review of their potential and limitations. *Journal of Earthquake Engineering, 8*(3), 415-429.

Elnashai, A. S., and Pinho, R. (1998). Repair and retrofitting of RC walls using selective techniques. *Journal of Earthquake Engineering, 2*(4), 525-568.

Elnashai, A. S., and Salama, A. I. (1992). *Selective repair and retrofitting techniques for RC structures in seismic regions* (Research Report ESEE/92-2). London, England: Engineering Seismology and Earthquake Engineering Section, Imperial College.

Fintel, M. (1991). Shearwalls - an answer for seismic resistance? *Concrete International, 13*(7), 48-53.

Fiorato, A. E., Oesterle, R. G., and Corley, W. G. (1983). Behavior of earthquake resistant structural walls before and after repair. *ACI Journal, 80*(5), 403-413.

Haroun, M., Pardoen, G., Bhatia, H., Shahi, S., and Kazanjy, R. (2000). Structural behavior of repaired pier walls. *ACI Structural Journal, 97*(2), 259-267.

Hii, A. K. Y., and Al-Mahaidi, R. (2006). An experimental and numerical investigation on torsional strengthening of solid and box-section RC beams using CFRP laminates. *Composite Structures, 75*(1-4), 213-221.

References

Kachlakev, D., Miller, T., and Yim, S. (2001). *Finite element modeling of reinforced concrete structures strengthened with FRP laminates* (Final Report SPR 316). Washington, DC: Oregon Department of Transportation.

Khalil, A., and Ghobarah, A. (2005). Behaviour of rehabilitated structural walls. *Journal of Earthquake Engineering, 9*(3), 371-391.

Lefas, I. (1988). Behaviour of reinforced concrete walls and its implication for ultimate limit state design. (Ph.D. Thesis, Imperial College, University of London). London, England.

Lefas, I. D., and Kotsovos, M. D. (1990). Strength and deformation characteristics of reinforced concrete walls under load reversals. *ACI Structural Journal, 87*(6), 716-726.

Li, Z. J., Balendra, T., Tan, K. H., and Kong, K. H. (2005). Finite element modeling of cyclic behavior of shear wall structure retrofitted using GFRP. *Proceedings of 7th International Symposium on Fibre-Reinforced Composite Reinforcement for Concrete Structures-FRPRCS-7, SP-230 Vol 1* (499-514). Kansas City, MO, USA: American Concrete Institution.

Liao, W. I., Effendy, E., Song, G., Mo, Y. L., Hsu, T. T. C., and Loh, C. H. (2006). Effect of SMA bars on cyclic behaviour of low-rise shear walls. *Smart Structures and Materials 2006: Sensors and Smart Structures Technologies for Civil, Mechanical, and Aerospace Systems, Proceedings of SPIE Vol 6174* (61743H, pp. 1-8). San Diego, CA, USA: SPIE.

Lombard, J., Lau, D. T., Humar, J. L., Foo, S., and Cheung, M. S. (2000). Seismic strengthening and repair of reinforced concrete shear walls. *Proceeding of 12th World Conference on Earthquake Engineering [CD-ROM]* (2032, pp. 1-8). Auckland, New Zealand: New Zealand Society for Earthquake Engineering.

References

Mohele, J. P. (2000). State of research on seismic retrofit of concrete building structures in the US. *US-Japan Symposium and Workshop on Seismic Retrofit of Concrete Structures-State of Research and Practice.* Berkeley, CA, USA: Pacific Earthquake Research Center.

Ngo, D., and Scordelis, A. C. (1967). Finite element analysis of reinforced concrete beams. *ACI Journal, 64*(3), 152-163.

Nilson, A. H. (1968). Nonlinear analysis of reinforced concrete by the finite element method. *ACI Journal, 65*(9), 757-766.

Oesterle, R. G., Aristizabal-Ochoa, J. D., Fiorato, A. E., Russell, H. G., and Corley, W. G. (1979). *Earthquake resistant structural walls - tests of isolated walls, phase II* (Report to National Science Foundation). Skokie, IL, USA: Portland Cement Association.

Oesterle, R. G., Fiorato, A. E., Johal, L. S., Carpenter, J. E., Russell, H. G., and Corley, W. G. (1976). *Earthquake-resistant structural walls - tests of isolated walls* (Report to National Science Foundation). Skokie, IL, USA: Portland Cement Association Engineering.

Palermo, D., and Vecchio, F. J. (2002). Behavior of three-dimensional reinforced concrete shear walls. *ACI Structural Journal, 99*(1), 81-89.

Palermo, D., and Vecchio, F. J. (2004). Compression field modeling of reinforced concrete subjected to reversed loading: Verification. *ACI Structural Journal, 101*(2), 155-164.

Palermo, D., and Vecchio, F. J. (2007). Simulation of cyclically loaded concrete structures based on the finite-element method. *Journal of Structural Engineering, 133*(5), 728-738.

Paterson, J., and Mitchell, D. (2003). Seismic retrofit of shear walls with headed bars and carbon fiber wrap. *Journal of Structural Engineering, 129*(5), 606-614.

References

Paulay, T., Priestley, M. J. N., and Synge, A. J. (1982). Ductility in earthquake resisting squat shearwalls. *ACI Journal, 79*(4), 257-269.

Pham, H. B., and Al-Mahaidi, R. (2005). Finite-element modelling of RC beams retrofitted with CFRP fabrics. *Proceedings of 7th International Symposium on Fibre-Reinforced Composite Reinforcement for Concrete Structures-FRPRCS-7, SP-230 Vol 1* (499-514). Kansas City, MO, USA: American Concrete Institution.

Rahimi, H., and Hutchinson, A. (2001). Concrete beams strengthened with externally bonded FRP plates. *Journal of Composites for Construction, 5*(1), 44-56.

Ritter, W. (1899). Die bauweise hennebique. *Schweizerische Bauzeitung, 33*(7), 59-61.

Ritz, W. (1909). Über eine neue methode zur lösung gewisser variationsprobleme der mathematischen physik. *J.Reine Angew.Math., 135*(1), 1-61.

Sato, Y., and Vecchio, F. J. (2003). Tension stiffening and crack formation in reinforced concrete members with fiber-reinforced polymer sheets. *Journal of Structural Engineering, 129*(6), 717-724.

Schlaich, J., Schäfer, K., and Jennewein, M. (1987). Toward a consistent design of structural concrete. *PCI Journal, 32*(3), 74-150.

Smith, G. M., and Young, L. E. (1955). Ultimate theory in flexure by exponential function. *ACI Journal, 52*(3), 349-359.

Taghdi, M., Bruneau, M., and Saatcioglu, M. (2000). Analysis and design of low-rise masonry and concrete walls retrofitted using steel strips. *Journal of Structural Engineering, 126*(9), 1026-1032.

Taghdi, M., Bruneau, M., and Saatcioglu, M. (2000). Seismic retrofitting of low-rise masonry and concrete walls using steel strips. *Journal of Structural Engineering, 126*(9), 1017-1025.

References

Thermou, G. E., and Elnashai, A. S. (2006). Seismic retrofit schemes for RC structures and local-global consequences. *Progress in Structural Engineering and Materials, 8*(1), 1-15.

Vecchio, F. J. (2000). Disturbed stress field model for reinforced concrete: Formulation. *Journal of Structural Engineering, 126*(9), 1070-1077.

Vecchio, F. J., and Bucci, F. (1999). Analysis of repaired reinforced concrete structures. *Journal of Structural Engineering, 125*(6), 644-652.

Vecchio, F. J., Haro de la Peña, O. A., Bucci, F., and Palermo, D. (2002). Behavior of repaired cyclically loaded shearwalls. *ACI Structural Journal, 99*(3), 327-334.

Vecchio, F. J. (1989). Nonlinear finite element analysis of reinforced concrete membranes. *ACI Structural Journal, 86*(1), 26-35.

Vecchio, F. J., and Collins, M. P. (1986). The modified compression-field theory for reinforced concrete elements subjected to shear. *ACI Journal, 83*(2), 219-231.

Walraven, J. C. (1981). Fundamental analysis of aggregate interlock. *ASCE Journal of the Structural Division, 107*(11), 2245-2270.

Wong, P. S., and Vecchio, F. J. (2002). *VecTor2 and FormWorks user's manual* (Publication No. 2002-02). Toronto, ON, Canada: University of Toronto, Department of Civil Engineering.

Wong, R. S. Y., and Vecchio, F. J. (2003). Towards modeling of reinforced concrete members with externally bonded fiber-reinforced polymer composites. *ACI Structural Journal, 100*(1), 47-55.